Experimental Investigation of Magnetohydrodynamic Flow For An Intense Proton Target

A Dissertation Presented

by

Hee Jin Park

to

The Graduate School

in Partial Fulfillment of the

Requirements

for the Degree of

Doctor of Philosophy

in

Mechanical Engineering

Stony Brook University

December 2009

Stony Brook University

The Graduate School

Hee Jin Park

We, the dissertation committee for the above candidate for the

Doctor of Philosophy degree,

hereby recommend acceptance of this dissertation.

Harold G. Kirk, Dissertation Co-Advisor,
Physicist, Department of Physics, Brookhaven National Laboratory

Foluso Ladeinde, Dissertation Co-Advisor,
Professor, Department of Mechanical Engineering

Thomas Cubaud, Chairperson of Defense,
Professor, Department of Mechanical Engineering

Kirk T. McDonald , Outside Member,
Professor, Physics Department, Princeton University

James Glimm, Outside Member,
Professor, Department of Applied Math. & Stat., Stonybrook University

This dissertation is accepted by the Graduate School.

Lawrence Martin
Dean of the Graduate School

ii

Abstract of the Dissertation

Experimental Investigation of Magnetohydrodynamic Flow For An Intense Proton Target

by

Hee Jin Park

Doctor of Philosophy

in

Mechanical Engineering

Stony Brook University

2009

Efficient production of pions can be achieved by colliding an intense proton beam with a high-Z target. It is required to investigate the effect of Hg jet disruption by the interaction of an intense proton beam for high power target design. The experiment of mercury (Hg) jet on the interaction of an intense proton beam in magnetic fields has been carried out. The primary diagnostics in the experiment employed the technique of back-illuminated laser shadow photography to freeze the transient events. The images are recorded by several high speed cameras. The performance of the optical diagnostic system is presented. Flowing mercury in magnetic fields causes induced currents, which produce distortions of the mercury jet. The various effects of Lorentz force induced by magnetic field to liquid flow is investigated in a stability analysis

iii

50   of the conducting flow in the presence of magnetic fields. Also, the role of

51   joule damping as a loss on a time scale of magnetic damping term in global

52   kinetic energy is discussed. Quantitative and qualitative data analysis using

53   image processing based on statistic approach is described. The experimental

54   measurements of jet distortion as well as flowing velocity of Hg jet in magnetic

55   fields through image processing are presented. In experiment, it is observed

56   that the imposition of magnetic field tends to suppress the fluctuating motion

57   in Hg jet and correspondingly the jet surface is more stabilized, where Re is

58   turbulent and Re_m is 0.26. Numerical Monte Carlo simulation for calculation

59   of energy deposition by proton beam to Hg jet in magnetic fields is performed

60   based on the jet shape, trajectory, and proton beam spot size from experiment.

61   The jet disruption, the filament velocity on the jet surface by the impact of

62   high energy of protons up to 30 Tp, and magnetic field effect to its suppression

63   up to 15 T as well as energy deposition to Hg jet are presented. Finally, the

64   experimental results investigate the performance and feasibility of utilizing

65   liquid jet as a high power target for future particle accelerator.

Table of Contents

vii

List of Figures

xviii

List of Tables

ACKNOWLEDGEMENTS

Nomenclature

B	Magnetic induction field, T (Wb/m^2)
H	Magnetic field, A/m
E	Electric field, N/C (V/m); Global kinetic energy, J
J	Current density, A/m^2
V	Electric potential, V
D	Electric displacement field, C/m^2; Energy dissipation, J/s
P	Polarization density, C/m^2; Probability; Particle momentum, $J \cdot s/m$
M	Magnetization density, $J/(T\ m^3)$
J	Jacobian matrix
T	Temperature, °C (K); Time, s
B$_o$	Applied magnetic field, T (Wb/m^2)
v	Directional fluid velocity, m/s; Mean velocity, m/s
U	Mean velocity in the x coordinate direction, m/s
e	Specific internal energy, J/kg
$x,\ y,\ z$	Cartesian coordinates, m
μ	Magnetic permeability, H/m (N/A^2)
ε	Electrical permittivity, F/m $(C^2/(N\ m^2))$
χ_e	Electrical susceptibility
χ_m	Magnetic susceptibility
ε_o	Electrical permittivity of free space, F/m $(C^2/(N\ m^2))$
μ_o	Magnetic permeability of free space, H/m (N/A^2)
t	Time, s
ϵ	Amplitude of a sinusoidal wave, m

α_v	Volume coefficient of thermal expansion, K^{-1}
c_p, c_v	Specific heat capacity, $J/(g\ K)$
λ	Wavelength of a sinusoidal wave, m
c	Wave velocity, m/s
p	Pressure, N/m^2
ρ	Density, kg/m^3
g	Gravity, m/s^2
M	Mass, kg; Molar mass, g/mol
ζ	Intermittency factor
Γ	Surface tension, N/m
γ	Ratio of specific heats, c_p/c_v
η	Absolute viscosity, $kg/(m\ s)$
ν	Kinematic viscosity, η/ρ, m^2/s
σ	Electrical conductivity, S/m; Standard deviation
κ	Compressibility, m^2/N
L	Characteristic length; Pipe length, m
τ	Joule damping term
I_T	Initial intensity of light, cd
I_o	Intensity of light, cd
ω	Vorticity, s^{-1}
ψ	Stream function, m^2/s
ϕ	Velocity potential, m^2/s
ϕ_E	Electric potential, V
E_{dep}	Energy deposition, J/g
f	Focal length, m; Force, N; Friction factor

τ	Wall shear stress, N/m^2
ξ	free surface perturbation, m
h	Head loss, m
K	Loss coefficient; Bulk modulus, N/m^2
A	Cross sectional area, m^2
e	Surface roughness, m; Error, %
a	Radius of circular pipe, Radius of jet, m
c	Local speed of sound, m/s
d	Diameter of circular pipe, Diameter of nozzle, m
D	Diameter of jet, m
R	Gas constant, $J/(K\ mol)$; Radius of curvature of the centerline of the elbow, m
G	Pressure ratio
C	Contraction coefficient; Discharge coefficient; Constant
Q	Flow rate, m^3/s
r	Residual; Radial coordinates
β	Ratio of diameter
Re_m	Magnetic Reynolds number
Re	Reynolds number
Fr	Froude number
Al	Alfv en Number
Ha	Hartmann number
We	Weber number
N	Stuart number; Number of events; Augmented Jacobian matrix
$\nabla\cdot$	Divergence operator
$\nabla\times$	Curl operator

$\times$	Cross product operator
$\cdot$	Inner product operator; Multiplication

Superscripts

$'$	Differentiation with respect to variable; Perturbation; Fluctuation
$\cdot$	Differentiation with respect to time

Subscripts

x, y, z	Component values over the cartesian coordinates
o	Component mean value, Initial value at the nozzle
R	Reference location
a	Air
l	Liquid
T	Transpose of matrix

Chapter 1

Introduction

Accelerator-based sources of exceptionally intense, tightly focused beams of x rays and ultraviolet radiation make possible both basic and applied research in fields from physics to biology to technology that are not possible with more conventional equipment. The development of a high-intensity source of muons can be useful for the production of high-energy neutrino, thereby opening the door for a broad range of important new physics experiments such as neutrino oscillation. The concept is to use a high-intensity proton beam incident on a mercury jet to produce pions which decay to give the muons. These muons is magnetically captured, accelerated, and then inserted into a storage ring.

1.1 Neutrino Factory For High Power Neutrino Beam

1.1.1 The concept of neutrino factory

Accelerators are used to accelerate primary particle beams such as protons and electrons. The required statistics in the collision processes demand a very

1

high flux of primary particles. On interaction of the primary particles with a target, it is possible to produce secondary beams of elementary particles like pions, neutrons, and gammas. Primary protons pass through a linear accelerator and further through a synchrotron, bunch compressors, and accumulators to achieve a beam with a certain energy, intensity and beam structure. This beam is directed toward a target. On interaction with the target, secondary particles of different kinds are produced. A neutrino factory is the ultimate tool for producing a high-intensity neutrino beam to study neutrino oscillations. The neutrino factory is based on a new concept of an accelerator that produces a high-intensity, high-energy beam of muon and electron neutrinos. It will allow an investigation of a new domain in neutrino physics such as

- High intensity. Its flux is 10^3 times greater than conventional neutrino beams.

- High energy. It features a very high beam energy of 20 to 50 GeV.

- In a neutrino factory, the muon sign can be selected. Thus, it is possible to deliver particles and anti-particles.

The basic concept of the Neutrino Factory is the production of muon neutrinos and anti-electron neutrinos from the decay of muons that are circulating in a storage ring. An intense proton beam is delivered to a target, where pions are produced. These pions are collected in a solenoidal magnetic field, which can capture both charged states of pions. The pions decay into muons in a decay channel. The muon beam has both a large energy spread and trans-

2

587 verse emittance. The energy spread is reduced using a phase rotation, while
588 emittance is improved by ionization cooling. The cooled beam is accelerated
589 to energies of 20 to 50 GeV and injected into a storage ring.

1.1.2 Neutrino physics

591   Muons cannot be produced directly, so pions have to be produced first.
592 The first stage of a neutrino factory is thus a high-power proton driver that
593 deliver protons onto a target, where pions are produced. These pions have
594 to be collected and transported. After about 20 m, most of the pions decay
595 into muons. A neutrino beam can be produced from the decay of high-energy
596 muons:

597   • Pions from $Proton + Material \longrightarrow \pi^{\pm} + X$

598   • Muons from $\pi^{\pm} \longrightarrow \mu^{\pm}\nu_{\mu}(\overline{\nu_{\mu}})$

599   • Neutrinos from $\mu^{\pm} \longrightarrow e^{\pm}\overline{\nu_{\mu}}\nu_{e}(\nu_{\mu}\overline{\nu_{e}})$

600   At this stage, the muon beam has a low phase space density and resembles
601 more a cloud than a beam. Phase rotation as well as ionization cooling is
602 applied to reduce the energy spread and the emittance of the muon beam.
603   Once the beam is cooled, it can be accelerated to a final energy of 20 to
604 50 GeV. In the final stage of a neutrino factory, the accelerated muons are
605 injected into a storage ring with long straight sections.

1.2 A High Power Target For Neutrino Factory

1.2.1 Material consideration for a high power target

The intensity of muon beam is directly proportional to the power of the proton beam which initiates the process. Considering that a high intensity proton beam is required in order to generate the required muons, the choice of the target material becomes a particularly important issue. Modeling studies (Osaki, Palmer, Zisman, Gallardo, 2001) point to high-Z materials being more efficient at producing pions of both signs, whereas low-Z materials are better at preventing the absorption of the produced pions. The pion yield per proton increases with the atomic number of the target, as shown in Fig. 1.1 from MARS calculation. A high-Z material is desirable because the pion production cross-section increases with increasing Z. However, the intense proton beam would melt a target made of a solid high-Z material. A target system using a flowing stream of mercury could recycle the spent target. Several types of target material have been proposed including copper, graphite, and mercury.

Since these targets are envisaged as being stationary, one must consider the problem of removing the energy deposited by the beam without interfering with the production of the particles.

1.2.2 Moving metallic target for pion production

While schemes for moving solid targets can be envisaged (Thieberger, Kirk, Weggel, McDonald, 2003), a flowing liquid target is simpler, and mercury as a high Z material presents itself as the liquid metal. The liquid target should be in the form of a free jet, rather than being confined in containment, since the beam-induced cavitation of the liquid metal can be destructive to solid walls in the immediate vicinity of the interaction region. Another issue associated with the proton beam is the effect of the energy that it deposits in the target. The temperature of the target rises almost instantaneously after the beam pulse, resulting in large internal stresses that might crack a solid target or disperse a liquid target (Kirk *et al*, 2001). In the case of a liquid jet target, the dispersal of the jet by the beam should not be destructive to the surrounding target system components and should not adversely affect pion production during subsequent beam pulses, either on the microsecond scale, if several micro-pulses are extracted from a proton synchrotron, or on the scale of the macro-pulse period. The operation of a liquid metal jet inside a strong magnetic field raises several magnetohydrodynamic issues such as possible deformation of the jet's shape and trajectory, as well as the effect of the magnetic field on the beam-induced dispersal of the jet.

1.2.3 Free mercury jet flow in magnetic field for a high power target

The free mercury jet in magnetic field is proposed for a high power target to overcome the issues described in the above chapter. The concept is to use a high intensity proton beam incident on a Hg jet to produce pions which decay to give the muons (Gabriel *et al*, 2001). The key elements of the target system are an intense proton source, mercury jet, and capture of the generated pions in a high field solenoidal magnet (McDonald, 2001). The schematics of the key elements of the target system is described in Fig. 1.3.

Previous studies (Osaki, Palmer, Zisman, Gallaro, 2001) indicated that pion yield is maximized with a mercury target in the form of a 1 cm diameter at the interacting center, tilted by about 150 milliradian with respect to the magnetic axis. The target is tilted with respect to the axis of the capture solenoid, thus permitting the pions, whose trajectories are spirals, to leave the side of the target with a minimal probability for re-entering the target volume. The pion yield per proton increases with the atomic number of the target, as shown in Fig. 1.1 from MARS calculation. For 24 GeV protons, a high-Z target is superior in yield. As the pions emerge from the target at large angles to the beam, and follow helical paths that may intersect the target at more than one point, it is advantageous for the target to be in the form of a narrow rod, tilted at a small angle to the magnetic axis. As shown in Fig. 1.2, suitable parameters for a mercury target are a tilt angle of 150 mrad and a target radius of 5 mm.

667   Based on the previous studies described in the above, the experimental

668   setup parameters are determined. The layout of experimental setup is briefly

669   described in the below and will be more discussed in chapter 3. Fig. 1.4

670   shows the detailed schematic of the overlap between key components of the

671   experiment. The trajectory of the mercury jet overlaps with the proton beam

672   over 30 cm. The velocity of the jet is 15 m/s. The facility is a closed piping

673   loop, constructed primarily of 316 stainless steel, and designed to circulate

674   liquid mercury. The parameters of the proton beam and solenoid system are

675   determined by the required conditions of particle production rates (Alessi *et*

676   *al*, 1998). Basic system parameters consist of a proton energy 24 GeV, number

677   of protons in one pulse $\approx 3 \times 10^{13}$. Only $\sim 6 \sim 8$ % of beam energy is absorbed

678   inside the target. The solenoid length is 100 cm, inside radius is 7.5 cm, and a

679   maximum magnetic field is 15 T. The solenoid magnet is titled at 67 milliradian

680   angle with respect to the beam. The beam arrives at an angle 34 milliradian

681   with respect to the jet which has a radius ≈ 0.5 cm, as schematically shown

682   in Fig. 1.4. The 24 GeV proton beam is directed on to the solenoid at 67

683   milliradian off the solenoid axis, so that most high momentum particles do

684   not travel straight down the beam line (Gallardo *et al*, 2001). If there are

685   no magnetic and gravitational effects on the mercury jet trajectory, the beam

686   should enter at the bottom surface of Hg jet at Viewport 1, which is located

687   at approximately 30 cm from the nozzle and the beam should exit on the top

688   surface of Hg jet at Viewport 3, which is located at approximately 60 cm from

689   the nozzle. The required jet velocity is determined by two conditions: 1),

7

690 the need to replenish the target before the arrival of subsequent proton beam

691 pulse, and 2), it should be high enough to overcome the deceleration force

692 induced by Lorentz force (Hassanein, Kinkashbaev, 2001).

693   Initial tests involving the interaction of proton beams on mercury targets

694 were performed at the Brookhaven Alternating Gradient Synchrotron (AGS)

695 (Kirk *et al*, 2001), and continued at the CERN ISOLDE facility (Lettry *et*

696 *al*, 2003). The BNL test featured a 24 GeV proton beam interacting with a

697 free mercury jet with a nozzle diameter of 1 cm and a velocity of 2.5 m/s.

698 The delivered proton bunch was focused to <1 mm radius, resulting in a peak

699 energy deposition of 80 J/g, delivering 24 GeV proton beam at 15 Hz (Tsoupas

700 *et al*, 2003). These initial tests did not have a magnetic field on the target.

701 A parallel effort was undertaken to study the effects of high velocity mercury

702 jets in the presence of high-magnetic fields, but with no proton beam.

1.2.4   Impact of the MHD mercury jet experiment for an intense proton target

703
704

705   The previous experiments did not perform the mercury jet in a high mag-

706 netic field interacting with an intense proton beam. In this work, we integrated

707 the mercury jet, solenoid magnet, and intense proton beam all together. The

708 performance and feasibility of utilizing liquid metal jet as a target for an in-

709 tense proton beam is explored experimentally, which is an explicit objective

710 of the experiment. The liquid jet target concept is recyclability otherwise the

711 target would be destroyed. Therefore, the power of the target has to be eval-

uated in terms of the replacing capability and validated experimentally. In order to validate the performance of the target, the MHD jet behavior in a strong magnetic field has to be investigated. The response of the mercury jet due to the energy deposition by interacting with an intense proton beam has to be studied and the magnetic field effect to the disruption of mercury jet has to be studied, as well. The experimental results reveals that the effect of the Lorentz force to the jet stabilization as well as the deflection of jet. The experimental results provide feasibility of utilizing liquid metal jet as a target for an intense proton beam. Also, the results validates the phenomenology of conduction flow in magnetic field based on the MHD theory.

1.3   Mercury Target Issues

1.3.1   Mercury jet disruption by energy deposition from an intense proton beam

The production of large fluxes of particles using high energy, high intensity proton pulses impinging on solid or liquid targets presents unique problems which have not yet been entirely solved. The large amount of power deposition required in the material coupled with the short pulse duration produce large, almost instantaneous local heating. The resulting sudden thermal expansion can result in damage causing stresses in solids and in the violent disruption of liquid jets. The volume expansion initiates vibrations in the material. The amplitude of these vibrations is such that stresses that exceed the strength of the material can be generated, causing mechanical failure (Thieberger *et al*,

734 2003).

735 The interaction of the proton beam with the mercury target leads to very

736 high heating rates in the target. When proton beam energy reaches approx-

737 imately 100 kJ/pulse range, the heat from the beam could melt or crack a

738 high-Z target.

1.3.2 Magnetohydrodynamic issues in mercury jet target

739

740

741 Liquid metal jets are proposed as potential target candidates because the

742 heat energy can be removed along with the moving liquid. There are three

743 important problems that are associated with the use of liquid metal targets

744 in these environments. First, as the liquid jet penetrates the magnetic field,

745 perturbations in jet motion and deceleration may occur because of the large

746 field gradients at the entrance and exit of the solenoid. Second, during the

747 intense pulse of energy deposition in a short time, the resultant stress could

748 break up the target. Third, the liquid jet can develop instabilities in the

749 strong inhomogeneous magnetic field and after beam interaction, because of

750 the jet break up induced by the energy deposition of beam. Theses instabilities

751 can change the jet shape into one that is significantly less efficient for pion

752 production (Hassanein, Kinkashbaev, 2001).

753 Mercury flow in a magnetic field experiences induced currents, which cause

754 the jet to produce transverse forces normal to jet axis direction resulting de-

755 flection normal to jet axis (Gallardo *et al*, 2001). In addition, axial currents

10

756 are induced if the jet axis does not coincide with the magnetic field axis. These

757 axial currents produce elliptical distortions of the mercury jet. Faraday's law

758 can be used to obtain the azimuthal current density from changing the axial

759 field in the local coordinate system of the Hg jet. The transverse component

760 of the magnetic field normal to the jet axis also varies along the trajectory

761 of the mercury jet. The axial current density can be related to the changing

762 transverse component of the magnetic field normal to the jet axis. These axial

763 currents produce a magnetic force. This force will be balanced by a restoring

764 force from the surface tension of the mercury, and with the condition that the

765 mercury is an incompressible liquid, will produce an elliptic deformation of

766 the mercury jet.

1.3.3 Overview of experimental investigation of MHD flow and discussion

769 A proof-of-principle experiment at the CERN Proton Synchrotron that

770 combined a free mercury jet target with a 15T solenoid magnet and a 24 GeV

771 primary proton beam was performed. The experiment validates the liquid type

772 of target for producing an intense secondary source of muons by showing the

773 jet repetition rate to replace the disrupted target by the energy deposition from

774 an intense proton beam. For the investigation of feasibility, various behavior of

775 mercury jet in magnetic field interacting with proton beam is reported based

776 on experimental measurement.

777 The PS runs in a harmonic-16 mode and can fill up to 2×10^{12} pro-

11

778   tons/bunch. This allows up to 30 $\times 10^{12}$ protons per pulse on the mercury

779   target, generating a peak energy deposition of 130 J/g. For this experiment,

780   a high magnetic field pulsed solenoid with a bore of 15 cm is designed. This

781   magnet is capable of delivering a pulsed peak field of 15 T, which is cooled to

782   80 K by liquid nitrogen to reduce the resistance of its copper coils. The Hg

783   jet delivery system generates a mercury jet from 1 cm diameter nozzle with

784   velocities up to 15 m/s. The primary diagnostic of the beam-jet interaction is

785   optical. A set of four view-ports along the interaction region is connected by

786   imaging fiber-optic bundles to four high speed cameras.

787   Each pulse of the proton beam delivered to this system constitutes a sep-

788   arate experiment. About 360 beam pulses are utilized in a beam-on-demand

789   mode at CERN. These pulses span a range of intensities and time intervals

790   between the multiple extracted bunches per pulse. The magnet operates over

791   a range of field strengths of 0   15 T.

792   In chapter 2, the full MHD governing equation using Maxwell's equations

793   are presented. Various modeling of conducting flow in a magnetic field are

794   formed, where the contribution of Lorentz force to the hydrodynamic equa-

795   tions is presented and discussed. The formulated and reviewed equations are

796   introduced to explain and understand MHD experimental results.

797   In chapter 3, the detailed layout of experimental setup and its installa-

798   tion are presented. The design of each key components for the experiment

799   is presented. As a primary diagnostics, the scientific development of optical

800   diagnostics employing the high speed cameras and infrared lasers to freeze the

801 transient motion of mercury jet is presented and the performance of the scien-

802 tific instrument as well as the methodology to capture images are discussed.

803   In chapter 4, 5, and 6, MHD behaviors of mercury jet in various magnetic

804 field are discussed based on the observation from experiment. Also, the char-

805 acteristics of mercury jet in magnetic field interacting with an intense proton

806 beam are presented, where the effect of magnetic field to suppression of dis-

807 ruption of jet and reducing of filament velocity are investigated to validate the

808 performance and feasibility of utilizing mercury jet as a high power target. The

809 key results to validate the feasibility of the High-Z liquid target is addressed

810 based on the experimental measurements and the beam pulse structures.

811   To conclude investigation MHD flow for an intense proton target, discus-

812 sion based on understanding from MHD equations in various literatures and

813 experimental results is summarized in chapter 7.
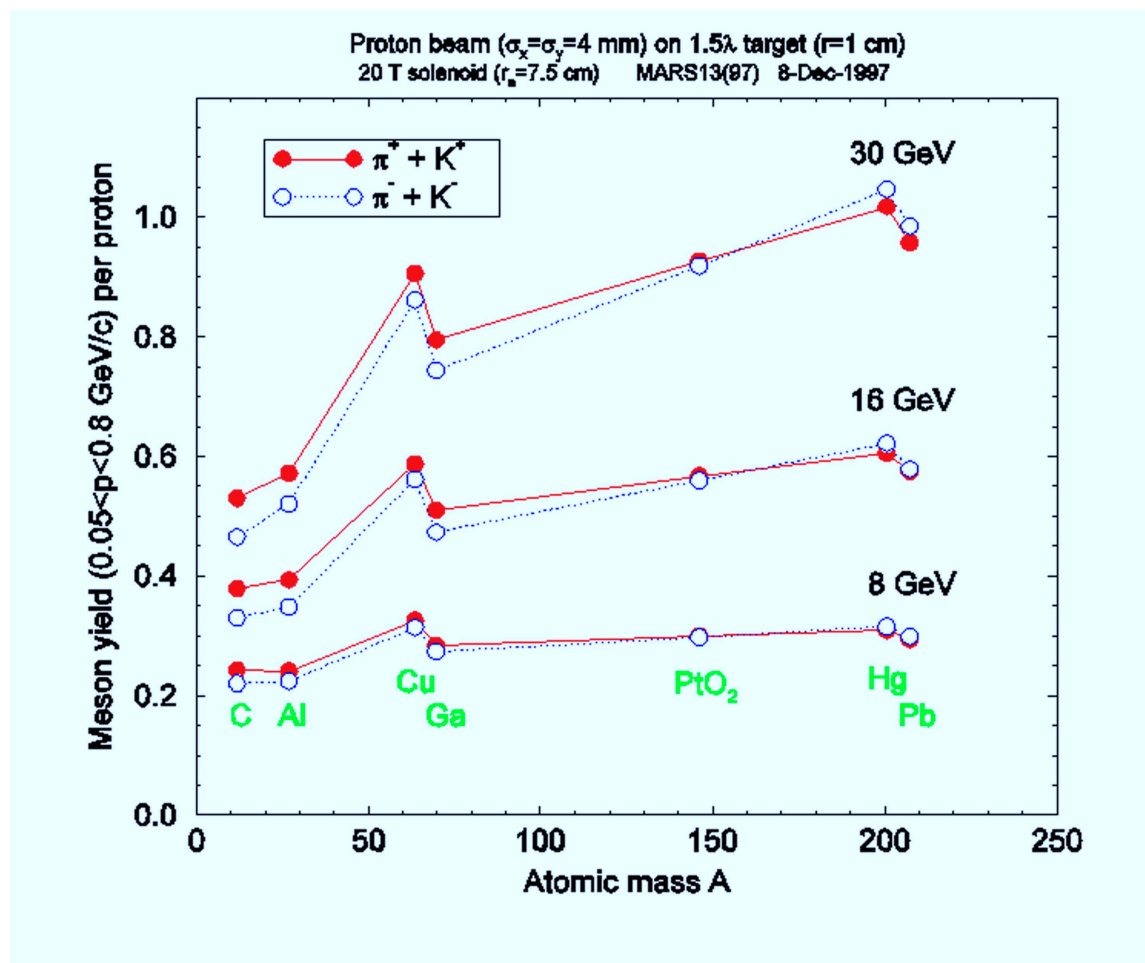
Figure 1.1: Pion yield versus atomic mass number of the target at three proton beam energies, Osaki (2001) and Mokhov (2000).
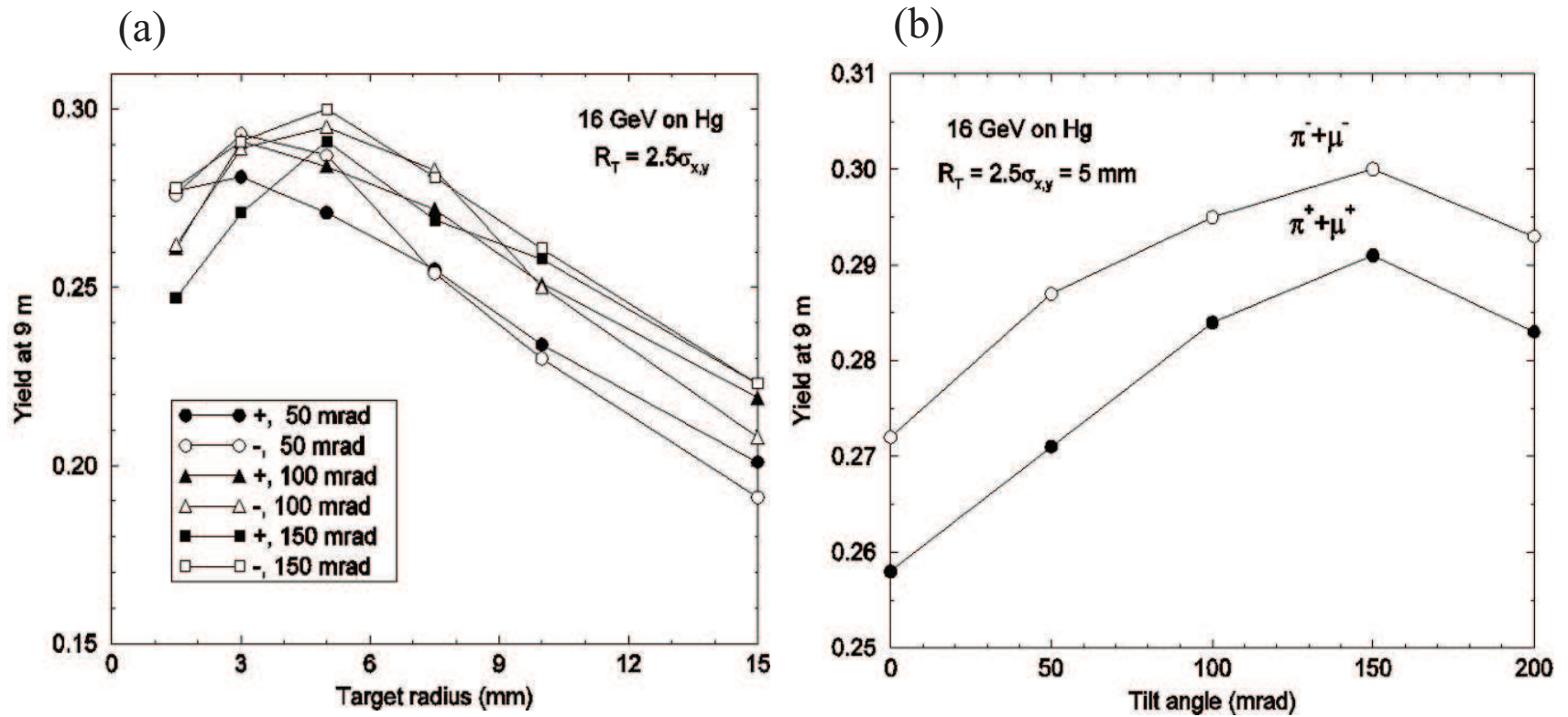
Figure 1.2: Pion yield from Hg targets versus tilt angle between the target/beam axis and the solenoid axis and versus the radius of the target, Osaki (2001) and Mokhov (2000). a.) Pion yield versus tilt angle. b.) Pion yield versus target radius.

(a)

Viewport 1 Viewport 2 Viewport 3 Viewport 4

Blue, Proton Beam at 7 mrad to magnet axis   Red, Magnet axis

(b) Mercury inlet pipe (OD=1")   Secondary containment (ID=6")

Green, Mercury jet at 33 mrad to magnet axis   Red, Magnet axis
Blue, Proton beam at 67 mrad to magnet axis
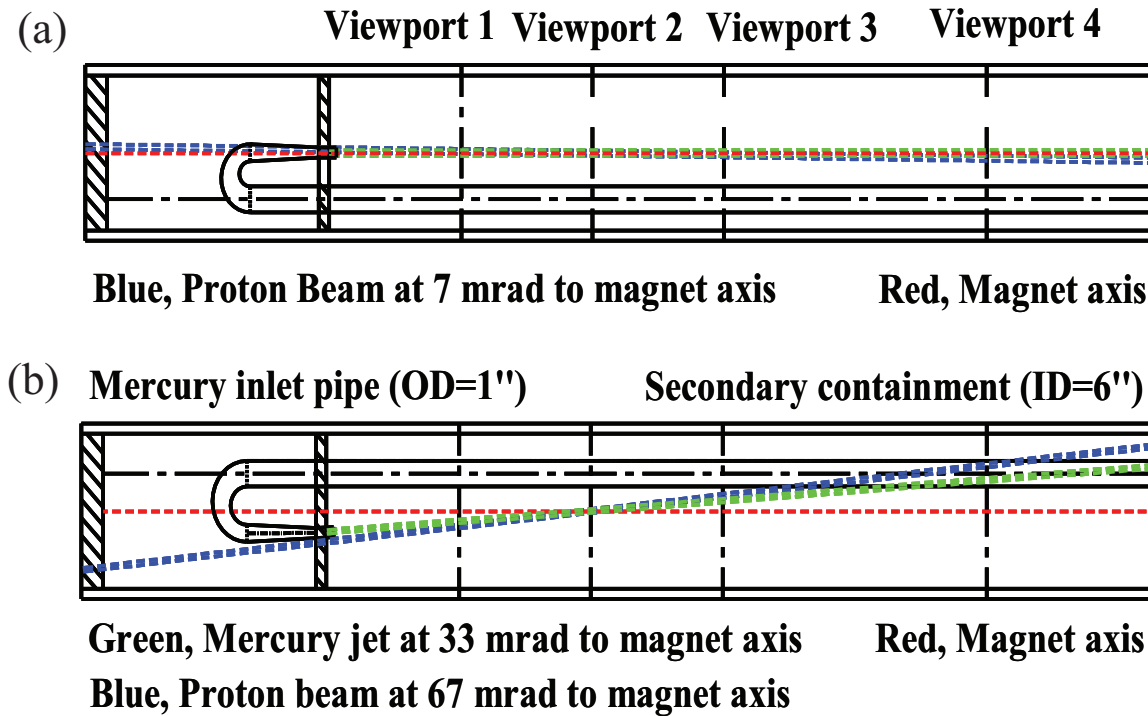
Figure 1.3: Geometry of key elements of target system and Viewports, showing the overlap between the mercury jet, magnetic axis, and the proton beam. a.) Top view. b.) Side view.
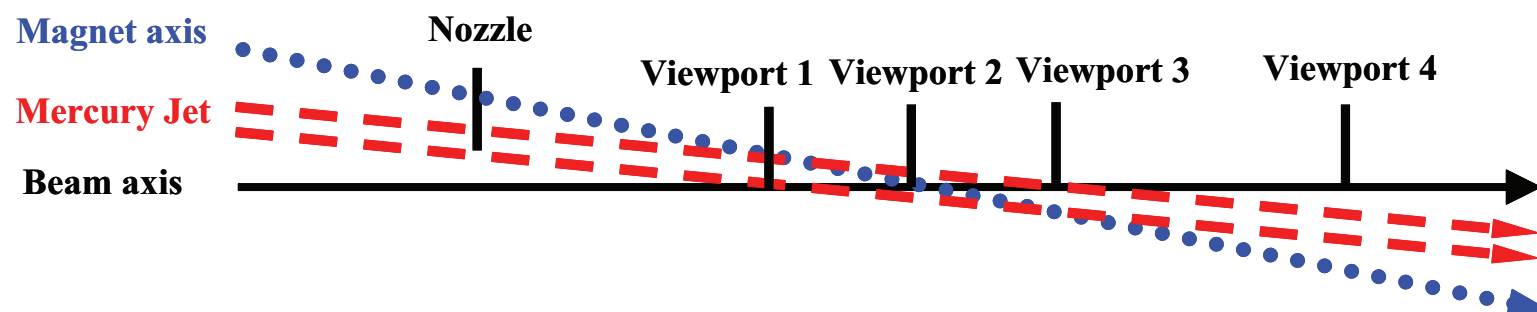
Figure 1.4: Schematics of the relative overelap between proton beam axis, Hg jet axis , and solenoid magnet axis.

Chapter 2

Magnetohydrodynamics of Conducting Flow in Magnetic Field

In this chapter, the issues of electrically conducting fluid in a pipe and jet flow in a magnetic field are presented. The governing equations for magnetohydrodynamics, based on electrodynamic relations of Maxwell's equation and hydrodynamic Navier-Stokes equation, are given and the effects of Lorenz force induced by magnetic field are discussed. The review of previous work provides a basis for these studies. Hartmann (1937) considered the flow between two parallel, infinite, non-conducting walls, with magnetic field applied normal to the walls. An exact solution was obtained for this case by Hartmann (1937). Shercliff (1953) solved the more general problem of three dimensional flow in a rectangular duct. Exact solutions demonstrated the fact that for large Hartmann number, the velocity distribution consists of a uniform core with a boundary layer near the walls. This result enabled the solution of the corresponding problem for a circular pipe in an approximate manner for large

832 Hartmann numbers, assuming walls of zero conductivities (Shercliff, 1956).

833 Chang and Lundgren (1961) considered the effects of wall conductivity for the

834 same problem. Gold (1962) considered a steady one-dimensional flow of an

835 incompressible, viscous, electrically conducting fluid through a circular pipe

836 in the presence of a uniform transverse field. A no-slip condition on the veloc-

837 ity is assumed at the electrically non-conducting wall because if the walls are

838 conducting, there is a electromagnetic force on the wall and a corresponding

839 force on thee fluid. The flow is along the z-axis, which coincides with the axis

840 of the cylinder, and the uniform applied magnetic field is along the x-axis,

841 which is normal to the flow direction. The solution is exact and valid for all

842 values of the Hartmann number. The conducting liquid jet inside a strong

843 magnetic field raises several magnetohydrodynamic(MHD) issues, such as the

844 possible deformation of the jet's shape and trajectory, as well as the effect of

845 the magnetic field on the beam-induced dispersal of the jet. The electrically

846 conducting flow moving in a magnetic field experiences induced currents (Gal-

847 lardo, 2002). These induced currents cause the jet to experience anisotropic

848 pressure distribution with respect to the major and minor axis of jet cross

849 section normal to the jet flowing axis while the jet penetrates the nonuniform

850 magnetic field (Gallardo, 2002). In addition, axial currents are induced if the

851 jet axis does not coincide with the magnetic field axis. These currents in turn

852 produce transverse elliptical distortions of the mercury jet. Finally, the liquid

853 jet can develop surface instabilities such as surface wavelength growing and jet

854 breakup during both liquid motion in a inhomogeneous magnetic field and af-

855 ter the interaction of intense proton beam, because of the Rayleigh instabilities

856 in a magnetic field and the sudden energy deposition leading to jet breakup.

857 These instabilities can change the jet shape into a significantly less efficient

858 target for pion production. The analytical approach to describe the behaviors

859 of MHD conducting flow in a magnetic field is provided in this chapter.

860 ## 2.1 Governing Equations for MHD Flow

861 ### 2.1.1 Electromagnetic equations

862 In this section, we describe the electromagnetic relations that have been

863 used in the derivation of the MHD governing equations. The following prop-

864 erties are defined as follows:

865 - polarization density $\mathbf{P}$: the vector field that expresses the density of

866 permanent or induced electric dipole moments in a dielectric material.

867 It is defined as the dipole moment per unit volume.

868 - magnetization density $\mathbf{M}$: the magnetic dipole moment per unit volume.

869 - electrical susceptibility χ_e: a measure of how easily a dielectric material

870 polarizes in response to an electric field. This determines the electric per-

871 mittivity of the material. It is defined as the constant of proportionality

872 when relating an electric field $\mathbf{E}$ to the induced dielectric polarization

873 density $\mathbf{P}$.

874 - magnetic susceptibility χ_m: the degree of magnetization of a material in

875 response to an applied magnetic field.

- electric displacement field **D**: It accounts for the effects of bound charges within materials. It is the macroscopic field average of electric fields from charged particles that make up otherwise electrically neutral material. It can be considered the field after taking into account the response of a medium to an external field such as reorientation of electric dipoles.

- magnetic field strength **H**: A vector field that permeates space and which can exert a magnetic force on moving electric charge and on magnetic dipoles such as permanent magnets.

- electric field **E**: the electric force per unit charge. The direction of the field is taken to be the direction of the force it would exert on a positive test charge.

2.1.1.1 *electromagnetic relation in a linear material*

In a linear material, the polarization density **P** and magnetization density **M** are given by

$$\mathbf{P} = \chi_e \varepsilon_o \mathbf{E} \ , \tag{2.1}$$

$$\mathbf{M} = \chi_m \mathbf{H} \ , \tag{2.2}$$

where χ_e is the electrical susceptibility and χ_m is the magnetic suscepti-bility of the material. Electric displacement field, **D**, and magnetic induction field, **B**, are related to electric field, **E**, and magnetic field **H** by

21

$$\mathbf{D} = \varepsilon_o \mathbf{E} + \mathbf{P} = \varepsilon \mathbf{E} \ , \tag{2.3}$$

$$\mathbf{B} = \mu_o(\mathbf{H} + \mathbf{M}) = \mu \mathbf{H} \ , \tag{2.4}$$

where ε is the electrical permittivity and μ is the magnetic permeability of the material.

2.1.1.2 *Maxwell's equations*

The solenoidal condition for the magnetic induction, indicating that there are no magnetic monopoles, is given by

$$\nabla \cdot \mathbf{B} = 0 \ , \tag{2.5}$$

That is there are no sources and sinks for magnetic field lines.

Faraday's law of magnetic induction is given by

$$\nabla \times \mathbf{E} = -\partial \mathbf{B}/\partial t \tag{2.6}$$

showing that a spatially varying electric field can induce a magnetic field.

Charge conservation gives

$$\nabla \cdot \mathbf{E} = \rho^*/\varepsilon_o \ , \tag{2.7}$$

where $\rho^* = \varepsilon_o(n^+ - n^-)$ is the charge density, n^+ is the number of ions, and n^- is the number of electrons.

Ampère's law is given by

$$\nabla \times \mathbf{B} = \mu \mathbf{j} + \mu\varepsilon \partial \mathbf{E}/\partial t \ , \tag{2.8}$$

where the last term on the right hand side is the displacement current. Introducing the fundamental units of mass M, length L, velocity v, and time t, we consider the dimensions of the displacement current in Eqn. (2.8). The dimensions of the magnetic field B, electric field E, and the speed of light c itself respectively are considered for simplicity.

$\nabla \times \mathbf{E} \sim \frac{E}{L}, \frac{\partial \mathbf{B}}{\partial t} \sim \frac{B}{t}$ gives $E = vB$. From the speed of light, $c = \frac{1}{\sqrt{\mu\varepsilon}}$, $\mu\varepsilon \partial \mathbf{E}/\partial t = \frac{1}{c^2}\partial \mathbf{E}/\partial t \sim \frac{1}{c^2}\frac{E}{t} = \frac{v}{c^2}\frac{B}{t} = \frac{B}{L}\frac{v^2}{c^2}$.

Therefore, The displacement current in Ampère's law can be neglected if the flow velocity is much less than the speed of light.

By assuming the flow obeys charge neutrality, $n^+ - n^- \ll n$, where n is the total number density, the charge density in Eqn. (2.7) can be neglected.

Finally, Ohm's law without Hall effect is given by

$$\mathbf{j} = \sigma(\mathbf{E} + \mathbf{v} \times \mathbf{B}) \ . \tag{2.9}$$

This is the generalization of the relation between voltage and current in a moving conductor. It provides the link between the electromagnetic equations and the fluid equations.

The electric charge is conserved, which is given by Kirchhoff's law:

$$\nabla \cdot \mathbf{j} = 0. \tag{2.10}$$

2.1.2 The Navier Stokes and magnetic induction equations in a conducting liquid flow

The motion of an electrically conducting fluid in the presence of magnetic field obeys the equations of magnetohydrodynamics. The fluid is treated as a continuum and the classical results of fluid dynamics and electro-dynamics are combined in the derivation of the equations. The first equation is from mass conservation:

$$\frac{\partial \rho}{\partial t} + \nabla \cdot (\rho \mathbf{v}) = 0 \ . \tag{2.11}$$

Next, Newton's second law of motion gives

$$\rho \frac{D\mathbf{v}}{Dt} = -\nabla p + \mathbf{F} \ , \tag{2.12}$$

where the external force $\mathbf{F}$ consists of several terms, such as the Lorentz force, given by $\mathbf{j} \times \mathbf{B}$, the gravitational force $\rho \mathbf{g}$, and the viscous force. The viscous term is given by a kinematic viscosity of the form $\rho \nu \nabla^2 \mathbf{v}$ for an incompressible flow. Thus, Eqns. (2.12) become

$$\rho \frac{\partial \mathbf{v}}{\partial t} + \rho (\mathbf{v} \cdot \nabla)\mathbf{v} = -\nabla p + \rho \mathbf{g} + \eta \nabla^2 \mathbf{v} + \mathbf{j} \times \mathbf{B} \ . \tag{2.13}$$

Note that the Lorentz force couples the fluid equations to the electromagnetic equations. Eqn. (2.13) can be reduced to a dimensionless form.

$$\frac{\partial \mathbf{v}}{\partial t} + \mathbf{v} \cdot \nabla \mathbf{v} = -\nabla p + \frac{\mathbf{g}}{\text{Fr}^2} + \frac{1}{\text{Re}} \nabla^2 \mathbf{v} + \text{Al}(\mathbf{j} \times \mathbf{B}) \ , \tag{2.14}$$

963   where Fr $= v/\sqrt{gL}$, Re $= \rho v L/\eta$, Re$_m = \mu\sigma vL$, and Al $= B_o^2/\mu\rho v^2$ denote

964   the Froude, Reynolds, magnetic Reynolds, and Alfvén numbers, respectively.

965   The Hartmann number gives the ratio of magnetic forces to viscous forces.

966   Thus, this number is the important parameter in cases where the inertial effects

967   are small. On the other hand, the Stuart number gives the ratio of magnetic

968   forces to inertial forces, Thus, this number is the important parameter where

969   dealing with inviscid or turbulence. The Hartmann number Ha and Stuart

970   number N are related through Ha$^2 =$ ReRe$_m$Al and N $=$ Re$_m$Al. Note that

971   the ratio of Hartmann number and Reynolds number represents a mixture

972   parameters and involving viscous, magnetic, and inertial forces and can be

973   thought of the square root of the product of the viscous and magnetic forces

974   divided by the inertial forces.

975   We consider components of the magnetic induction field B_x, B_y, B_z. Note

976   that the longitudinal magnetic field along the jet axis x and the transverse mag-

977   netic field normal to the jet axis are given by $B_x = B_X cos\theta - B_Y sin\theta, B_y =$

978 $-B_X sin\theta + B_Y cos\theta$ respectively, where B_X is axial magnetic field and B_Y

979   is radial magnetic field. Also note that the (x, y, z) coordinate system is re-

980   lated with the dynamics of jet dynamics and the (X, Y, Z) coordinate system

981   is related with the magnetic field direction in solenoid. The nondimension-

982   alized momentum equations in the (x, y, z) coordinate system in Fig. 2.1 is

983   represented as Eqn. (2.15) using Ohm's equation.

984

$$\frac{\partial v_x}{\partial t} + v_x \cdot \nabla v_x = -\nabla p + \frac{1}{\text{Re}}\nabla^2 v_x - \frac{\text{Ha}_y^2}{\text{Re}}v_x + \frac{\text{Ha}_x\text{Ha}_y}{\text{Re}}v_y \ ,$$

$$\frac{\partial v_y}{\partial t} + v_y \cdot \nabla v_y = -\nabla p + \frac{1}{\text{Re}}\nabla^2 v_y - \frac{\text{Ha}_x^2}{\text{Re}}v_y + \frac{\text{Ha}_x\text{Ha}_y}{\text{Re}}v_x \ ,$$

985
$$\frac{\partial v_z}{\partial t} + v_z \cdot \nabla v_z = -\nabla p + \frac{1}{\text{Re}}\nabla^2 v_z - \frac{\text{Ha}_x^2}{\text{Re}}v_z - \frac{\text{Ha}_y^2}{\text{Re}}v_z \ . \tag{2.15}$$

986   In MHD, to eliminate the electric field $\mathbf{E}$ and the electric current density

987 $\mathbf{j}$, we use the Ampere's law and Ohm's law. Then, the Faraday's law gives the

988   magnetic induction equation:

989

990
$$\frac{\partial \mathbf{B}}{\partial t} = \nabla \times (\mathbf{v} \times \mathbf{B}) - \frac{1}{\mu\sigma}\nabla \times \nabla \times \mathbf{B} = \nabla \times (\mathbf{v} \times \mathbf{B}) + \frac{1}{\mu\sigma}\nabla^2\mathbf{B} \tag{2.16}$$

991   **2.1.2.1**   *magnetic Reynolds number*

992   In Eqn. (2.16), the dimension of the term on the left hand side is $\frac{B}{t}$ and

993   the second term on the right hand side is $\frac{B}{\sigma\mu L^2}$. Therefore, $\sigma\mu \sim \frac{t}{L^2}$. The

994   magnetic induction equation can be reduced to a dimensionless form.

995

996
$$\frac{\partial \mathbf{B}}{\partial t} = \nabla \times (\mathbf{v} \times \mathbf{B}) + \sigma\mu L v \nabla^2\mathbf{B} \ , \tag{2.17}$$

997   where the quantity $\sigma\mu L v$ is a dimensionless number, Re_m, called the mag-

998   netic Reynolds number. Re_m is a measure of the size of the advection term

999   , $\nabla \times (\mathbf{v} \times \mathbf{B})$, relative to the diffusion term, $\sigma\mu L v \nabla^2\mathbf{B}$. Reynolds number

1000   Re measures the extent to which a convective process prevails over a diffusive

1001   one. In viscous flow, the viscosity causes vorticity to diffuse in the face of

1002   convection and the Reynolds number measures the power of convection over

1003   diffusion of vorticity. In MHD, the conductivity causes convection to overcome

1004   diffusion of the magnetic field to a degree measured by the magnetic Reynolds

1005   number Re_m. If Re_m is large, convection dominates over diffusion and mag-

1006   netic boundary layer near the fields are to be expected. The magnetic Prandtl

1007   number measures the ratio of viscous diffusivity and magnetic diffusivity and

1008   is defined as Re_m/Re. When it is small, magnetic fields diffuse much more

1009   rapidly than vorticity and magnetic boundary layers are much thicker than

1010   viscous layers. This makes for simplifications such as the neglect of viscosity

1011   in the magnetic boundary layer.

1012   In any region of length scale δ where convection and diffusion are equally

1013   important, δ must be of order $1/\mu\sigma v$. Only within limited regions where B

1014   changes significantly in a distance δ can the gradients be high enough for

1015   diffusion and dissipation to matter. The characteristic time in the flow is the

1016   transit time L/v, during which a field disturbance diffuses a distance of order

1017 $(L/\mu\sigma v)^{1/2}$. This is much less than L if $\text{Re}_m \gg 1$, in which case diffusion

1018   is negligible. It will diffuse a distance of order $(t/\mu\sigma)^{1/2}$, which is negligible

1019   in comparison with the length scale L if $L^2\mu\sigma/t \gg 1$. This is the required

1020   criterion for the perfect conductivity approximation to be valid. At the other

1021   extreme case where diffusion is dominant is that the medium diffuses to the

1022   form it would be in stationary fluid, where no induced magnetic field would

1023   occur. The ratio of the induced magnetic field and the imposed magnetic field

1024   is of order $\mu\sigma vL$, which is Re_m. The low Re_m approximation is to ignore the

1025 induced field, to replace $\mathbf{B}$ by the known field $\mathbf{B}_o$ in all MHD equations.

1026 **2.1.2.2 *frozen-in theorem in magnetic induction equation***

1027 If $\mathrm{Re}_m \gg 1$, the induction equation Eqn. (2.16) is approximated by

1028

1029
$$\frac{\partial \mathbf{B}}{\partial t} = \nabla \times (\mathbf{v} \times \mathbf{B}) \qquad (2.18)$$

1030 The timescale with changes due to the fluid motion from Eqn. (2.18) is

1031 given by $t_{motion} \sim \frac{L}{v}$. In the case $t_{motion} \ll t_{diffusion}$, which corresponds to

1032 $R_m \gg 1$, the diffusion term is negligible. According to the frozen-flux theorem

1033 of Alfvén, in a perfectly conducting fluid, where $\mathrm{Re}_m \to \infty$, the magnetic

1034 field lines move with the fluid: the field lines are 'frozen' into the fluid. This

1035 theorem states that motions along the field lines do not change the field but

1036 motions transverse to the field carry the field with them. If the area of the flux

1037 tube is small, the field strength will be approximately constant across the area

1038 of the tube. Thus, the $|\mathrm{B}| \times$ cross sectional area is constant so that the field

1039 strength becomes stronger if the cross sectional area is reduced by the fluid

1040 motion. The vorticity flux through any loop moving with the fluid is constant

1041 and the particles which initially lied on a vorticity line continue to do so. All

1042 the fluid particles which initially lie on a magnetic field line continue to do so

1043 in a perfect conductor.

1044 **2.1.2.3 *the diffusion limit in induction equation***

1045 If $\mathrm{Re}_m \ll 1$, the induction equation Eqn. (2.16) is approximated by

$$\frac{\partial \mathbf{B}}{\partial t} = \frac{1}{\mu\sigma}\nabla^2\mathbf{B} \tag{2.19}$$

The timescale with changes due to field diffusion from Eqn. (2.19) is given by $t_{diffusion} \approx \sigma\mu L^2$. The diffusion equation indicates that any irregularities in an initial magnetic field will diffuse away and be smoothed out. The field will tend to be a simpler uniform field. This process of smoothing out will occur on the given diffusion timescale.

2.2   The Energy Equation in MHD

In general, the energy equation can be written in the form

$$\frac{\rho^\gamma}{\gamma - 1}\frac{D}{Dt}\left(\frac{p}{\rho^\gamma}\right) = -\mathbf{D} \ , \tag{2.20}$$

where $\mathbf{D}$ is the total energy loss function, γ is the ratio of specific heats, c_p/c_v. The energy loss function consists of thermal conduction, radiation, and heating. The heating consists of several terms, such as small scale magnetic wave heating, ohmic heating, and viscous heating. However, such losses (gains) can be neglected if the medium is either isentropic or adiabatic. There are cases where no energy is added to the flow and no energy losses occur. The adiabatic term can be represented as follows, using Eqn. (2.11):

$$\rho^\gamma\frac{D}{Dt}\left(\frac{p}{\rho^\gamma}\right) = \frac{\partial p}{\partial t} + \mathbf{v} \cdot \nabla p + \gamma p \nabla \cdot \mathbf{v} = -(\gamma - 1)\mathbf{D}. \tag{2.21}$$

To close the system of equations, an equation of state is needed, which is taken as ideal gas law:

$$p = \frac{\rho}{M}RT \; , \tag{2.22}$$

where M is molar mass and R is the gas constant ($8.3 \; J \cdot mol^{-1}K^{-1}$).

2.2.1 Energetics and effects of Lorentz force

The energy equation that contains all the various types of energy, including kinetic energy, gravitational energy, the internal energy, and the magnetic energy is obtained using the MHD governing equations. The gravitational potential Φ is defined by $-\nabla\Phi = \mathbf{g}$. The kinetic energy is obtained by multiplying Eqn. (2.11) by $v^2/2$ and dotting Eqn. (2.12) with $\mathbf{v}$. The energy equation can then be written as

$$\frac{\partial}{\partial t}(\frac{1}{2}\rho v^2) + \nabla \cdot (\frac{1}{2}\rho v^2 \mathbf{v}) = -\mathbf{v}\cdot\nabla p + \mathbf{v}\cdot(\mathbf{j}\times\mathbf{B}) - \mathbf{v}\cdot\rho\nabla\Phi + \mathbf{v}\cdot\eta\nabla^2\mathbf{v} \; . \tag{2.23}$$

The gravitational term can be expressed as follows using Eqn. (2.11) and the fact that $\partial\Phi/\partial t = 0$.

$$\mathbf{v}\cdot\rho\nabla\Phi = \nabla\cdot(\rho\Phi\mathbf{v}) + \frac{\partial}{\partial t}(\rho\Phi) \; . \tag{2.24}$$

Eqn. (2.24) gives the flux of the gravitational potential energy and the rate of change of gravitational potential energy in time. The Lorentz force term can be expressed as follows using Eqn. (2.9):

30

$$\mathbf{v} \cdot (\mathbf{j} \times \mathbf{B}) = -\mathbf{j} \cdot (\mathbf{v} \times \mathbf{B}) = -\frac{j^2}{\sigma} + \mathbf{j} \cdot \mathbf{E} \ . \tag{2.25}$$

Eqn. (2.25) is rearranged using Eqn. (2.6):

$$\mathbf{v} \cdot (\mathbf{j} \times \mathbf{B}) = -\frac{j^2}{\sigma} - \nabla \cdot (\frac{\mathbf{E} \times \mathbf{B}}{\mu}) - \frac{\partial}{\partial t}(\frac{B^2}{2\mu}) \ . \tag{2.26}$$

The pressure gradient term gives

$$-\mathbf{v} \cdot \nabla p = -\nabla \cdot (p\mathbf{v}) + p\nabla \cdot \mathbf{v} \ . \tag{2.27}$$

Eqn. (2.27) can also be expressed as follows using Eqn. (2.21):

$$p\nabla \cdot \mathbf{v} = -\frac{\partial}{\partial t}(\frac{p}{\gamma - 1}) - \nabla \cdot (\frac{p}{\gamma - 1}\mathbf{v}) - \mathbf{D} \ . \tag{2.28}$$

Substituting the foregoing relations, the full energy equation can be expressed as

$$\frac{\partial}{\partial t}[\frac{1}{2}\rho v^2 + \rho\Phi + \frac{p}{\gamma - 1} + \frac{B^2}{2\mu}] + \nabla \cdot \{[\frac{1}{2}\rho v^2 + \rho\Phi + \gamma\frac{p}{\gamma - 1}]\mathbf{v} + \frac{\mathbf{E} \times \mathbf{B}}{\mu}\} = -\frac{j^2}{\sigma} - \mathbf{D} \ . \tag{2.29}$$

2.2.2 Proton beam induced energy deposition and equation of state

Due to the sudden energy deposition by proton beam, it is worthy to consider the components of added energy and the state of energy from compressible density variation as well as ionization to the right hand side of full energy equation Eqn. (2.29. The instantaneous beam energy deposition is

31

1108

$$E_{beam}(r) = E_{beam}(r) \cdot \delta(t - t_{beam}), \qquad (2.30)$$

1110   where

1111

$$E_{beam}(r) = E_o exp[-\frac{r}{a}] \qquad (2.31)$$

1113   and

1114

$$E_o = \frac{E_{beam}}{\pi r_{beam}^2}. \qquad (2.32)$$

1116 $E_{beam}(r)$ is radial energy density distribution of the beam and the proton

1117   beam energy is assumed to be deposited as a δ function at time $t = t_{beam}$. E_{beam}

1118   is the peak energy deposition corresponding to the beam spot radius r_b. The

1119   equation of state (EOS) is considered as the sum of compression, ion thermal,

1120   and electron thermal terms. The EOS can be expressed for simplification. The

1121   compressible pressure P_c and energy E_c are

1122

$$P_c = P_{co}[(\frac{\rho}{\rho_o})^\gamma - 1], \qquad (2.33)$$

1124

$$E_c = E_{co}[(\frac{\rho}{\rho_o})^{\gamma-1} - 1]\frac{\rho}{\rho_o} + P_{co}(1 - \frac{\rho}{\rho_o}), \qquad (2.34)$$

1126   where

1127

$$P_{co} = \frac{\rho c^2}{\gamma} \quad , \quad E_{co} = \frac{P_{co}}{\gamma - 1}. \qquad (2.35)$$

1129   Ion and electron thermal pressure and energy are

32

$$E_I = 3nk(T - T_o) \quad , \quad P_I = G_I E_I \quad , \tag{2.36}$$

$$E_e = \frac{1}{2}\beta(T - T_o)^2 \quad , \quad \beta = \beta_o(\frac{\rho_o}{\rho})^{2/3} \quad , \quad P_e = G_e E_e, \tag{2.37}$$

where $n = \frac{\rho}{M}$ and k is Boltzmann's constant. Thus, the total energy and pressure are

$$E = E_c + E_I + E_e \quad , \quad P = P_c + P_I + P_e \quad , \tag{2.38}$$

where subscripts c, I, and e correspond to compression, ion thermal, and electron thermal components, respectively. G_I and G_e are the Gruneisen coefficients for the ion and electron. c is the speed of sound in the material. Initial mercury pressure P is 0 at $T = T_o = T_{melting}$ and normal density $\rho = \rho_o$. At higher temperatures, the mercury can be ionized and the resulting energy and pressure by free-electron component is added to the EOS. Accordingly, the solid state partition of the electron thermal energy and pressure decreases $(1 - f_z)$ times, where f_z is the ionization fraction.

2.2.3 Magnetic damping with joule dissipation

It is known that a static magnetic field can suppress motion of an electrically conducting liquid. If a conducting liquid moves through an imposed static magnetic field, electric currents are generated. These, in turn, lead to ohmic heating such as Joule dissipation. As the thermal energy of the fluid

1151 rises, there is a corresponding drop in its kinetic energy, and so the fluid decel-

1152 erates. This is to suppress the motion of liquid jets. In many applications, it is

1153 believed that the imposition of a static magnetic field is used as one means of

1154 suppressing unwanted motion. Considering the uniform perpendicularly im-

1155 posed magnetic field to the flow direction for simplicity, the damping effect of

1156 Lorentz force can be quantified. If the magnetic field is uniform, the Faraday'

1157 law requires that $\nabla \times \mathbf{E} = 0$. Using Ohm's law and the fact that the current

1158 density is solenoidal, the current relationship is given by

1159

$$1160 \qquad \nabla \cdot \mathbf{J} = 0 \quad , \quad \nabla \times \mathbf{J} = \sigma \mathbf{B} \cdot \nabla \mathbf{v} \ . \qquad (2.39)$$

1161 Thus, $\mathbf{J}$ is zero if $\mathbf{v}$ is independent of the magnetic field direction. By doing

1162 cross product of $\mathbf{J}$ and $\mathbf{B}$ and using the vector identity, Lorentz force per unit

1163 mass is given by

1164

$$1165 \qquad \mathbf{F} = -\frac{\mathbf{v}}{\tau} + \frac{\sigma(\mathbf{B} \times \nabla \phi_E)}{\rho} \ , \qquad (2.40)$$

1166 where $\tau = \rho/\sigma B^2$ is Joule damping term and ϕ_E is electrical potential,

1167 which is given by the divergence of Ohm's law: $\phi_E = \nabla^{-2}(B \cdot \omega)$. The Lorentz

1168 force then simplifies to $-\mathbf{v}/\tau$ when the magnetic field and the vorticity field

1169 are mutually perpendicular. Thus, the perpendicular $\mathbf{v}$ to magnetic field de-

1170 clines on a time scale of τ, which clearly explains the mechanism of magnetic

1171 damping. The ratio of the damping time τ to the characteristic time L/v gives

1172 the interaction parameter $N = \sigma B^2 L/\rho v$, which is also used for the indication

1173 of the ratio of the magnetic and inertial forces.

1174   To investigate the role of Joule dissipation, consider the fully derived energy

1175   equation in inviscid flow.

1176

1177
$$\frac{dE}{dt} = -\frac{1}{\sigma\rho}\int \mathbf{J}^2 dV = -\mathbf{D} , \qquad (2.41)$$

1178   where $\mathbf{D}$ is joule dissipation and E is global kinetic energy.

1179 $\mathbf{J}^2$ from Eqn. (2.39) was estimated (Davidson, 1999) and is given.

1180
$$\frac{dE}{dt} \sim -(\frac{L_{min}}{L_{\parallel}})^2 \frac{E}{\tau} , \qquad (2.42)$$

1181   from which

1182

1183
$$E \sim E_o \ exp \ (-\tau^{-1}\int_0^t (L_{min}/L_{\parallel})^2 dt) , \qquad (2.43)$$

1184   where $L_{\parallel}$ is the characteristic length for the flow, parallel to the magnetic

1185   field. Fig. 2.3 (a) shows the decay of energy depending on the Joule damping

1186   term with various magnetic field. The energy is dissipated as a result of

1187   energy decay by Joule dissipation. So, the time constant required for energy

1188   dissipation is getting smaller as the magnetic field strength increases. As a

1189   result, the magnetic field affect to the integration of energy, which is shown in

1190   Fig. 2.3 (b). It indicates that the flow decays on a time scale of τ provided

1191   that L_{min} and $L_{\parallel}$ are of the same order. However, the Lorentz force can not

1192   create or destroy linear (angular) momentum despite the Joule dissipation.

1193   This indicates that the flow can not be decayed on a time scale of τ and the

1194   Eqn. (2.42) and (2.43) infer that $L_{min}/L_{\parallel}$ must increase with time. Therefore,

1195 it is expected that these flow will experience anisotropy, with $L\|$ increasing as
1196 the flow evolves.

2.3 Vorticity Equations in MHD flow

1198 The possibility of using an electromagnetic field for vortices control in
1199 conducting fluids needs to be investigated. Electromagnetic force can influence
1200 the stability of a flow, thus prevents its transition to turbulence by suppressing
1201 disturbances or changing mean velocity profiles. A significant drag reduction
1202 is possible when the surface boundary condition is modified to suppress the
1203 vortices. Transverse magnetic field does not reduce drag because the magnetic
1204 field increases the skin friction drag by directly altering the mean flow, so called
1205 Hartmann flow, even though turbulent fluctuations are significantly reduced.
1206 The longitudinal magnetic field does not directly interact with the mean flow
1207 although it can reduce turbulent fluctuations. Thus it is possible that the
1208 longitudinal magnetic field can result in drag reduction.

2.3.1 Governing equations for vorticity

1210 It is useful to transform the governing equations in terms of vorticity trans-
1211 port. The equation for the vorticity ω of an incompressible conducting fluid
1212 in MHD is

$$\frac{\partial \omega}{\partial t} + (\mathbf{v} \cdot \nabla)\omega - (\omega \cdot \nabla)\mathbf{v}$$

$$= \nu\nabla^2\omega + \frac{1}{\rho}\nabla \times (\mathbf{j} \times \mathbf{B})$$

$$= \nu\nabla^2\omega + \frac{1}{\rho}\{(\mathbf{B} \cdot \nabla)\mathbf{j} - (\mathbf{j} \cdot \nabla)\mathbf{B}\} . \tag{2.44}$$

The term $(\omega \cdot \nabla)\mathbf{v}$ in Eqn. (2.44) expresses the effect of stretching and turning vorticity lines. From the Faraday's law and $\partial\mathbf{B}/\partial t = 0$, the electric field in terms of an electric potential, ϕ_E, is

$$\mathbf{E} = -\nabla\phi_E . \tag{2.45}$$

From the Ohm's law, Kirchhoff's law, and Eqn. (2.45), the electromagnetic equation can be simplified as Eqn. (2.47) using nondimensionalized Ohm's law Eqn. (2.46).

$$\mathbf{j} = \mathrm{Re}_m(-\nabla\phi_E + \mathbf{v} \times \mathbf{B}) . \tag{2.46}$$

$$\nabla^2\phi_E = \nabla \cdot (\mathbf{v} \times \mathbf{B}) . \tag{2.47}$$

The important parameter in vortices dynamics is the Stuart number N $(= \mathrm{Re}_m\mathrm{Al} = \sigma\mathbf{B}^2 L/\rho v)$, which is the ratio of the electromagnetic force to the inertial force. Therefore, one can fix the Reynolds number and change the Stuart number to see the effect of magnetic field over the vortices strength. The Hartmann numbers, $\mathrm{Ha} = \sqrt{\mathrm{ReN}}$, can be determined correspondingly.

1232 The Stuart number gives the ratio of Ha to Re. Thus, the Stuart number will

1233 indicate the stabilizing effect of magnetic field to the unique characteristic of

1234 transition to turbulence.

2.3.2 Vorticity suppression

1235

1236 The vorticity is suppressed by the magnetic field, transverse to the vortic-

1237 ity. The result is altered if the conductivity σ is nonuniform and varies with

1238 coordinates, in which case vorticity will be created. When a conducting liquid

1239 flows along a pipe with an axial magnetic field, there will be no magnetic effect

1240 if the motion is laminar, though the vorticity is perpendicular to the magnetic

1241 field, but if the flow is turbulent, adding the field damps the turbulence and

1242 reduces the Reynolds stresses and the frictional drag. Adding the field also

1243 raises the critical Reynolds number for instability of flow (Shercliff, 1965).

1244 #### 2.3.2.1 *spanwise magnetic field effect to vorticity suppression*

1245 For a spanwise magnetic field, $B = (0, 0, B_z)$, the corresponding Lorentz

1246 force, $f = (f_x, f_y, f_z)$ can be represented as follows.

1247

$$
f_x = \mathrm{N}(-\frac{\partial \phi_E}{\partial y}B_z - B_z^2 v_x) \ ,
$$

$$
f_y = \mathrm{N}(\frac{\partial \phi_E}{\partial x}B_z - B_z^2 v_y) \ ,
$$

1248
$$
f_z = 0 \ . \tag{2.48}
$$

1249 Introducing the stream function ψ,

$$\frac{\partial^2 \psi}{\partial x^2} + \frac{\partial^2 \psi}{\partial y^2} = -\omega_z \ , \qquad (2.49)$$

where the spanwise vortex $\omega_z = \partial v_y / \partial x - \partial v_x / \partial y$. The Ohm's law Eqn. (2.47) yields

$$\frac{\partial^2 \phi_E}{\partial x^2} + \frac{\partial^2 \phi_E}{\partial y^2} = \omega_z \ , \qquad (2.50)$$

where unity quantity of B_z is assumed.

From Eqn. (2.47) and (2.50), $\phi_E = \psi + const.$ Correspondingly this relation yields $\mathbf{f} = 0$. Therefore, the spanwise vortex flow is not affected by the spanwise magnetic field (Lim, 1998). However, it can reduce turbulent fluctuations without directly interacting with the mean flow.

2.3.2.2 *longitudinal and transverse magnetic field effect to vorticity suppression*

For longitudinal and transverse magnetic field $\mathbf{B} = (B_x, B_y, 0)$ in a two dimensional flow, Eqn. (2.47) yields $\nabla^2 \phi_E^2 = 0$ assuming that there is no velocity (v_z) onto the normal to the flow direction. The corresponding forces can be represented as follows:

$$f_x = \mathrm{N}(B_y \frac{\partial \phi_E}{\partial z} - B_y^2 v_x + B_x B_y v_y) \ ,$$

$$f_y = \mathrm{N}(-B_x \frac{\partial \phi_E}{\partial z} - B_x^2 v_y + B_x B_y u_x) \ ,$$

$$f_z = \mathrm{N}(-B_y \frac{\partial \phi_E}{\partial x} + B_x \frac{\partial \phi_E}{\partial y} - B_x^2 v_z - B_y^2 v_z) \ . \qquad (2.51)$$

39

1269 The effect of the longitudinal and transverse magnetic field on the strength

1270 of spanwise vortices can be shown from the vorticity equation where additional

1271 vortices term $\omega_{Lorentz} = \nabla \times \mathbf{f}$ caused by the Lorentz force has been added.

1272

$$\frac{\partial \omega_z}{\partial t} + (\mathbf{v} \cdot \nabla)\omega_z = (\omega_z \cdot \nabla)\mathbf{v} + \frac{1}{\text{Re}}\nabla^2 \omega_z + \text{N} \left(-B_x \frac{\partial^2 \phi_E}{\partial x \partial z} \right.$$

1273
$$\left. - B_y \frac{\partial^2 \phi_E}{\partial y \partial z} + B_x B_y \left(\frac{\partial v_x}{\partial x} - \frac{\partial v_y}{\partial y}\right) - B_x^2 \frac{\partial v_y}{\partial x} + B_y^2 \frac{\partial v_x}{\partial y} \right) . \quad (2.52)$$

1274 If we consider the longitudinal magnetic field $\mathbf{B} = (B_x, 0, 0)$ and the trans-

1275 verse magnetic field $\mathbf{B} = (0, B_y, 0)$ independently, the corresponding force can

1276 be shown in Eqn. (2.53), Eqn. (2.54) respectively.

1277

$$f_x = 0 ,$$
$$f_y = \text{N}(-B_x \frac{\partial \phi_E}{\partial z} - B_x^2 v_y) ,$$

1278
$$f_z = \text{N}(B_x \frac{\partial \phi_E}{\partial y} - B_x^2 v_z) \quad . \quad (2.53)$$

1279

$$f_x = \text{N}(B_y \frac{\partial \phi_E}{\partial z} - B_y^2 v_y) ,$$
$$f_y = 0 ,$$

1280
$$f_z = \text{N}(-B_y \frac{\partial \phi_E}{\partial x} - B_y^2 v_z) . \quad (2.54)$$

1281 Eqns. (2.53) and (2.54) clearly show that the Lorentz force retards the

1282 local velocity. The vorticity equation is shown as Eqn. (2.55), Eqn. (2.56).

1283

1284
$$\frac{\partial \omega_z}{\partial t} + (\mathbf{v} \cdot \nabla)\omega_z = (\omega_z \cdot \nabla)\mathbf{v} + \frac{1}{\text{Re}}\nabla^2 \omega_z + \text{N}(-B_x \frac{\partial^2 \phi_E}{\partial x \partial z} - B_x^2 \frac{\partial v_y}{\partial x}) . \quad (2.55)$$

$$\frac{\partial \omega_z}{\partial t} + (\mathbf{v} \cdot \nabla)\omega_z = (\omega_z \cdot \nabla)\mathbf{v} + \frac{1}{\text{Re}}\nabla^2 \omega_z + \text{N}(-B_y\frac{\partial^2 \phi_E}{\partial y \partial z} + B_y^2\frac{\partial v_x}{\partial y}) \ . \quad (2.56)$$

The Lorentz force is negatively correlated with the spanwise vorticity. Therefore, the Lorentz force induced by the longitudinal and transverse magnetic field reduces the strength of the spanwise vorticity effectively.

2.4 One Dimensional Pipe Flow in Transverse Magnetic Field

In one-dimensional problem, the governing equations and the boundary conditions are assumed that there is only one component of the velocity, v_z, and only one component of the induced magnetic field, $\mathbf{B}_z$, along with the applied field $\mathbf{B}_o$, so that the total velocity and magnetic fields are given by

$$v_r = v_\theta = 0, \quad v_z = v_z(r,\theta), \quad B_r = B_o\cos\theta \ ,$$

$$B_\theta = -B_o\sin\theta, \quad B_z = B_z(r,\theta) \ . \quad (2.57)$$

Substituting these expressions into Eqn. (2.13) using cylindrical coordinates, we obtain

$$p(r,\theta,z) = -(1/2\mu)B_z^2 + O_1 z + O_2 \ , \partial p/\partial z = O_1 = constant \ , \quad (2.58)$$

$$O_1 = \eta[\frac{\partial^2 v_z}{\partial r^2} + (\frac{1}{r})\frac{\partial v_z}{\partial r} + (\frac{1}{r^2})\frac{\partial^2 v_z}{\partial \theta^2}] + (\frac{1}{r})B_\theta\frac{\partial B_z}{\partial \theta} + B_r\frac{\partial B_z}{\partial r} \ , \quad (2.59)$$

1304   where O_2 is a constant.

1305   Eqn. (2.5), Eqn. (2.11), Equation (2.57) are identically satisfied and Eqns. (2.16)

1306   become

1307
$$\frac{1}{\mu\sigma}\left[\frac{\partial}{\partial r}\left(r\frac{\partial B_z}{\partial r}\right) + \left(\frac{1}{r}\right)\frac{\partial^2 B_z}{\partial \theta^2}\right] + \left[B_r\frac{\partial}{\partial r}(rv_z) + \frac{\partial}{\partial \theta}(v_z B_\theta)\right] = 0 \; . \qquad (2.60)$$

2.4.1   Non-dimensional form of the governing equations using cylindrical coordinates

1310   The modified non-dimensional form of Navier-Stokes equations and the

1311   magnetic induction equations using cylindrical coordinates is expressed as fol-

1312   lows:

1313

1314
$$\nabla^2 v_z - \left(\frac{\mathrm{Ha}^2}{\mathrm{Re}_m}\right)\left[\left(\frac{\sin\theta}{r}\right)\frac{\partial B_z}{\partial \theta} - \cos\theta\frac{\partial B_z}{\partial r}\right] = O \; , \qquad (2.61)$$

1315

1316
$$\nabla^2 B_z - \mathrm{Re}_m\left[\left(\frac{\sin\theta}{r}\right)\frac{\partial v_z}{\partial \theta} - \cos\theta\frac{\partial v_z}{\partial r}\right] = 0 \; , \qquad (2.62)$$

1317   where $\nabla^2 \equiv \frac{\partial^2}{\partial r^2} + \left(\frac{1}{r}\right)\frac{\partial}{\partial r} + \left(\frac{1}{r^2}\right)\frac{\partial^2}{\partial \theta^2}$, $\mathrm{Ha} = B_o a(\sigma/\eta)^{1/2}$, $\mathrm{Re}_m = \sigma\mu va$, and

1318 $O = O_1 a^2/v\eta$.

1319   Eqn. (2.61) and (2.61) apply to any general incompressible, steady magne-

1320   tohydrodynamic duct flow. The restriction as to geometry and the conditions

1321   at the wall enters through the boundary conditions.

2.4.1.1   *boundary conditions in pipe flow*

1323   No fluid slip at the wall is given by

$$v_z(a, \theta) = 0 \ , \tag{2.63}$$

where a is the radius of the cylinder, while the assumption of non-conducting walls implies that (Shercliff, 1953)

$$B_z(a, \theta) = 0 \ . \tag{2.64}$$

We can also obtain the current density $\mathbf{j}$ and the electric field $\mathbf{E}$ from Ampere's and Ohm's laws:

$$j_r = (\frac{1}{r})\frac{\partial B_z}{\partial \theta}, \ \ j_\theta = -\frac{\partial B_z}{\partial r}, \ \ j_z = 0 \ , \tag{2.65}$$

$$E_r = (1/\sigma)j_r + v_z B_\theta, \ \ E_\theta = (1/\sigma)j_\theta - v_z B_r, \ \ j_z = 0 \ . \tag{2.66}$$

2.4.2 Exact solutions of pipe flow in magnetic field

Shercliff (1953) uncoupled the Eqn. (2.61) and (2.62) by a linear transformation. The boundary conditions could also be reduced by the transformation. The velocity and magnetic field distribution are obtained from the uncoupled equations (Gold, 1962):

$$v_z = \frac{-Kv}{4\alpha}[e^{-\alpha \frac{r}{a}\cos\theta} \sum_{n=0}^{\infty} \epsilon_n \frac{I_n'(\alpha)}{I_n(\alpha)} I_n(\alpha\frac{r}{a})\cos n\theta$$

$$+ e^{\alpha \frac{r}{a}\cos\theta} \sum_{n=0}^{\infty} (-1)^n \epsilon_n \frac{I_n'(\alpha)}{I_n(\alpha)} I_n(\alpha\frac{r}{a})\cos n\theta] \ , \tag{2.67}$$

43

1343

$$B_z = \frac{-\mathrm{Re}_m K B_o}{8\alpha^2} [e^{-\alpha\frac{r}{a}\cos\theta} \sum_{n=0}^{\infty} \epsilon_n \frac{I'_n(\alpha)}{I_n(\alpha)} I_n(\alpha\frac{r}{a}) \cos n\theta$$

$$- e^{\alpha\frac{r}{a}\cos\theta} \sum_{n=0}^{\infty} (-1)^n \epsilon_n \frac{I'_n(\alpha)}{I_n(\alpha)} I_n(\alpha\frac{r}{a}) \cos n\theta - 2\frac{r}{a}\cos\theta] , \qquad (2.68)$$

1344

1345   where $\alpha = \frac{1}{2}\mathrm{Ha}$, I_n is the modified Bessel function of order n, $\epsilon_n = 1$ for

1346   n=0, and $\epsilon_n = 2$ for n>0. Equation (2.65) and (2.66) are used to obtain the

1347   electric field **E**:

1348

1349
$$E_r = (\frac{a\mu v}{\mathrm{Re}_m r})\frac{\partial B_z}{\partial \theta} - v_z B_o \sin\theta . \qquad (2.69)$$

1350 I_n identities are given by

1351

1352 $$I_n(\alpha) = I_{-n}(\alpha) , I_n(-\alpha) = (-1)^n(\alpha) , I_n(\alpha)' = \frac{1}{2}(I_{n+1}(\alpha) + I_{n-1}(\alpha)) , \quad (2.70)$$

1353   and

1354

1355 $$I_n(x) = \frac{1}{\pi}\int_0^\pi e^{x\cos\theta}\cos n\theta d\theta - \frac{1}{\pi}\int_0^\infty e^{-x\cosh u - nu}du . \qquad (2.71)$$

1356 2.5   Stability of Conducting Flow in a Mag-
1357 netic Field

1358   The problem of the flow of liquid metal jets in magnetic field arises in

1359   certain applications of magnetohydrodynamics. The stability of the flow of a

1360   conducting film in the presence of two components of the magnetic field (in

44

the direction of the flow and normal to the surface) was investigated by B.A. Kolovadin (1965) using the approximation of small Reynolds numbers: The ratio of transverse magnetic field to longitudinal magnetic field changes due to the finite inclination of jet axis to the magnetic field axis. The magnitude of the inclination angle affects the stability of the liquid jets.

Theses instabilities can change the jet shape into one that makes the jet a significantly less efficient target for particle production. As described in Chapter 1, the particle production depends on several parameters such as jet size and jet angle. Thus, the unstable behaviors of jet in a magnetic field yields less or unexpected production of particle. In addition, the larger inclination of jet axis makes the jet size become bigger than the nominal jet size due to the increased magnetic field. Thus, the mercury jet interacting with beam will have different energy deposition leading to different particle production. Therefore, the stable motion of mercury jet is required for stable particle production and it then needs to be investigated.

2.5.1 Propagation of waves at an interface separating two flows in magnetic field

To investigate the surface wave motion of free jet in magnetic field, we followed the procedure of a direct extension of Currie (1993) to the case with a magnetic field. The detailed procedures and derivations are described in Appendix C.2.

We consider the (x, y, z) coordinate system in Fig. 2.1. The magnetic field

1383   along and normal to the Hg jet axis can be derived from the solenoid mag-

1384   netic field map. From trigonometry, the longitudinal magnetic field along the

1385   jet axis and the transverse magnetic field normal to the jet axis are given by

1386 $B_x = B_X cos\theta - B_Y sin\theta, B_y = -B_X sin\theta + B_Y cos\theta$, respectively, where B_X is

1387   the axial component of the magnetic field and B_Y is the radial component.

1388   To investigate the effect of sinusoidal wave perturbation at the interface, the

1389   equation of the interface is chosen to be $\xi(x,t) = \epsilon e^{i(2\pi/\lambda)(x-ct)} + a$, where ϵ is

1390   the wave amplitude, λ is the wavelength, and c is the wave propagation speed.

1391   Small perturbations from the basic flow in the form $v_{xi} = U_i + v'_{xi}$, $v_{yi} = v'_{yi}$,

1392 $p_i = P_i + p'_i$, $v'_{xi} = \frac{\partial \phi_i}{\partial x}$, $v'_{yi} = \frac{\partial \phi_i}{\partial y}$ are assumed, where ϕ_i is the velocity potential

1393   for the perturbation to the uniform wavy flows at the interface. Substituting

1394   the perturbed expressions into the equations of motion, neglecting second or-

1395   der terms in the perturbed quantities, and making use of the fact that U, P

1396   satisfy the flow equations and the current density in Lorentz force term can

1397   be represented using Ohm's law, we have the linearized equations governing

1398   the motion of disturbance, which yields the Rayleigh's stability equation of

1399   conducting flow in a magnetic field by replacing the perturbed quantities with

1400   the equation of motion. The Rayleigh's equation must be solved subject to the

1401   boundary conditions. The dynamic boundary condition at interface yields the

1402   effect of a magnetic field and the conditions of interfacing flows such as flow

1403   velocity and density to the wave velocity and wave number. Without a mag-

1404   netic field, the quantity c has an imaginary part that results in the interfacial

1405   wave growing exponentially with time. Thus, the interface at the shear layer

1406   is unstable. However, the magnetic effects to the wave propagation velocity to

1407   reduce the wave amplitude and correspondingly the wavelength increases due

1408   to the magnetic field.

1409   Several investigations have suggested that magnetic field suppresses tur-

1410   bulent fluctuations in conducting liquid by stabilizing the flow (Shercliff 1956,

1411   Gold 1962, Kozyrev 1981, Bernshtam 1982) and the stabilizing action of the

1412   longitudinal component of a magnetic field is considerably weaker than that

1413   of the transverse component, where stabilization is judged by an increase in

1414   the characteristic wavelength of the flow and Re_{cr}.

2.5.2   Magnetic pressure and tension

1415

1416   Once the jet surface is stabilized and flattened by a magnetic field, the

1417   magnetic pressure caused by the Lorentz force is contributing to the hydro-

1418   dynamic pressure. It gives rise to deflect the jet in directions perpendicular

1419   to the magnetic field. Considering that the continuity condition has to be

1420   satisfied, the Lorentz force makes the jet shape change elliptically. There-

1421   fore, the contributions of each magnetic pressure components to the isotropic

1422   hydrodynamic pressure needs to be investigated.

1423   Lorentz force is $\mathbf{F} = \mathbf{J} \times \mathbf{B} = \frac{1}{\mu}(\nabla \times \mathbf{B}) \times \mathbf{B} = \frac{1}{\mu}(\mathbf{B} \cdot \nabla)\mathbf{B} - \frac{1}{2\mu}\nabla \mathbf{B}^2$.

1424   Suppose the Maxwell stress tensor $T_{ij} = \frac{1}{\mu}(B_{ij} - \frac{1}{2}\delta_{ij}B^2)$, which represents

1425   the deviatoric stress tensor of magnetic field. The divergence of the Maxwell

1426   stress tensor is represented as follows, which gives the same expression with

1427   Lorenz force.

47

1428

$$\nabla \cdot T = \frac{1}{\mu} \begin{bmatrix} \frac{\partial}{\partial x} & \frac{\partial}{\partial y} & \frac{\partial}{\partial z} \end{bmatrix} \begin{bmatrix} \frac{B_x^2 - B_y^2 - B_z^2}{2} & B_x B_y & B_x B_z \\ B_y B_x & \frac{B_y^2 - B_x^2 - B_z^2}{2} & B_y B_z \\ B_z B_x & B_z B_y & \frac{B_z^2 - B_x^2 - B_y^2}{2} \end{bmatrix}$$

1429
$$= \frac{1}{\mu}((\mathbf{B} \cdot \nabla)\mathbf{B} + (\nabla \cdot \mathbf{B})\mathbf{B} - \nabla(\frac{\mathbf{B}^2}{2})) \tag{2.72}$$

1430   T has units of pressure. The shear is given by the off-diagonal elements

1431   of T and the diagonal elements of T correspond to the pressure acting on a

1432   differential area element. Total force on a volume is represented as follow.

1433

1434
$$F = \int \int \int_V \nabla \cdot T dV = \oint_S T \cdot dS \tag{2.73}$$

1435   The conservation of momentum in inviscid flow is represented as follow.

1436

$$\frac{d}{dt} \int \int \int_V \rho \mathbf{v} dV + \oint_S \rho \mathbf{v}(\mathbf{v} \cdot \hat{n}) dS$$

1437
$$= -\oint_S p\hat{n} dS + \int \int \int_V \rho \mathbf{g} dV + \int \int \int_V \nabla \cdot T dV \tag{2.74}$$

1438

1439
$$\frac{d\mathbf{v}}{dt} + (\mathbf{v} \cdot \nabla)\mathbf{v} = -\frac{1}{\rho}\nabla p + \mathbf{g} + \frac{1}{\rho}\nabla \cdot T = -\frac{1}{\rho}\nabla \mathbb{P} + \mathbf{g} \tag{2.75}$$

1440   ,where

$$\mathbb{P} = \begin{bmatrix} p - \frac{B_x^2 - B_y^2 - B_z^2}{2\mu} & -B_x B_y & -B_x B_z \\ -B_y B_x & p - \frac{B_y^2 - B_x^2 - B_z^2}{2\mu} & -B_y B_z \\ -B_z B_x & -B_z B_y & p - \frac{B_z^2 - B_x^2 - B_y^2}{2\mu} \end{bmatrix} \tag{2.76}$$

1441

1442   Note that the magnetic field increases the pressure by an amount $\mathbf{B}^2/2\mu$,

1443   in directions perpendicular to the magnetic field and decreases the pressure

1444   by the same amount in the parallel direction. Thus, the magnetic field gives

1445   rise to a magnetic pressure $\mathbf{B}^2/2\mu$, acting perpendicular to field lines, and a

1446   magnetic tension $\mathbf{B}^2/2\mu$, acting along field lines.
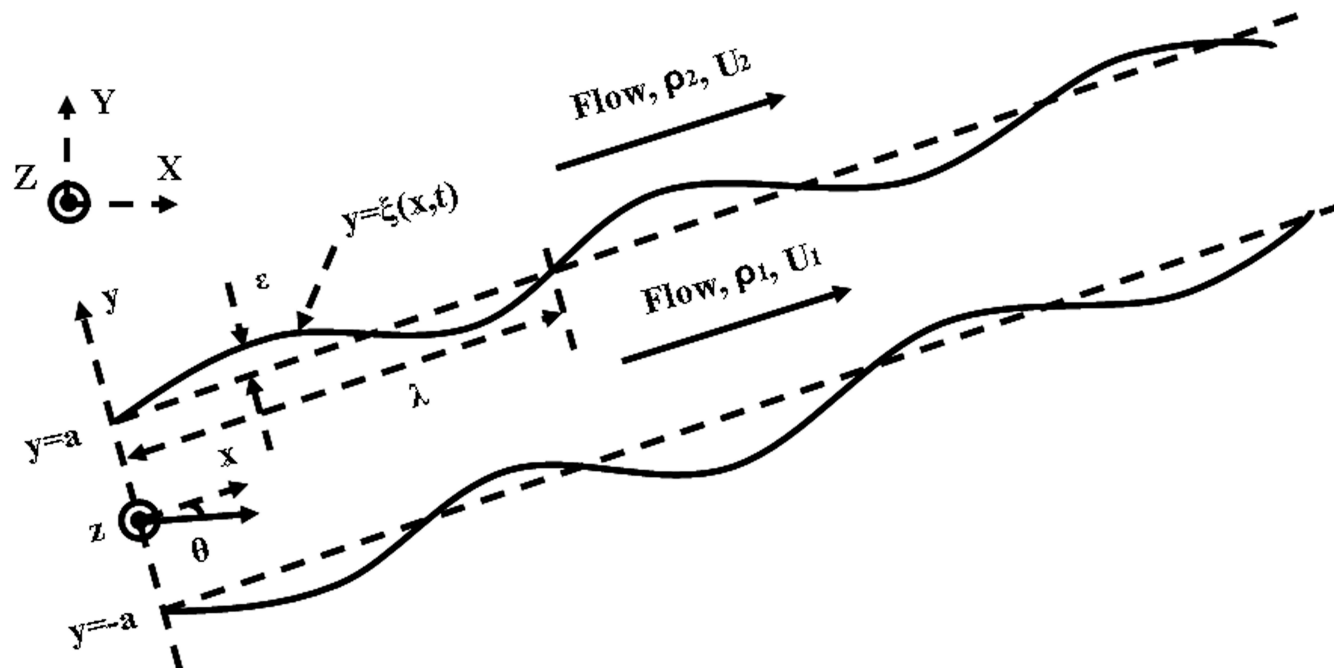
Figure 2.1: Wave-shaped interface separating two different fluids traveling at different average speeds.
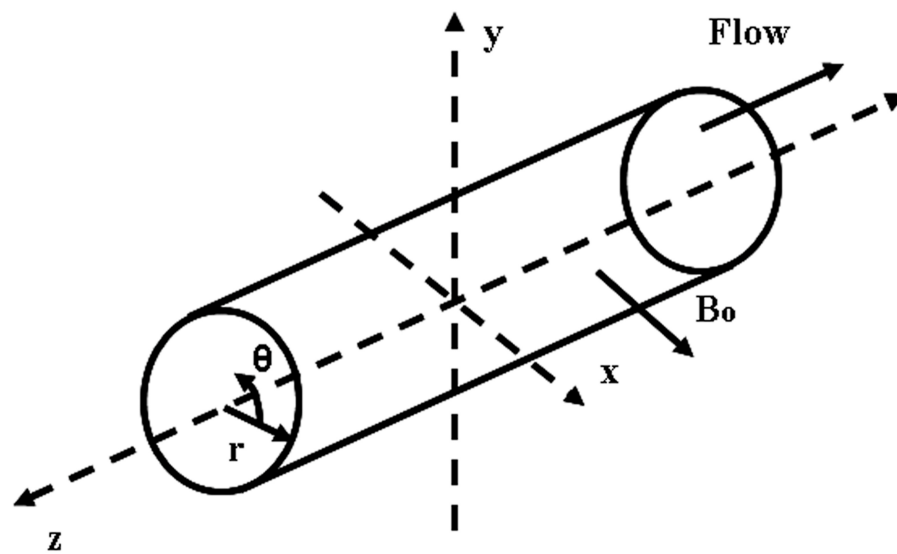
Figure 2.2: Axes and electrodes of circular duct.
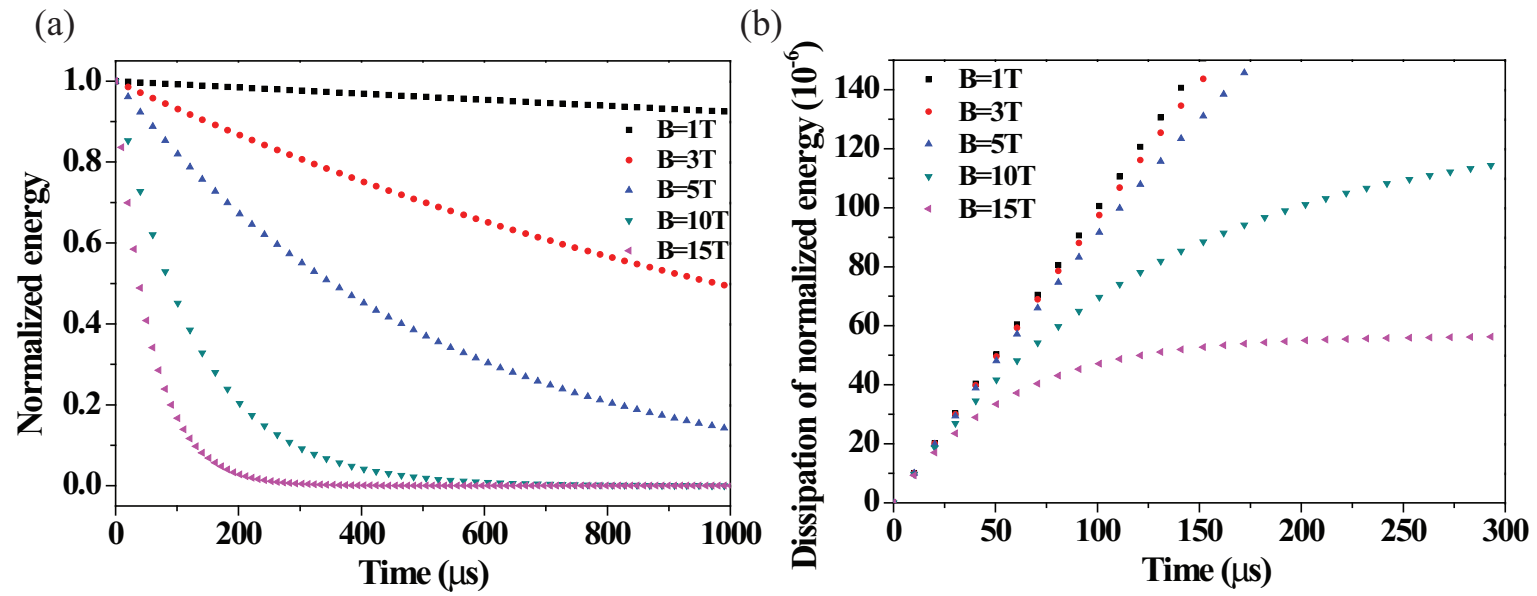
Figure 2.3: Energy decay in magnetic field. a.)Normalized energy decay. b.)Dissipation of normalized energy.

Chapter 3

Experimental Method for Investigation of Magnetohydrodynamic Mercury Jet Flow

The optical method is considered to investigate MHD processes. Optical methods have considerable advantages over other measurement techniques: they do not introduce any perturbations into the medium being investigated, they possess high sensitivity and accuracy, their response is practically instantaneous, which enables them to be used to investigate turbulent flows and transition states, since they provide the possibility of visually following the phenomenon being investigated, and they enable one to obtain the physical characteristics for the whole space being investigated at the same instant of time. Unlike other probeless methods, optical methods possess high spatial resolution. All these features enable optical methods to be widely employed in MHD experiments and underlie the need to search for new ways of using modern optical methods which have not yet been employed.

Direct visualization techniques for hydrodynamic examination have often been employed to investigate the dynamics of MHD flows. In this method, one measures the time taken for the particles to traverse a given path. Because no quantitative results can be deduced from direct visualization methods and difficulties often arise when investigating thin boundary layers in liquids, attention has turned to the use of optical techniques for the investigations of fluid dynamics and MHD (Fedin, 1973).

It should be noted that visualization is usually employed for qualitative investigations, but this method can also be used to measure the average flow velocity and a change in the velocity profile. To do this one measures merely the time taken for the particles to traverse a given path or the path traversed in a given time.

3.1 Optical Diagnostics as a Principal Diagnostics of High Power Target Experiment

3.1.1 Working principle of shadowgraph for optical diagnostics

Optical measurements have many advantages over other techniques. The major one is the absence of an instrument probe that could influence the flow field. The light beam can also be considered as essentially inertialess, so that very rapid transient effects can be studied.

Shadowgraph is often employed in studying shock and flame phenomena,

in which very large density gradients are present. It integrates the quantity measured over the length of the light beam. For this reason they are well suited to measurements in two dimensional fields, where there is no index of refraction or density variation in the field along the light beam.

In a shadowgraph system the linear displacement of the perturbed light is measured. Consider the illumination at the exit of the test section. Figure 3.1 shows the displacement of a light beam for shadowgraph. If the illumination is uniform entering the test section, it should still be closely uniform there. The beam is deflected by an angle α, which is a function of y. The illumination within the region defined by Δy at this position is within the region defined by Δy_{sc} at the screen. If the initial intensity of light is I_T, then at screen,

$$I_o = \frac{\Delta y}{\Delta y_{sc}} I_T \ .$$ (3.1)

If Z_{sc} is the distance to the screen, then the contrast is

$$\frac{\Delta I}{I_T} = \frac{I_o - I_T}{I_T} = \frac{\Delta y}{\Delta y_{sc}} - 1 \simeq -z_{sc} \frac{\partial \alpha}{\partial y} \ ,$$ (3.2)

$$\frac{\Delta I}{I_T} = -\frac{z_{sc}}{n_a} \int \frac{\partial^2 n}{\partial y^2} dz = -\frac{z_{sc}}{n_a} \int \frac{\partial^2 \rho}{\partial y^2} \cdot \frac{\partial n}{\partial \rho} dz \ ,$$ (3.3)

where n is the index of refraction of a homogeneous transparent medium and $n_a \simeq 1$ for the ambient air.

For gas, Eqn. (3.4) could be substituted into Eqn. (3.3). Eqn. (3.3) is integrated twice to determine the density distribution. (Goldstein, 1991)

1509

$$\frac{\partial^2 n}{\partial y^2} = C[-\frac{\rho}{T}\frac{\partial^2 T}{\partial y^2} + \frac{2\rho}{T^2}(\frac{\partial T}{\partial y})^2] \ , \qquad (3.4)$$

1510

1511 where the constant C, called the Gladstone-Dale constant, is a function of

1512 the particular gas and T is temperature of medium on Kelvin scale.

1513 Shadowgraph is used principally for qualitative descriptions of a density

1514 field. Because it yields information on the first and second derivatives of

1515 density, its application can be found in systems with steep gradients of density

1516 and temperature, such as flame fronts and shock waves.

1517 Optical techniques are non-invasive and do not cause any perturbation of

1518 the subject being investigated. Furthermore, their sensitivity increases with

1519 photon intensity and the resolution of the subject can reach the diffraction-

1520 limited resolution. The optical response of fluid dynamics and MHD are prac-

1521 tically instantaneous, enabling the optical technique to study details of tur-

1522 bulent flows and transition states. Coupled to a state-of-the art high-speed

1523 camera and the long interaction path length of a light beam with a field of

1524 view adjustable to arbitrary dimensions, the optical technique enables one to

1525 obtain the physical characteristics for the entire subject being investigated in

1526 a short period of time.

3.1.2 Development of optical diagnostic system

1527

1528 An optical diagnostic system is designed and constructed for imaging a free

1529 mercury jet interacting with a high intensity proton beam in a pulsed high-

1530 field solenoid magnet. The optical imaging system employs a back-illuminated,

56

1531   laser shadow photography technique. Object illumination and image capture

1532   are transmitted through radiation-hard multi-mode optical fibers and flexible

1533   coherent imaging fibers. A retro-reflected illumination design allows the en-

1534   tire passive imaging system to fit inside the bore of the solenoid magnet. A

1535   sequence of synchronized short laser light pulses are used to freeze the tran-

1536   sient events and the images are recorded by several high speed charge coupled

1537   devices.

1538   3.1.2.1   *the optical imaging system and Viewports design*

1539   Laser back-illuminated shadow photography technique is employed in ex-

1540   periment to capture the dynamics of the interaction of the proton beam with a

1541   moving free mercury jet. The design of the optical imaging system is based on

1542   a few essential criteria which are described below. The entire optical imaging

1543   head has to fit inside a small portion of a 1 meter long, 150 mm diameter bore

1544   magnet. Fig. 3.2(a), Fig. 3.2(b), and Fig. 3.2(c) show the conceptual back

1545   illuminated optics design, the installation of 4 Viewports on the primary con-

1546   tainment vessel, and the schematic layout of optical components, respectively.

1547   Note that all optics placed inside the interaction beam tunnel are required

1548   to be radiation-hard because of high radiation levels in the beam tunnel and

1549   the activation of the mercury after proton beam interactions. In our setup, all

1550   cameras, lasers, and all other associated electronics are placed in an adjacent

1551   beam tunnel controlled locally by several desktop computers. Remote control

1552   of the entire system is achieved through designated control desktops located

1553   in the control room via MS Window XP remote desktop connections from the

57

1554 ethernet network (see Fig. 3.7).

1555 A Viewport is located at the beam interaction center and two additional View-
1556 ports are located at ±152.4 mm up/down stream locations. Viewport 4 is
1557 positioned at +457.2 mm and is designed to capture the residual dynamics
1558 of the proton interaction. Because of limited space inside the magnet bore,
1559 object illumination and image capture are transmitted through multi-mode
1560 optical fibers and coherent imaging fibers, respectively, all positioned on one
1561 side exterior to the primary containment vessel. Fig. 3.3 shows the fabricated
1562 and assembled optical head containing the integration of ball lens, imaging
1563 lens, illumination fiber, and imaging fiber.

1564 The arrangement resembles a compact endoscope design but with a different
1565 illumination scheme. Illumination light pulses are coupled into a 15 meter
1566 long multi-mode fiber (ThorLabs BFL22-200). It has a numerical aperture of
1567 0.22, 25° cone angle, with a core diameter of 200 μm that matches that of the
1568 fiber-coupled lasers. To provide a $\sim$ 55 mm illumination area at the center
1569 of the primary containment vessel over a limited short working distance of $<$
1570 100 mm, the illumination cone angle has to be opened up to a 43° full cone
1571 angle. This is achieved by placing a tiny $\sim$ 0.5 mm diameter sapphire ball lens
1572 (Edmund Optics M46-117) at the tip of the illumination fiber and secured by
1573 a thin stainless steel plate. At the heart of the illumination arrangement is a
1574 76 mm diameter Au-coated concave spherical retro-reflector that has a short
1575 radius of curvature of 124 mm (Rainbow Research Optics). When the much
1576 diverged illumination fiber is placed at the radius of curvature and shined

58

onto the optical axis of the reflector, a retro-reflected beam returns back to the illumination fiber providing the back-illumination scheme. Again, because of the tight environment inside the primary, a Au-coated 90° prism mirror turns the optical path from longitudinal to transverse onto the center of the primary. Two anti-reflection coated sapphire windows (Swiss Jewel Company) are mounted on the primary with airtight seals tested up to 1.4 bar pressure. The diameter and the thickness of the window is 100 mm and 6 mm respectively, sufficiently large enough for the observation of a 1 cm diameter jet and mechanically strong enough to withstand the momentum of a direct impact from mercury jet with a mean velocity of 20 m/s (Simos, 2005).

Based on this optical arrangement, a mercury jet in front of the reflector naturally makes a shadow on the retro-reflected beam. The shadow is collected by a 1 mm diameter AR-coated cylindrical grin objective lens (GrinTech, GT-IFRL-100-inf-50-CC) which has an optical path length of 2.43 mm. The grin lens is coupled onto a coherent image fiber. This flexible coherent imaging fiber is the key optical element of the imaging system. It is a 10 meter long Sumitomo IGN-08/30 fiber with 30,000 picture elements (pixels). Each individual fiber has a core diameter of $\sim$ 4 μm with a total fiber diameter of merely 0.96 mm including coating. It has a bending radius of 40 mm, sufficiently small to allow curving and arching inside the primary containment vessel. All imaging fiber ends are hand polished in-house to optical finished quality to allow high quality images with maximum light intensity transmission. Fig. 3.4 shows the final finished end of an imaging fiber after polishing with 0.3 μm lapping

film (ThorLabs, LFG03P). The surface quality and the flatness of the imaging fibers are inspected under a microscope. The imaging fibers are jacketed in-house with reinforced furcation tubing (ThorLab FT030-BK). One end of the imaging fiber is finished with an SMA 905 fiber-optics connector to facilitate coupling to a CCD camera. The other ends of the illumination and imaging fibers are positioned next to each other with ~ 2 mm separation inserted inside a specially fabricated plastic ferrule. The integrated optical head is shown in Fig. 3.3, where a red laser diode is used to illuminate the optical head. The integrated all-in-one ferrule (ball lens, illumination fiber, objective lens, and imaging fiber bundle) is placed at the radius of curvature as well as on the optical axis of the reflector so that it allows both the illumination and the imaging collection to work on one side of the primary. The liquid mercury target is enclosed in a stainless steel primary containment vessel which is placed in the primary beam tunnel (TT2A). A total of four optical imaging heads for each Viewport are mounted on the exterior of the primary, designated as channels 1 to 4. All fibers are routed through a ~ 150 mm diameter, 2 meter long concrete passage to an adjacent beam tunnel (TT2), where radiation is much reduced. All electronics control for the optical diagnostic as well as all other electronics control for the solenoid magnet operation and hydraulic power unit used to generate the mercury jet are also placed in the adjacent tunnel. The exit end of each imaging fiber is coupled to an SMA fiber adaptor (ThorLabs SM1SMA) mounted on an x-y translator (ThorLab LM1XY). Four $40\times$ infinitely corrected microscope objective (Newport M-40x) relay the $\sim$

1623 0.96 mm image outputs of each imaging fiber onto each corresponding CCD

1624 with appropriate lens tubes to fully expand the images onto a typical 10×10

1625 mm CCD array. A non-rotating adjustable lens tube zoom housing (ThorLabs

1626 SM1ZM) provides fine and accurate adjustment of image focus on CCD.

1627 **3.1.2.2** *the consideration for focusing and tilting alignment of op-*
1628 *tics*

1629 A retro-reflective mirror captures the output beam of the laser diode and

1630 focuses it through the field of view at the target onto the lens of the telescope.

1631 The CCD camera views the target through the telescope. Tilting alignment by

1632 using fine adjustments on the side of the retro-reflecting mirror can be made

1633 and the field of view can be adjusted by moving the imaging lens forwards or

1634 backwards. The system is designed to make 6 possible alignment adjustments.

1635 After the retro-reflecting mirror is moved forward or backward, the field of

1636 view can also be adjusted. The maximum field of view that we can obtain is

1637 ~ 5.0 cm diagonally. The distance d from the objective lens to the imaging

1638 lens is related to the field of view at the target. For target to be in focus, one

1639 must obey the lens formula,

1640

1641
$$\frac{1}{f} = \frac{1}{c} + \frac{1}{d} \ , \tag{3.5}$$

1642 where c is the distance from the target to the objective lens and d is the

1643 distance from the objective lens to the camera.

61

3.1.2.3 *high speed cameras and light sources*

Table 3.1 gives the specifications of high speed cameras in terms of some selected attributes. Two FastVision cameras with CCD size of 15.4×12.3 mm run with a full 1280×1000 pixel resolution at a 0.5 kHz frame rate. One Olympus Encore PCI 8000S camera with 1/3 inch CCD size runs with a 480×420 pixel resolution at a 4 kHz recording rate. A high speed "Silica Mountain Devices (SMD)" 64KIM camera with a CCD size of 13.4×13.4 mm runs with a reduced single frame size of $(960 \times 960)/4$ pixel resolution at up to 1 MHz frame rate. For the three slower cameras, images collected by each individual imaging fiber overfill the CCD pixels by a factor of ~ 6 and ~ 3, respectively, i.e. one fiber projected onto 6×6 and 3×3 CCD pixel area, respectively. However, for the SMD camera, each imaging fiber slightly underfills the CCD pixels by a factor of 0.83, i.e. one fiber projected onto nearly a single CCD pixel area. Due to the nature of spatial superposition, an array of imaging fibers imaged by an array of CCD pixels, some images might compose of a honeycomb pattern caused by this pixelation artifact. However, the artifact can be minimized by slightly defocusing the image on the CCD. However, the FastVision and Olympus CCDs are capable of recording at a frame rate higher than 500 Hz, the architecture for binning at reduced resolution requires a change of the zoom ratio on the image head doom. The SMD camera has a different but fixed binning architecture so that the full field of view is taken at a high speed frame rate with reduced resolution. Except for the SMD camera where images are frozen by the short 150 ns illumination laser pulses, all other

1667 images are arrested by the short adjustable electronic exposure time of $10 \sim$

1668 50 μs set on the CCDs.

1669 Synchronized short laser light pulses are used to illuminate the target and

1670 freeze the motion of the jet after the impact of the proton beam. For SMD cam-

1671 era, the mask reduces the photosensitive area to 0.03 of the nominal pixel area.

1672 The quantum efficiency of the photo-resistive area is 0.18 at 800 nm, and the

1673 pixel fill is 200000 electrons. Therefore, a full exposure of a frame of the CCD

1674 therefore requires $(960)^2 \times 200000/0.03/0.18 \approx 3.4 \times 10^{13}$ photons or 10 Watts

1675 for 800 nm photons. For FastVision camera, the sensor is 1280×1024 pixel

1676 (1.03 megapixel) of CCD of total area $15.36 \times 12.29 mm^2$ in 8 bits at 500 frames

1677 per second (10 bits at 400 frames per second). Maximum frame rate is 500,000

1678 at 1×1280. The mask reduces the photosensitive area to 0.4 of the nominal

1679 pixel area. Based on the estimation of required photons, a full exposure of a

1680 frame of the CCD therefore requires $1280 \times 1024 \times 200000/0.4/0.18 \approx 3 \times 10^{12}$

1681 photons or 1 Watts for 800 nm photons.

1682 Optical light pulses are sent through 15 meters of multi-mode illumination

1683 fibers. The light sources used in the experiment are all Class 4 lasers, emit-

1684 ting at wavelengths of 808 to 850 nm. Three lasers are capable of emitting a

1685 peak optical power of 1 Watt (JDS Uniphase SDL-2300-L2) driven by three

1686 independent current drivers (ThorLabs LDC220C). These 1 Watt lasers can be

1687 operated from CW to a minimum programmable pulse width of 1 μs limited by

1688 the trigger logic pulse. The 4th laser emits at a peak optical power of 25 Watt

1689 (Bright Solution BDL20-808-F6) limited by the pulsed current driver (Avtech

1690   AXOZ-A1A-B). It provides a current pulse of 150 ns and is capable of running

1691   at the maximum 1 MHz repetition rate, i.e. a frame rate of 1 μs/frame.

1692   The complete transmission of the imaging system is ~ 0.2 per Viewport

1693   channel, including 0.85 for the 15 meter long illumination fiber, 0.86 for the

1694   sapphire ball lens, 0.86 for each pass of the sapphire Viewport, 0.91 for the

1695   retro-reflector, 0.67 for the 10 meter long imaging fiber, and 0.86 for the grin

1696   lens and the relay lens. For the SMD camera, the imaging circle filled $\pi/4$

1697   of the CCD array. A measured output energy of 3.5 μJ/pulse is obtained

1698   from the Bright Solution (BDL20-808-F6) laser illumination light source for

1699   Viewport 2. Therefore the calculated number of photons impinging on the

1700   SMD camera reaches 4.2×10^6 photons/pixel. After taking into account the

1701   18% quantum efficiency of the CCD, 7.5×10^5 photoelectrons are generated at

1702   the full illumination intensity. Since the SMD camera has full well capacity of

1703 $2.2 \times 10^5 \ e^-$, there is a factor of ~ 3 on the optical power budget reserved for

1704   unanticipated optical power loss and for overcoming the possible attenuation

1705   due to ionization radiation. Similar calculations for Viewport channels 1 and 3

1706   give a factor of ~ 10 on the optical power budget. This larger factor is mostly

1707   due to the long, 10 μs, exposure time set on the FastVision cameras. Overall,

1708   the imaging system is designed to have sufficient optical power budget for the

1709   illumination of each Viewport throughout the entire experiment.

3.1.2.4 *radiation-hardness*

Because of the high radiation level in the beam tunnel and the activation of the mercury after the proton beam interactions, all optics placed inside the interaction beam tunnel are required to be radiation-hard. One complete set of optics was selected for radiation resistance test done at CERN. This complete set of optics included an Au-coated reflector, sapphire window, illumination fiber, imaging fiber, and Grin objective lens. The experiment has anticipated a total of 200 proton pulses at 14 and 24 GeV with a total of $\sim 3 \times 10^{15}$ protons. The calculated total radiation reaches ~ 1 Mrad equivalent radiation dose. Therefore, all optics except the grin objective lens were irradiated at CERN to a lower energy 1.4 GeV proton beam but up to an equivalent radiation dose of 5×10^{15} protons. Because we missed an opportunity to deliver the grin lens to the CERN irradiation facility, the grin objective lens was instead irradiated at BNL using a Co-60 source up to a total dose of ~ 3 Mrad.
The reflectance of the Au-coated reflector and the transmittance of all other optics are measured at the wavelength of 830 nm before and after irradiation. Table 3.2 shows the effects of irradiation up to an equivalent radiation dose of 1 Mrad on the reflectance and transmittance of the components of the optical diagnostic system. No noticeable change in the reflectance was observed on the Au-coated reflector even though the substrate of the reflector has turned nearly opaque. The sapphire, 5 meter long of illumination fiber, and 0.3 meter long of imaging fiber do not show any additional insertion loss. They are all radiation hard up to a 1 Mrad dose. However, the small grin objective lens did suffer

1733   radiation damage resulting in a 0.73 transmission. This tiny grin objective lens

1734   is made of silver-ion exchanged index modification internal to a glass substrate.

1735   Therefore it was not anticipated to have a high radiation resistance. However,

1736   it is well known that although glass (and silica fibers) lose its transmission in

1737   the visible wavelengths, near infrared (NIR) light can still has adequate light

1738   throughput for some applications (Kakuta, 1999). This is one of the reason we

1739   select NIR rather than visible laser light for back-illumination of the mercury

1740   jet. Since the back-illuminated NIR light passes the grin objective only once,

1741   the 0.27 transmission loss over the entire experiment is tolerable and can be

1742   recovered with the present designed laser capability. We should note that the

1743   integrity of the imaging properties of the grin lens was unchanged, i.e. no

1744   image distortion was observed after the 1 Mrad radiation resistance test.

1745   ### 3.1.2.5 *scintillating fiber channel*

1746   A jacketed 2 meter long 1 mm diameter blue emitting scintillating fiber is

1747   attached along with the imaging head to register gamma emission during the

1748   proton beam and mercury jet interaction. A 12 meter long 1 mm diameter

1749   fiber patch-cord (ThorLabs BFH37-1000) carries the blue scintillated light

1750   signal and is fiber-coupled to an Avalanche photodiode (ThorLabs APD210),

1751   designated as channel 0. The overall transmission at the center wavelength of

1752   480 nm of the fiber patch-cord is measured to be 0.77. The scintillating signal

1753   trace is displayed on an oscilloscope and data can be retrieved remotely from

1754   the control room. This scintillating signal serves to confirm the arrival of the

1755 proton beam and has the potential to extract the proton intensity from the
1756 scintillating signal pulse level.

3.1.3 Schematic of electronic trigger and high speed camera control

1759 Because we are using several high speed cameras from different vendors, we
1760 must use separate camera control software for each camera. The limitation on
1761 their exposure time also requires two different set of illumination laser pulse
1762 trains. A master trigger pulse, synchronized to the arrival of the proton bunch,
1763 is delivered to trigger the mercury loop system, the solenoid magnet system,
1764 and the optical diagnostic system together. The mercury jet reaches its steady
1765 state for 1 second when the solenoid magnet reaches the highest magnetic
1766 induction field of 15 T. However, there is a significantly long time lag of ~ 10
1767 seconds for the solenoid system to power up to its full capacity. Therefore,
1768 the master trigger signal is first sent to a digital delay generator (Stanford
1769 Research DG535) to provide a sufficient long delay to synchronize with all
1770 other electronic components. These relative and absolute delays are measured
1771 by an oscilloscope. By adjusting each independent delay channel, complete
1772 synchronization of all cameras with the pulsing of the laser light sources can
1773 be achieved and verified by comparing the bright/dark image intensities of
1774 each frame of each CCD.

1775 Fig. 3.5 shows the two sets of pulse sequences used to simultaneously trigger
1776 all cameras. The 25W infrared laser consisted of a 17 pulse sequence with a

pulse width of 150ns. This determines the exposure time of the SMD camera on the Viewport 2. The laser pulse period is set to match the frame rate of the images. The SMD camera collects 16 frames of image. Fig. 3.6 shows the traced signals on an oscilloscope when the beam and the beam triggering are delivered. After the master trigger from the synchrotron is delivered at time t = 0, the proton beam comes in ~ 3 μs. The photodiode response from scintillating fiber has a 20 ns rise time and the level indicates the beam intensity and beam position. The scintillating fiber signal gives the beam arrival time. Therefore, it is possible to set the trigger timing for the cameras and laser driver inputs, which is ~ 2 μs after the master trigger from the proton synchrotron.

Three 1 Watt lasers pulsed to a 0.5 second duration are used to independently illuminate Viewport 1, Viewport 3, and Viewport 4, respectively. Typically the FastVision and Olympus cameras continuously collect 220 frames of images. The exposure times on the cameras are set at $10 \sim 50$ μs respectively to give a sharp image quality. Although the sharpness of images increases with reduced exposure time, much more light is required for illumination. Therefore, a trade off between exposure time and laser intensity is made. On the contrary, the exposure time for SMD camera is determined by the laser pulse width. As the pulse width of the laser decreases, the laser intensity also decreases. In order to utilize the maximum allowable intensity of the 25W laser, the maximum pulse width of 0.15 μs is used. This pulse width should not seriously jeopardize the image quality even running at its highest frame rate

of 1 μs/frame. A schematic diagram linking all cameras, triggering electronics, and controlling computers is shown in Fig. 3.7. 2 desktops reside in the control room to master the optical diagnostics system. All other electronics and desktops are placed in the TT2 tunnel adjacent to the interaction beam tunnel TT2A.

3.2 Windows Consideration as Viewports for Observation

The mercury jet target is observed through four windows. These windows must contain any possible spray of mercury due to intense beam energy deposition, and remain transparent after a radiation dose from the interaction of beam and mercury.

3.2.1 Fiducial mark on windows

We put fiducial mark on each sapphire window to use the magnitude of the referenced length. The size of fiducial on the back and front windows is varying on images according to the changing field of view. i.e, the back fiducial looks smaller than the front fiducial. Fig. 3.8 shows the artificially marked fiducial on the sapphire window. It gives referencing length scale when we measure the size of jet, velocity, rotation of windows, and the location of magnetic axis on images.

3.2.2 Impact resistance test

We used sapphire windows to obtain enough strength and did surface coating on both sides for anti-reflection at 800nm wavelength. In order to check the survival from mercury droplet impact, we tested sapphire window using a paint ball gun. A paint ball is a 2.75 gram sphere of radius 8.6 mm containing a colored gel that readily "splats" on impact. The velocity of a paint ball was 95m/s. The ratio of the force from a paint ball to that due to the dispersal of the entire mercury jet by the proton beam is

$$\frac{F_{paintball}}{F_{mercury}} = \frac{m_{paintball} v_{paintball}^2 r_{mercury}}{m_{mercury} v_{mercury}^2 r_{paintball}} \; . \tag{3.6}$$

The momentum of the paint ball is the same as that of a 7 mm diameter mercury drop at 95 m/s. The sapphire window survived in the test.

3.2.3 Pressure leaking test of sapphire windows

The primary containment is mostly welded and the window ports are sealed with rubber gaskets (BUNA-N). Each window is sealed with two sheets of rubber gaskets per port. 21 psi is loaded inside the primary containment to check the sealing of the primary containment. To locate leaks, a Metheson 8850 flammable gas sniffer, which has a 5ppm sensitivity, and Ar/Methane (90 % / 10 %) was used. All of 8 windows survived the 21 psi pressure for over 17 hours.

3.3 Integrated Experimental Setup for High Power Target

3.3.1 Mercury loop system in solenoid magnet

The cross-section and actual equipment for the mercury system with high field solenoid magnet is shown in Fig. 3.9. The horizontal line in Fig. 3.9(a) represents the proton beam. The Hg jet, which is ejected from right to left in Fig. 3.9(a), co-propagates with the proton beam. Four Viewports are shown within the solenoid bore, which represent viewing locations for observation of the Hg jet within its primary containment vessel (see Fig. 1.3). Viewport 2 is positioned at the center of the solenoid and is the location where the center of the proton beam interacts with the Hg jet. The Hg system provides for double containment vessel of the hazardous liquid metal, and can be inserted or removed from the solenoid bore without disassembly. A hydraulic syringe pump, with a piston velocity of 3 cm/s was used to pulse the mercury jet. This pump minimizes the heat added to the Hg as opposed to a centrifugal pump. The syringe pump also reduces the discharge pressure which is the limitation of a centrifugal pump. The Hg system provides a jet duration of a ~ 3 seconds of constant velocity profile. A total of 180 kg of Hg is loaded in the system. A 30 KW, 200 bar hydraulic power unit drives the syringe pump.

The pulsed solenoid incorporates a magnetic induction field ramp up of 10 seconds and is capable of sustaining its peak field for a duration of approximately 1 second. A 5.5 MW, 700 V power supply delivers 7500 A of current

71

1861 to pulse the solenoid. The magnet is cryogenically cooled to 77 K prior to

1862 operation and warms up by 30 K during pulsing due to 30 MJ coil heating.

1863 Therefore, a 30 minute cooling time is needed for each single shot. The mag-

1864 netic axis is positioned at an angle of 67 milliradian to the proton beam, with

1865 the tilt provided by a common baseplate supporting all the equipment (see

1866 Fig. 3.9(a)). The applied magnetic induction field has been measured with a

1867 gaussmeter placed both perpendicular and parallel to the magnetic induction

1868 field. The relationship between the measured magnetic induction field and

1869 the applied solenoid current was mapped to deduce the maximum magnetic

1870 induction field at the center of the solenoid. It was found that the maximum

1871 magnetic induction field reached 15 T at Plasma Science and Fusion Center

1872 in Massachusetts Institute of Technology.

1873 **3.3.1.1** *the considerations in nozzle design*

1874 Better yields of low energy pions are obtained from the mercury jet target

1875 when the proton beam and target are tilted with respect to the axis of the

1876 capture solenoid magnet. Monte Carlo simulations have indicated that a tilt

1877 angle of about 100 milliradian between the mercury jet and the proton beam

1878 is optimal (Mokhov, 2000). However, jet motion in a magnetic induction field

1879 behaves differently, depending on the angle between the axis of the magnet and

1880 that of the jet, as a result of the differences in the magnitude of the compo-

1881 nents of the magnetic induction field (Samulyak, 2006). As the crossing angle

1882 increases, the transverse component of the magnetic induction field increases,

72

1883 but with no significant change in the longitudinal component. The increase in
1884 the transverse component of the magnetic induction field raises the induced
1885 current on the Hg jet. Therefore, the angle of the Hg jet is launched at 33
1886 milliradian with respect to the axis of the magnet, resulting in an interaction
1887 region about 30 cm long in case of a 1 cm diameter mercury jet with a 1.5 mm
1888 RMS diameter of proton beam. Since the proton beam in TT2A beamline at
1889 CERN is horizontal, the mercury jet should make a 34 milliradian angle with
1890 respect to the proton beam axis, and the magnetic axis should make an angle
1891 of 67 milliradian with respect to the proton beam. The mercury will flow from
1892 the upstream end of the magnet to the downstream end of the magnet. The
1893 jet velocity is designed to be 20 m/s and the center of the jet to intersect the
1894 center of the proton beam at center of magnet.

1895 ### 3.3.2 Water jet observation for nozzle performance test

1896 Prior to mercury injection in the primary at Oak Ridge National Labora-
1897 tory(ORNL), extensive optical diagnostics were carried out by pulsing water
1898 jets in the system using 4 different types of nozzle configurations. One nozzle
1899 showed the most stable shape of jet motion with fairly uniform velocity, ~ 10
1900 mm diameter and 20m/s respectively.
1901 Due to the spray and wetting of water on the interior of windows, only ambigu-
1902 ous shadow of the water jet was observed. A clear surface motion is required
1903 in order to obtain accurate velocity measurement. Therefore, only qualitative
1904 diagnostics was made on the water jet. The field of view of each Viewport is $\sim$

73

1905   50 mm. The diameter of the jet is measured by overlaying a grid of referenced

1906   field of view onto the images. The time lapse of each frame is read from the

1907   camera frame rates. The trajectory of the jet between several frames can then

1908   be measured and the velocity of the jet surface motion is estimated.

1909   These measurements of the water jet tests were done at ORNL. The observa-

1910   tions led us to select the design of the final nozzle for the subsequent jet runs.

1911   It was fabricated from Titanium and the assembly was anodized for electrical

1912   insulation.
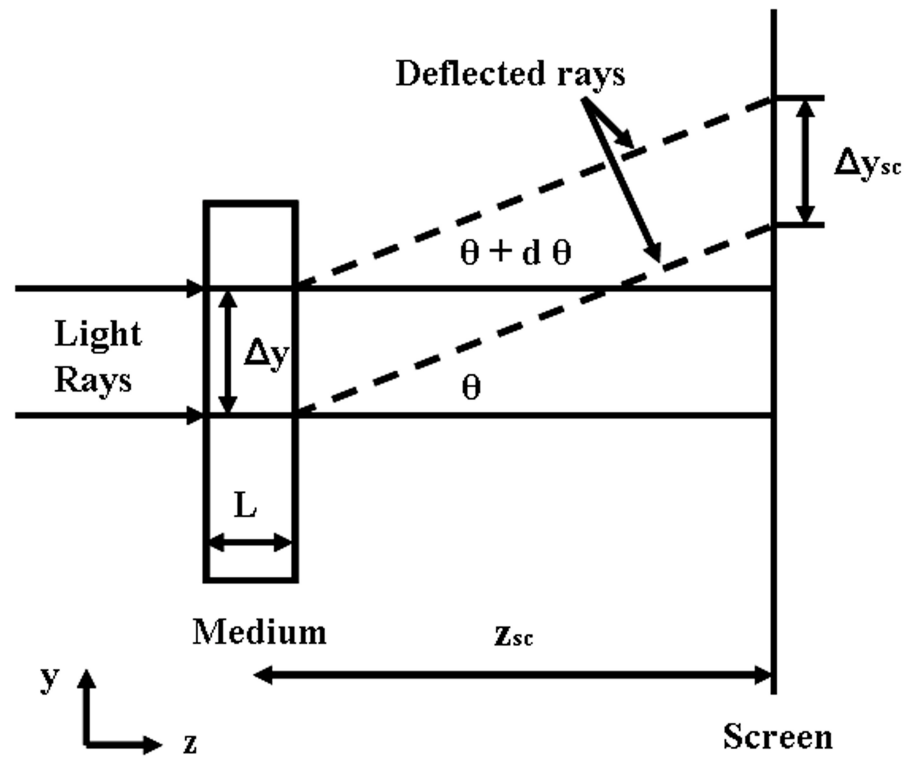
Figure 3.1: Displacement of light beam for shadowgraph.

(a)

(b)

(c)

retroreflector

sapphire
viewport

mercury jet

all-in-one
ferrule

prism mirror

imaging and illumination fibers
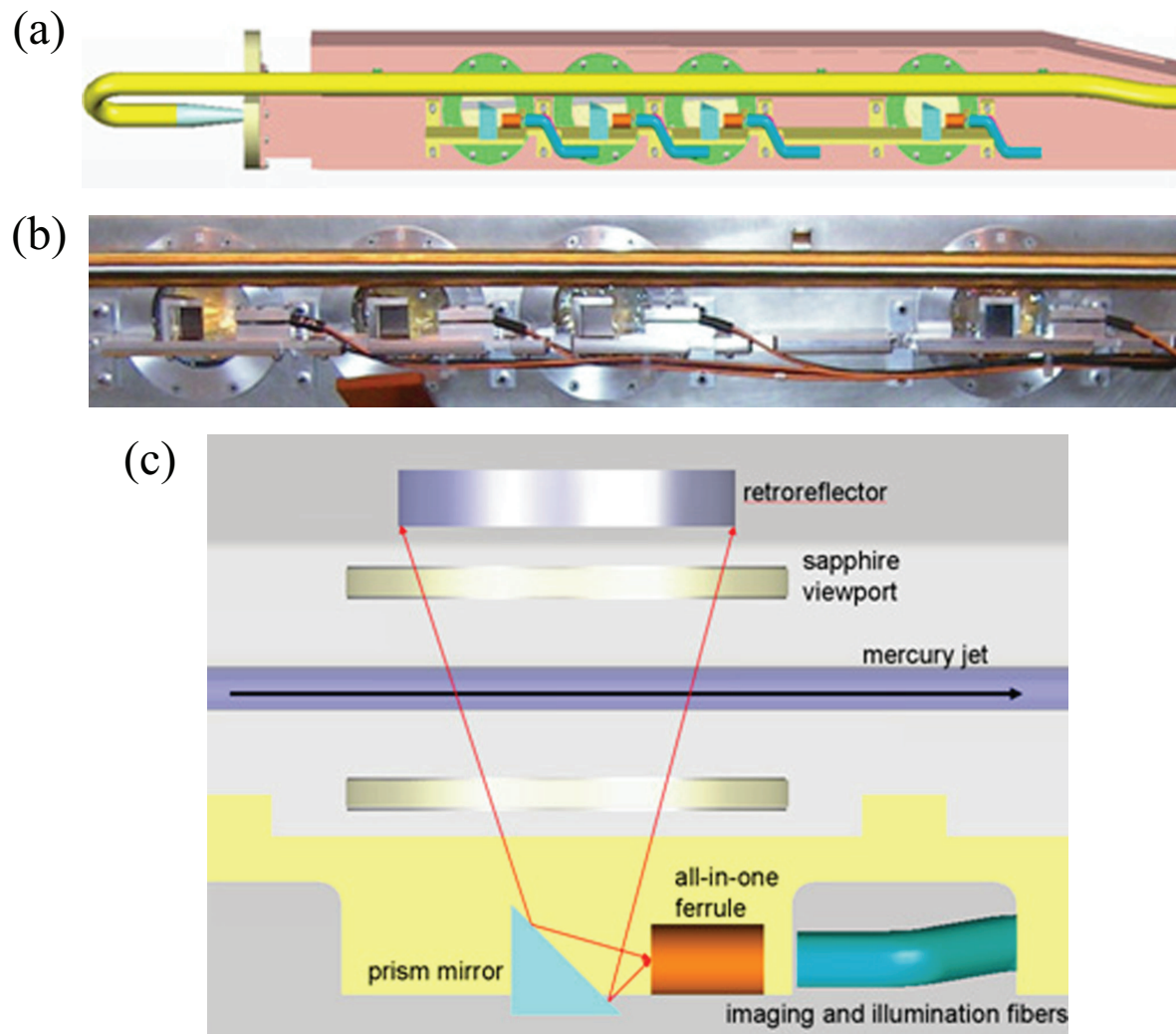
Figure 3.2: Design of optical layout and installation of 4 Viewports of primary containment vessel. a.) Conceptual integration of optics to primary containment vessel. b.) Photograph of installation of optics to primary containment vessel. c.) Schematic layout of optical components.
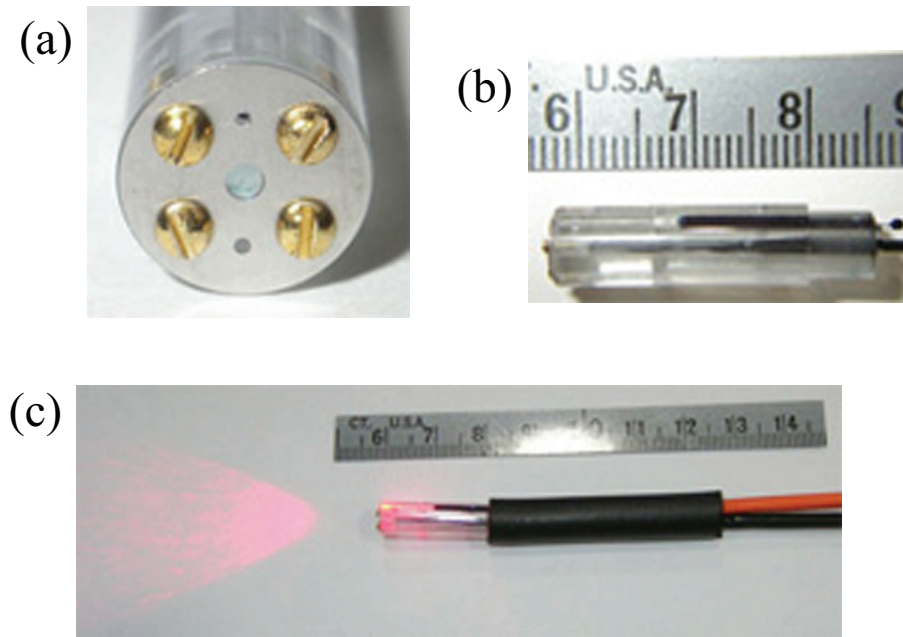
Figure 3.3: Photograph of optical head assembly and its illumination of laser. a.) Front view of optical head assembly. b.) Side view of optical head assembly. c.) Illumination of fiber-optics head assembly.
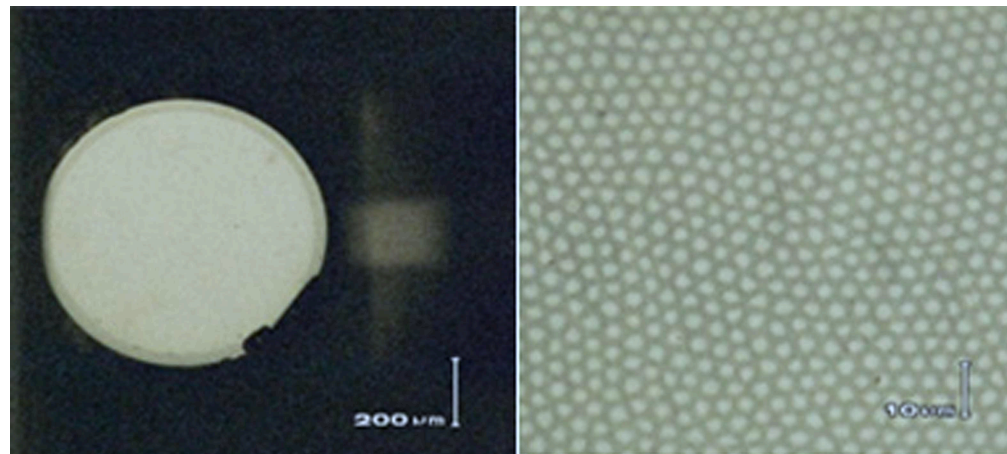
Figure 3.4: Polished fiber end, 50X and 800X magnifications, respectively
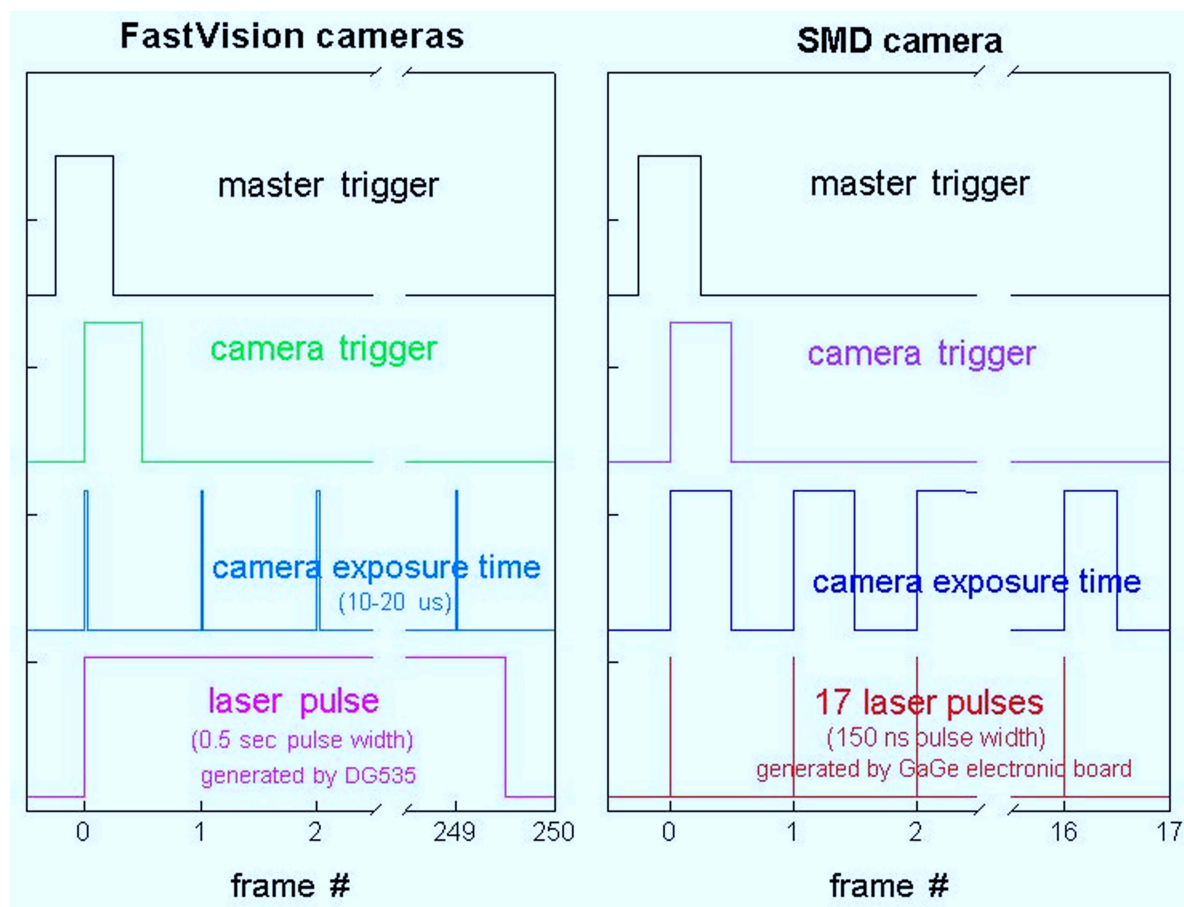
Figure 3.5: Schematic of synchronized signal of high speed camera and laser pulse.
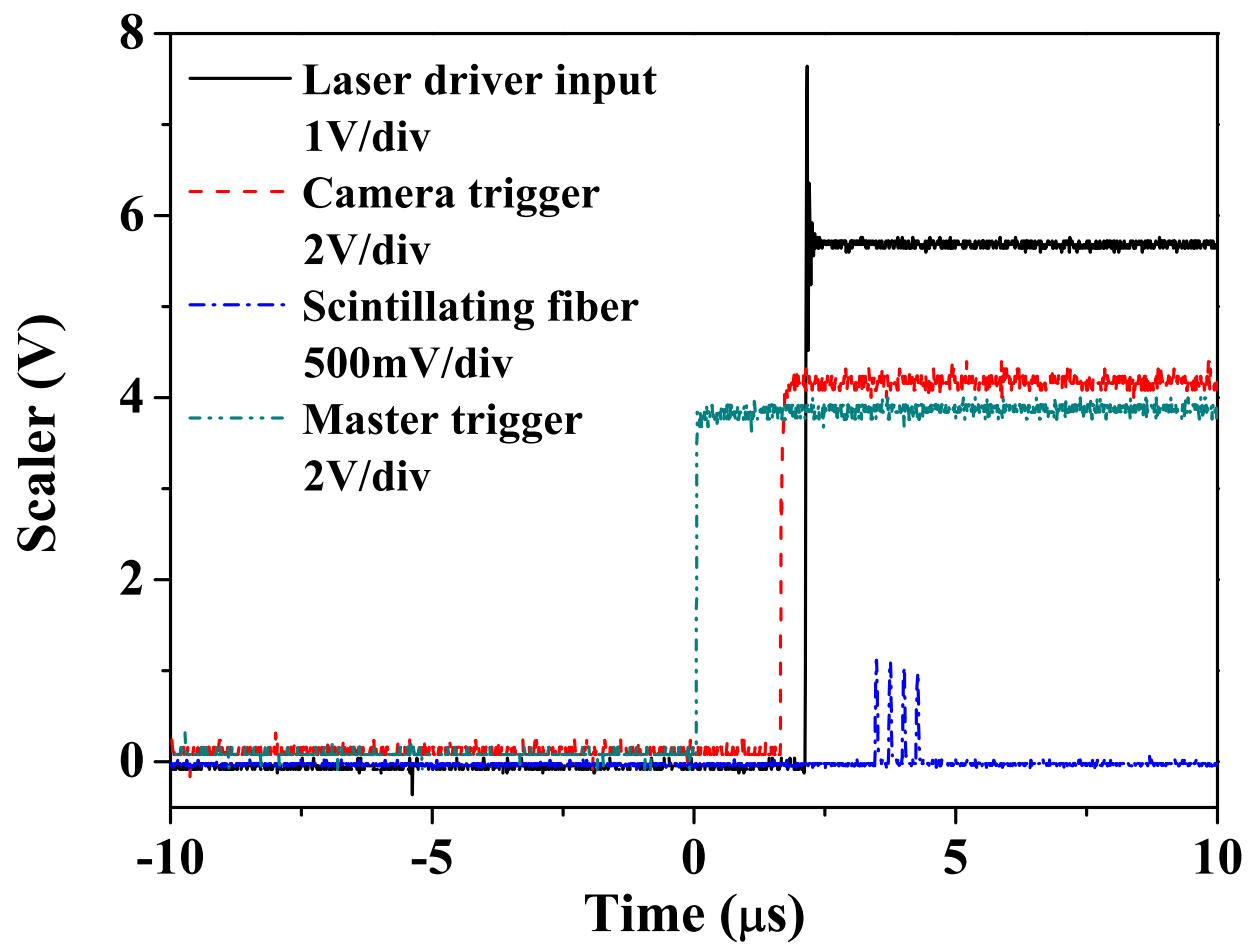
Figure 3.6: The triggering time for high speed camera upon beam arrival.
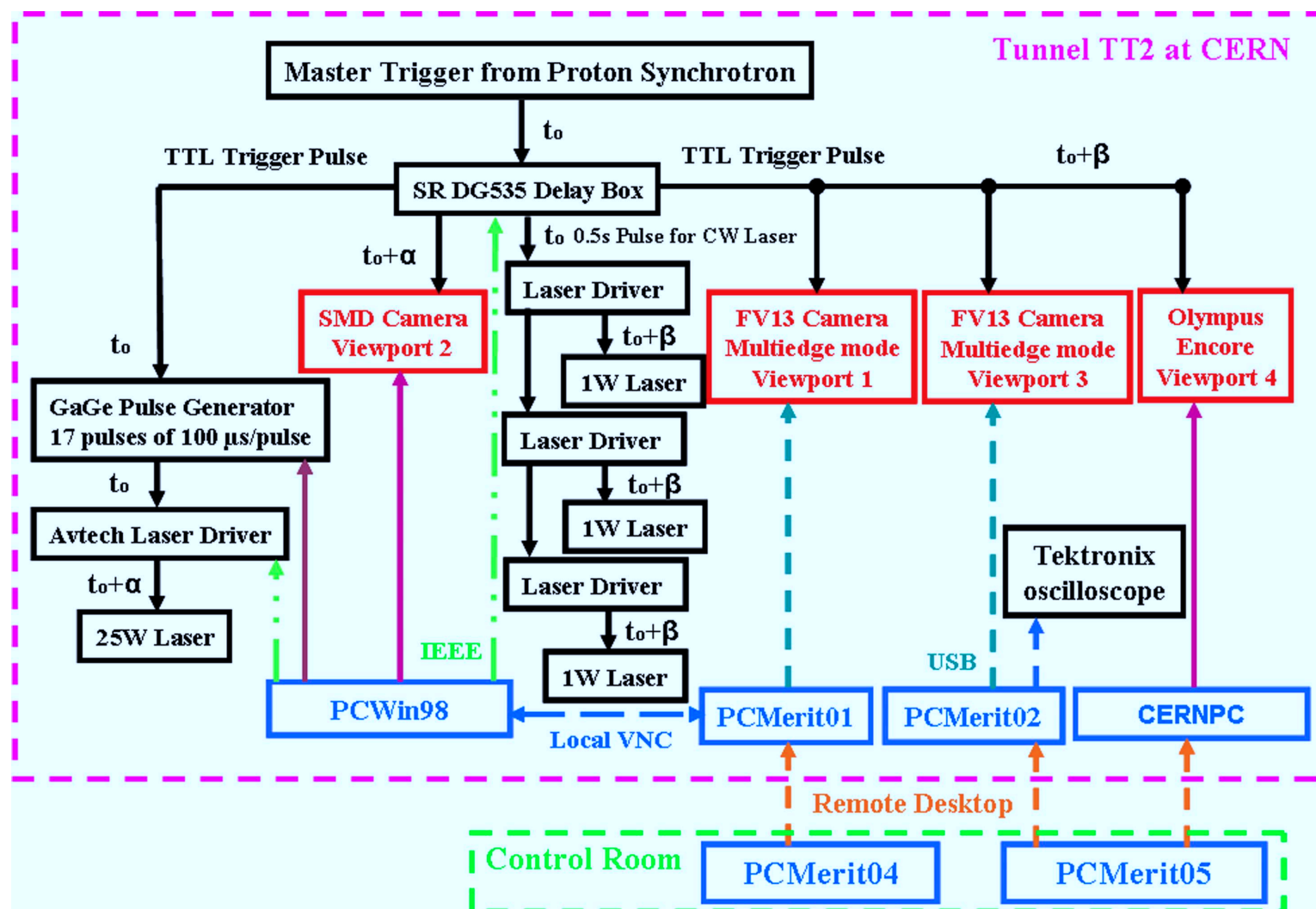
Figure 3.7: Schematic of electrical triggering and high speed camera control in tunnel for experiment.
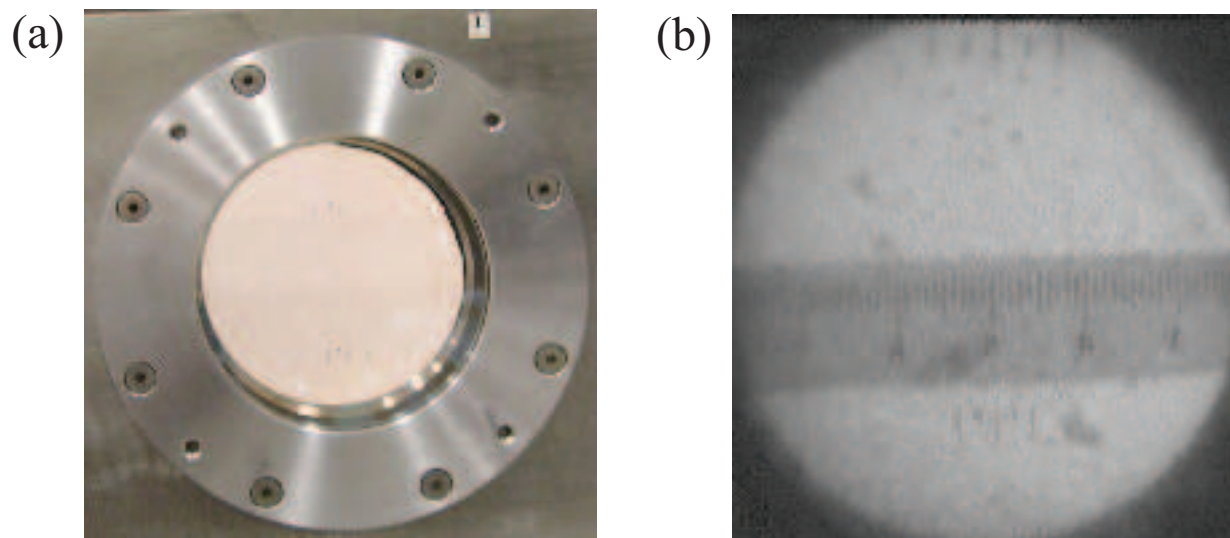
Figure 3.8: Top fiducial on the front window and bottom fiducial on the rear window. a.) Photo of fiducial on the sapphire window assembled in Viewport. b.) Image of fiducial captured by camera.
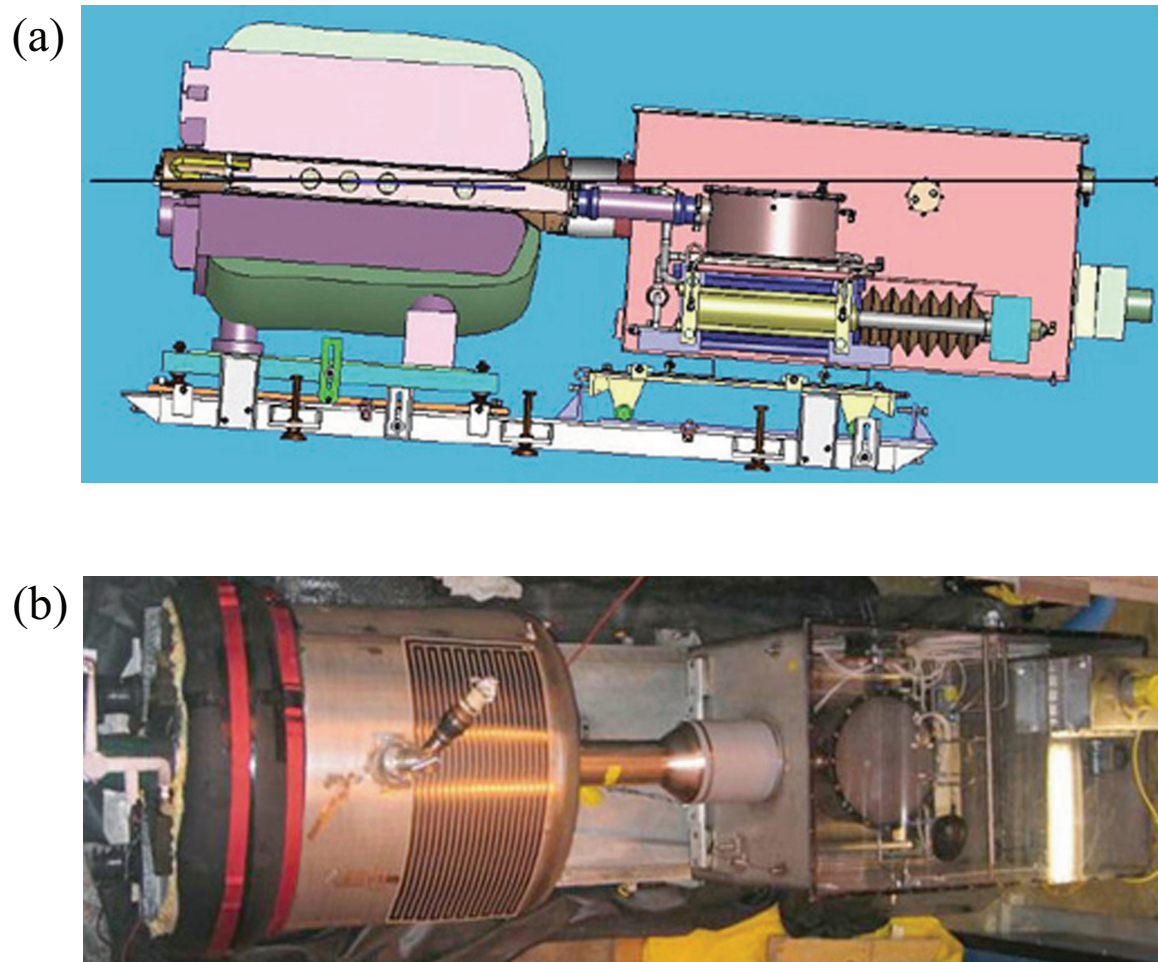
Figure 3.9: Photographs of the entire MERIT experiment. a.) Sectional side view of mercury loop system integrated with 15 T solenoid magnet. b.) Fabricated mercury loop system assembled with 15 T solenoid magnet (Top view).

Table 3.1: Specifications of high speed cameras.

Attributes	SMD 64KIM	FastVision	Olympus Encore PCI 8000S
CCD chip size	13.4 mm × 13.4 mm	15.4 mm × 12.3 mm	1/3 inch
Pixels	960 × 960	1280 × 1024	480 × 420
Pixel size	14 μm	12 μm	13 μm
Single frame	240 × 240	1280 × 1000	480 × 420
Maximum frame rate	1 MHz[1]	0.5 kHz[2]	4 kHz[3]
Full well Capacity	220,000 e^-	∼ 1000 LSB/lux-sec	-
ADC	12 bit	8 bit	8 bit

---

[1] 16 frames.

[2] at full resolution.

[3] 12.5 μs electronic shutter, with reduced frame size.

Table 3.2: Effects of irradiation up to an equivalent radiation dose of 1 Mrad on the reflectance and transmittance of the components of the optical diagnostic system. Reflectance is inferred on the Au-coated mirror and transmittance is inferred on all other components.

Optical component	Before radiation	After radiation	% difference
Large Au-coated mirror	0.91	0.92	no change
Sapphire window(1-mm)	0.86	0.87	no change
Illumination fiber(5m)	1	1.02	no change
Imaging fiber (30 cm)	0.67	0.71	no change
Grin lens	0.90	0.66	73 %

Chapter 4

Experimental Investigation of Mercury Jet Flow in Magnetic Fields

In this chapter, the jet behavior in magnetic field are investigated. To do this, the collected images are read digitally and the characteristic jet parameters are evaluated based on the probability approach. It effectively diagnoses the jet condition on each collected image. Jet deformation such as the free jet surface deformation and surface stabilization is investigated by measuring the pixels on the collected images based on 2-D shadow photography. Aa a result, we will discuss the magnetic field effect to the dynamic behavior of freely moving jet in a solenoid magnetic field. The driving pressure of mercury flow entering inlet pipe is measured to monitor the effect of the magnetic field and assure if the input condition for driving the jet is affected. In order to diagnose the flow rate, the flow velocity in magnetic field is discussed and the deflection of jet size in various magnetic field is investigated. Based on the observed flow rate of jet, the shape of jet is suggested for the energy deposition calculation

1931 by proton beam interaction with Hg jet target.

4.1 Image Analysis for Data Reduction

4.1.1 Image acquisition

1934 ~ 360 complete integrated tests (i.e., with magnet, proton beam, Hg loop
1935 system, and optical diagnostic system) were conducted at CERN (European
1936 Organization for Nuclear Research) with various values of the proton beam
1937 structure (8 harmonic and 16 hamonic) and the beam intensity up to 30×10^{12}
1938 protons and the beam energy (14 Gev/c and 24 GeV/c) and the the magnetic
1939 field (0T, 5T, 7T, 10T, and 15T) and two Hg jet velocities (15 m/s and 20
1940 m/s). Fig. 4.4 and 4.5 are representative optical diagnostic results collected by
1941 the 3 cameras, with and without a magnetic induction field at Plasma Science
1942 and Fusion Center in Massachusetts Institute of Technology. Note that the
1943 Olympus Encore PCI 8000S camera for Viewport 4 was integrated in the beam
1944 interacting target study done at CERN.

1945 The current in the magnet system generates heat, which is cryogenically
1946 removed using liquid nitrogen. As the magnet cools down, all Viewports be-
1947 come foggy up due to condensation. It was found out that $\sim 0.5 \; \ell$ of water
1948 (from nozzle performance test at Oak Ridge National Laboratory) was not
1949 removed from the system prior to loading Hg. Flexible heater strips were
1950 installed both on the exterior of the primary containment vessel and on the
1951 snout in order to prevent the condensation of the humid air on the Viewports.
1952 Although residual Hg droplets in sizes less than 1 mm often adhere to the

1953 sapphire Viewports after every shot, jet motion with adequate image quality
1954 could still be collected.

1955 4.1.2 Image processing

1956 To measure the shape of the jet, 8 and 12 bit grey scaled TIF images are
1957 converted into digital forms. Background images are subtracted to reject the
1958 noise in the image digitization process. The residual data is then transformed
1959 into a 2 bit scaled image. Fig. 4.1 shows the collected image and its trans-
1960 formed 2 bit scaled image. Only the black and white colored pixels in the 2
1961 bit depth images are used to differentiate the shadow of the jet and the back-
1962 ground. Due to the image quality caused by the Hg droplet on window and
1963 the quality in fiber optic system, the noise such as black dots exits. A thresh-
1964 old is adjusted according to Otsu's method to highlight the interface between
1965 the mercury and background (Otsu, 1979). Otsu's method selects the thresh-
1966 old by minimizing the within-class variance and maximizing the between-class
1967 variance of the two groups of pixels separated by the thresholding operator.
1968 Otsu's method, which relies on the assumption that all image pixels belong to
1969 one of two classes, background or foreground, has been shown to be efficient
1970 in image segmentation for bi-level thresholding.
1971 Fig. 4.2 show the sensitivity of 2 bit scaled image conversion to the mea-
1972 surement of jet height using Otsu's method. As the threshold level increases,
1973 the mean value of the jet height as well as the σ value of the jet height in mea-
1974 surement is approaching an asymptotic level. The optimally selected threshold

1975 value by the Otsu's method in this example is 0.35.

1976 The Hg jet was observed at upstream (Viewport 1), midstream (Viewport

1977 2), and downstream (Viewport 3) locations from the nozzle exit. 220 images

1978 are collected at each run for both the upstream and downstream locations,

1979 with an image size of 1280×1000 pixels. The most probable transverse

1980 jet height within the longitudinal pixel range of 300 to 1000 is shown in the

1981 histogram of Fig. 4.3(a). Note that within this range, the transverse jet height

1982 probability P is obtained by counting the number of longitudinal pixel events

1983 in the jet image. If z denotes the transverse direction (in terms of pixels), the

1984 histogram in Fig. 4.3(a) can be written as (Eqn. (4.1)) using the least square

1985 curve-fairing approach:

1986

1987
$$P(z) = P_1 \frac{1}{\sqrt{2\pi}\sigma_1} e^{-\frac{(z-\mu_1)^2}{2\sigma_1^2}} + P_2 \frac{1}{\sqrt{2\pi}\sigma_2} e^{-\frac{(z-\mu_2)^2}{2\sigma_2^2}} , \qquad (4.1)$$

1988 where μ_1, μ_2 are the means, σ_1, σ_2 are the standard deviations, and P_1, P_2

1989 are the a-priori count of the histogram distribution. Note that, in pixel units,

1990 μ_1=386, μ_2=401, σ_1=3.8, and σ_2=21.6. The number of background events

1991 (i.e., outside of the jet) is always larger than that within the jet because the

1992 portion of bright background on each image is larger than that of the black

1993 jet shadow. The distribution on the left in Fig. 4.3(a) (i.e., $0 < z < 200$)

1994 represents the background pixels and is not included in the faired curve in

1995 Fig. 4.3(b).

1996 On the other hand, rather than using the fitting of the histogram of number

1997 of events, the number of pixels corresponding to the jet height is counted within

89

1998   the longitudinal pixel range of 300 to 1000. Each counted pixel numbers are

1999   directly average to give a jet height measurement and then added up over $\sim$

2000   200 images for 1 jet shot, where the time elapse corresponds to ~ 0.4 s at

2001   Viewport 1 and 3. Multiple shots are then used to add up all of the counted

2002   vertical jet height. The average of the individually counted vertical pixels is

2003   given to indicate the nominal jet height. In a mathematical form, the direct

2004   averaging method is described as Eqn. (4.2) and its measurement is shown at

2005   Fig. 4.7 (b).

2006

2007
$$D_{jet} = \frac{1}{i + j + k} \sum_{1}^{i} \sum_{1}^{j} \sum_{1}^{k} N_{vertical} \qquad (4.2)$$

2008   where D_{jet} and $N_{vertical}$ denote the averaged vertical jet height and a in-

2009   dividually counted number of vertical pixels respectively. i, j, k represent the

2010   number of shots, images in a shot, and vertical lines in a image respectively.

2011   On Viewport 2, 16 image files are collected at each run, with an image size

2012   of 316×316 pixels. The images are analyzed in the same manner as described

2013   above. Viewports 1 and 3 give the same resolution for the images: $1280 \times$

2014   1000. Thus, no image re-scaling is needed when comparing the pixel size for

2015   these images. However, Viewport 2 gives a resolution of 316×316. Based on

2016   the 1 cm scale fiducial mark on the exterior of all Viewports, all images taken

2017   on this Viewport are re-scaled to match the resolution of Viewport 1 prior to

2018   comparison.

4.1.3 Study on the scaling length and the location of center of window

In order to relate the lengths on the collected images at each Viewport, the pixel length on the images has to be investigated. Since the image size corresponds to the CCD size, any discrepancy in horizontal and vertical pixel size is not considered. Viewports 1 and 3 give the same resolution for the images: 1280×1000. Thus, no image re-scaling is actually needed when comparing the pixel size for these images but did the scaling to see any difference on the image length of Viewport 1 and Viewport 3. The fiducial length on the top front window and the bottom back window is measured and then interpolated to get the length at the mid-span on the primary containment. The interpolated pixel length at the mid-span corresponds to 1 cm at the mi-span of primary containment. Thus, in Viewport 3, a pixel length at the mid-span where the jet is moving is approximated ~ 0.05 mm. Same scaling was done at images in Viewport 3. The ratio of the pixel length in Viewport 3 to Viewport 1 is 1.06.

Viewport 2 gives a resolution of 245×252. Based on the 1 cm scale fiducial mark on the exterior of all Viewports, all images taken on this Viewport are re-scaled to match the resolution of Viewport 1 prior to comparison. A pixel length at the mid-span is approximated ~ 0.21 mm. Viewport 4 gives a different resolution of images depending on the frame rate setting but typically the resolutions of 320×280 was used. A pixel length at the mid-span is approximated ~ 0.21 mm, which is same with Viewport 2.

91

2042   The distance of the center position between the fiducial and the window is

2043 0.75 inch apart. In order to locate the center of the window at the mid-span,

2044 the positions where 0.75 inch is apart from the top fiducial and bottom fiducial

2045 is found on each image and then the averaged difference in the located position

2046 is considered as the center of window.

2047   Based on these scaling study, the measurement is performed for the fol-

2048 lowing investigation. The measurement is averaged for ~ 200 images to give

2049 a result of the following investigation and the standard deviation is also cal-

2050 culated for the individual measurement respectively. Based on the standard

2051 deviation and the number of events, the error bar, $\sigma/\sqrt{N}$, is calculated to give

2052 error estimation for each measurement.

2053 ## 4.2   Motion of Mercury Jet and Stability in
2054   Magnetic Field

2055 ### 4.2.1   Jet deflection and surface flattening

2056   When the jet is injected without an applied magnetic field, it is difficult

2057 to discern the jet surface because of blockage by Hg droplets on the win-

2058 dow. Therefore, some errors in the measurement exists (see images Fig. 4.4(a)

2059 through Fig. 4.4(c) and 4.5(a) through 4.5(c)). On the contrary, when a mag-

2060 netic field is applied, the measurement errors are significantly reduced,leading

2061 to significantly less intermittent jet boundaries.

2062   The inertial forces appear to dominate the jet movement when the jet

2063 velocity is 15 m/s. The turbulent jet motion is unstable but becomes stabilized

2064 as the magnetic field approaches 5 T. It has been reported that the radial force

2065 induced by the transverse component of magnetic field caused by the axially

2066 induced current due to the tilted jet angle can significantly increase the jet

2067 height (Gallardo *etal*, 2002). The phenomena of increasing jet thickness with

2068 high magnetic induction field is observed for the first time when the magnetic

2069 field exceeds 10T.

2070 The Fig. 4.7 (a) shows the jet height variation by the magnetic field

2071 strength and the jet height is measured by fitting the histogram of number

2072 of events resulted from the image processing. The standard error is used to

2073 give the error bar, where the standard deviation is divided by the number of

2074 samples. The Fig. 4.7 (b) shows the jet height measurement by direct aver-

2075 age of vertical jet height from scanned pixels on each image. The standard

2076 deviation is used to give the error bar. This two plot shows the extreme two

2077 conditions of evaluation of the measured jet height, but one can effectively

2078 observe the fluctuating amount relative to the nominal jet height according to

2079 the various magnetic fields.

2080 At a jet velocity of 15 m/s, the relatively low inertial force reduces the

2081 extent of turbulent fluctuation. For this case, the magnetic field does not

2082 significantly affect the dynamics of the jet until the magnetic field strength

2083 of ~ 5 T reaches. Consequently, the height of the jet decreases only slightly

2084 until 5T since the magnetic field reduces the fluctuating surfaces and the jet

2085 is more likely to elongate axially to the jet axis. The results shown in Fig. 4.4

2086 and 4.5 clearly suggest that the magnetic field has constrained (stabilized)

2087   the Hg jet flow by smoothing out the edges of the otherwise turbulent flow.

2088   At large number of the magnetic field (>10 T), stability is maintained at all

2089   Viewports. At 15 T, a larger height (cross sectional distortion) is observed on

2090   all Viewports.

2091   The fact that the Hg jet size is relatively reduced from 0 T to 5 T but

2092   increases from 10 T to 15 T suggests that the Hg jet might encounter a different

2093   type of instability at high field, namely a quadrupole effect. The quadrupole

2094   effect would alter the jet's circular cross-section to become elliptical. From

2095   the data obtained with a 15 m/s jet, the jet height at a 10 T is smaller

2096   than that at 15 T, which is manifested in the vertical elongation of the jet.

2097   However, the height at a 10 T is smaller than that at 5 T. The issues for such

2098   a behavior have to be addressed. There are two possibilities. First, the jet

2099   is elongating axially up to 10 T. The equivalence of hydrodynamic pressure

2100   with magnetic pressure is more dominantly affecting to the axial elongation of

2101   jet than the transverse pressure. Eqn. (2.76) shows the magnetohydrodynamic

2102   stress tensor, which indicates the ration of the axial pressure and the transverse

2103   pressure. The increasing axial pressure of jet is more elongating from 0 T to

2104   10 T. However, the transverse magnetic pressure becomes significant once the

2105   magnetic field exceeds 10 T. Thus, the jet at 15 T is experiencing the transverse

2106   deflection as well as axial deflection, but the the role of transverse deflection

2107   plays significantly on the behavior of jet. That can explain why the reduction

2108   of jet is appearing up to 10 T and then the expansion of jet is appearing at 15

2109   T.

94

2110   Second, the optical diagnostics depends only on the side sectional view of

2111   jet movement. The reduction of jet size on the minor axis of the elliptical

2112   core has to be accompanied by the gain in jet size on the major axis in order

2113   to satisfy the continuity condition in flow. In other words, the cross-sectional

2114   are in flow should be constant. Although the two dimensional nature of the

2115   image data does not distinguish between an elliptical cross section and a cir-

2116   cular one, occasional observation of a smaller jet thickness at 15 m/s with 10

2117   T field as opposed to a 5 T indicates that the jet cross section might vary

2118   between the major and minor axis of an elliptical core. It is important to note

2119   that within the axial distance of interest, the jet diameter is approximately

2120   constant. Therefore, references to "larger jet height" should be interpreted

2121   to mean larger distortions of the jet cross section. Since the jet and solenoid

2122   field are cylindrically symmetric, it is hard to estimate in what direction the

2123   jet is going to be distorted but the ratio of the deflection can be determined

2124   experimentally. The ratio also can be compared with the transverse magnetic

2125   pressure $B^2/2\mu$ considering the reversed direction of deflection on each plot.

2126   If then, the Fig. 4.7 (a) gives the deflection ratio with magnetic field in an in-

2127   creasing sequence from 0 T to 15 T approximately consistent with the ratio of

2128   magnetic pressure $B^2/2\mu$. Samulyak (2007) suggested that the deflection ratio

2129   of jet size $\triangle R/R_o$ is proportional to the magnitude $\mathbf{B}_o^2/U$. by using the devel-

2130   oped MHD code, where the governing MHD equations and free jet boundary

2131   condition including Maxwell's equations using low magnetic Reynolds approx-

2132   imation are employed and calculated the Hg jet deflection in magnetic field

2133 using a hybrid of Eulerian and Lagrangian method, so called Front tracking

2134 method. Fig. 4.8(a) shows the deflection ratio of Hg jet along the distance from

2135 nozzle at 10 T and 15 T magnetic field. As shown in Fig. 4.4 and Fig. 4.5,

2136 the magnetic field stabilizes the Hg jet surface so that the jet surface is getting

2137 flattened. In MHD simulation, constant 1 cm diameter of Hg jet is considered.

2138 Although the magnetic field causes the jet surface flattening, the nature of

2139 turbulence such as growth of jet size is observed in experiment. Therefore, in

2140 order to avoid such a turbulent nature between simulation and experiment,

2141 the ration of jet deflection ratio between 10 T and 15 T is evaluated to see the

2142 comparison of the magnetic field effect $\mathbf{B}_o^2/U$ between Fig. 4.8(a) and Fig. 4.7

2143 (b), which is shown in Fig. 4.8(b). It shows somewhat consistency at upstream,

2144 but still the ratio diverges as the jet flows to downstream.

2145 As expected, jet motion in a magnetic field behaves differently, depending

2146 on the angle between the axis of magnet and the axis of jet, as a result of

2147 the differences in the magnitude of components of magnetic field (Samulyak,

2148 2006). Fig. 4.6(a) and 4.6(b) show the axial and radial components of the

2149 magnetic field in a solenoid. Fig. 4.6(c) and 4.6(d) show the transverse and

2150 longitudinal components of the magnetic field along the jet axis at different

2151 crossing angles. As the crossing angle increases, the transverse component of

2152 the magnetic field increases, but with no significant change in the longitudinal

2153 component of the magnetic field. An increase of the transverse component of

2154 the magnetic field raises the induced axial current on the Hg jet. Therefore,

2155 the angle of the Hg jet is launched at 33 milliradian with respect to the axis

96

2156 of solenoid magnet.

2157   The jet surface can readily be extracted from each collected image. The

2158 jet axis is approximated by fitting the averaged positions between top surface

2159 and bottom surface. This jet axis is moved with an offset until it interferes the

2160 top surface bottom surface. The amount of fluctuations of surface is measured

2161 by getting the difference between the fluctuation surfaces and the interfering

2162 jet axis on a RMS scale. Let $\delta(r,t)$ denotes the probability of turbulence at r,

2163 such that δ is 0 in the non-turbulent fluid, where the background is considered

2164 here, and is 1 in the turbulent fluid, where the jet is considered here. Time av-

2165 erage of δ yields $\zeta(r)$, the intermittency factor at r. The turbulent fluctuations

2166 are produced by the intermittency effect and these fluctuations are significant

2167 for scalar quantities. The intermittency characteristics of the turbulence are

2168 the appropriate input to be used in defining rough surface for a scattering

2169 analysis. When the intermittency phenomenon is present, the conventional

2170 turbulent fluctuation is modified by the intermittency function and there is

2171 an additional contribution depending on the difference between the mean tur-

2172 bulent quantity and the non-turbulent quantity (Yen, 1967). However, the

2173 probability of the fluctuating jet surface area is introduced to define the in-

2174 termittency in the following work. The pixel information along the jet axis

2175 by changing the translational offset is added to represent the intermittency of

2176 jet on the top/bottom surface. The intermittency within the jet represents 1

2177 and it is gradually decrease to 0 at the background. The intermittency is be-

2178 tween 0 and i at the jet surface depending on the surface fluctuations. Fig. 4.9

shows the intermittency as a function of magnetic field and time. Total evaluated time is 160 μs. Without magnetic field, the slope of intermittency at the jet surface is broad and it is oscillating as a function of time. With higher magnetic field, the slope of intermittency at the jet surface is more steep and it keeps same shape with respect to time. This result clearly tells that the magnetic field suppresses the fluctuation of jet surface.

The Fig. 4.10 shows the measured fluctuations on the jet surface. Surface fluctuations is monotonically decreasing and the surface is flattened approximately at 5 T. The fluctuations at Viewport 3 (downstream) is larger than that at Viewport 1 (upstream) since the tendency to be more turbulent grows. The amount of fluctuations at top surface and bottom surface of jet is almost same, though the magnetic field is varied. Thus, the symmetry on the jet surface in terms of the surface variations such as fluctuations and wave amplitude is valid. The amount of difference of surface fluctuations at Viewport 1 and Viewport 3 becomes same. It indicates that the jet surface becomes flattened at 5 T in flow velocity 15 m/s. The decreased amount of surface fluctuation at Viewport 1 and Viewport 3 is $\sim$ 0.5 and 1.5 mm RMS respectively. This explains why the jet height is reducing from 0 T to 5 T in Fig. 4.7 (a). The magnetic field makes the wavelength on the jet surface increases. Correspondingly, the wave propagation speed is increasing. Thus, it causes Re_{cr} to increase and the flow becomes laminar due to the stabilization by the magnetic field. The transverse component of magnetic field prevails more over the jet stabilization. Though there is some measurement errors due to the

2202   saturation in image brightness, the measurement could show the field effect to

2203   the reduction of fluctuation on jet surfaces.

2204   The these observations are supported by previous results. For example,

2205   several investigations have suggested that magnetic field suppresses turbulent

2206   fluctuations in conducting liquid by stabilizing the flow (Shercliff 1956, Gold

2207   1962, Kozyrev 1981, Bernshtam 1982), where stabilization is judged by an

2208   increase in the characteristic wavelength of the flow.

4.2.2   Trajectory of mercury jet projectile in magnetic field

2209
2210

2211   The Hg jet and the beam are launched at 33 and 67 milliradian with respect

2212   to the magnetic axis respectively. The trajectory of Hg jet projectile is acted

2213   upon by gravity, which is represented as follow:

2214

$$t = \frac{x}{v_o \cos\theta} \, ,$$

$$y = -\frac{g}{2} \, t^2 + v_o \sin\theta \, t + y_{nozzle} \, ,$$

$$|v| = \sqrt{v^2 - 2gx\tan\theta + (\frac{gx}{v\cos\theta})^2} \, , \tag{4.3}$$

2215

2216   where x is the jet traveling distance, y is the height at x, y_{nozzle} is the

2217   vertical position of nozzle, v_o is the launched velocity, and θ is the launched

2218   angle of Hg jet. Based on the governing trajectory equation Eqn. (4.3), fit

2219   function of the jet flow height can be expressed as

2220

$$y = A_1 + B_1 x - \frac{g(1 + B_1^2)x^2}{2C_1^2}, \tag{4.4}$$

2221

2222   where $A_1 = y_{nozzle}$, $B_1 = \tan\theta$, and $C_1 = v_o$. The values and error are

2223   given in Table 4.3. The distance of jet elevation is determined by measuring

2224   the distance from the magnetic axis at center of each window to the jet axis,

2225   which is approximated by fitting the averaged positions between top surface

2226   and bottom surface. The Fig. 4.11 shows the trajectory of Hg jet and it's effect

2227   by the magnetic field and gravity. The solid line represents the globally fitted

2228   value using the trajectory of projectile with different initial launching speed of

2229   jet for the case of 15 m/s and 20 m/s respectively. It shows that the trajectory

2230   of Hg flow approximately agrees well with the trajectory of projectile for both

2231   15 m/s and 20 m/s shots. Experiment shows that the trajectory of the Hg jet

2232   is parabolic. The magnetic field caused some elevation of Hg jet closer to the

2233   center of magnetic field. As the jet moves to downstream, magnetic field effect

2234   is more clearly observed since the jet is more likely to elongate to the axial

2235   direction. The longitudinal magnetic force is more increasing as one can see the

2236   magnetic pressure term in the longitudinal direction increasing at Eqn. (2.76).

2237   Therefore, it is observed that the jet is behaving more like straight at Viewport

2238   4 with higher magnetic field. At 15 T, the elevation of jet is observed from

2239   Viewport 1 to Viewport 4. It shows that the magnetic force is overcoming the

2240   inertia force at 15 T similarly as there is the increase in jet height at 15 T. The

2241   overall increase of the jet elevation in upstream, midstream, and downstream

2242   at 15 T may have been caused by the asymmetric change of jet height. Possibly

2243   the stable equilibrium between magnetic force and gravitational force could be

2244   varying according to the variation of magnetic field (Geim, 1999).

2245 The beam trajectory is also given to show the overlap with the Hg jet. It
2246 is shown that the overlap length is ~ 30 cm when we consider the height of
2247 jet at various position with various magnetic field.

2248 Based on the result of the jet trajectory, the angle of jet axis at Viewport 2
2249 (midstream) is determined by the trigonometric approach using the elevation of
2250 jet and the distance along the magnetic axis between Viewport 1 and Viewport
2251 3. Fig. 4.12 shows the estimation of jet angle at centner of magnetic axis
2252 (Viewport 2), which is approximately $7 \sim 11$ milliradian. The jet angle is
2253 slightly decreasing with higher magnetic field, which indicates that the jet is
2254 more likely to move horizontally following the field line direction.

2255 4.3 Dynamics of Liquid Jet Flow From Nozzle

2256 4.3.1 Jet flow in surrounding medium

2257 Lee (1977) investigated the phenomenon of air wake caused by a cylindrical
2258 jet emerging from a nozzle and showed the boundary layer of jet by applying
2259 continuity of jet mass and matching the loss of jet momentum with air drag on
2260 the jet. Fig. 4.13 depicts schematically the boundary layer of jet emerging from
2261 a nozzle. The conservation of axial momentum and the rate of momentum loss
2262 to the skin friction on the jet and the continuity of the liquid jet are expressed
2263 as follows:

2264

2265
$$2\pi\rho_a \int_0^{\delta(x)} [a(x) + y]v^2(x, y)dy + \rho_l \pi a^2(x)v_l^2(x) = \rho_l \pi a_o^2 v_{lo}^2, \qquad (4.5)$$

$$\frac{d}{dz}[\pi \rho_l a^2(x) v_l^2(x)] = 2\pi a(x) \mu_a \frac{\partial v}{\partial y}\Big|_{y=0}, \tag{4.6}$$

and

$$\pi a^2(x) v_l(x) = \pi a_o^2 v_{lo}, \tag{4.7}$$

where velocity, density, and viscosity are denoted by v, ρ, and μ, respectively, with subscripts a and l for air and liquid, respectively. The subscripts o denotes the initial values at the nozzle. For boundary layer analysis of cylindrical objects, because of the diverging flux characteristics in radial direction, a logarithmic profile is the most appropriate (Stewartson, Glanert, 1955). Thus, the velocity profile of the air induced by the liquid jet is assumed to be as follow:

$$v(x, y) = v_l(z)\{1 - \frac{1}{\beta(x)} \ln[1 + \frac{y}{a(x)}]\}. \tag{4.8}$$

$$\frac{\delta(x)}{a(x)} = e^{\beta(x)} - 1. \tag{4.9}$$

Substitution of Eqns. (5.15) into Eqns. (5.8)   Eqns. (5.13) results in

$$\bar{v}_l(\bar{x}) = \frac{v_l(\bar{x})}{v_{lo}} = \frac{1}{1 - \bar{\rho}[1 + \frac{1}{\beta} - \frac{1}{2\beta^2}(e^{2\beta} - 1)]}, \tag{4.10}$$

$$\frac{d\beta(\bar{x})}{d\bar{x}} = \frac{\beta^2 - \bar{\rho}[\beta^2 + \beta - \frac{1}{2}(e^{2\beta} - 1)]}{\beta(1 + e^{2\beta}) - (e^{2\beta} - 1)}, \tag{4.11}$$

2287   where $\bar{x} = \frac{4x}{\mathrm{Re}_e a_o}$, $\mathrm{Re}_e = \frac{2a_o \rho_a v_{lo}}{\mu_a}$, and $\bar{\rho} = \frac{\rho_a}{\rho_l}$. For a given value of ρ,

2288   the stream velocity $\bar{v}_l(\bar{x})$ and boundary layer thickness $\bar{\delta}(x)$ are obtained.

2289   As seen in Fig. 4.14, the Reynolds number plays its role implicitly and this

2290   makes the density ratio $\bar{\rho}$ to be varied. Since the cylindrical jet has larger

2291   volumes, for the initial momentum of the jet to be maintained, the liquid

2292   density must be reduced and the value of the density parameter to be used

2293   must be modified to $\bar{\rho} = \rho_a D^2 / (\rho_l d_o^2)$, where D and d_o denote diameter of jet

2294   and nozzle, respectively.

4.3.2   Pressure loss and magnetic effect to the Hg delivery pipe

2295

2296

2297   Fig. 4.15 (a) and 4.15 (b) show the pipe inlet pressure for driving jet in

2298   various magnetic field strength. The Hg jet is driven by the piston in syringe

2299   and the piston velocity is measured by position sensor. The piston velocity

2300   determines the flow rate so that the dynamic pressure head at pipe inlet is

2301   determined using the conservation of flow rate. The pressure sensor installed

2302   at the pipe wall measures the static pressure. No significant pressure drop

2303   is observed at the pipe inlet in magnetic field strength. It indicates that

2304   the driving pressure in pipe for nozzle is at same condition regardless of the

2305   magnetic field variation.

2306   To obtain the jet velocity, the distance traveled by a fixed point on the

2307   jet surface is tracked over a given time period. Fig. 4.16 (a) shows the jet

2308   velocity measured at Viewport 1, Viewport 2, Viewport 3, and Viewport 4 in

2309 various magnetic field strength. Note that this velocity does not change with
2310 the imposition of a magnetic field. Therefore, considering the measurement
2311 error in Fig. 4.16 (a), the averaged flow velocity, regardless of magnetic fields,
2312 can reasonably indicate the flow velocity given in Fig. 4.16 (b). This explains
2313 why the pressure is approximately constant in the pipe, consistent with the
2314 report (Graves, 2007).

2315 Another interesting result is that the cross section of Hg jet is more likely to
2316 be elliptical since the longitudinal jet flow velocity is constant from upstream
2317 to downstream. Regardless of the magnetic field, the Hg jet does not show jet
2318 velocity change. Thus, the jet is changing its shape once it leaves the nozzle
2319 from circular to elliptical. Hence, the result in Fig. 4.7 (a) should be again
2320 interpreted by the result in Fig. 4.16 in the manner that the jet height at 5
2321 T is elongated on the minor axis followed by the reduction of jet height on
2322 the major axis of the elliptical core, and the jet is deflecting further at 10
2323 T. However, the jet height at 15 T is elongated on the major axis, which is
2324 manifested by the comparison between the ratio of the reduction of jet height
2325 and the increased ratio of the jet height at 15 T. This approach is already
2326 mentioned in the above, but it is examined again.

2327 Considering that the driving pressure and the jet velocity are not signifi-
2328 cantly changed in various magnetic field, it is concluded that the longitudinal
2329 magnetic field does not affect to the pressure loss or velocity degradation while
2330 Hg passes the solenoid magnet two times along with the direction of magnetic
2331 field line. It is reported that the gradient of longitudinal jet velocity depends

104

2332 on the integration of gradient of longitudinal magnetic field along the magnetic

2333 axis plus it's multiplication to longitudinal magnetic field itself. (Gallardo *etal*,

2334 2002) It is expressed as follow:

2335

2336
$$\Delta v(x) = \frac{\kappa}{\rho} \frac{r_o^2}{8} \left(\int_{x_1}^{x_2} (\frac{dB_x}{dx})^2 + \frac{d}{dx}(B_x \frac{dB_x}{dx}) \ dx \ \right) , \tag{4.12}$$

2337 where r_o is the radius of jet and κ is electrical conductivity. Since the gradient

2338 of magnetic field is increasing (plus) at entrance and decreasing (minus) at

2339 exit, it seems that there is an increasing velocity gradient (acceleration) at

2340 upstream and decreasing velocity gradient (deceleration) at downstream but

2341 it is ≤ 0.5 m/s due to the relatively high density comparing with the electrical

2342 conductivity only if we consider the effect by the magnetic field. The exper-

2343 imental result shows slight effect of magnetic field but is consistent with the

2344 reported result in terms of the gradient of longitudinal velocity in magnetic

2345 field.

2346 ### 4.3.2.1 *pressure loss in pipe flow*

2347 Schematic pipe geometry is given in Fig. 1.3, where the pipe is connected

2348 from the syringe pump to nozzle and it is passing parallel with solenoid mag-

2349 netic field line next to the primary containment. A loss coefficient is defined

2350 as follows:

2351

$$(h_{loss}) = K_1 \frac{v_1^2}{2g} + K_2 \frac{v_2^2}{2g} + \ldots + K_N \frac{v_N^2}{2g} ,$$

2352
$$A_1 v_1 = A_2 v_2 = \ldots = A_N v_N = A_R v_R , \tag{4.13}$$

2353   where the subscript R signifies a reference location and K represents the

2354   loss coefficient.

2355   The general thermodynamic loss, so called the head loss h_{loss} is defined as

2356   follow:

2357

2358
$$\int_1^2 \delta F = (h_{loss})_{1,2} = \frac{p_1 - p_2}{\rho g} + \frac{v_1^2 - v_2^2}{2g} + (z_1 - z_2) \ . \qquad (4.14)$$

2359   Darcy-Weisbach equation is given to express the head loss of wherever

2360   the density is constant, when the pipe diameter is constant and the pipe is

2361   horizontal.

2362

2363
$$\frac{\Delta p}{\rho g} = f \frac{L}{d} \frac{U^2}{2g} \ , \qquad (4.15)$$

2364   where f, L, d are friction factor, the pipe length, and the diameter of

2365   pipe respectively. Considering that the Re $= 1800000$ and $e/d = 0.002$ for

2366   commercial steel in terms of Nikuradse's sand grain scale, turbulent friction

2367   factor f via Moody plot or by Colebrook Eqn. (4.16) is approximated to 0.024.

2368   Colebrook simply combined the expressions for the friction factor for smooth

2369   and rough pipes into a single transition equation of the equivalent form.

2370

2371
$$\frac{1}{\sqrt{f}} = 1.74 - 2 \ log \ (\ 2\frac{e}{d} + \frac{18.7}{\mathrm{Re}\sqrt{f}} \ ) \ . \qquad (4.16)$$

2372   Note that Colebrook's expressions for the friction factor in the transition

2373   region reduces to Prandtl's smooth pipe equations when the relative roughness

2374   approaches zero, and reduce to von Karman's fully rough pipe equation at very

2375   high pipe Reynolds number.

2376   The loss coefficients for elbows are presented as follows, where a and R

2377   represent the inside radius of the elbow and the radius of curvature of the

2378   centerline of the elbow respectively. For $\text{Re}(a/R)^2 > 91$, the loss coefficient is

2379   expressed as follow (Ito, 1960):

2380

2381
$$K_{elbow} = 0.00241 \; \alpha \; \theta \; (\; \frac{R}{a} \;)^{0.84} \text{Re}^{-0.17} \; , \qquad (4.17)$$

2382   where θ is the bend angle in degrees and α is an empirical factor given by Ito

2383   as,

2384
$$\alpha_{\theta=90°} = 0.95 + 17.2 \; (\; \frac{R}{a} \;)^{-1.96} \; . \qquad (4.18)$$

2385   Inputting $R = 1.942$ and $a = 0.442$, $\alpha = 1.9$ and $K_{elbow} = 0.1232$.

2386   A correction term is applied to the 90° elbow to determine the loss coeffi-

2387   cient for arbitrary angle of elbow (SAE, 1960).

2388

2389
$$K_\theta = (\; C_\theta \;)_{elbow} \; K_{90°} \; , \qquad (4.19)$$

2390   where C_{elbow} is given in the referenced manual (SAE, 1960). The C_θ is 0.28

2391   at $\theta = 23°$ and $K_\theta = 0.0345$.

2392   The loss coefficient for the reducer or well-rounded inlet loss is $K_{reducer} =$

2393   0.05 based on the flow area of the smaller piping section (Benedict, 1980).

2394   The loss coefficient for the abrupt enlargement is determined by combining

2395   the momentum balance over the area of interest. Then, it yields the Carnot-

2396   Borda equation, which shows the head loss in the abrupt enlargement. By

2397   equating it to the head loss equation Eqn. (4.13), the loss coefficient is given

2398   based on the inlet velocity as follow:

2399

$$K_{enlargement} = (1 - \frac{v_2}{v_1})^2 = (1 - \frac{A_1}{A_2})^2 = (1 - \beta^2)^2 \; ,$$

2400
$$\frac{p_1}{p_2} = 1 + (\frac{1 - G_1}{G_1})(2\beta^2 - 2\beta^4) \; , \tag{4.20}$$

2401 where G_1 is the inlet pressure ratio of static pressure to total pressure,

2402 p_t/p_{t1}. The fluid experiences pressure loss when going from a piping system

2403 to a plenum, so called exit loss. According to Eqn. (4.20), the loss coefficient

2404 for exit K_{exit} is 1, where $\beta = 0$. It applies regardless of whether the pipe

2405 protrudes into the exit plenum, is well rounded at exit, or is flush.

2406 Finally, the loss coefficient for the abrupt contraction is given based on the

2407 velocity at exit as follow (Benedict, 1980):

2408

$$K_{contraction} = (\frac{1}{C_D^2} - 1)(1 - \beta^4) \; ,$$

2409
$$C_D = \frac{Q_{acutal}}{Q_{ideal}} \; , \tag{4.21}$$

2410 where the discharge coefficient C_D is given in reference (Benedict, 1980).

2411 The mean discharge coefficient is given as 0.815 based on the water tests in

2412 short pipes. According to Eqn. (4.21), this yields a maximum loss coefficient

2413 at $\beta = 0$ of 0.506. Assuming $\beta = A_2/A_1 = 0.9$, $K_{contraction}$ yields 0.1738.

2414 The head losses and the contribution of each geometry are given in Ta-

2415 ble 4.2. Total length of pipe is 87.1 inch. The diameter of inside pipe is 0.884

2416 inch. The diameter of inside nozzle is 0.4 inch. Total pressure head loss is

2417 4.5344 m., which corresponds to $\sim$ 30 % of input pressure head. The main

2418 loss is caused by the exit from nozzle, which is over $\sim$ 50 %. The following

108

2419   loss is caused by the friction due to the large length, which is ~ 27 %. The

2420   loss from pipe bend is somewhat low comparing with others.

2421   Based on the calculated head loss, the jet velocity at nozzle is determined

2422   assuming the pressure right after the nozzle is atmospheric. The pipe inlet

2423   pressure is given in Fig. 4.15 (a) and 4.15 (b). The elevation of the pipe inlet

2424   and the nozzle is 2.9 inch. The calculated jet velocity from nozzle including the

2425   pressure loss in pipe is 13.4 m/s, which is consistent with the measured result

2426   in Fig. 4.16 where the jet velocity is ~ 13.5 m/s. According to Eqn. (2.76), the

2427   magnetic field increases the fluid pressure by an amount $B^2/2\mu$, in directions

2428   perpendicular to the magnetic field, and decreases the fluid pressure by the

2429   same amount, in the parallel direction of the magnetic field. The fluid pressure

2430   including the magnetic pressure has to balance with the atmospheric pressure

2431   and surface tension of jet and satisfy the continuity condition. The fluid

2432   pressure will find equilibrium point since the fluid pressure perpendicular to the

2433   magnetic field line is mutually symmetric. Therefore, the jet is changing to be

2434   elliptical in Fig. 4.7 (a). Hence, the pressure drop is not occurred significantly

2435   and correspondingly the longitudinal jet velocity is not changed with magnetic

2436   field in Fig. 4.16.

2437   **4.3.2.2**   *the measurement of wall tap pressure*

2438   Wall taps is used in order to sense static pressure, wherein small pressure

2439   taps are located at a point on such surface as cylindrical pipe so that it does

2440   not disturb the fluid. Tap size error arises because of a local disturbances of

2441 the boundary layer.

2442

$$\mathrm{Re}_d^* = \frac{v^* d_{tap}}{\nu} \ ,$$

2443
$$\mathrm{Re}_d^* = \sqrt{\frac{f}{8}} \ (\frac{d_{tap}}{d}) \ \mathrm{Re} \ , \qquad (4.22)$$

2444 where d_{tap} is the tap diameter, Re_d^* is the tap Re number, and v^* is the

2445 friction velocity. The friction factor is 0.024. The tap inside diameter and pipe

2446 inside diameter are 0.5, 0.884 inch respectively, which yields $\mathrm{Re}_d^* = 55764$.

2447 At tap Re greater than 385, the error in static pressure caused by the tap

2448 size is given as follow:

2449

2450
$$\frac{e_{tap}}{\tau} = 0.269 \ (\mathrm{Re}_d^*)^{0.353} \ , \qquad (4.23)$$

2451 where $\frac{e_{tap}}{\tau} = 12.74$.

2452 Combining the Darcy friction factor with the wall shear stress yields

2453

2454
$$f = 4 \ (\frac{\tau}{\rho v^2 / 2g}) \ . \qquad (4.24)$$

2455 Therefore, the error in a static pressure can be expresses as non-dimensionalized

2456 form by the dynamic pressure $p_{dynamic}$.

2457

2458
$$\frac{e_{tap}}{p_{dynamic}} = (\frac{e_{tap}}{\tau})\frac{f}{4} \ , \qquad (4.25)$$

2459 where $\frac{e_{tap}}{p_{dynamic}} = 0.0764$. The error of static pressure in Fig. 4.15 (a) is

2460 estimated to give 7.64 % uncertainty of the dynamic pressure in Fig. 4.15 (b).

Table 4.1: Error estimation of fiducial length at each viewport.

Viewport number	Fiducial length (cm)	Scaling factor
1	1.0 ± 0.095	1.0 (reference)
2	1.0 ± 0.091	4.3 ± 0.81
3	1.0 ± 0.062	1.0 ± 0.16
4	1.0 ± 0.067	4.3 ± 0.70

Table 4.2: Pressure head losses by geometry in pipe for mercury loop.

Geometry in pipe for mercury loop	Calculated pressure head loss	Percentage in total pressure head loss (%)
Friction by surface roughness	1.4176	60.7
Elbows in pipe bend (3 ×90°, 2 ×23°)	0.2629	11.3
Reducer, Contraction in nozzle	0.6553	28

Table 4.3: Parameterized coefficients, its error, and statistics summary of fit function in figures.

Figure	1	2	3	4	5	6	7	8	9	10
4.11(B=0T,V=15m/s)	-0.01448	9.97E-04	0.03375	0.00379	-	-	-	-	13.6445	0.85213
4.11(B=5T,V=15m/s)	-0.01448	9.97E-04	0.03375	0.00379	-	-	-	-	13.85258	0.89937
4.11(B=10T,V=15m/s)	-0.01448	9.97E-04	0.03375	0.00379	-	-	-	-	14.13407	0.96089
4.11(B=15T,V=15m/s)	-0.01448	9.97E-04	0.03375	0.00379	-	-	-	-	14.48514	0.99102
4.11(B=15T,V=20m/s)	-0.01448	9.97E-04	0.03375	0.00379	-	-	-	-	18.85852	2.2851

Figure	11	12	13	14	15	16	17	18	19	
4.11(B=0T,V=15m/s)	-	-	-	-	20	13	25.15504	0.92629	0	
4.11(B=5T,V=15m/s)	-	-	-	-	20	13	25.15504	0.92629	0	
4.11(B=10T,V=15m/s)	-	-	-	-	20	13	25.15504	0.92629	0	
4.11(B=15T,V=15m/s)	-	-	-	-	20	13	25.15504	0.92629	0	
4.11(B=15T,V=20m/s)	-	-	-	-	20	13	25.15504	0.92629	0	

1 : A1 value, **2** : A1 standard deviation,

3 : B1 value, **4** : B1 standard deviation, **5** : B2 value, **6** : B2 standard deviation,

7 : B3 value, **8** : B3 standard deviation , **9** : C1 value, **10** : C1 standard deviation,
11 : C2 value, **12** : C2 standard deviation, **13** : C3 value, **14** : C3 standard deviation,

15 : Number of points, **16** : Degrees of freedom, **17** : Reduced χ^2, **18** : Adjusted $\mathbf{R}^2$, **19** : χ^2 probability.
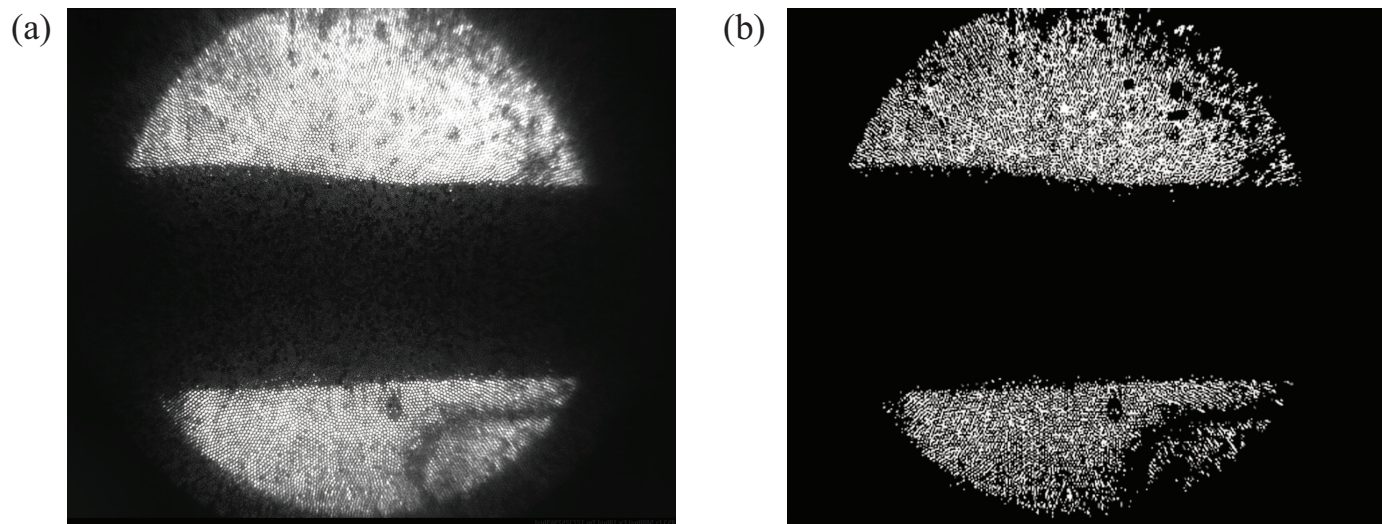
Figure 4.1: Image data conversion for image analysis. a.) Collected image data. b.) 2 bit scaled image data.
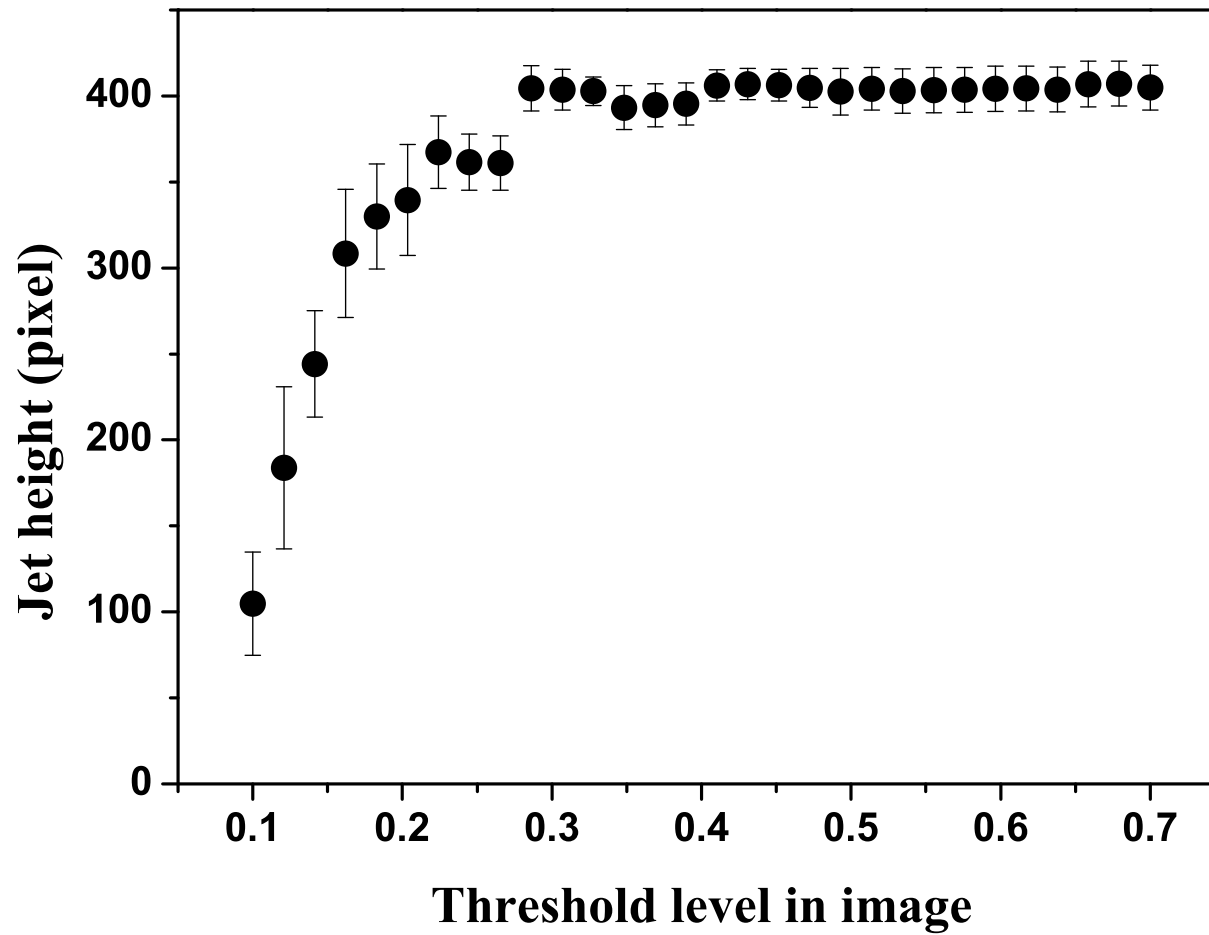
Figure 4.2: Sensitivity of threshold in a 2 bit scaled image conversion.
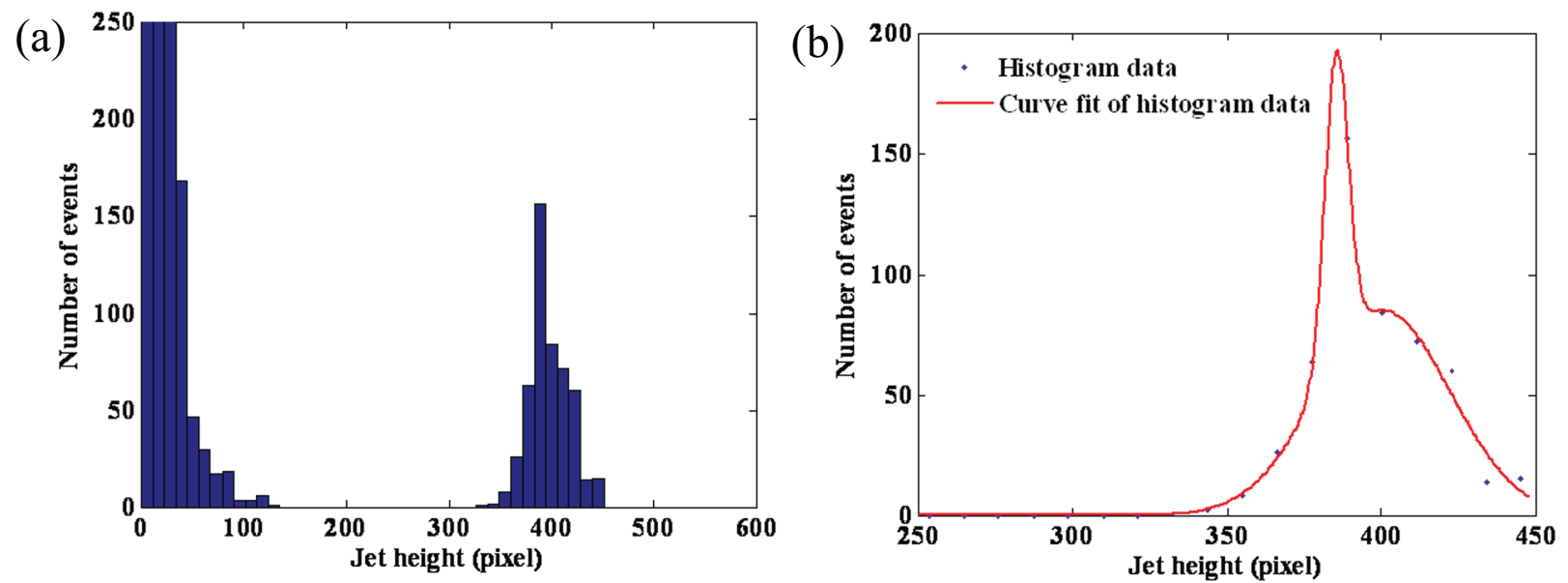
Figure 4.3: Jet height determination from image analysis. a.) Histogram of number of events in the jet height measurement. b.) Fitted histogram distribution.
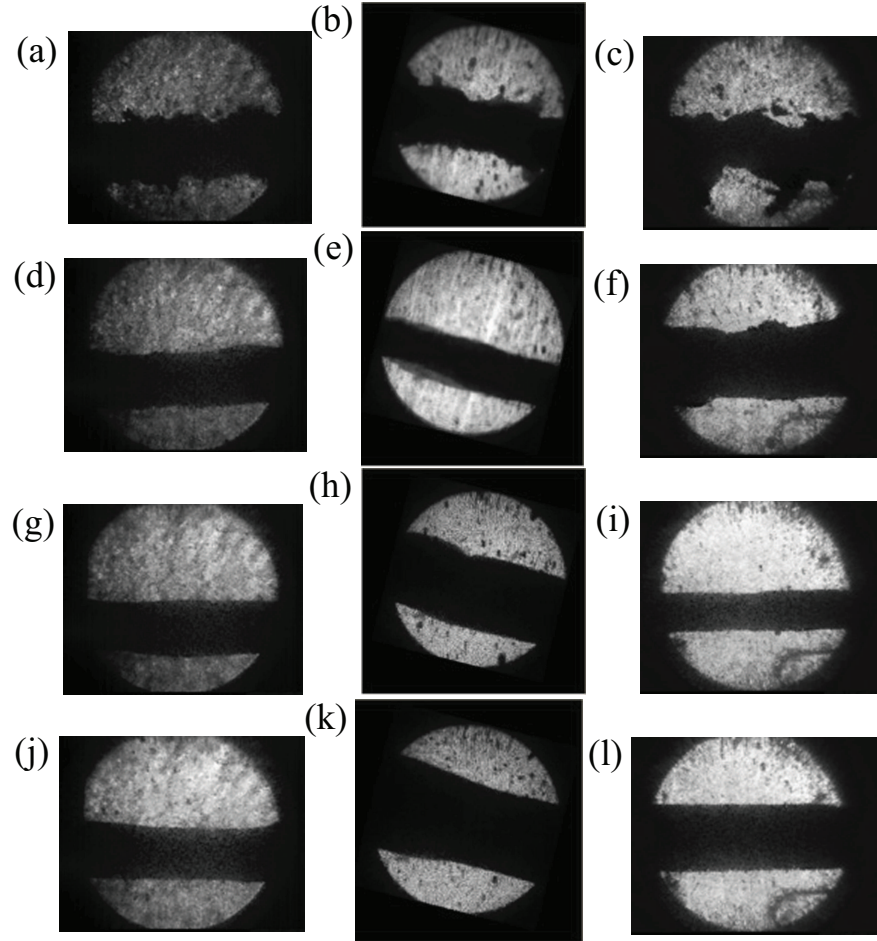
Figure 4.4: Mercury jet flows as observed from the 3 Viewports. The jet flows from left to right on each image. The first, second, and third columns represent Viewport 1, 2, and 3, respectively. The individual caption shows the applied magnetic induction field. The jet velocity is 15m/s. Images on Viewport 2 has a 14° clockwise rotation due to the SMD software. a.) B=0T. b.) B=0T. c.) B=0T. d.) B=5T. e.) B=5T. f.) B=5T. g.) B=10T. h.) B=10T. i.) B=10T. j.) B=15T. k.) B=15T. l.) B=15T.
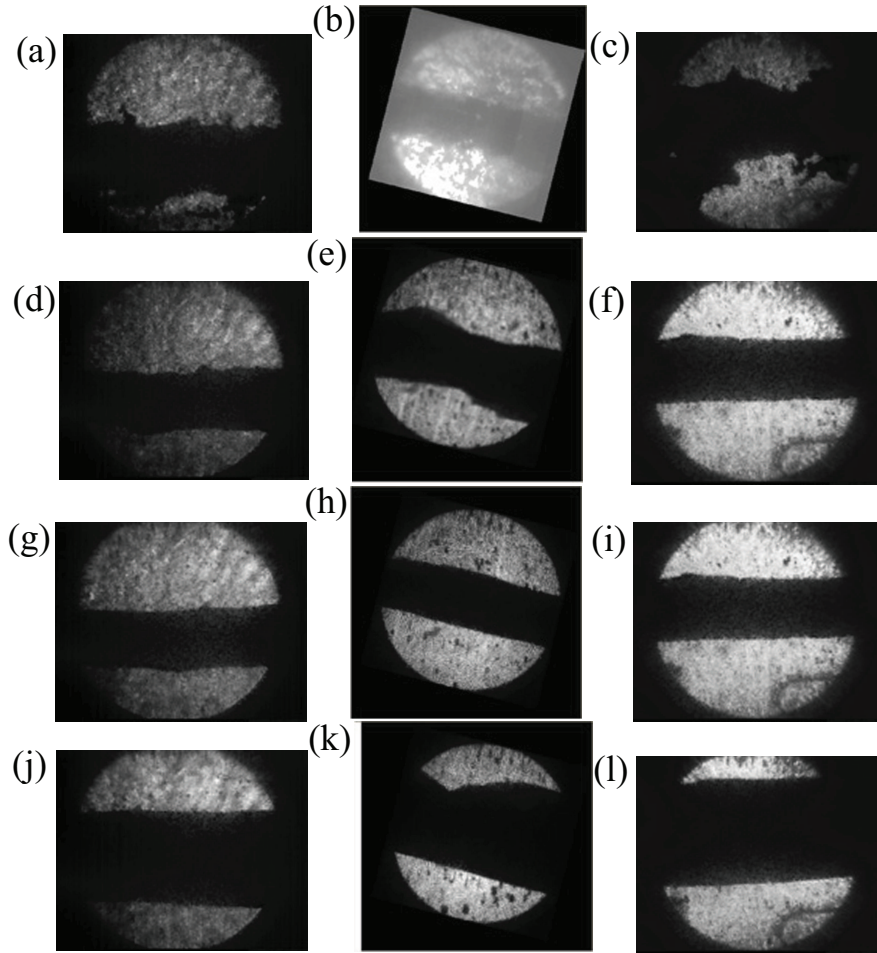
Figure 4.5: Same as Fig. 4.4 but with a jet velocity of 20 m/s. a.) B=0T. b.) B=0T. c.) B=0T. d.) B=5T. e.) B=5T. f.) B=5T. g.) B=10T. h.) B=10T. i.) B=10T. j.) B=15T. k.) B=15T. l.) B=15T.
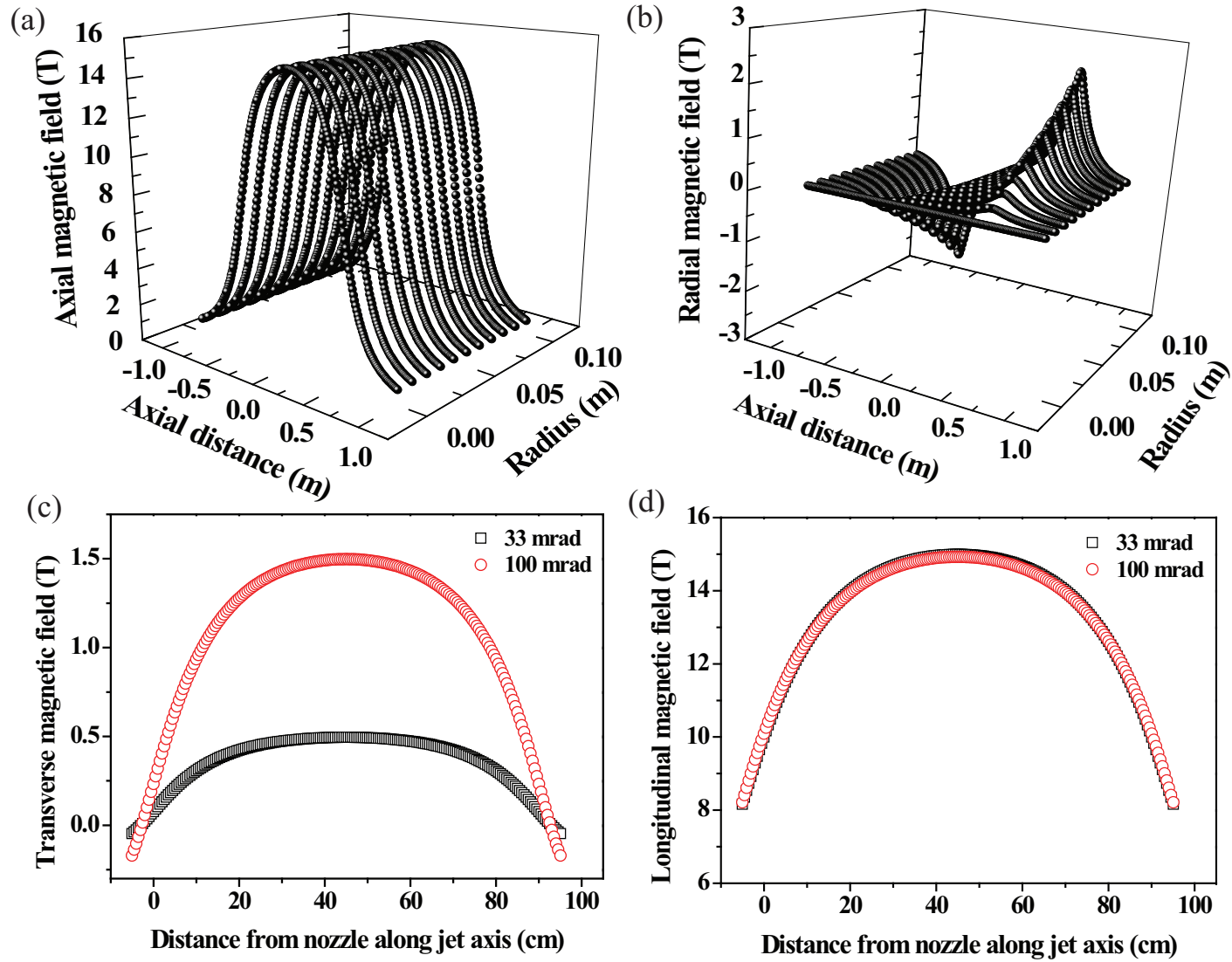
Figure 4.6: Calculated solenoid magnetic induction field map. a.) Radial field map. b.) Axial field map. c.) Transverse component of magnetic induction field along jet axis. d.) Longitudinal component of magnetic induction field along jet axis.
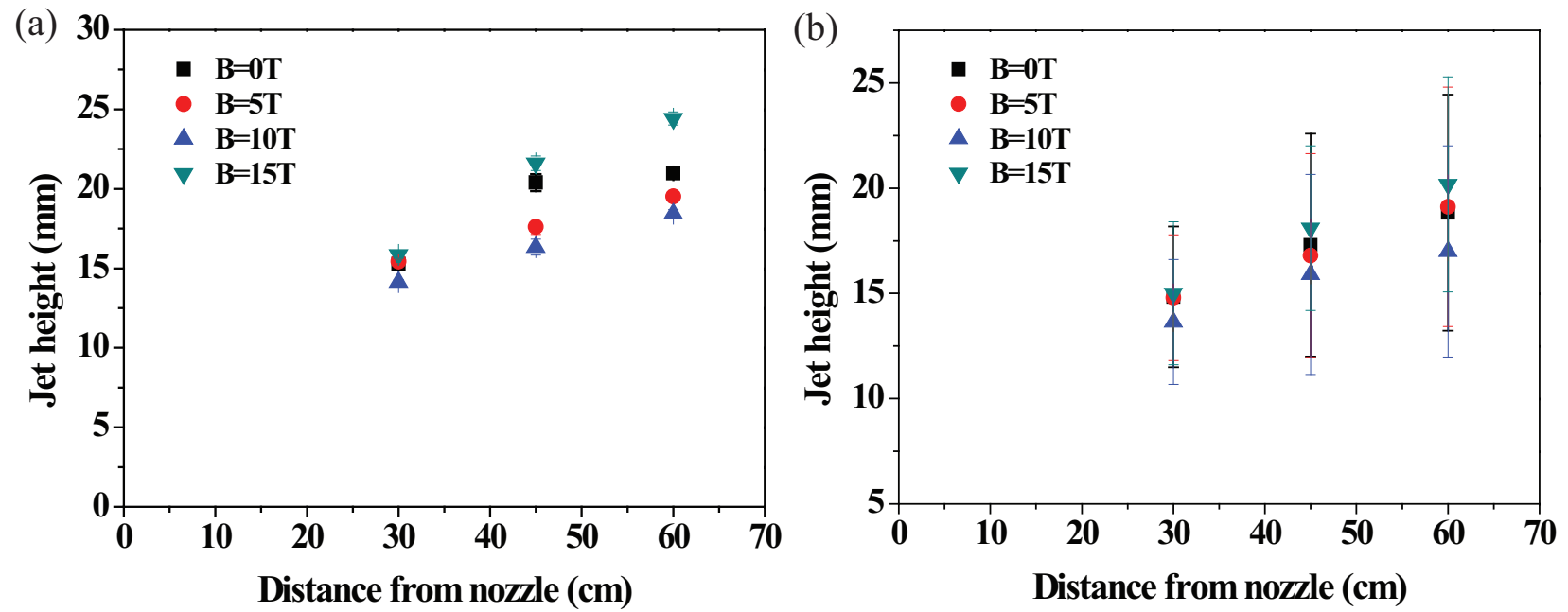
Figure 4.7: Hg jet height measurement in magnetic fields. a.) Histogram fitting of number of events. b.) Direct average of vertical height on each image.
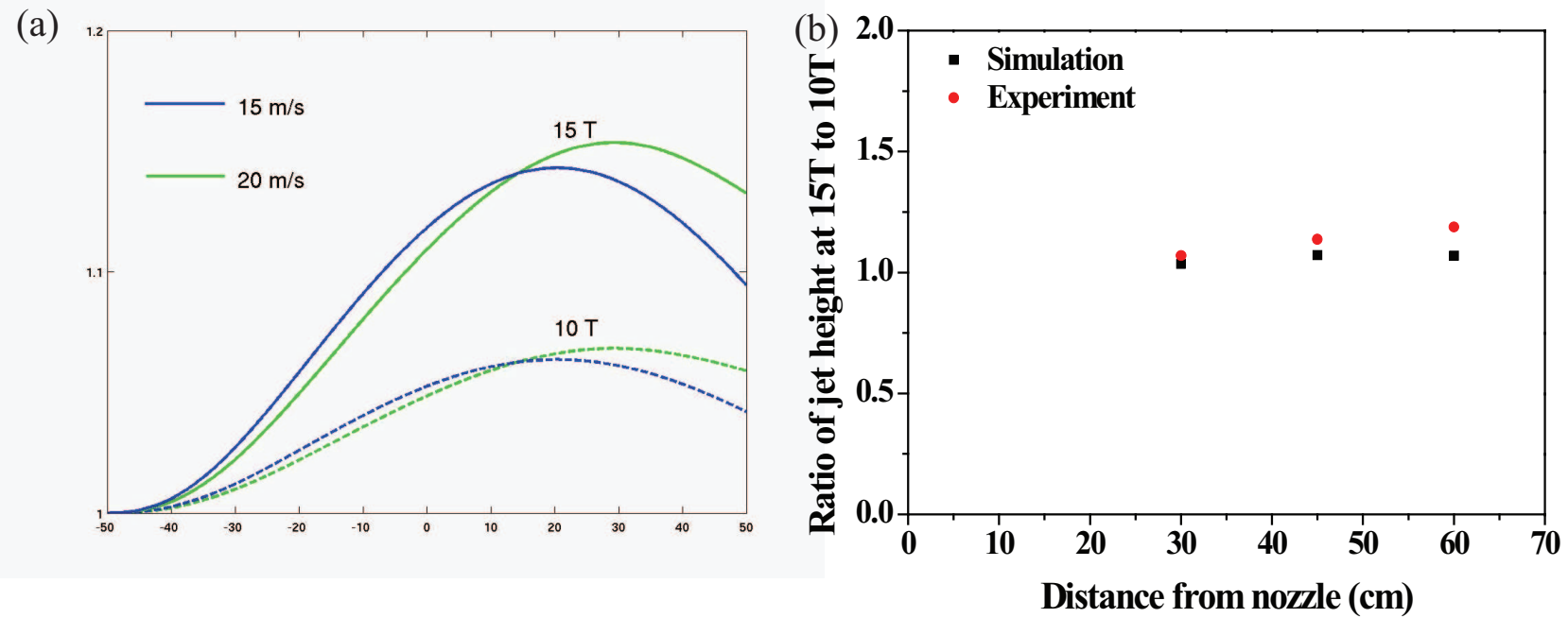
Figure 4.8: Comparison of Hg jet deflection ratio at 15 T to that at 10 T. a.) Numerical calculation of deflection ratio. b.) Comparison of ratio of jet deflection.
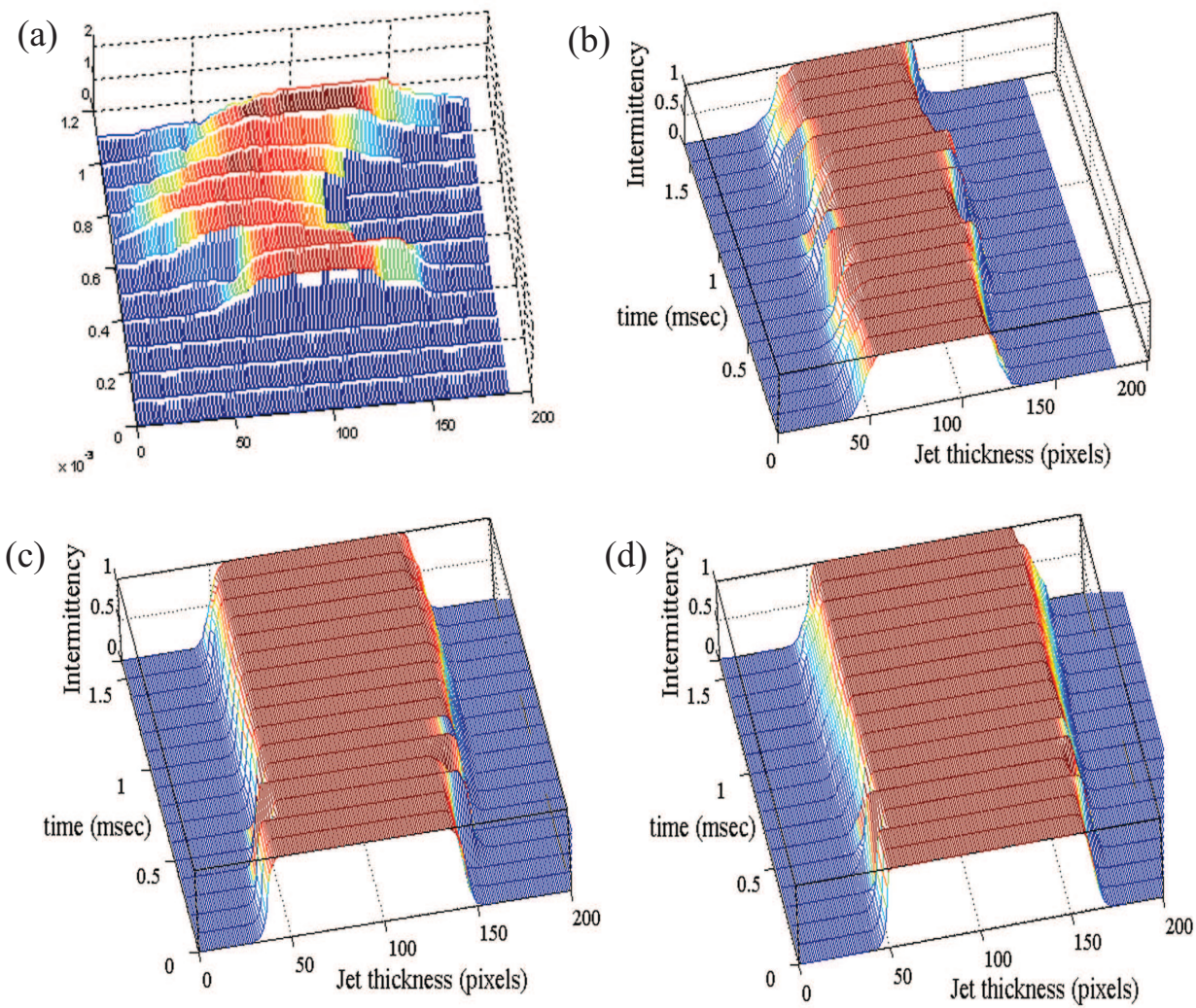
Figure 4.9: Intermittency of Hg jet at Viewport 2. The jet velocity is 15 m/s. a.) B=0T. b.) B=5T. c.) B=10T. d.) B=15T (continued).
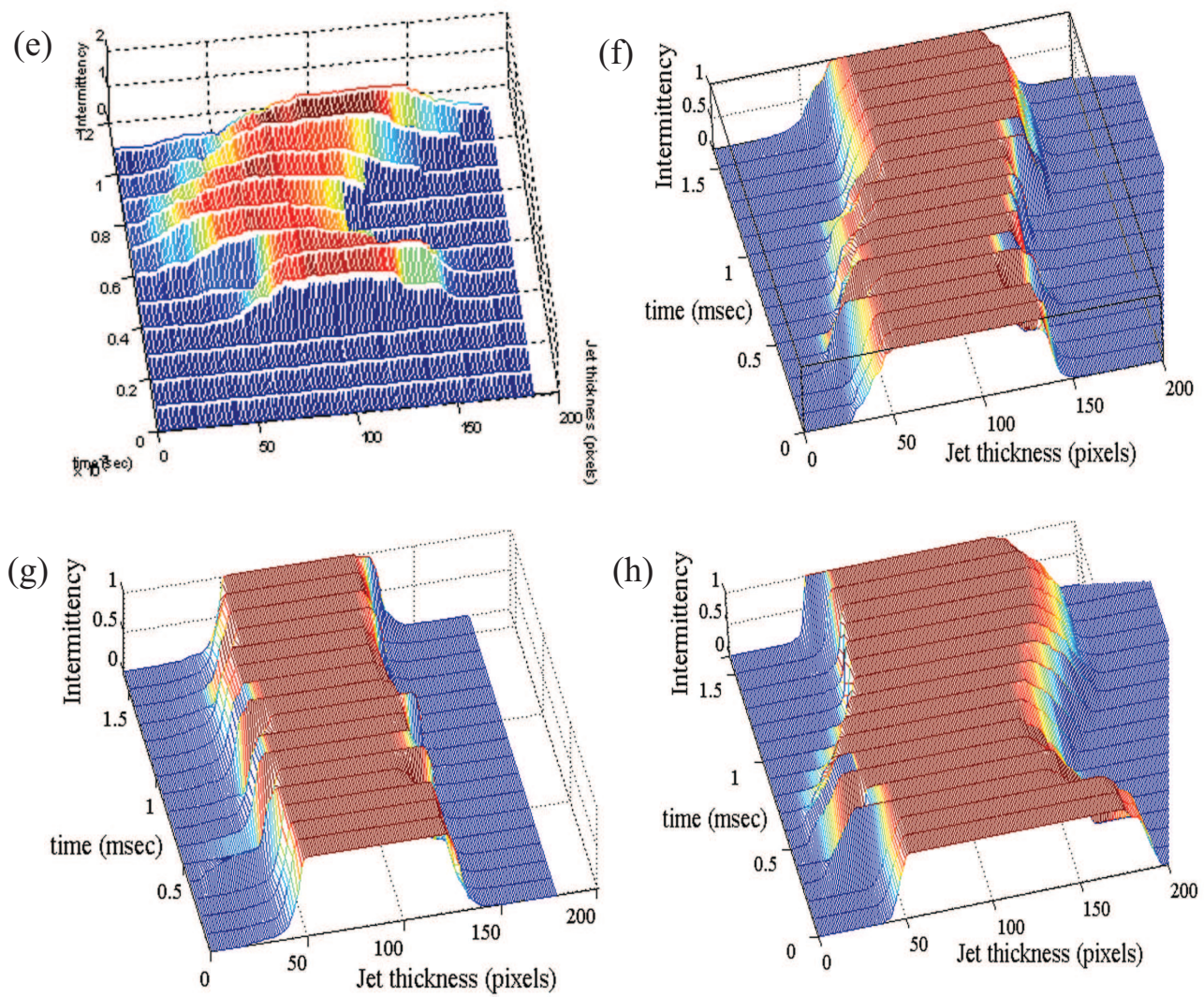
Figure 4.9: Intermittency of Hg jet at Viewport 2. The jet velocity is 20 m/s. e.) B=0T. f.) B=5T. g.) B=10T. h.) B=15T.
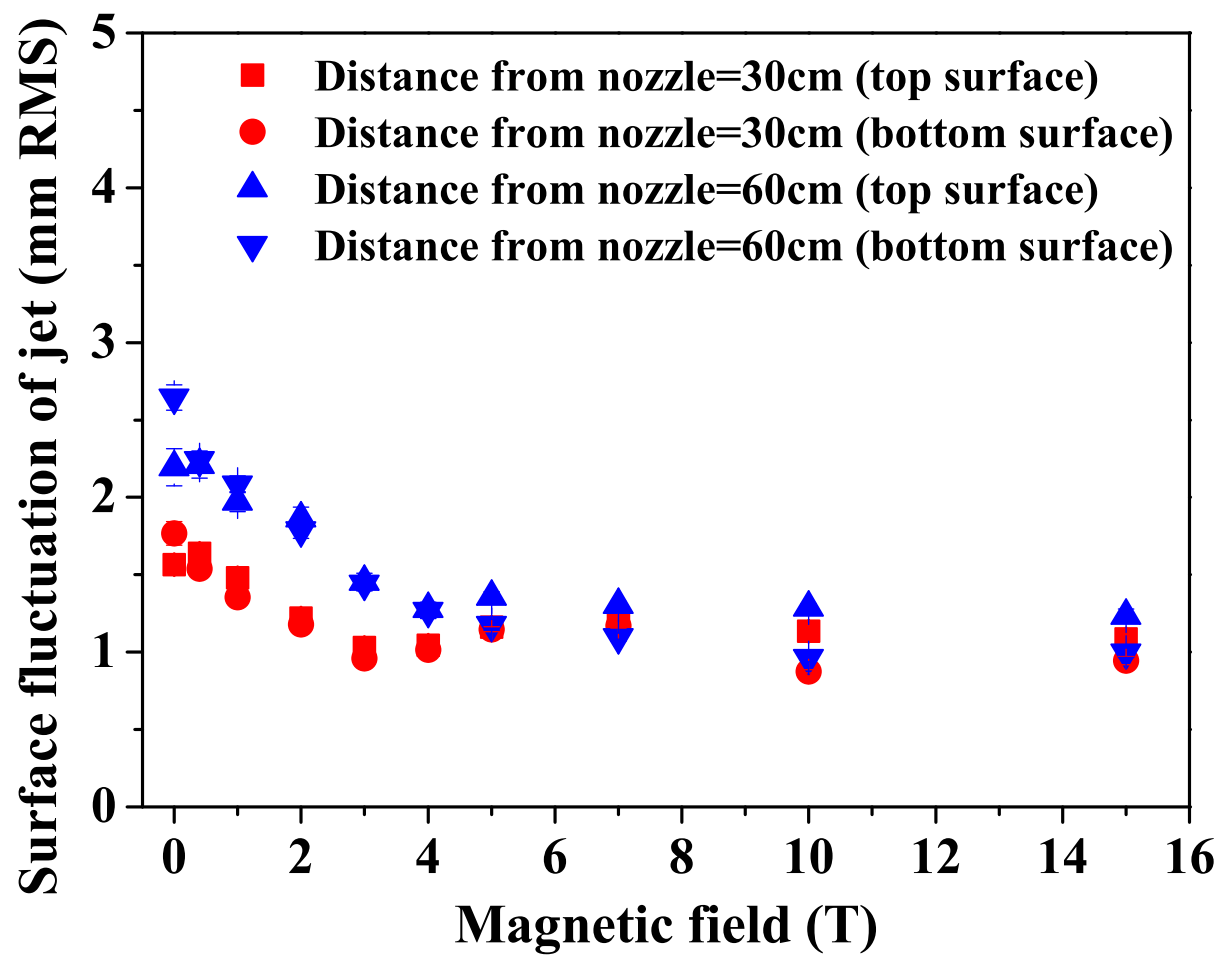
Figure 4.10: Surface fluctuations in a magnetic field.
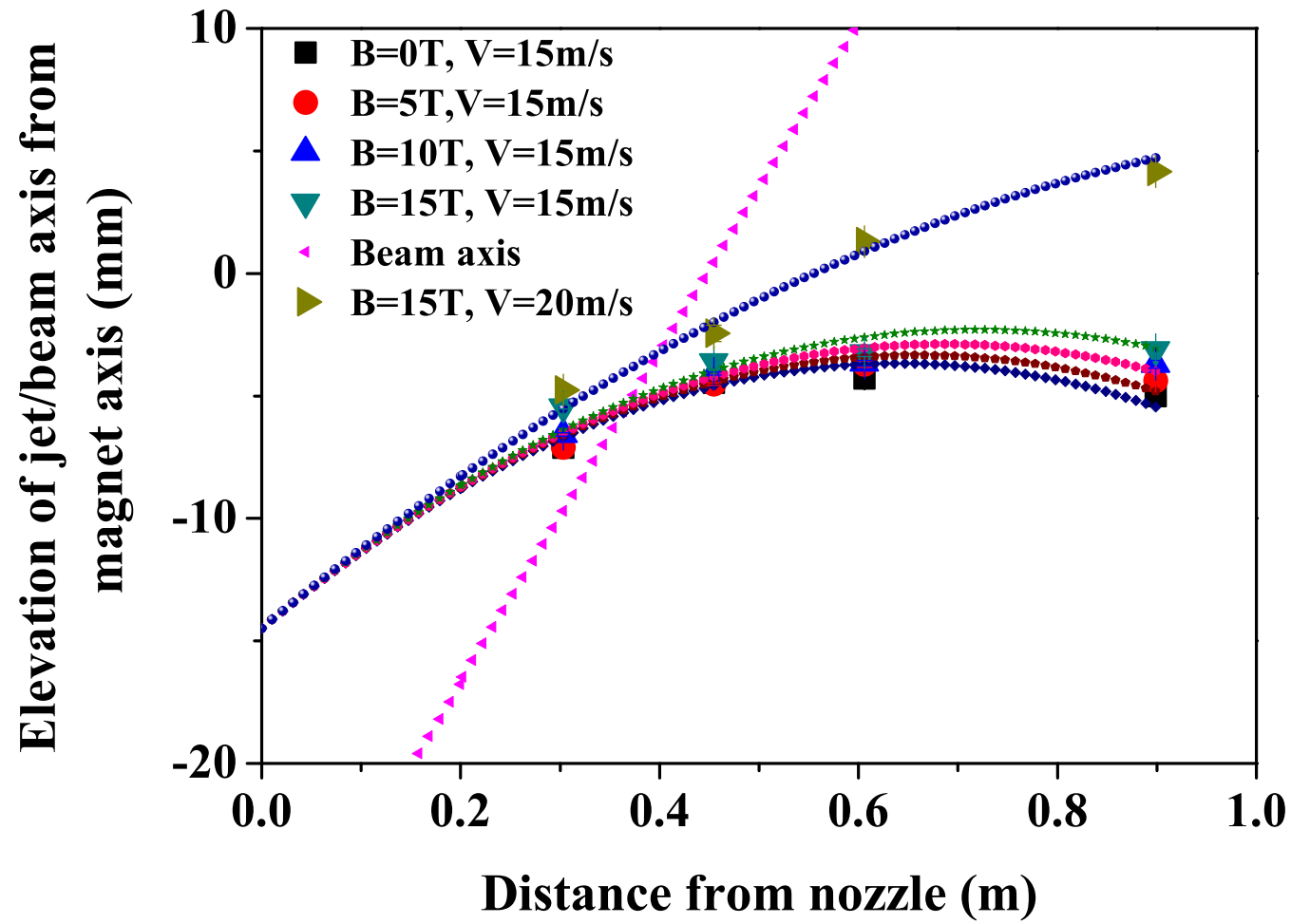
Figure 4.11: Trajectory of beam axis and Hg jet axis projectile with respect to magnetic axis in magnetic field. Solid line represents the simulated value using trajectory of projectile with different velocity.
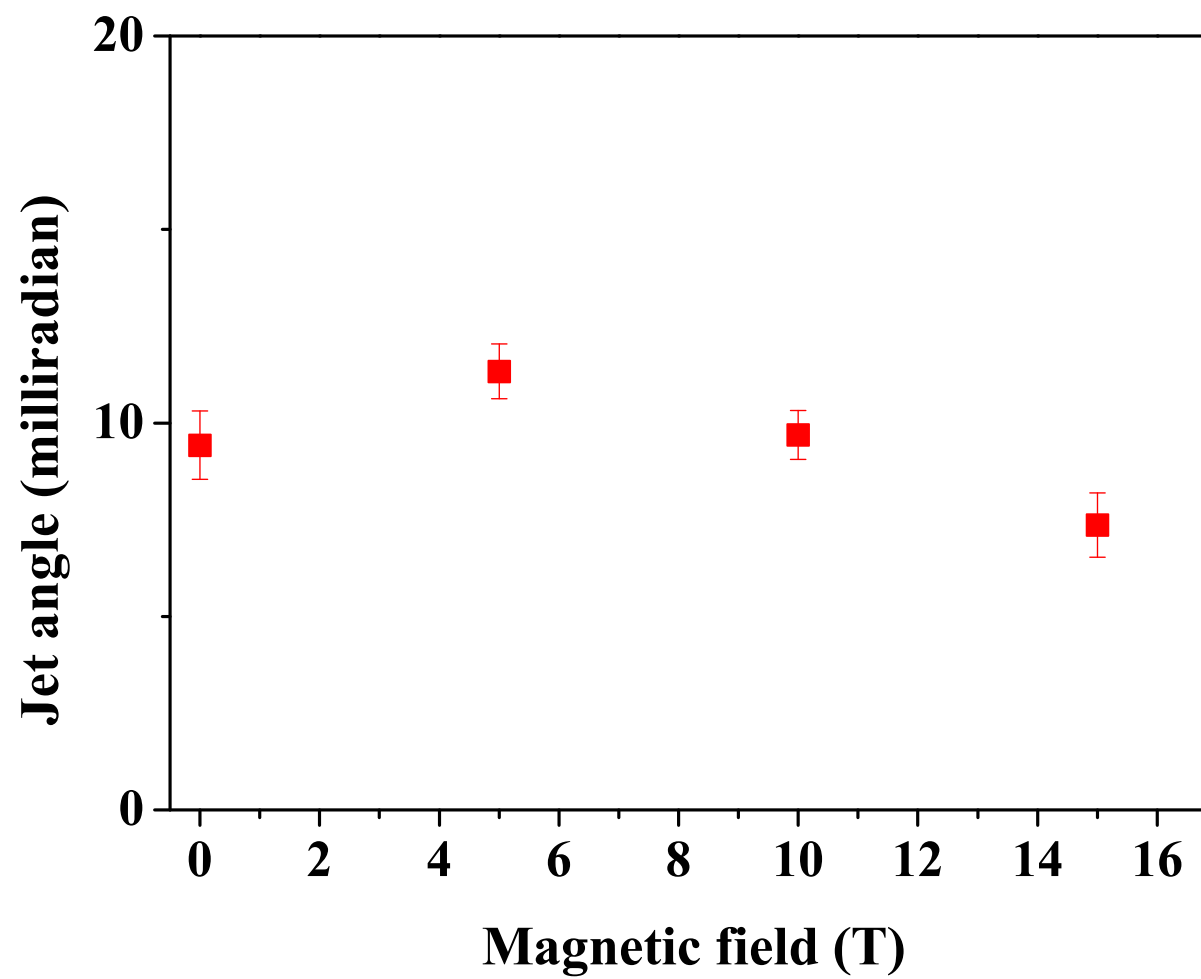
Figure 4.12: Hg jet angle at the center of magnetic axis (Viewport 2) as a function of magnetic field.

Nozzle

$\delta(x)$

y

$a(x)$

$v_l(x)$

v_{lo}

x

Jet Stream
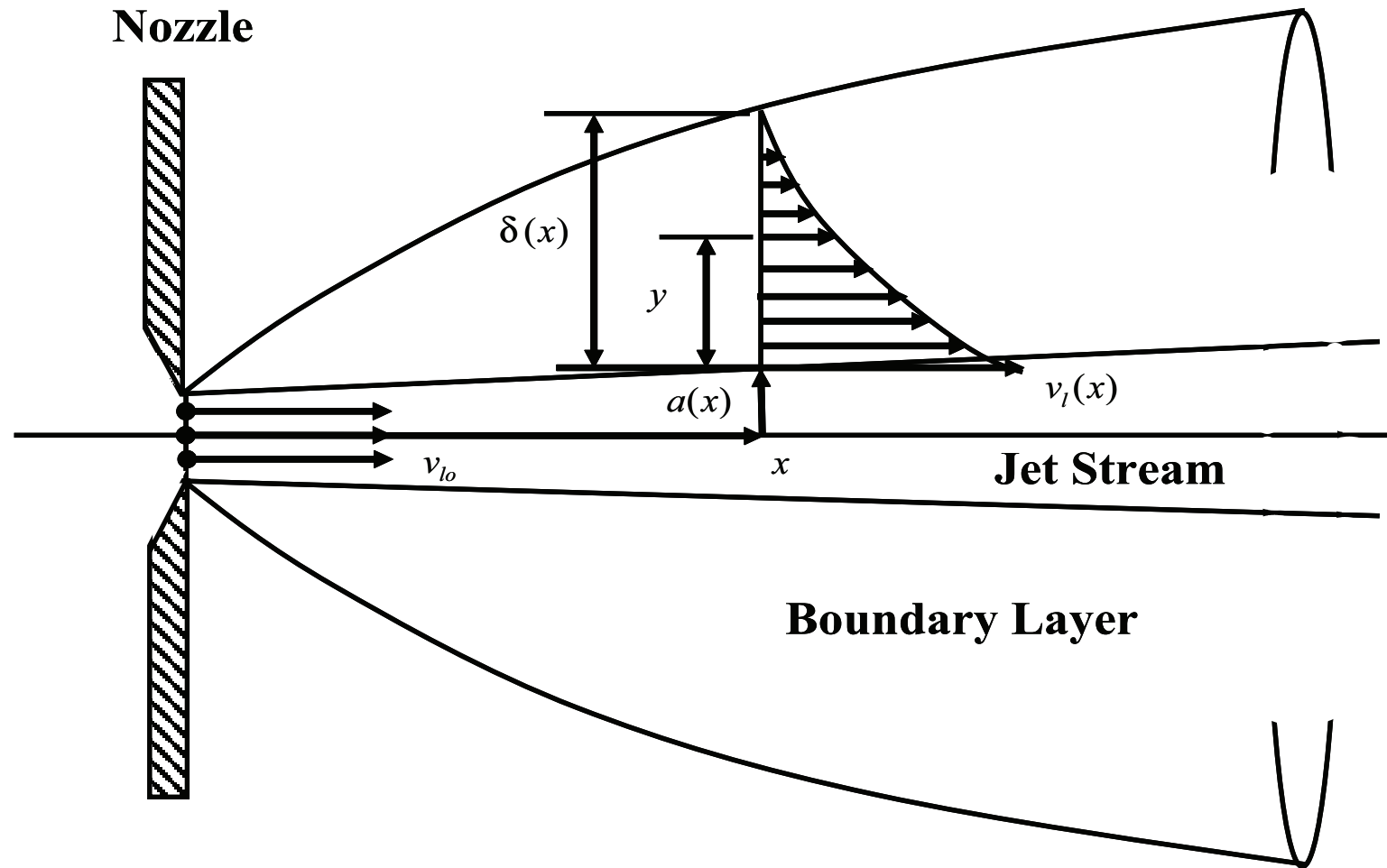
Boundary Layer

Figure 4.13: Boundary layer induced by a jet emerging from a nozzle.
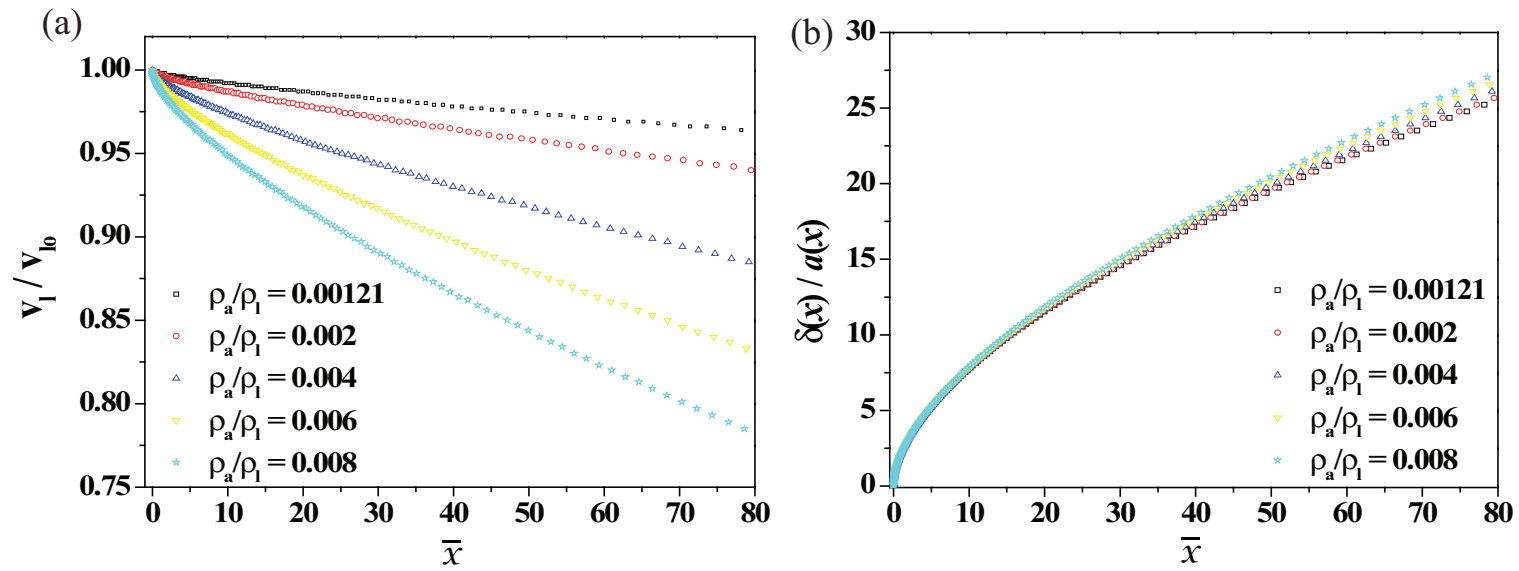
Figure 4.14: Stream velocity and boundary layer thickness for various values of density ratio.
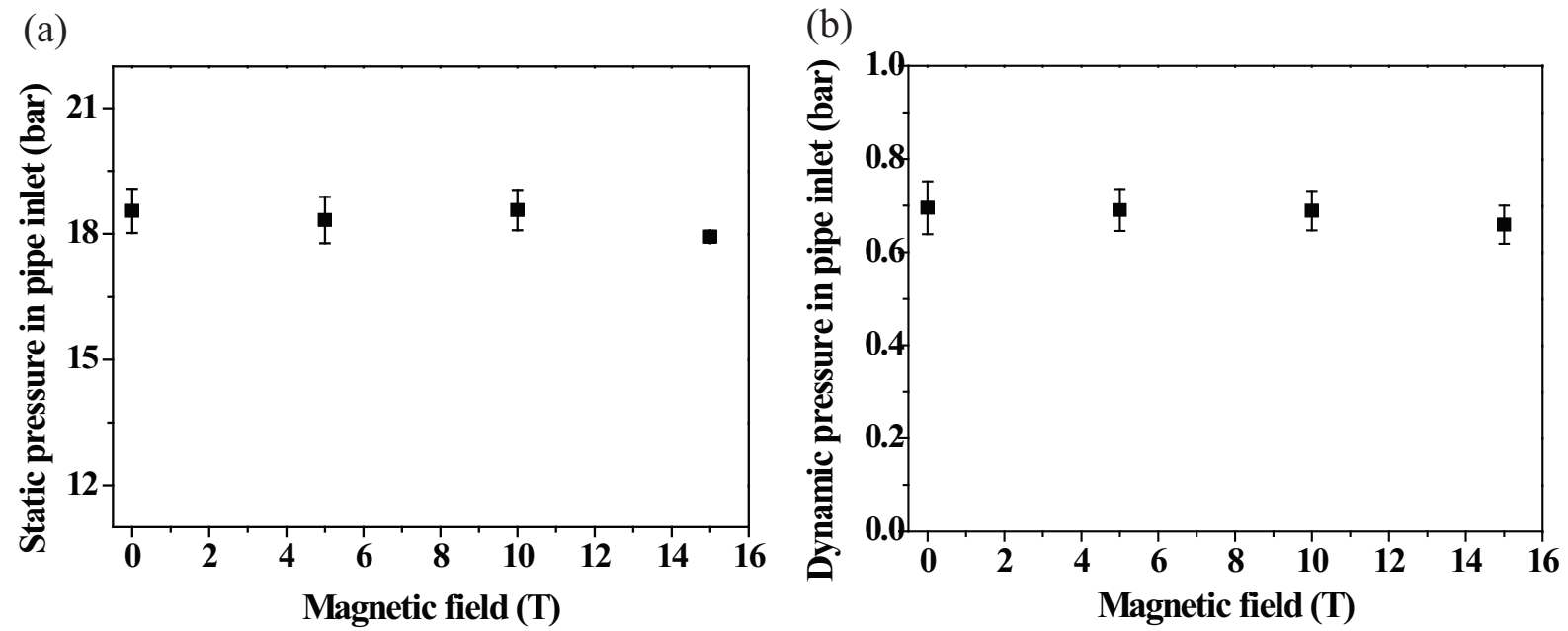
Figure 4.15: Pipe inlet pressure for driving Hg jet. a.) Static pressure. b.) Dynamic pressure.

(a)

(b)
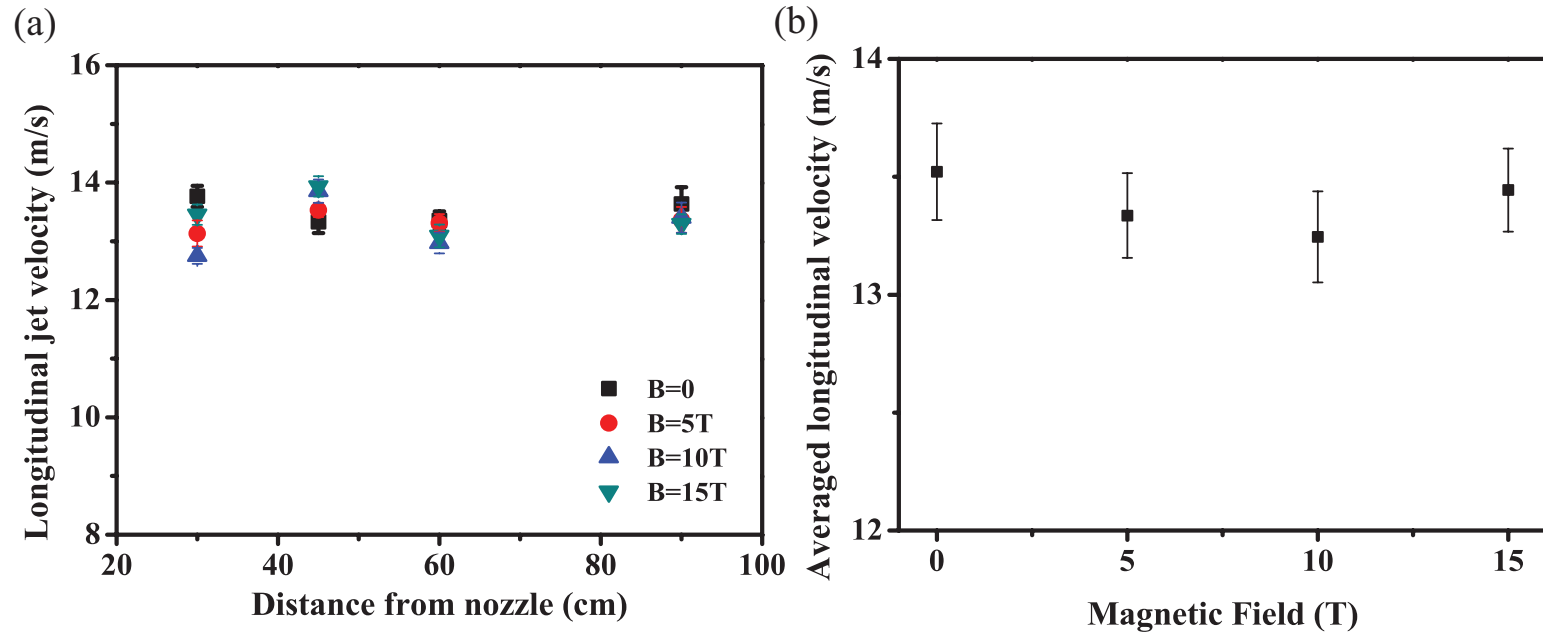
Figure 4.16: Longitudinal Hg jet flow velocity in magnetic field. a.) Velocity at each Viewport dependent of magnetic field. b.) Averaged velocity at each Viewport independent of magnetic field.

Chapter 5

Interaction of an Intense Proton Beam with Hg Jet in Magnetic Field

In this chapter, the jet's interacting characteristics in magnetic field are investigated. The disruption of the jet interacting with various beam intensities and beam energy is observed and the magnetic suppression to it is discussed. The captured images show the mechanism of the beam-jet interaction and the qualitative consistency with the distribution of calculated energy deposition is discussed. The energy deposition induced by the proton beam generates filaments on the Hg jet surface due to thermal stresses. The filaments velocity and its reduction by magnetic field are discussed. It explains that the joule damping dissipates the kinetic energy on a time scale of joule damping term.

5.1   High Energy Proton Beam Structure

5.1.1   Proton synchrotron machine

Neutrino factories requires a large number of muons, which are obtained from the decay of pions. Efficient production of pions can be achieved by

colliding an intense proton beam with a high-Z target. An important consideration is the problem of removing the power deposited by the proton beam without interfering with the process of extracting the end-product, which is the muon beam. The response of a liquid target in a high-magnetic induction field will have beam energy effects, which is investigated experimentally. Experiments on the interaction of a 14 GeV/c and 24 GeV/c proton beam with pulse structures of 4 to 16 bunches per pulse and the spot sizes in the order of 2 to 10 mm^2 RMS up to 30 tera-protons(TP) per pulse in magnetic field up to 15 T has been carried out at CERN. Fig. 5.1 (a) shows the infrastructures for experiment at CERN. All equipments for experiment are installed at tunnel TT2/TT2A and these are controlled remotely at control room. The proton beam is delivered from proton synchrotron ring and the beam setup is schematically shown in Fig. 5.1 (b). The PS machine is set up in harmonic 16 bunches and the extracted protons fill the machine in bunch pairs. A bunch in harmonic 8 mode is consisted of a bunch pair. Therefore, a bunch period in harmonic 8 mode is two times of a bunch period in harmonic 16 mode. Each bunch can fill protons up to 2 ~ 2.5 $\times 10^{12}$. Therefore, the maximum beam intensity can be achieved up to ~ 32 $\times 10^{12}$ protons. Fig. 5.2 shows the layout of tunnel at CERN, where equipments for experiment are installed. Electronic equipments for optical diagnostics, hydraulic power unit, and cryogenic system are positioned at tunnel TT2. Hg loop system, solenoid magnet, and beam diagnostic system are positioned at tunnel TT2A. The fibers for optical diagnostics of Hg target in solenoid magnet and cables for controlling the Hg loop

131

2502 system and solenoid magnet are connected between TT2 and TT2A passing

2503 through an artificially drilled hole.

5.1.2 Proton beam pulse length

2505 In order to produce the design number of $10^{21} muons/year$ in the muon

2506 storage ring, 4MW of proton beam power is desired. For our experiment, the

2507 CERN PS ran typically in a harmonic 16 mode. Hence, it is possible to fill with

2508 2×10^{12} protons/bunch and therefore up to 32×10^{12} protons/spill. One beam

2509 pulse consists of several beam bunches. The bunch lengths for harmonic 16

2510 mode are 50 ns and 30 ns at full width at half maximum (FMWH) respectively.

2511 The bunch lengths for harmonic 8 mode are 70 ns and 40 ns at full width

2512 at half maximum (FMWH) respectively. The bunch-to-bunch differences for

2513 harmonic 16 mode and harmonic 8 mode are multiples of 131 ns and 262 ns

2514 respectively. The proton beam pulse structure of harmonic 8 and harmonic 16

2515 in 14 GeV, 6 TP is shown in Fig. 5.18. The spot size at the experiment is in

2516 the order of 2 to 10 mm^2 RMS. This allows to place up to 32×10^{12} protons

2517 on the mercury target, generating a peak energy deposition of ~ 150 J/g.

2518 Power consumption is dominated by the repetition rate. Thus, the capability

2519 to replace the disrupted jet determines the ultimate beam power. The optimal

2520 interaction length for the 24 GeV beam energy is in the region of 30 cm which

2521 corresponds to approximately 2 interaction length for mercury (Kirk *et al*,

2522 2008). For a 20 m/s jet velocity, replacing two interaction lengths will be

2523 taken in 14 ms thus allowing for operations with a repetition rate of up to 70

2524 Hz. The beam energy per pulse is 115 kJ for a beam of 30×10^{12} protons with

2525 24 GeV beam energy. The disruption length at 30×10^{12} protons with 24 GeV

2526 beam energy in a magnetic field of 15 T is less than 20 cm at 24 GeV beam

2527 energy in Fig. 5.21, thus preserving the 70 Hz beam repetition rate option. It

2528 yields the key result that a target system capable of supporting proton beams

2529 with powers of up to 8 MW (Kirk *et al*, 2008).

2530 5.1.3 Proton beam envelope by optics and camera screen

2531 The proton beam with 14 GeV and 24 GeV beam energy is employed in the

2532 experiment. As the number of protons in a beam pulse increases, it is reported

2533 (Efthymiopoulos, 2008) that the beam spot size increases. The beam spot size

2534 is calculated by CERN using the measured beam emittance, dispersion, and

2535 the momentum spread of the beam particle. The emittance is measured by

2536 measuring the beam profile in a position of known beam parameters based

2537 on optics. Fig. 5.4 shows the estimated 1 σ beam spot size at the center of

2538 target based on optics (Efthymiopoulos, 2008). Fig. 5.5 shows the measured

2539 1 σ beam spot size at the phosphor camera screen installed $\sim$ 4.2 m away

2540 from the center of magnet before entering the magnet (Skoro, 2008). It is also

2541 reported (Skoro, 2008) that the beam spot size increases as the number of

2542 protons increases. Due to the saturation of image, the measured size is shown

2543 as $\sim$ 2 times larger than the estimated beam spot size from optics. Fig. 5.6 (c)

2544 shows the beam sizes distribution measured by phosphor screen monitor as a

2545 function of time interval between beam shots, where the histogram for events

133

2546 of beam size in horizontal plane is shown in Fig. 5.6 (a) and the histogram for

2547 events of beam size in vertical plane is shown in Fig. 5.6 (b). This plots show

2548 that the possible residual saturation of image by phosphor screen monitor is

2549 not related with time interval between each beam shot. The distribution of

2550 beam spot size is uniform regardless of the possible residual saturation by

2551 screen monitor.

5.2 MARS Simulation for Energy Deposition to Mercury Jet by Proton Beam

5.2.1 Physics model

2555 MARS is a Monte Carlo code for inclusive and exclusive simulation of

2556 3D hadronic and electromagnetic cascades, muon and heavy ion transport in

2557 accelerator, detector, and shielding components in the energy range from a

2558 fraction of an electronvolt up to 100 TeV. In MARS code, hadron production,

2559 neutrino interactions, electromagnetic interactions of heavy particles, and elec-

2560 tromagnetic showers are considered. For hadron production, information on

2561 the nuclides generated in nuclear collisions is scored, or reported in the results

2562 of the simulation, which covers a hadron kinetic energy range up to 100 TeV.

2563 For neutrino interactions, the model permits the selection of the energy and

2564 angle of each particle (ν, e, μ) emanating from a simulated interaction. These

2565 particles, and the showers initiated by them, are then further processed in the

2566 code. Four types of neutrino interactions are distinguished ($\nu_\mu, \bar{\nu}_\mu, \nu_e, \bar{\nu}_e$) and

2567 the model identifies all possible types of neutrino interactions with nuclei. The

134

2568 corresponding formulas for these processes as well as results of Monte Carlo

2569 simulations are considered. For electromagnetic interactions of heavy parti-

2570 cles, electromagnetic interactions of muons and charged hadrons in arbitrary

2571 materials are simulated. Radiative processes and atomic excitation and ion-

2572 ization with energy transfer are considered. The electromagnetic showers are

2573 based on the physics of electromagnetic interactions and it gives electron and

2574 photon interactions in composite solid, liquid and gaseous materials (Mokhov,

2575 2000).

5.2.2 Mercury jet modeling in MARS code

2577 Using MARS code, Calculation of energy deposition is performed at Fermi

2578 National Accelerator Laboratory (Striganov, 2009). For the modeling of jet in

2579 MARS, the experimentally measured Hg jet size and trajectory in magnetic

2580 field with assumption of sectionally elliptic jet shape and circular jet shape

2581 with equivalent reduced mass density to the initial flow rate from nozzle. The

2582 proton beam is passing through the center of magnetic axis. For simplicity, the

2583 z coordinate of modeling in MARS defines as 0 at the center of magnetic axis

2584 along the direction of magnetic field. Accordingly, the x coordinate of modeling

2585 in MARS defines as the vertical direction perpendicular to the direction of

2586 magnetic field. The experimentally measured jet size and vertical position to

2587 the center of magnetic axis is shown at Fig. 4.7 and Fig. 4.11. The vertical

2588 distance in cm in MARS code between center of jet and magnetic axis is

2589 employed by using Eqn. (5.1). The experimental measurement of vertical

135

2590 distance between magnetic axis and the center of jet is given in Table 5.1, where

2591 the experimentally measured jet size as well as approximated mass density for

2592 the simulation of circular jet case are also given.

2593

$$x_{vert} = -1.4522 - 3.65 \times 10^{-2} \times zz - 3.1672 \times 10^{-4} \times zz^2 + 5.4206 \times 10^{-9} \times zz^4,$$

2594 (5.1)

2595 where $zz = z - 46$ in cm.

2596 Fig. 5.7 (a), (b) show the sectional view of elliptic/circular jet and Fig. 5.7

2597 (c) shows the side view of jet interacting with proton beam in magnetic field,

2598 which is indicated as arrows. Using MARS code, Calculation of energy depo-

2599 sition with various magnetic field strength and beam intensity is performed at

2600 Fermi National Accelerator Laboratory (Striganov, 2009).

2601 ### 5.2.3 Energy deposition to mercury jet

2602 **5.2.3.1** *energy deposition in magnetic field*

2603 Fig. 5.8 shows the averaged energy deposition along the jet axis for the case

2604 of 2 Tp according to the variation of magnetic field. Calculated energy depo-

2605 sition in each meshed volume is averaged along the jet axis using Eqn. (5.2).

2606

$$E(z) = \frac{1}{N_\theta^r} \sum_r \sum_{\theta=0}^{2\pi} E_\theta^r(r, z, \theta),$$

2607 (5.2)

2608 where N_θ^r, E_θ^r represent the number of meshes along radial angle at each

2609 radial distance and its energy deposition respectively. As the magnetic field

increases, the distribution of energy deposition over the jet increases. This indicates interaction of charged particles with magnetic field, so that more atomic excitation and ionization with energy transfer occurs in higher magnetic field. Also, the electromagnetic shower produced by a particle that interacts via the electromagnetic force gives electron and photon interactions in mercury. From the equation of particle motion and Lorentz force in Eqn. (5.3), the momentum of charged particle has an influence of the intensity of magnetic field followed by Maxwell's equations.

$$\frac{d\mathbf{p}}{dt} = e[\mathbf{E} + \mathbf{v} \times \mathbf{B}], \tag{5.3}$$

where e is the charge on the particle and $\mathbf{v}$ is the particle velocity.

5.2.3.2 *geometric distribution of energy deposition in elliptic Hg jet cross section*

Fig. 5.9 (a) shows the radially averaged energy deposition over the orientation in sectional jet area along the jet axis for the case of 2 Tp in 5 T. Calculated energy deposition in each meshed volume is averaged along the jet axis using Eqn. (5.4).

$$E(z, \theta) = \frac{1}{N_\theta^r} \sum_r E_\theta^r(r, z, \theta). \tag{5.4}$$

The larger distribution of energy deposition occurs at bottom ($\sim 270°$)of jet where the beam enters. Gradually the larger distribution moves to the top ($\sim 90°$) of jet where the beam leaves. It again gives the consistent result with

2632   Fig. 5.15 (a) and Fig. 5.16 (a), where the profile of energy deposition shows

2633   its changes along with the beam path through Hg jet.

2634   Fig. 5.9 (b) shows the axially averaged energy deposition over the variation

2635   of magnetic field along the orientation in sectional jet area for the case of 2

2636   Tp in 5 T. Calculated energy deposition in each meshed volume is averaged

2637   along the orientation in sectional jet area using Eqn. (5.5).

2638

$$E(\theta) = \frac{1}{N_z^r} \sum_z \sum_r E_z^r(r, z, \theta), \tag{5.5}$$

2639

2640   where N_z^r, E_z^r represent the number of meshes along axial jet axis at each

2641   radial distance and its energy deposition respectively. The larger axially av-

2642   eraged energy deposition is at bottom ($\sim 270°$) of jet and the distribution of

2643   energy deposition increases as the magnetic field increases. The geometrical

2644   distribution of energy deposition depending on the applied magnetic field does

2645   not changes but keeps uniform profile of distribution, which indicates that the

2646   profile of distribution is most likely dependent to the shape of Hg jet.

2647   **5.2.3.3   *proton beam spot size to the energy deposition***

2648   Fig. 5.11 shows the averaged energy deposition per proton along the jet

2649   axis using Eqn. (5.2) according to the variation of number of protons in 10 T.

2650   As shown in Fig. 5.4, the beam spot size increases as the number of protons

2651   increase. As a result, the energy deposition per proton decreases due to the

2652   decrease of beam intensity caused by increasing beam spot size. Fig. 5.12 shows

2653   the variation of peak energy deposition per proton and total energy deposition

138

2654 to mercury jet with respect to the number of protons at both 14 GeV and 24

2655 GeV beam energy in magnetic fields. The total energy deposition amounts

2656 to $\sim 6 \sim 8$ % of the incident beam energy and the total energy deposition is

2657 slightly decreasing depending on the variation of beam spot size. However, the

2658 total energy deposition increases as the magnetic field increases. As discussed

2659 in Fig. 5.8, it again indicates interaction of charged particles with magnetic

2660 field, so that more atomic excitation and ionization with energy transfer occurs

2661 in higher magnetic field. However, the peak energy deposition is determined

2662 by the incident number of protons regardless of magnetic field strength. The

2663 solid line in Fig. 5.12 (a) and (b) represent the fit of calculated peak energy

2664 deposition per proton using Eqn. (5.6) and Eqn. (5.7) respectively shown as

2665

2666
$$z = (A_1 + B_1 x^{B_2}) w^{C_1} \qquad (5.6)$$

2667 and

2668

2669
$$z = A_1 (y - B_1)^{B_2 w^{C_1} + B_3} x w^{C_2}, \qquad (5.7)$$

2670 where x, y, z, and w denote number of protons, magnetic field, energy

2671 deposition, and beam energy respectively. Note that the parameterized values

2672 of coefficients and errors of the fit functions for energy deposition with respect

2673 to number of protons, magnetic field, and beam energy are given in Table 5.2.

2674 The energy deposition is estimated by using fit function and error. The peak

2675 energy deposition decreases with square rooted power of number of protons,

2676 and it increases with ~ 1.5 power of beam energy between 14 GeV and 24

2677 GeV. The ratio of beam energy between 14 GeV and 24 GeV is ~ 1.7. The

2678 total energy deposition decreases slightly linearly with number of protons and

2679 increases with 0.06 power of magnetic field strength. Thus, the total energy

2680 deposition has an increase with ~ 1.4 power of beam energy as an offset

2681 between 14 GeV and 24 GeV, and ~ 0.9 power of beam energy as an slope in

2682 fit function , which indicates possibly that the absolute ratio of power ~ 1.5

2683 due to the beam energy difference is separated into two coefficient terms ratio

2684 of C_1 to C_2 in fit function.

2685 Based on the result in Fig. 5.12, the number of protons are multiplied to

2686 the peak energy deposition per proton, which yields the result in Fig. 5.13 on

2687 logarithmic scale. The peak energy deposition with respect to the number of

2688 protons increases parabolically due to the increase of parabolically approxi-

2689 mated beam cross sectional area, which directly influences to the peak energy

2690 deposition to Hg jet. Also, the higher magnetic field again results in larger

2691 total energy deposition to Hg jet.

2692 The solid line in Fig. 5.13 (a) and (b) represent the fit of calculated peak

2693 energy deposition using Eqn. (5.8) and Eqn. (5.9) respectively shown as

2694

2695
$$z = A_1 x^{B_1} w^{C_1} \tag{5.8}$$

2696 and

2697

2698
$$z = A_1 x^{B_1 + B_2 y^{B_3}} w^{C_1}. \tag{5.9}$$

2699 The fit result from Eqn. (5.8) shows that the peak energy increases with $\sim$

0.8 power of number of protons on linear scale. As one expects, on logarithmic scale, it can be rephrased as a linear relation with ~ 0.8 between number of protons and peak energy deposition, and ~ 1.6 between beam energy and number of protons. The fit result from Eqn. (5.9) shows that the total energy deposition increases with ~ 0.9 power of number of protons, but it slightly increases with ~ 0.4 power of magnetic field. Again, on logarithmic scale, total energy deposition increases linearly with ~ 1.4 times of beam energy. This study is useful since it allows one to extrapolate the trend for estimation of profile of energy deposition, so that one can approximate the profile of energy deposition over all of the region of Hg jet based on the characteristics of relations in energy deposition to magnetic field, beam intensity, and Hg jet shape.

5.3 Observation of Interaction and Hg Jet Response to The Energy Deposition by Proton Beam

5.3.1 Hg jet pressurization by energy deposition of proton beam

The energy deposition E_{dep} due to ionization losses of the protons is ~ 33 J/g and additional ionization due to secondary particles from interactions of the protons in the target raises this to a peak of ~ 100 J/g at 10 cm into the target (McDonald, 2000). The energy deposition, E_{dep}, leads to peak pressure P that can be estimated as follow:

141

$$P \approx K\alpha_v \Delta T = \frac{\alpha_v K E_{dep}}{c_p} \ , \tag{5.10}$$

where α_v is the thermal volumetric expansion coefficient, which corresponds to 3 times of thermal linear expansion coefficient, K is the bulk modulus, E_{dep} is the energy deposition, and c_p is the specific heat capacity. For mercury, $\alpha_v = 180 \times 10^{-6}/K, \quad E_v = 25GPa, \quad c_p = 138J/(K\ kg)$. A peak value of E_{dep}=100J/g corresponds to a peak stress of $\sim$ 3000 MPa. The mercury target will be disrupted by the proton beam, leading to a breakup into droplets. The strain energy is built up in the jet due to compression (Sievers and Pugnat, 2000). The strain energy per unit volume can be estimated as follow based on the relationship between pressure thermal expansion:

$$E_{strain} = \frac{K}{2}(\alpha \Delta T)^2. \tag{5.11}$$

This deposited strain energy will be released as kinetic energy such as the generation of filaments on the jet surface. Hence, it indicates that the thermal volumetric expansion is possibly proportional to the jet expansion velocity with the coefficient of compressibility of jet material.

5.3.2 Observation of proton beam interaction and jet breakup

Fig. 5.14 is the photographs of the typical Hg jet interacting mechanism with a 16 TP, 14 GeV proton beam at 5 T captured at Viewport 3 at a 500 μs frame rate, which shows clearly how the Hg jet is responding from the

2744 sudden energy deposition by the proton beam. The beam hits the Hg jet at

2745 the bottom surface, passing through the center of jet at Viewport 2, leaving

2746 the Hg jet on the top surface. The captured photos show the response of the

2747 Hg jet upstream, midstream, and downstream with the interaction of proton

2748 beam. There are filaments on the top surface of jet downstream, where the

2749 beam is leaving, and on the bottom surface of the jet upstream, where the

2750 proton beam is hitting, entering the target. The jet break up voids midstream

2751 where the beam is passing through, possibly caused by the cavitations from

2752 energy deposition.

2753 ### 5.3.2.1 *energy deposition calculation with low intensity of proton*
2754 *beam and its observation*

2755 Fig. 5.15 (a) shows the distribution of energy deposition by 24 GeV, 3

2756 Tp intensity of proton beam in 5 T. Calculated energy deposition in each

2757 meshed volume is averaged along the jet axis and vertical radius of jet using

2758 Eqn. (5.12).

2759

2760
$$E(z, r) = \frac{1}{N_\theta^r} \sum_{\theta=0}^{2\pi} E_\theta^r(z, r, \theta), \tag{5.12}$$

2761 where N_θ^r, E_θ^r represent the number of meshes along radial angle at each

2762 radial distance and its energy deposition respectively.

2763 The spot size from optics is used. The energy density distribution is plotted

2764 depending on the radial position of Hg jet from jet center. Therefore, the

2765 peak of energy density exists respectively depending on the radial position in

143

2766 analysis. It shows that the maximum energy deposition density is obtained

2767 at the bottom surface of jet at $\sim$ 13 cm from the center of magnet, where

2768 Viewport 1 is actually positioned, and the peak energy deposition density

2769 moves to the center of the Hg jet followed by the larger energy deposition

2770 density is located at the top surface of the Hg jet. The peak energy deposition

2771 density is moving corresponding to the beam crossing trajectory in Hg jet. The

2772 most dense energy deposition is distributed at the center of Hg jet between

2773 upstream and midstream, where the Hg jet breaks. The collected photos in

2774 Fig. 5.15 (b) clearly supports these simulation results, where the frame rate is

2775 2 ms and measured disruption length at Viewport 3 is 11 cm.

5.3.2.2 *energy deposition calculation with high intensity of proton beam and its observation*

2778 Fig. 5.16 (a) shows the distribution of energy deposition by 24 GeV, 10 Tp

2779 intensity proton beam in 5 T. Averaged energy deposition is also calculated

2780 using Eqn. (5.12). The distribution profile of energy deposition throughout

2781 Hg jet is similar with low intensity of beam. The collected photos in Fig. 5.16

2782 (b) clearly supports these simulation results again, where the frame rate is

2783 2 ms and measured disruption length at Viewport 3 is 17 cm. However, the

2784 jet breakup voids the midstream where the beam is passing through, which is

2785 different with comparing with the observation of low intensity beam. These

2786 voids are not observed at 3 Tp intensity of beam, possibly indicates threshold

2787 of the existence of cavitation induced by energy deposition.

144

5.3.3 Hg jet disruption and magnetic suppression of the disruption

The disruption length is determined by counting the number of frames at Viewport 3 where the complete disruption of the jet is observed. The time delay between Viewport 2 and Viewport 3 is 10 ms. Thus, the disruption generated at Viewport 2 by the beam could be observed at Viewport 3 after 10 ms, where the jet is moving with a velocity of 15 m/s. Each image is separated into 10 segments vertically in order to locate the position of disruption. Thus, the accuracy of the measurement to define the location of starting(ending) disruption in measurement could be increased. The disruption length is given by multiplying the frame rate by the counted number of images and investigated with the beam energy, beam intensity, and magnetic field. 230 events out of 360 beam shots are evaluated for the disruption length. About 130 events out of 360 beam shots are evaluated for the detection of particles without Hg jet. Thus, the images for these events are not collected. Fig. 5.17 shows the standard deviation of the evaluated disruption lengths with respect to the disruption length. The solid line represents the curve fitted approximation of the reduced data distribution, where the line asymptote logarithmic. This curve fitted line is used for estimation of the standard deviation of the disruption length at respective disruption length. Correspondingly, the error bar is determined by dividing the the estimated standard deviation by the root square of the number of samples N for each data point.

2810 **5.3.3.1** *characteristics of beam structure in disruption length, har-*
2811 *monic 8 and 16*

2812   The proton beam pulse structure of harmonic 8 and harmonic 16 in 14

2813 GeV, 6 Tp is shown in Fig. 5.18. A pulse carries same number of protons with

2814 doubled bunch structures. Fig. 5.19 shows the dependence of the disruption

2815 length of the Hg jet on the proton beam pulse structure with a 14 GeV beam in

2816 5 T. The solid line in Fig. 5.18 (a) and (b) show the global fit and independent

2817 fit of disruption length with both harmonic 8 and harmonic 16 bunches as a

2818 function of total energy deposition respectively. A liner fit function is used as

2819 follow:

2820

2821
$$z = A_1(x - B_1), \tag{5.13}$$

2822   where x and z denote the total energy deposition and disruption length

2823 respectively. The χ^2 probability of global fit in Fig. 5.18 (a) is 0.056. The χ^2

2824 probability of each independent fit in Fig. 5.18 (b) by using the sum of χ^2 and

2825 degrees of freedom of each independent fit yields 0.051. From this point of

2826 view, there is no statistical difference between the two ways of fitting, so that

2827 one could conclude that the disruption length does not depend on harmonic

2828 number. The disruption of Hg jet is affected by the number of protons, resulted

2829 from energy deposition of interaction of number of protons. The short time

2830 in each bunch structure is negligible. The disruption on the Hg jet surface

2831 disappears when the beam intensity is less than $\sim$ 4 Tp in Fig. 5.20. The

2832 threshold of beam intensity is $\sim$ 4 Tp at 14 GeV in 5 T.

2833   **5.3.3.2**   *disruption length with 14 GeV proton beam*

2834   Fig. 5.20 shows the disruption length with beam intensities up to 30 Tp

2835   for a 14 GeV beam. The peak and total energy deposition to Hg with 14 GeV

2836   beam energy at 30 Tp and 15 T is $\sim$ 52 J/g and 3700 J by approximating

2837   it from Fig. 5.13, where the disruption length corresponds to $\sim$ 23 cm $\pm$ 5

2838   cm for 10 T to $\sim$ 18 cm $\pm$ 5 cm for 15 T respectively. At high intensities of

2839   beam, the disruption length appears to be approaching an asymptotic level.

2840   The magnetic field suppresses weak disruption such as onset of generation of

2841   the filaments on the jet surface. The threshold of the disruption for beam

2842   intensity is around 4 Tp at 5 T and the magnetic field can increases it, though

2843   the effect is not clear in Fig. 5.20 due to the difficulty in quantifying and

2844   judging to measure the small amount of the disruption length.

2845   **5.3.3.3**   *disruption length with 24 GeV proton beam*

2846   Fig. 5.21 shows the disruption length with the beam intensities up to 30 Tp

2847   for a 24 GeV proton beam. The estimation of disruption length is performed

2848   by calculating the extent of energy level of Hg jet larger than the energy

2849   experimentally determined by threshold intensity of beam as follow :

2850

2851 $$L_E^{disruption}(z) = z_2 - z_1, \ E(z) \geq E_{threshold}^{peak}(z), \quad L_{E_{threshold}^{peak}}^{disruption}(z) = 0, \quad (5.14)$$

2852   where $L^{disruption}$, $E_{threshold}^{peak}$ represent the length of disruption and peak

2853   energy of thresholding intensity of beam experimentally determined for jet

2854   disruption.

147

According to Fig. 5.13, the peak and total energy deposition to Hg with 24 GeV beam energy at 30 Tp in 10 T is $\sim$ 125 J/g and 8200 J, where the disruption length corresponds to $\sim$ 22 cm $\pm$ 5 cm for 10 T to $\sim$ 17 cm $\pm$ 5 cm for 15 T respectively. The results again show that the magnetic field suppresses the disruption length. The disruption length appears to be approaching an asymptotic level. If there is no magnetic field, the disruptions are always generated by proton beam regardless of the beam intensities, though very weak disruptions on the Hg jet surface are observed with low beam intensities. The threshold of the disruption for beam intensity is $\sim$ 1 Tp at 5 T but the higher magnetic field increases it. The estimation of disruption length in 10 T based on the calculation of energy deposition using the beam spot size from optics is well agreed with the experimental measurement, but the estimation in 0 T based on the beam spot size from optics underestimates the experimental results. Possibly, the difference in MARS model may cause the difference of energy deposition calculation and the beam spot size is more likely to be larger at 0 T. Therefore, possibly the estimation by energy deposition from larger beam spot size is more likely to be fit to the experimental measurement. For theses estimations, the independent threshold of beam intensity is chosen individually from the experimental results depending on the conditions of individual cases for estimation. Therefore, the energy for threshold is differently used for each case of estimation using the beam size from optics and camera. For the case of estimation of 0 T , 5 T, and 10 T, 0.8 Tp, 1.5 Tp, and 3.7 Tp of threshold beam intensity are chosen respectively.

2878 **5.3.3.4** *validation of measurements of Viewport 3 through com-*
2879 *parison with Viewport 4*

2880 In order to validate measurements of the disruption length at Viewport 3,

2881 measurements of disruption lengths at Viewport 4 are also performed. Fig. 5.22

2882 (a) shows the disruption length at Viewport 3 for 23 events with a harmonic

2883 16 beam structure, 16 Tp, 14 GeV beam energy in 5 T. Fig. 5.22 (b) shows

2884 the disruption length at Viewport 4 for the same events. Fig. 5.22 (c) shows

2885 the difference of disruption length between Viewport 3 and Viewport 4 for the

2886 same events. The solid line represents the average and distribution of the dis-

2887 ruption length difference based on gaussian distribution approximation. The

2888 difference of measured disruption length between Viewport 3 and Viewport 4

2889 is 1.3 ± 3.5 cm. The reason for the difference of the disruption length measure-

2890 ment between Viewport 3 and Viewport 4 is mainly caused by the fluctuation

2891 of the proton beam and the Hg jet in a magnetic field. The reduction of sur-

2892 face instabilities by the presence of a static magnetic field is a consequence of

2893 magnetic damping. Also, surface structure is frozen by magnetic field. There-

2894 fore, the same disrupted shape on the jet surface at Viewport 3 is observed at

2895 Viewport 4 without variation of the disruption length.

2896 **5.3.3.5** *disruption measurement in pump probe condition as a*
2897 *check of experiment*

2898 Fig. 5.23 shows the measured disruption length of multiple events with

2899 pump probe conditions as a check of experiment. The conditions of each

2900 group in pump probe events are given in Table A.3. There are 4 groups at 14

149

GeV and each group has different number of bunches and time delay between pump and probe. Fig. 5.23 (a) shows the histogram of disruption length and Fig. 5.23 (b) shows statistics summary such as average, min/max, and median value. In group 2, qualitatively meaningful distribution of measurements are shown, which is 19.8 ± 6.1 cm. In sub-category of group 2, 3 different time delay between 6 bunches and 2 bunches does not show significant difference in disruption length. This check is agreed with the result provided in both Fig. 5.20 and Fig. 5.24.

5.4 Disruption of Hg Jet By Total Energy Deposition

As discussed, the extent of disruption of jet is dominated by the distribution of energy deposition interacting with proton beam. Therefore, the total energy deposition plays a key role in determining of the extent of disruption of Hg jet. The total energy deposition in magnetic fields is investigated. The total energy deposition depending on colliding number of protons at both 14 GeV and 24 GeV beam energy is calculated by Fig. 5.13 (b). Thus, Fig. 5.20 and Fig. 5.21 are combined as a function of total energy deposition, which shows the results of experiment in disruption length at a glance. As a finally important result for experiment, Fig. 5.24 shows the disruption mercury jet in magnetic fields as a function of total energy deposition and its extrapolation up to 25 T. Fig. 5.24 combines a key results of experiment, also provides an estimation of the extent of disruption of jet up to 25 T. The employed global fit with multi-variables

150

for disruption length using the measured disruption length is

$$z = A_1(x - (B_1 + B_2 y^{B_3}))^{\frac{1}{C_1 + C_2 y + C_3 y^2}}, \tag{5.15}$$

where x and y are total energy deposition and magnetic field respectively. Note that the parameterized values of coefficients and errors of the fit functions are provided in Table 5.2. The threshold of disruption increases in 0.8 power of magnetic field, and it is 338 J of energy energy deposition with no magnetic field. The disruption length increases in square root power of total energy deposition with no magnetic field, but it is suppressed in $\sim 1/(2 + 0.04B)$ power of total energy deposition with magnetic field.

The disruption length at 15 T is less than 20 cm and the total energy deposition is ~ 8000 J. Approximately $6 \sim 8$ % of beam energy is deposited into mercury target. Therefore, $100 \sim 133$ kJ of beam energy can be recycled with a 70 Hz repetition rate for 20 m/s jet. This result validates that a target system capable of supporting proton beams with powers of up to 8 MW, which is a key result for this experiment.

Table 5.1: Measurement of vertical distances of center of jet from magnetic axis and jet size for modeling in MARS code for the cases of elliptic and circular jet sectional shape.

1 (T)	2 (mm)	3 (mm)	4 (mm)	5 (mm)	6 (mm)	7 (mm)	8 (g/cm^3)
Elliptic jet shape							
0	7.11	4.46	4.28	5.01	8.65	2.9	13.55
5	7.1	4.52	3.7	4.38	8.4	3.0	13.55
10	6.57	4.08	3.66	3.71	7.95	3.15	13.55
15	5.45	3.6	3.24	3.11	9.05	2.76	13.55
Circular jet shape							
0	7.11	4.46	4.28	5.01	8.65	8.65	4.50
5	7.1	4.52	3.7	4.38	8.4	8.4	4.77
10	6.57	4.08	3.66	3.71	7.95	7.95	5.32
15	5.45	3.6	3.24	3.11	9.05	9.05	4.11

1 : Magnetic field

2 : Vertical distance at Viewport1

3 : Vertical distance at Viewport2

4 : Vertical distance at Viewport3

5 : Vertical distance at Viewport4

6 : Vertical radius of jet

7 : Horizontal radius of jet

8 : Hg density

Table 5.2: Parameterized coefficients, its error, and statistics summary of fit function in figures.

Figure	1	2	3	4	5	6	7	8	9	10
5.12a	0.74078	0.03855	-0.06864	0.01598	0.50641	0.05307	-	-	1.48078	0.0158
5.12b	0.02228	8.60E-04	-1.09835	0.36388	0.0613	0.00759	-5.49E-04	1.62E-04	1.36185	0.01097
5.13a	0.06023	0.0073	0.80386	0.0105	-	-	-	-	1.5568	0.04025
5.13b	3.52931	0.3187	0.88872	0.01003	0.02553	0.01138	0.3758	0.16582	1.4208	0.02953
5.19a	1.43E-04	1.86E-05	647.56071	89.38814	-	-	-	-	-	-
5.19b(H8)	1.70E-04	3.77E-05	638.26526	126.57444	-	-	-	-	-	-
5.19b(H16)	1.39E-04	2.18E-05	680.28969	113.41709	-	-	-	-	-	-
5.24	0.00649	0.00348	338.24297	15.76037	115.38009	47.56862	0.82899	0.22938	1.92463	0.29005

Figure	11	12	13	14	15	16	17	18	19	
5.12a	-	-	-	-	32	28	14.67464	0.99691	0	
5.12b	0.91711	0.10273	-	-	32	26	256.24604	0.99909	0	
5.13a	-	-	-	-	32	29	95.44974	0.99168	0	
5.13b	-	-	-	-	32	27	3972.28821	0.99628	0	
5.19a	-	-	-	-	11	9	1.84	0.85406	0.056	
5.19b(H8)	-	-	-	-	5	3	1.97369	0.82927	0.1155	
5.19b(H16)	-	-	-	-	6	4	1.77779	0.88853	0.1301	
5.24	0.03939	0.01079	0	0	36	30	1.82037	0.88724	0.0039	

1 : A1 value, **2** : A1 standard deviation,

3 : B1 value, **4** : B1 standard deviation, **5** : B2 value, **6** : B2 standard deviation,

7 : B3 value, **8** : B3 standard deviation , **9** : C1 value, **10** : C1 standard deviation,
11 : C2 value, **12** : C2 standard deviation, **13** : C3 value, **14** : C3 standard deviation,

15 : Number of points, **16** : Degrees of freedom, **17** : Reduced χ^2, **18** : Adjusted $\mathbf{R}^2$, **19** : χ^2 probability.
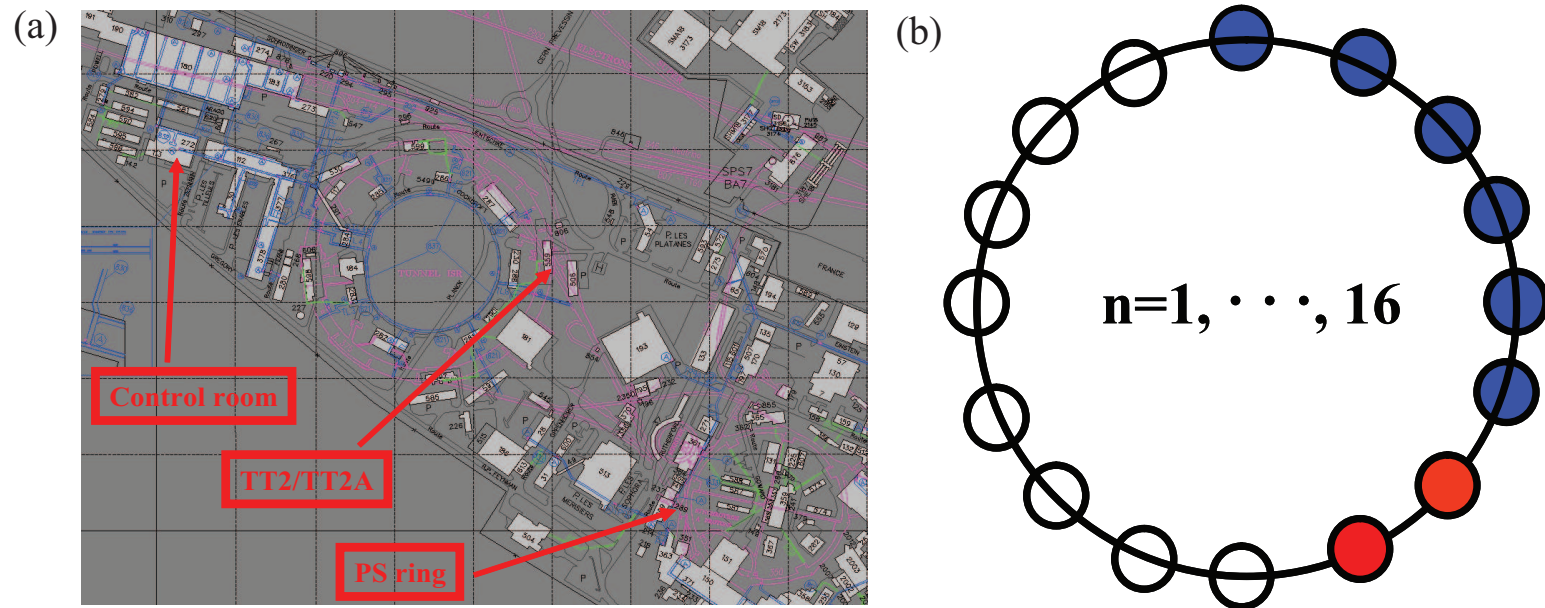
Figure 5.1: Infrastructures for experiment at CERN. a.) Proton synchrotron and TT2 tunnel for experiment. b.) 16 harmonics of beam extraction in proton synchrotron.
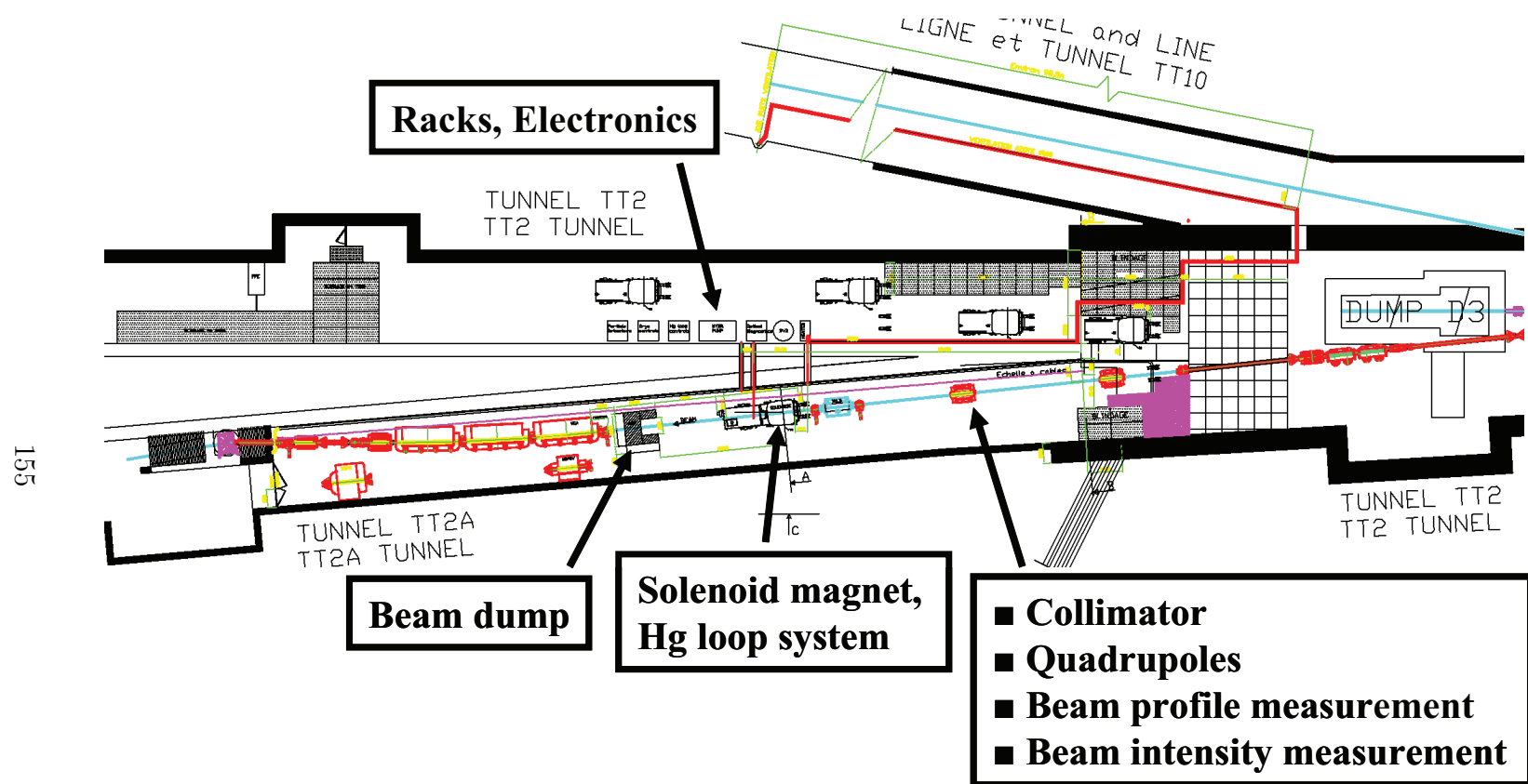
Figure 5.2: Installation of integrated experimental components in tunnel TT2/TT2A for high power target experiment. Extracted proton beam comes from right to left in tunnel TT2A.
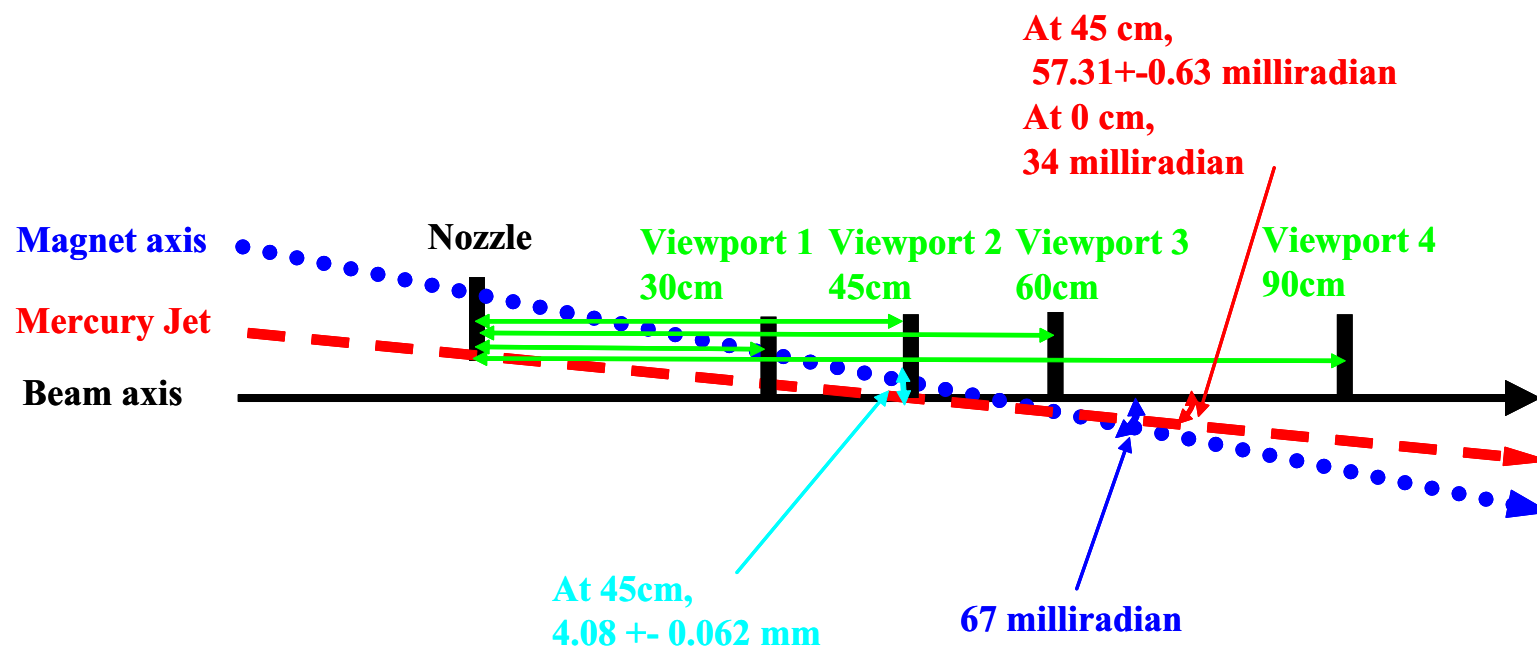
Figure 5.3: Schematics of beam to jet interaction in magnetic field and the location of each Viewport.
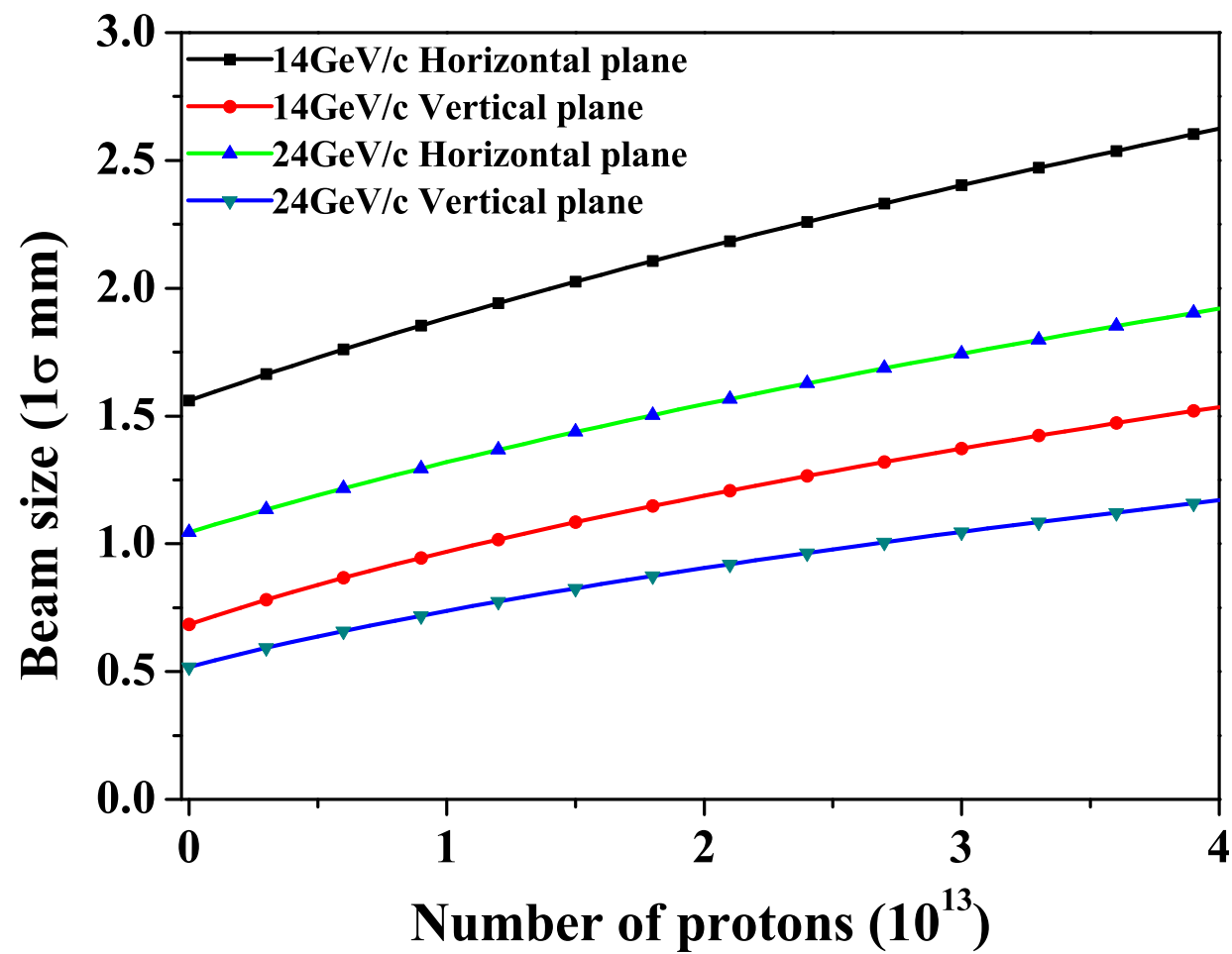
Figure 5.4: 1 σ proton beam size at the center of magnet by optics (Efthymiopoulos, 2008).
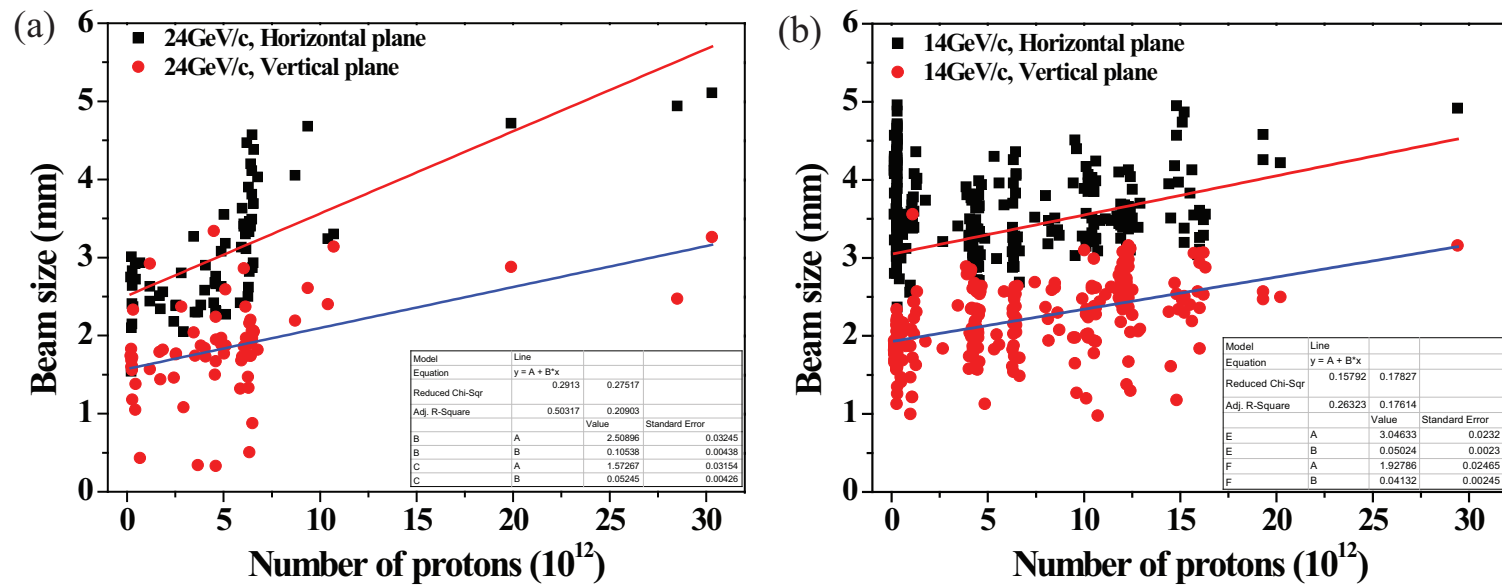
Figure 5.5: 1 σ proton beam size by camera screen (Skoro, 2008). a.) 14 GeV beam. b.) 24 GeV beam.
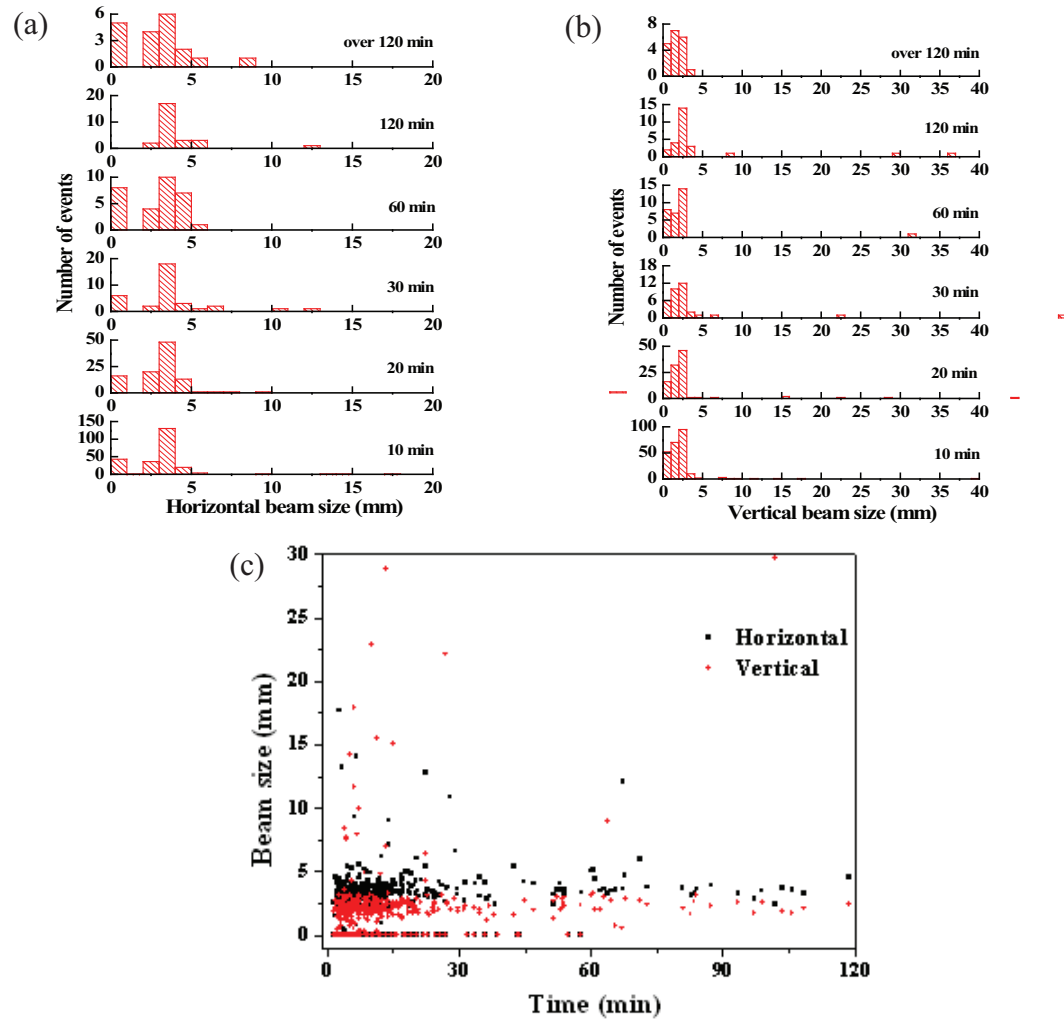
Figure 5.6: Beam size measured by phosphor screen monitor as a function of time interval between beam shots. a.) Histogram of beam size in horizontal plane. b.) Histogram of beam size in vertical plane. c.) Beam sizes distribution.
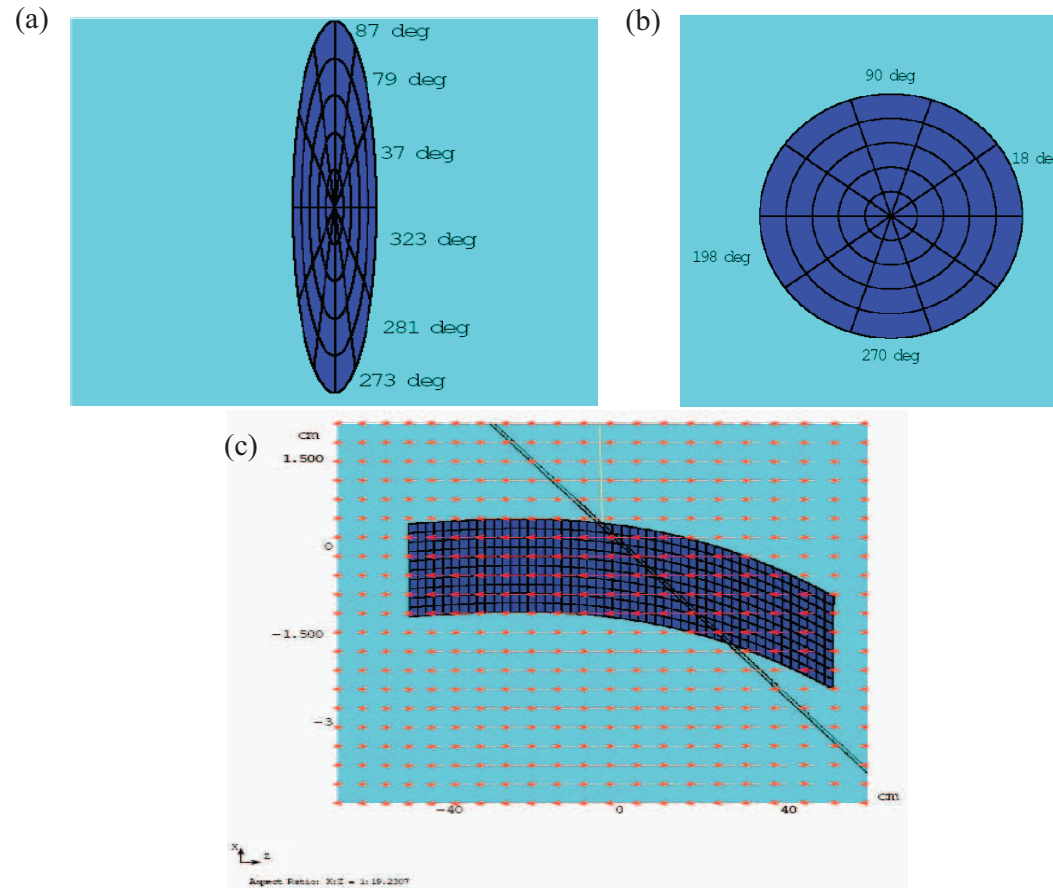
Figure 5.7: Modeling in MARS code for energy deposition calculation (Striganov, 2009). a.) Sectional view of elliptic jet. b.) Sectional view of circular jet. c.) Side view of mercury jet.
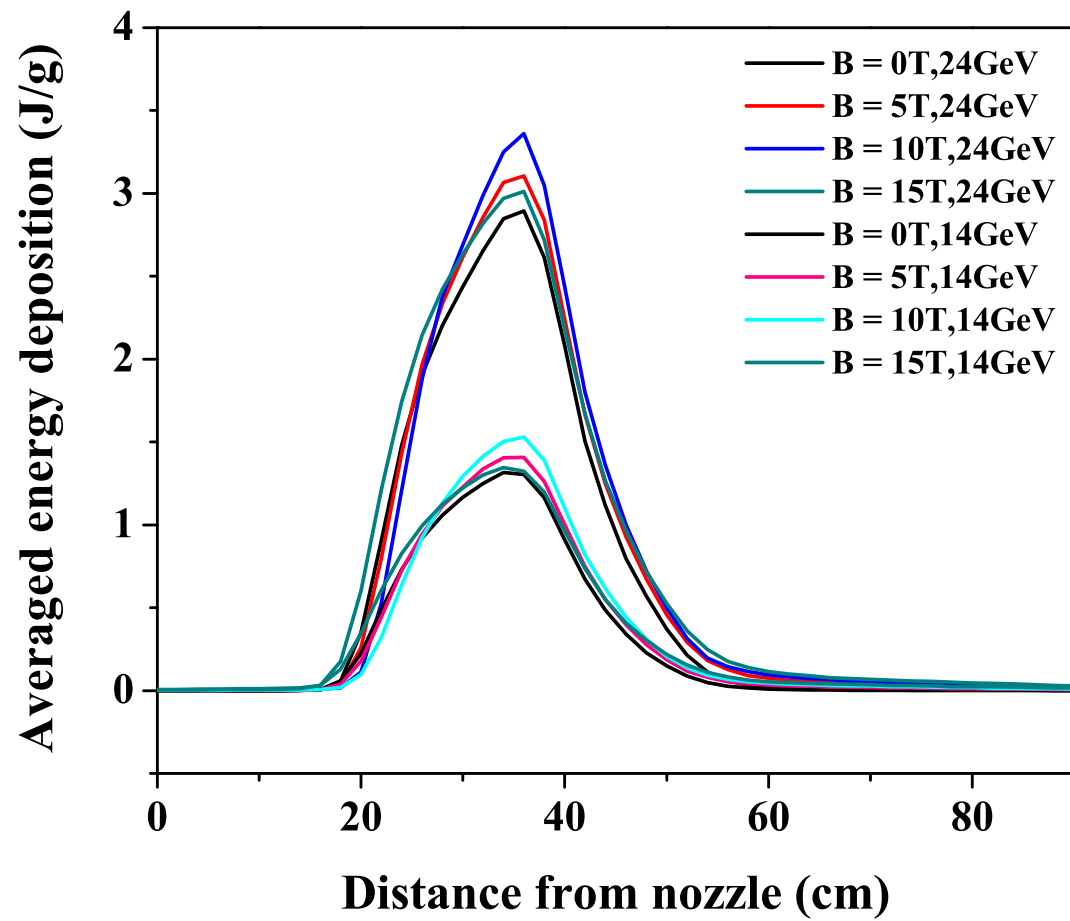
Figure 5.8: Influence of magnetic field to the energy deposition distribution to Hg jet considering experimentally measured jet parameters.
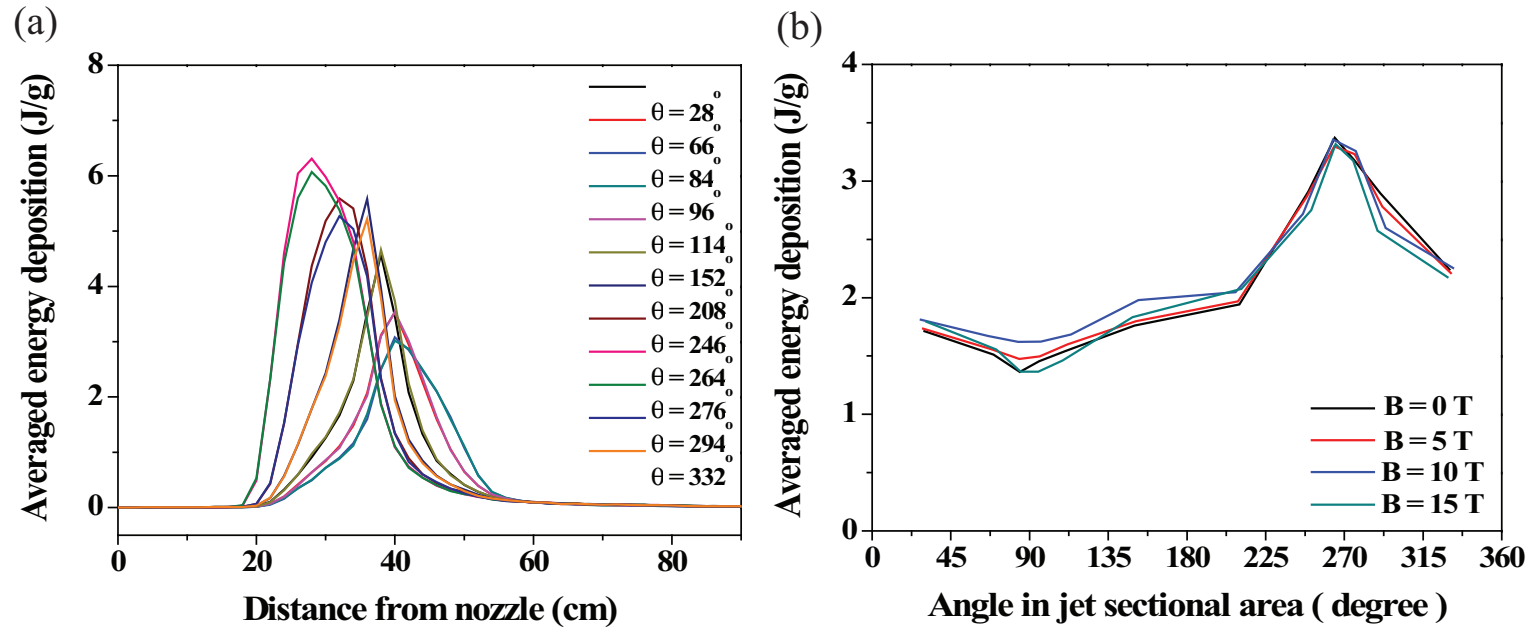
Figure 5.9: Radial energy deposition distribution along jet axis interacting with 24 GeV proton beam. a.) Along jet axis. b.) Along radial angle in jet cross section.
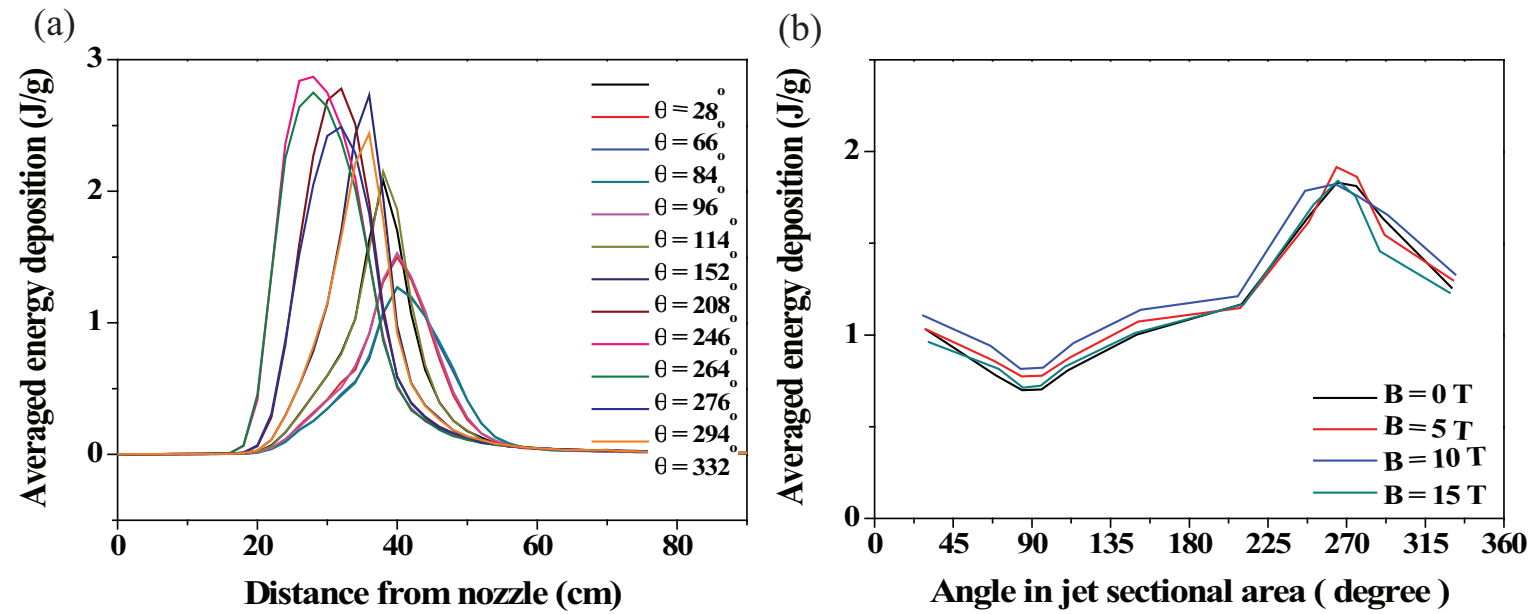
Figure 5.10: Radial energy deposition distribution along jet axis interacting with 14 GeV proton beam. a.) Along jet axis. b.) Along radial angle in jet cross section.
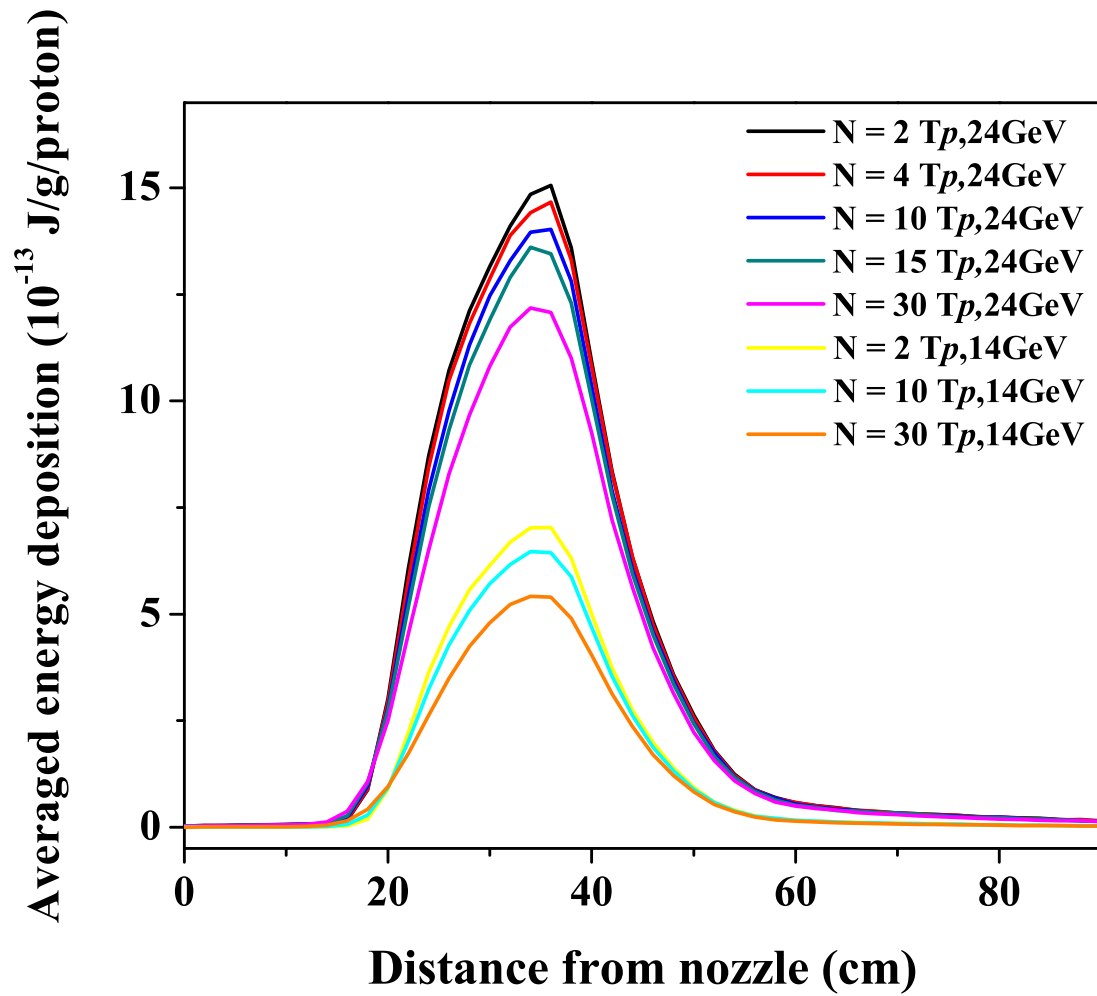
Figure 5.11: Energy deposition distribution per proton according to the variation of beam spot size along jet axis.
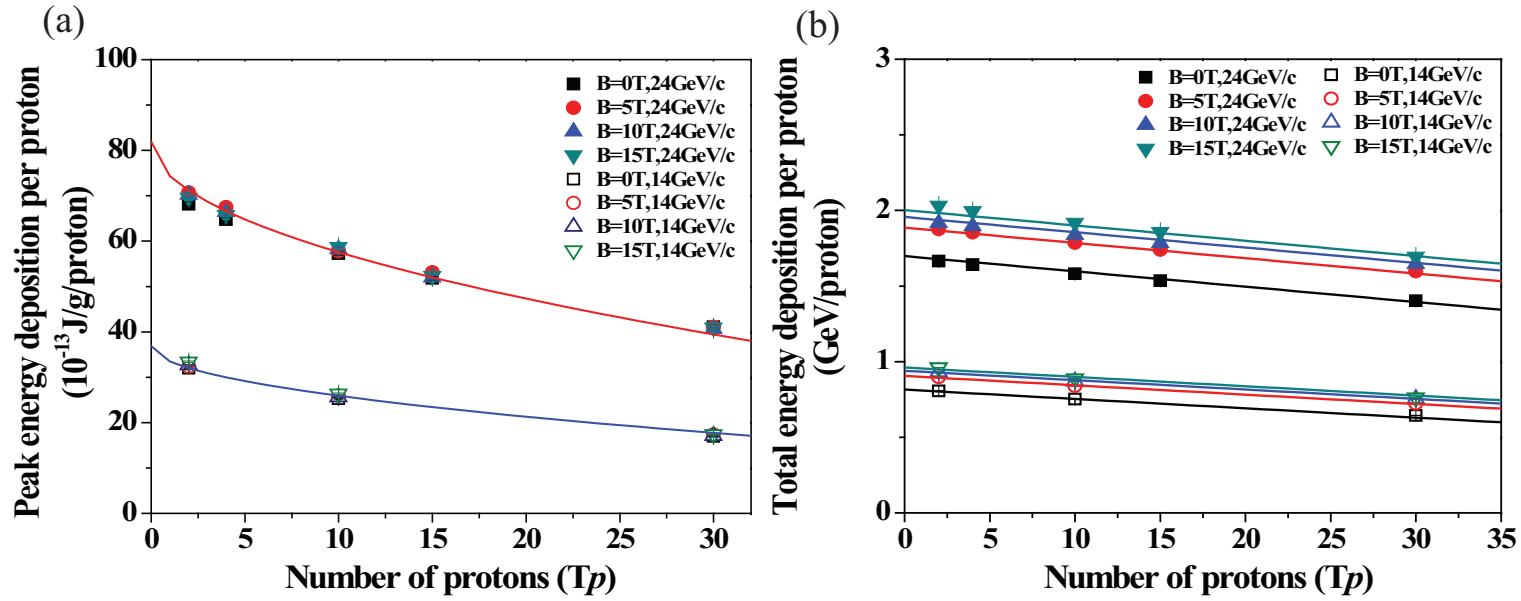
Figure 5.12: Peak energy deposition per proton and total energy deposition per proton according to the beam spot sizes by beam intensities. a.) Peak energy deposition per proton. b.) Total energy deposition per proton.
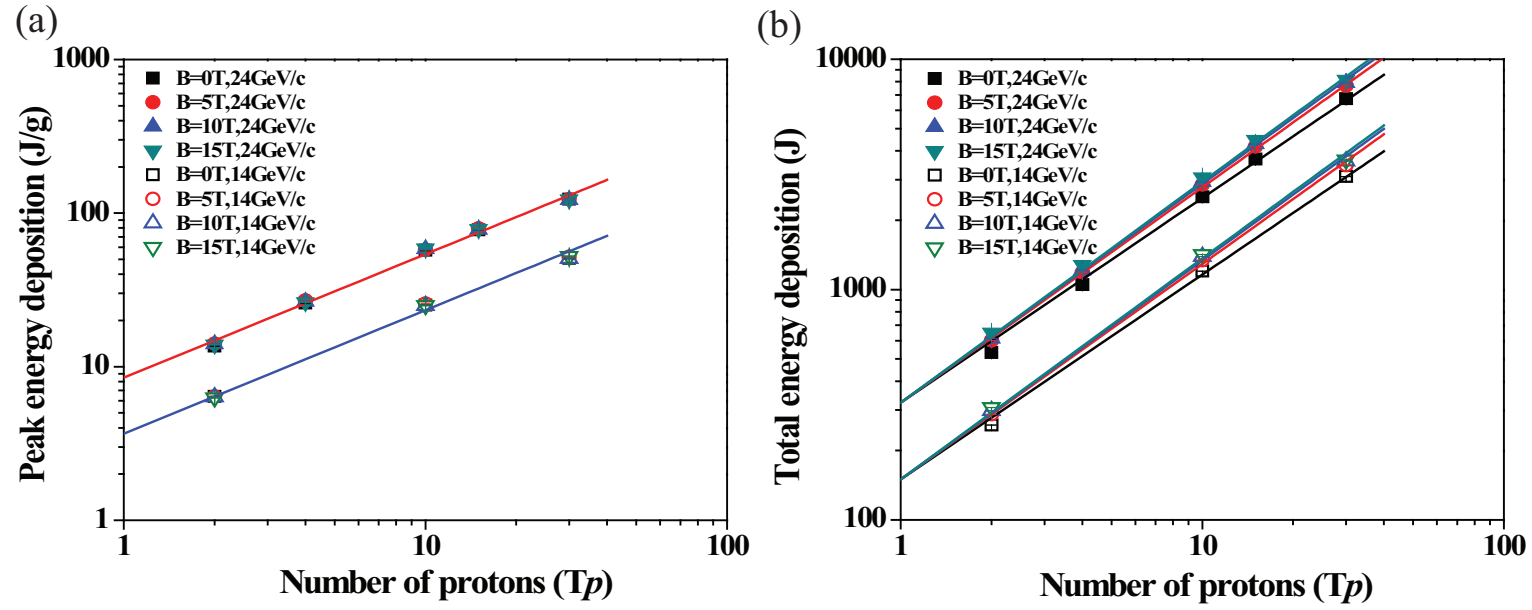
Figure 5.13: Peak energy deposition and total energy deposition in total number of protons. a.) Peak energy deposition. b.) Total energy deposition.
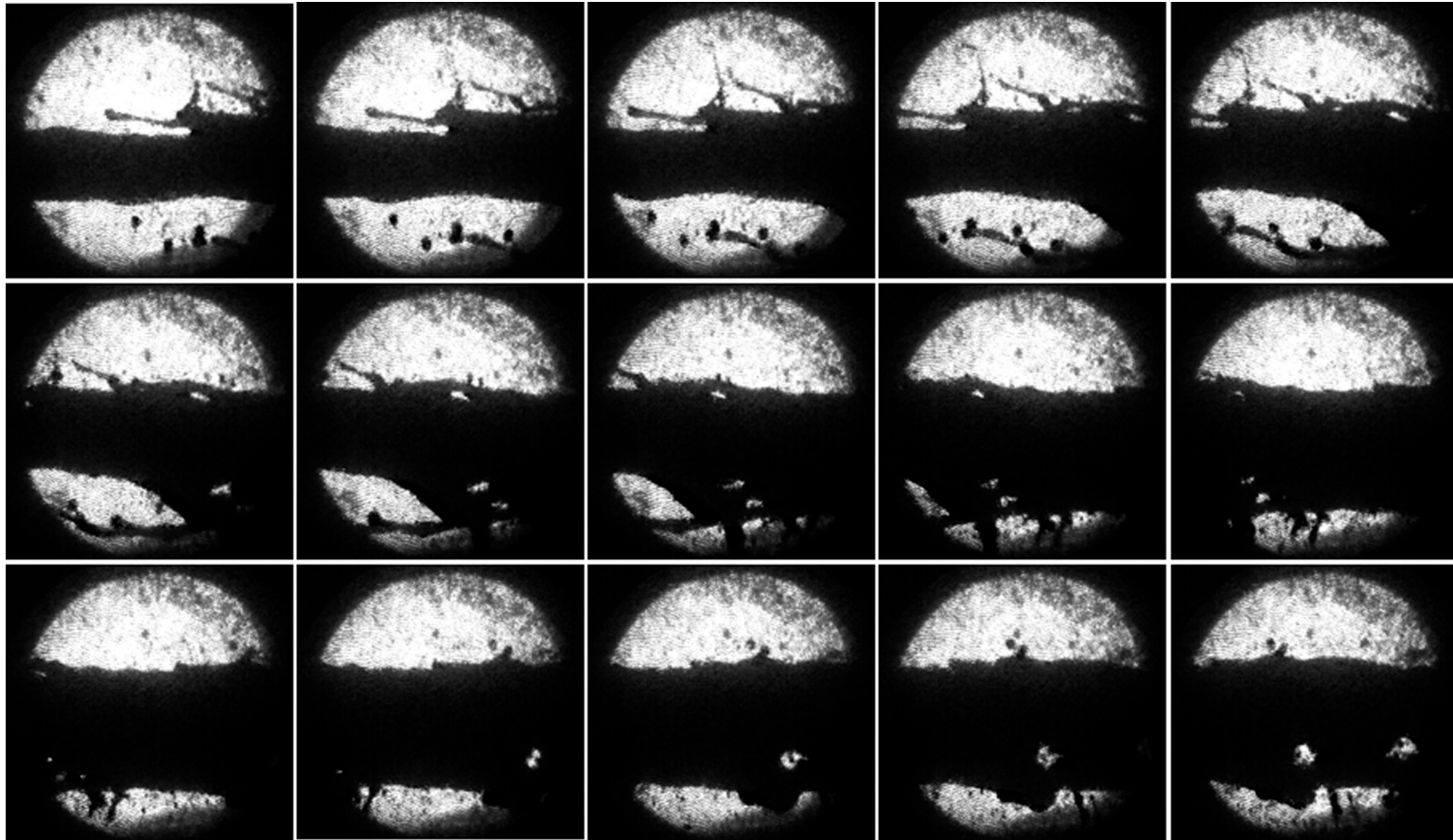
Figure 5.14: Photographs of the Hg jet interaction with 16 TP, 14 GeV proton beam at 5 T. Captured at Viewport 3 at 500 μs frame rate (continued).
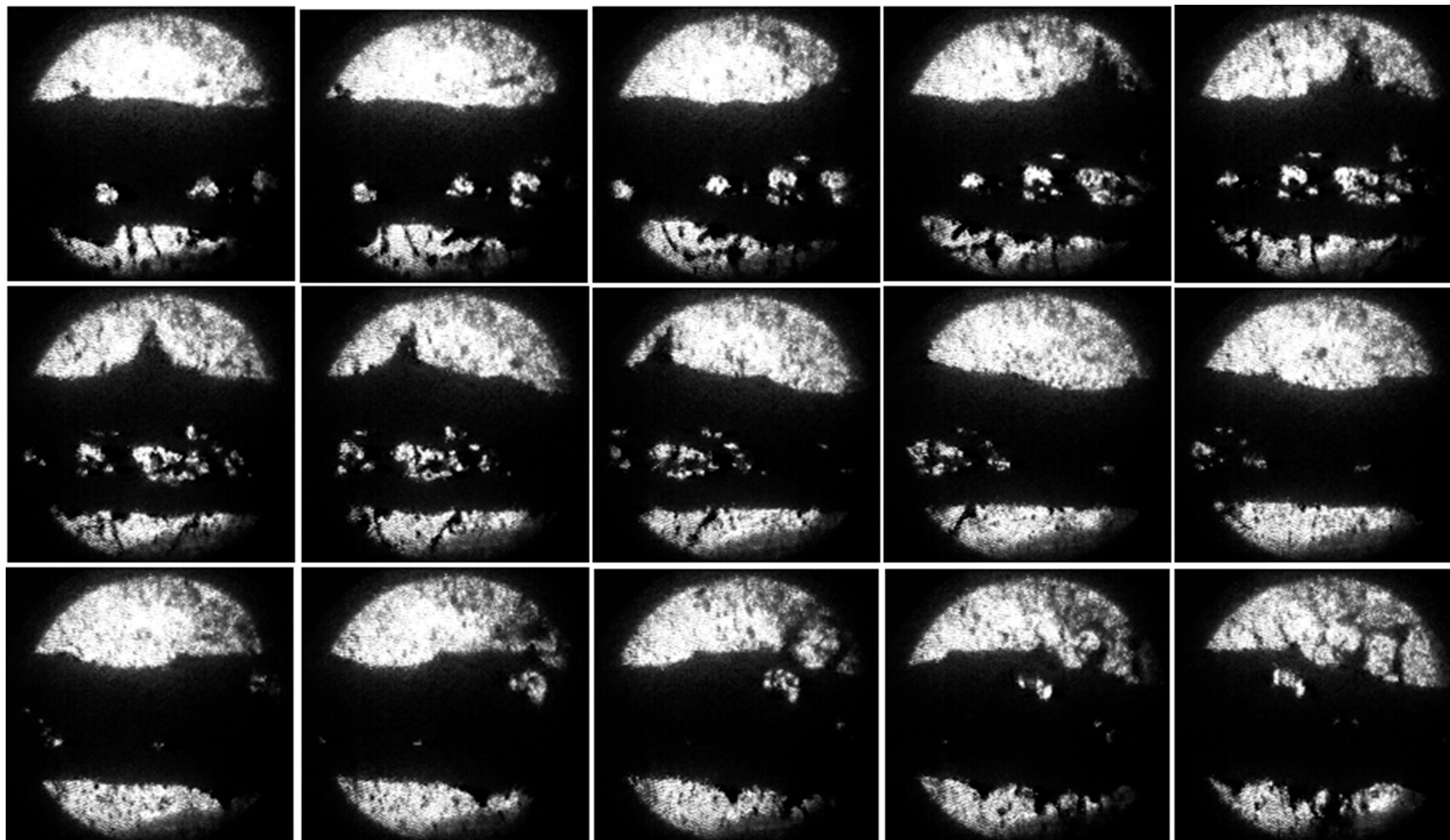
Figure 5.14: Photographs of the Hg jet interaction with 16 TP, 14 GeV proton beam at 5 T. Captured at Viewport 3 at 500 μs frame rate (continued).
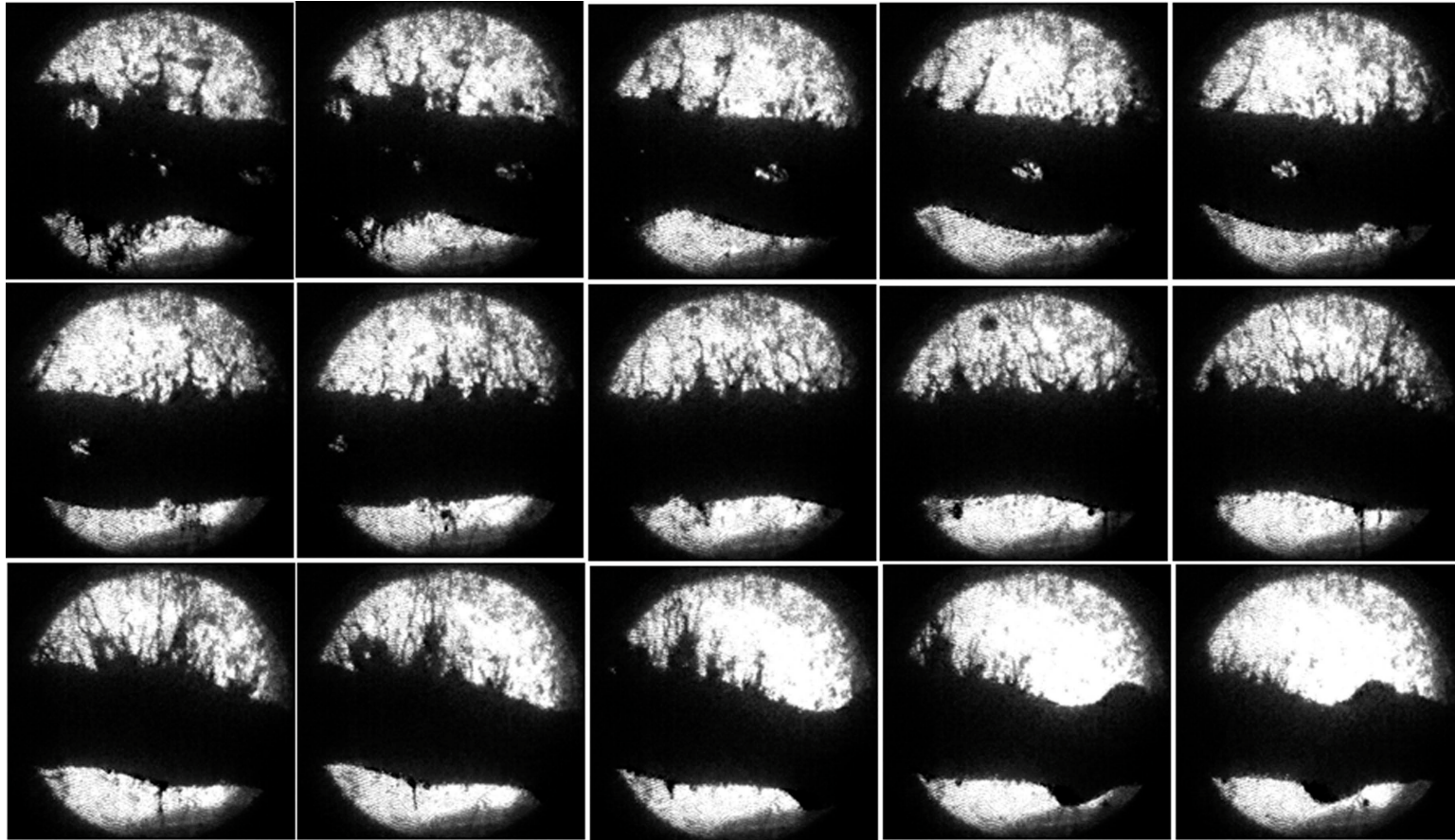
Figure 5.14: Photographs of the Hg jet interaction with 16 TP, 14 GeV proton beam at 5 T. Captured at Viewport 3 at 500 μs frame rate.
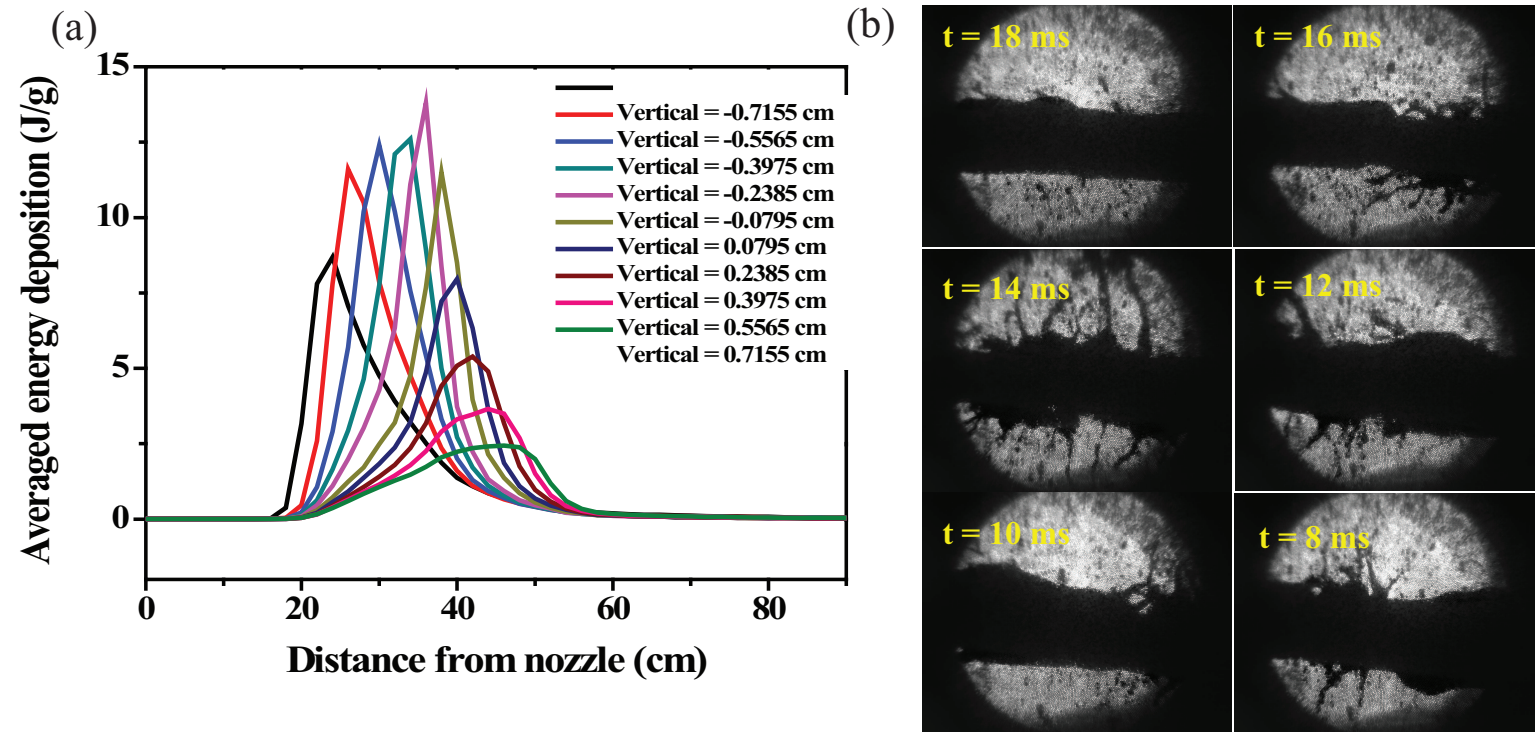
Figure 5.15: Qualitative comparison of the jet response incident by interaction of low intensity (3 Tp) of beam at 5 T. a.) Calculated averaged energy deposition profile to mercury jet according to the distance from jet center. b.) Jet response by captured image.
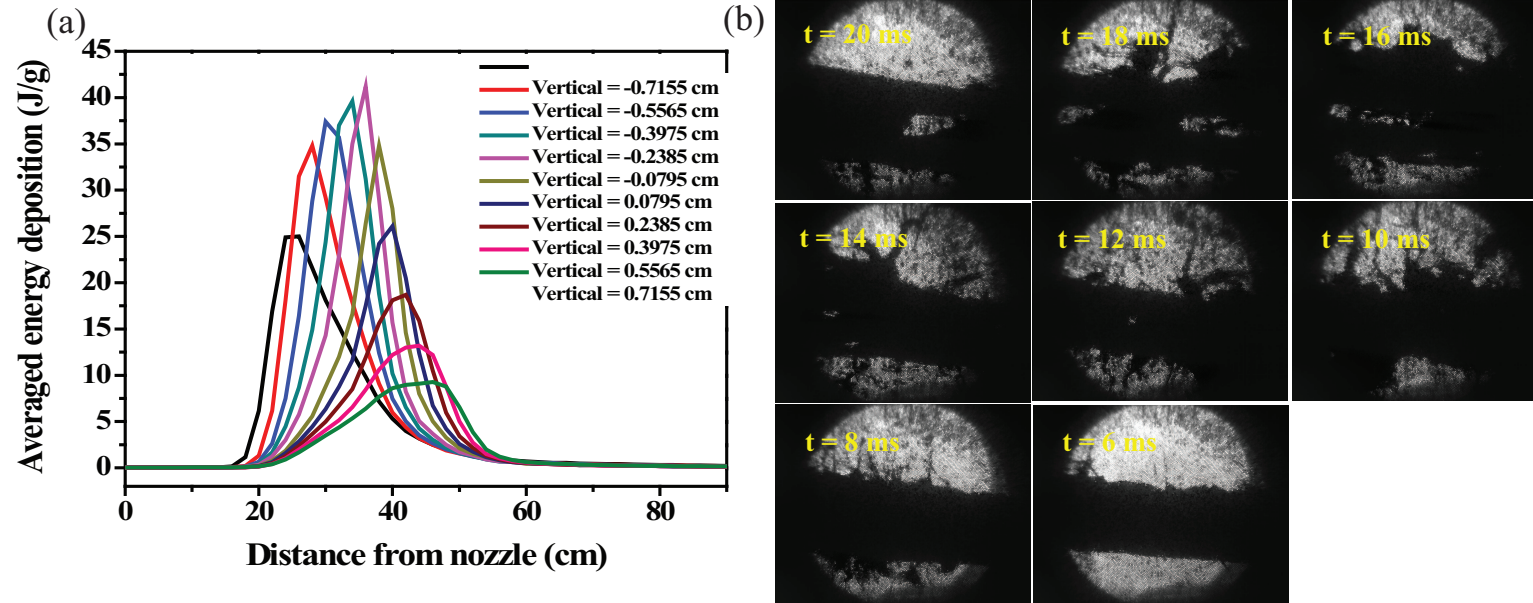
Figure 5.16: Qualitative comparison of the jet response incident by interaction of high intensity (10 Tp) of beam at 10 T. a.) Calculated averaged energy deposition profile to mercury jet according to the distance from jet center. b.) Jet response by captured image.
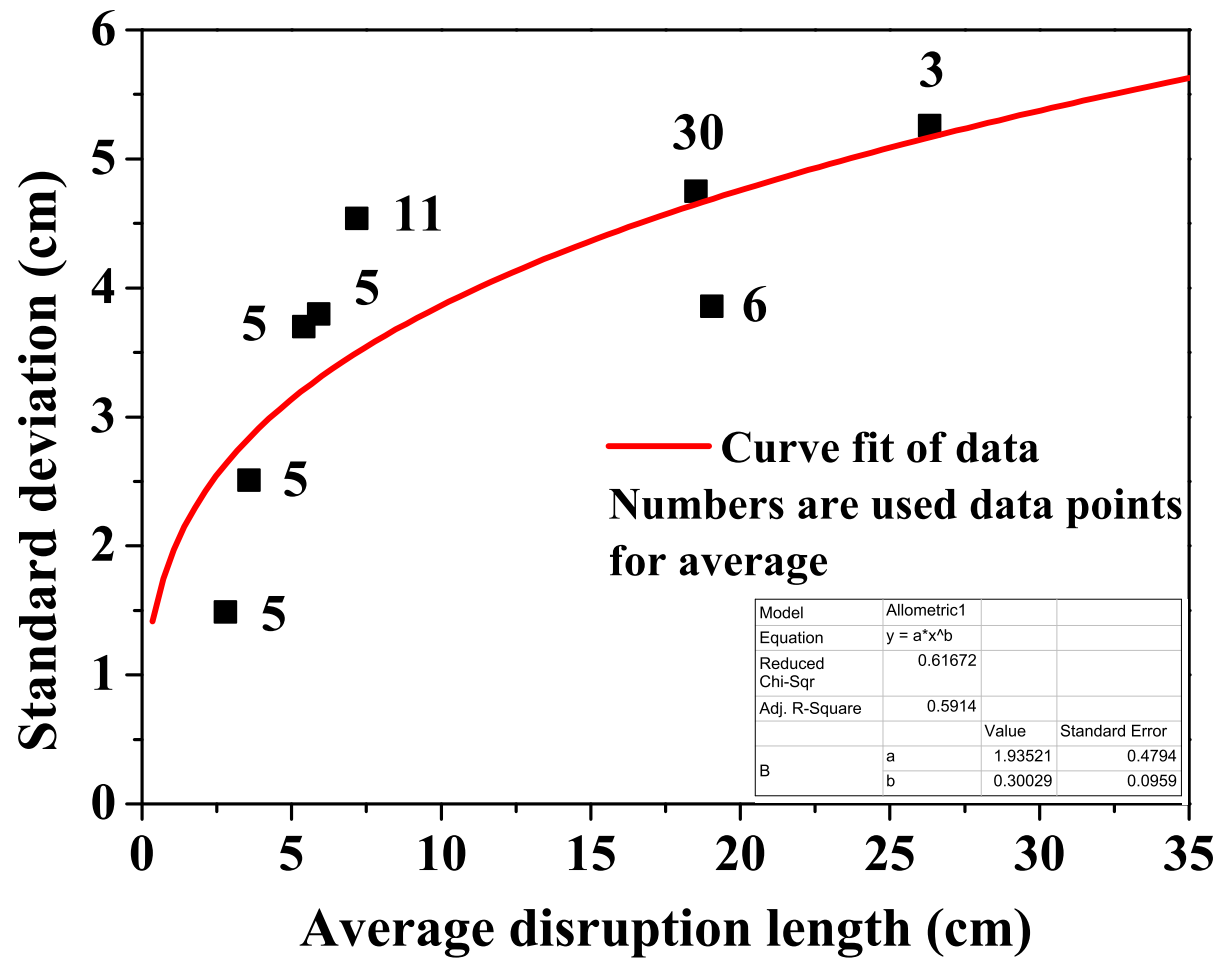
Figure 5.17: Standard deviation of disruption length as a function of disruption length and the function of fitted curve. The fitted curve is $\sigma_{disruption} = 1.9352 L_{disruption}^{0.3}$.
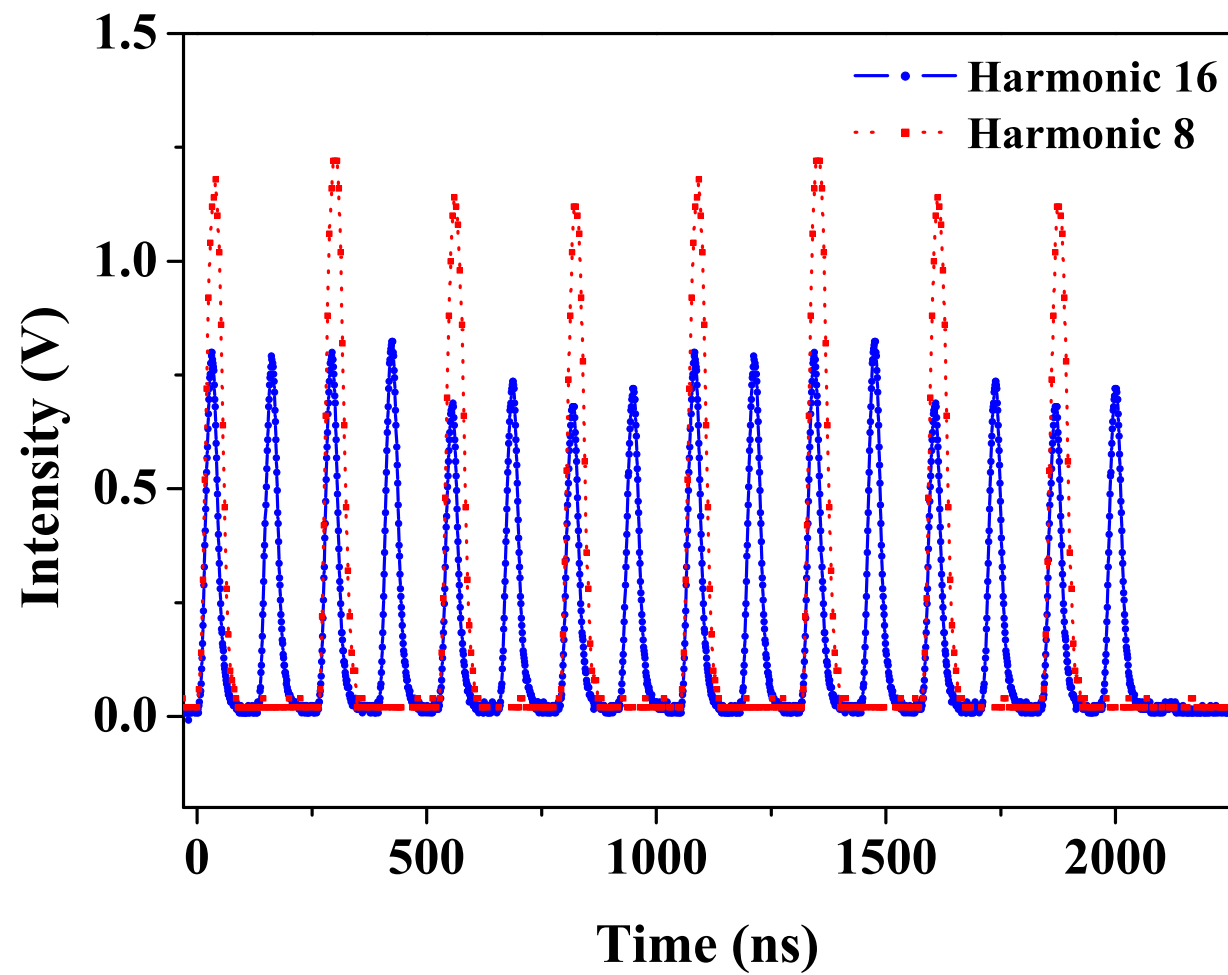
Figure 5.18: Proton beam pulse structure of harmonic 8 and harmonic 16 in 14 GeV and 6 TP.
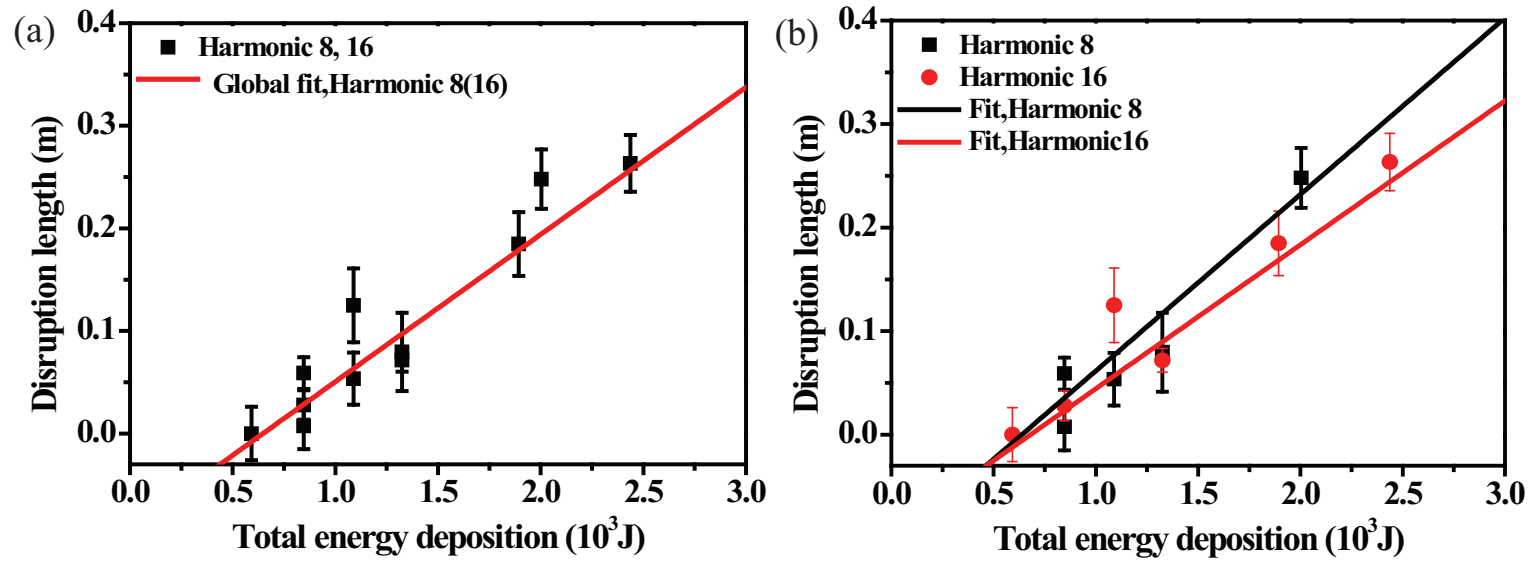
Figure 5.19: Disruption length of Hg jet depending on the beam pulse structure as a function of 14 GeV beam intensity in 5 T. $Tp = 10^{12}$ protons. a) Global fit of harmonic 8 and 16. b.) Independent fit of harmonic 8 and 16.
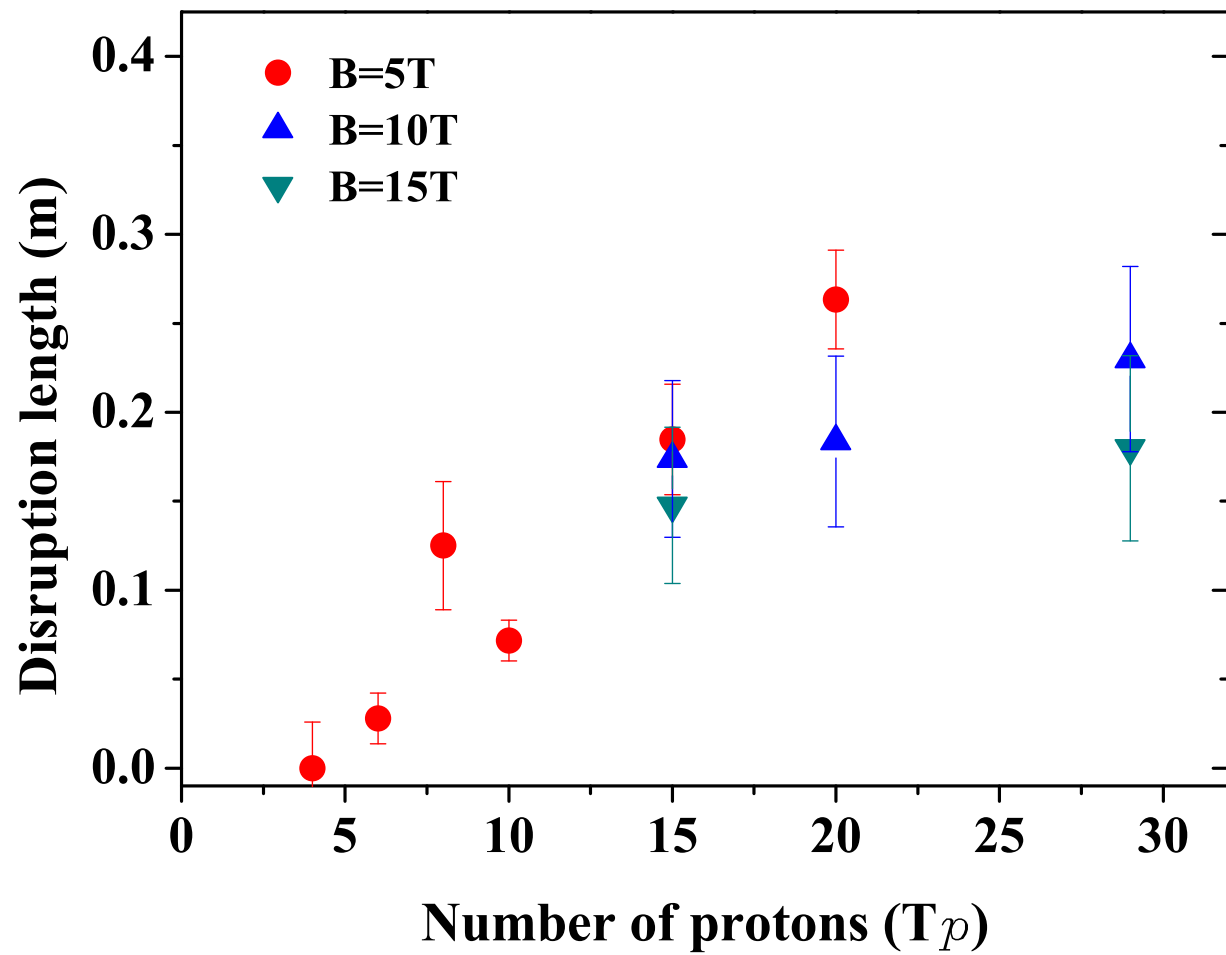
Figure 5.20: Disruption length of Hg jet as a function of 14 GeV beam intensity and magnetic field. Harmonic 16 with 16 bunches is used.
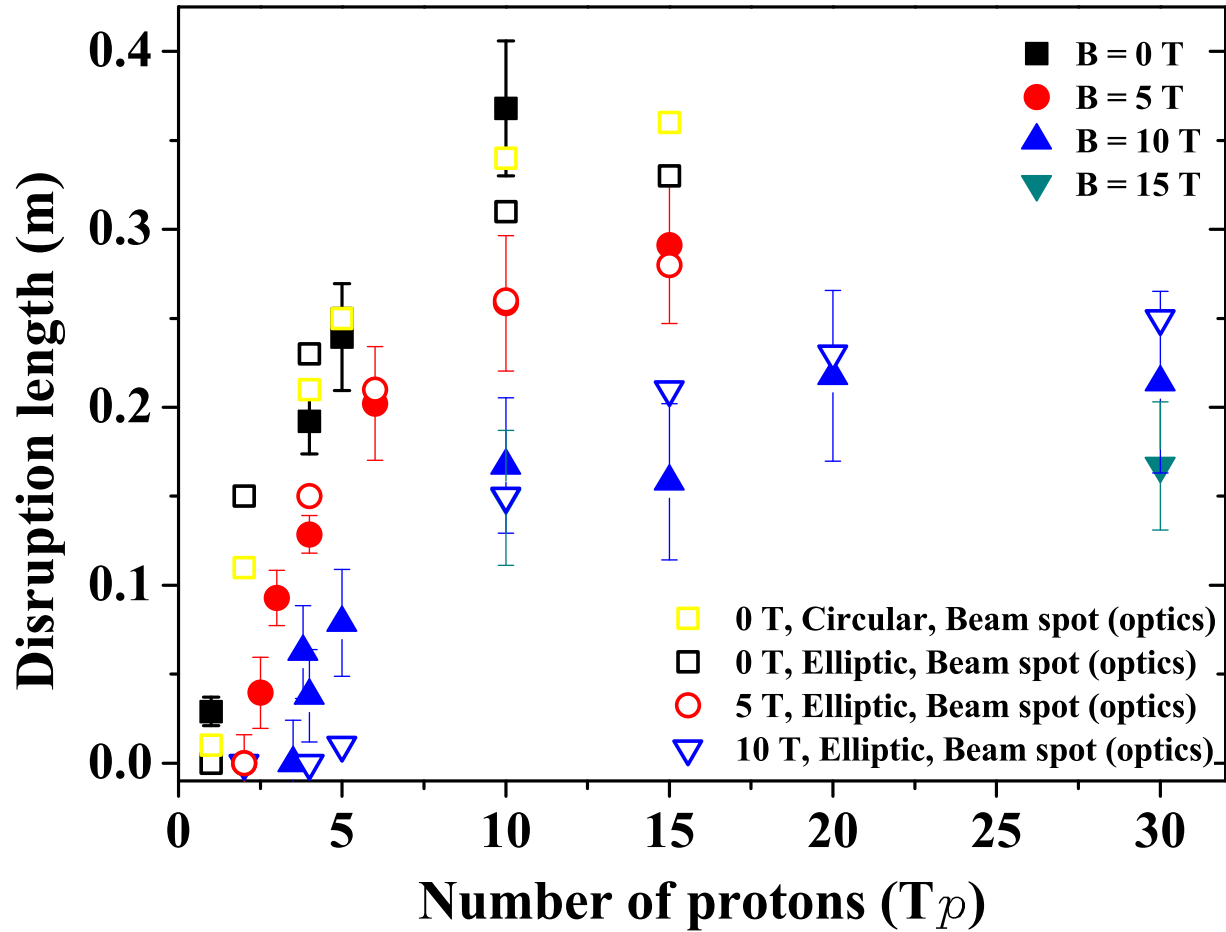
Figure 5.21: Disruption length of Hg jet and its estimation as a function of 24 GeV beam intensity and magnetic field. The estimation of disruption length by energy deposition calculation is compared.
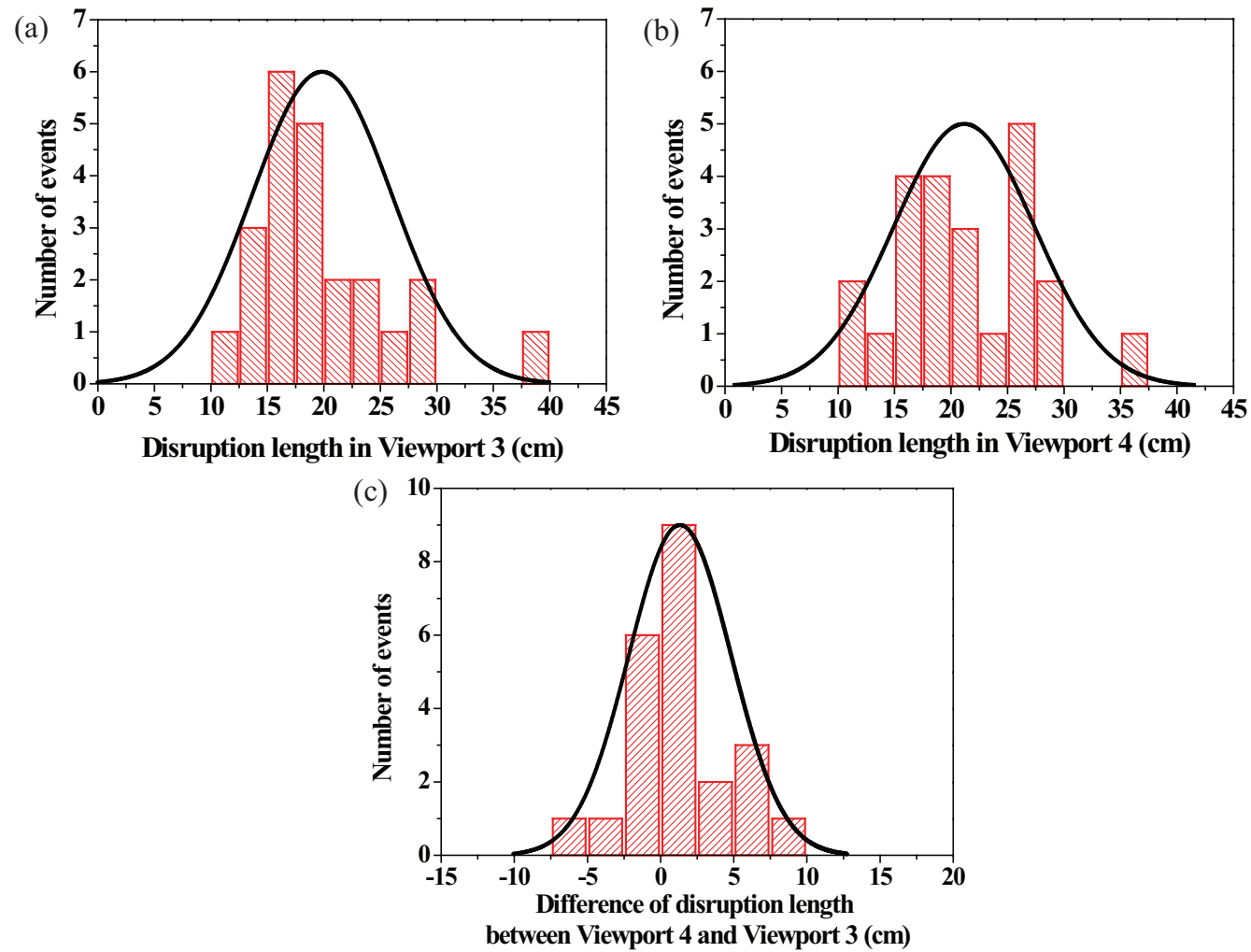
Figure 5.22: Validation of disruption measurement for the evaluation of evolution of disruption length from Viewport 3. a) Disruption length at Viewport 3. b.) Disruption length at Viewport 4. c.) Difference of the disruption length at Viewport 3 and Viewport 4.
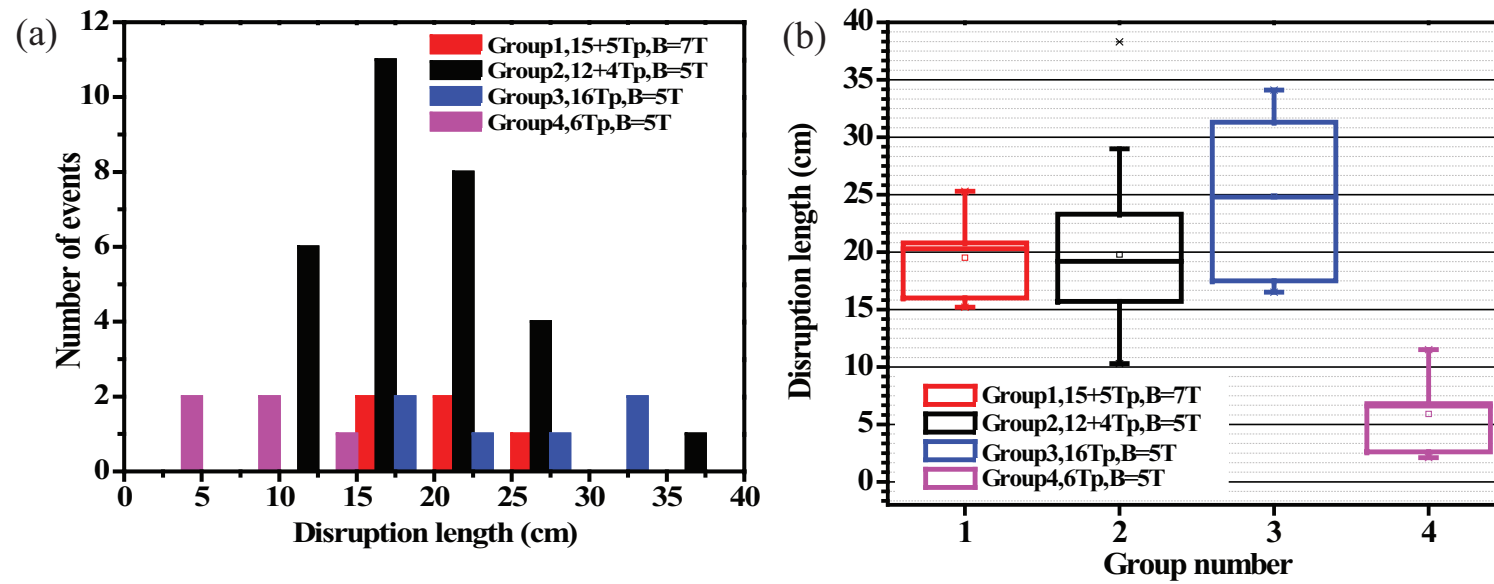
Figure 5.23: Disruption length distribution measurement in a same condition. Pump probe conditions with harmonic 8 and 16 bunches are used.
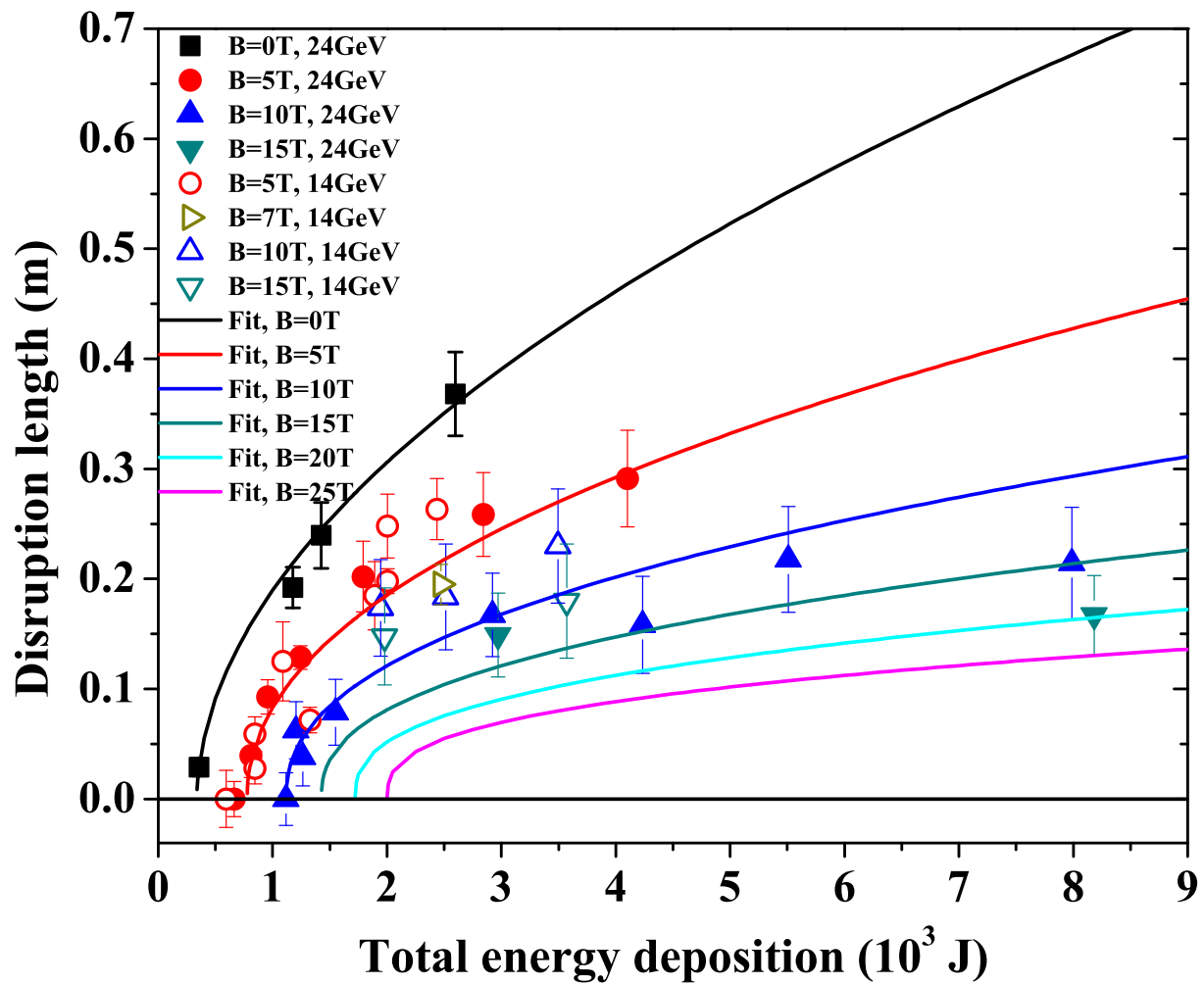
Figure 5.24: Disruption of mercury jet in magnetic fields as a function of total energy deposition and its extrapolation.

Chapter 6

Mercury Jet Surface Development in Magnetic Field

In this chapter, the motions of filaments emanating from jet surface caused by disruption in magnetic field are investigated. The energy deposition induced by the proton beam generates filaments on the Hg jet surface due to thermal stresses. The filaments velocity leaving from the jet surface and the effect of magnetic field to it are discussed. It explains that the joule damping dissipates the kinetic energy on a time scale of joule damping term.

6.1   Filament Model on Jet Surface

6.1.1   Geometry of viewing mercury filaments

It is investigated (McDonald, 2009) that the observed motion of filament by images has geometric relation with the viewing angle by focal length in optics. The filaments ejected from mercury jet by the proton beam interaction are viewed via shadow photography from a focal length $f = 9.15$ cm from the center of the jet. The jet is supposed to have elliptical cross section. The schematic geometry of viewing mercury filaments is shown in Fig. 6.1. The

2957   measurements describes the projection $y_m(t)$ onto the y axis of a ray from

2958   the observer to the surface. McDonald (2009) assumes that the filaments

2959   leave perpendicularly as shown in Fig. 6.1. The elliptic expression is given as

2960   Eqn. (6.1).

2961

2962
$$\frac{x^2}{a^2} + \frac{y^2}{b^2} = 1, \tag{6.1}$$

2963   where the jet is circular with radius b if $a = b$. Suppose a filament leaves

2964   the surface with velocity v_o at time t_o from point (x_o, y_o), at time $t > t_o$, the

2965   travel distance d is then $v_o(t - t_o)$ assuming that the velocity is constant. The

2966   position of the filament is $x_d = x_o + d\sin(\theta)$, $y_d = y_o + d\cos(\theta)$. Using the

2967   trigonometric notation of slope at point (x_o, y_o), the position of the filament,

2968 y_m, as projected onto the y axis is

2969

$$y_m = y_d \frac{f}{f - x_d} \approx y_d(1 + \frac{x_d}{f})$$

2970
$$= b\cos\theta + v_o(t - t_o)\cos\theta + \frac{[a + v_o(t - t_o)][b + v_o(t - t_o)]}{2f}\sin 2\theta. \tag{6.2}$$

2971   Thus, the apparent velocity of the filament along y axis is

2972

2973
$$v_m = \frac{dy_m}{dt} \approx v_o[\cos\theta + \frac{a + b + 2v_o(t - t_o)}{2f}\sin 2\theta]. \tag{6.3}$$

2974   The earliest time t_{om} that a filament can be seen vis projected shadow

2975   photography when $y_m = b$ is given as

2976

2977
$$t_{om} \approx t_o + \frac{b(1 - \frac{v_m}{v_o})}{v_m} \tag{6.4}$$

and

$$v_m \approx \frac{v_o}{1 + v_o \frac{(t_{om} - t_o)}{b}}. \tag{6.5}$$

6.1.2 Distribution of filaments on jet surface

McDonald (2009) suggested three cases of possible distribution of filaments on the jet surface, which can indicate the probable existence of filaments in observation depending on the assumed orientation of the filaments. First, in case that the filaments are distributed uniformly in angle θ, the probability of the existence of the filaments is

$$P(\theta)d\theta = \frac{d\theta}{2\pi}. \tag{6.6}$$

Second, in case that the filaments are distributed uniformly in angle θ, the probability of the existence of the filaments is

$$P(\theta)d\theta = \frac{d\phi}{2\pi} = \frac{ab}{a^2 \sin^2 \theta + b^2 \cos^2 \theta} \frac{d\theta}{2\pi}. \tag{6.7}$$

Third, in case that the filaments are distributed uniformly in position s around the circumference C of the ellipse, the probability of the existence of the filaments is

$$P(\theta)d\theta = \frac{ds}{C} \approx \frac{2\sqrt{a^2 \cos^2 \theta + b^2 \sin^2 \theta}}{3(a+b) - \sqrt{(3a+b)(a+3b)}} \frac{d\theta}{2\pi}. \tag{6.8}$$

182

6.1.3 Approximation of filaments velocity

Sievers and Pugnat (2000) reported the response of solid and liquid target to rapid heating by the incident proton beam. The parabolic radial energy deposition density E_{beam} is considered, dropping to 0 at the outer radius $a = 1$ cm as follow :

$$E_{beam} = E_o[1 - (r/a)^2].\tag{6.9}$$

The increase in temperature causes pressure rise. It is assumed that the rise time for the temperature is of the same order of magnitude with the beam energy deposition, 10^{-9} s, thermal expansion is initially prevented by the mass inertial of the material. From the definition of bulk modulus K, the resulting instantaneous thermal pressure for mercury is

$$\Delta p(r) = K\alpha_v\Delta T(r).\tag{6.10}$$

If the thermal heating occurs very slowly comparable to the material's dynamic frequency, it would correspond to quasi-static thermal expansion. It is believed that the energy stored in the material due to the initial thermal expansion may be converted into kinetic energy bombarding the liquid flow away. Corresponding to the thermal expansion caused by the pressure rise, strain energy is stored in the liquid flow due to the compression, which is expressed as

$$\frac{E_c}{V} = \frac{K(\alpha_v \Delta T(r))^2}{2},$$ (6.11)

where E_c represents the converted beam energy. The order of the velocity with which the boundary of the liquid material is given by the thermal expansion at the boundary divided by the time over which the sound travels across the radius of the jet, which is in units of $c\alpha_v T_o$. The pressure and the velocity at the boundary are reduced by extending the time of heating, which depends on the compressibility like

$$p \sim \frac{1}{\kappa} \quad , \quad v \sim \frac{1}{\sqrt{\kappa}},$$ (6.12)

where κ is the compressibility of material.

6.2   Observation of Filaments Development on Mercury Jet Surface

6.2.1   Image calibration

6.2.1.1   *image calibration with proton beam arrival signal*

In order to investigate the time response of filaments, we need to establish the accuracy and calibration of the measurement based on the experimental setup. Fig. 3.6 shows the traced signals on an oscilloscope when the beam and the beam triggering are delivered. The scintillating fiber signal gives the beam arrival time. Therefore, it is possible to set up the trigger timing for the cameras and laser driver inputs, which is $\sim 2~\mu$s after the master electronic

triggering signal from the proton synchrotron. Therefore, the first image of the SMD camera tells the status of jet for the time before the beam arrives since the exposure time of SMD camera is 150 ns. All of the electronic delays including the cable delays are less than 1 μs. The maximum frame rate of SMD camera is up to 1 MHz. The accuracy of camera frame rate is checked by using laser pulses. Laser pulses with certain periods are generated and then monitored at oscilloscope through photodiode. The frame rate of camera is set at the corresponding values of laser pulse period. The frame rate is checked by monitoring the variation of intensity of image captured from camera, which is judged as negligibly uniform.

6.2.1.2 *time delay structure of proton beam to light source triggering*

Fig. 6.2 shows the time structures between freezing image after laser enabling and proton beam arrival. Fig. A.1 shows the specifications of 25 W laser, where the response time to reach the peak laser, wavelength of laser, and optical power for various pulse rates are shown (Tsang, 2006). Laser emits ~ 250 ns after receiving the 16 pulse trigger from the pulse generator. The time of flight of light to the primary vessel is ~ 60 ns. Once the light source arrives at the primary vessel, the freezing image of mercury jet flow is instantaneously generated and it is then transmitted through the optical fiber corresponding to the light speed ~ 4 ns/m, where ~ 60 ns is taken for the used imaging fiber length. From the traced signals in Fig. 3.6, the proton beam arrival time is measured. Considering the time of flight from primary

185

3063 vessel through scintillating fiber, ~ 60 ns delay is estimated, so that the time

3064 delay between the 1st acquired image and the actual proton beam arrival is

3065 given as $T_3 - T_2$ in Fig. 6.2, which is considered for the velocity analysis of

3066 filaments.

3067 6.2.2 Parameter optimization with uncertainty

3068 6.2.2.1 *linear curve fit for estimation of model*

3069   Selecting a model of the right form to fit a set of data requires the use of

3070 empirical evidence in the data, knowledge of the process and some trial-and-

3071 error experimentation. Much of the need to iterate stems from the difficulty

3072 in initially selecting a function that describes the data well. Some scientific

3073 theory describing the mechanics of a physical system provide a functional form

3074 for the process, which type of function makes an ideal starting point for model

3075 development. So, a practical approach is to choose the simplest possible func-

3076 tions that have properties ascribed to the process. Complex models are fine,

3077 but they should not be used unnecessarily. Fitting models that are more com-

3078 plex than necessary means that random noise in the data will be modeled as

3079 deterministic structure. This will unnecessarily reduce the amount of data

3080 available for estimation of the residual standard deviation, potentially increas-

3081 ing the uncertainties of the results obtained when the model is used. Numerical

3082 methods for model validation, such as R^2 statistic, are useful. Graphical meth-

3083 ods have an advantage over numerical methods for model validation because

3084 they illustrate a broad range of complex aspects of the relationship between

186

3085   the model and the data. Numerical methods tend to be focused on a particular

3086   aspect of the relationship between the model and the data and try to compress

3087   that information into a single descriptive number. The residuals from a fitted

3088   model are the differences between the responses observed at each combination

3089   values of the explanatory variables and the corresponding prediction of the

3090   response computed using the regression function.

3091   The linear regression model is

3092

3093
$$\mathbf{Y} = f(\mathbf{X}, \Theta) + \epsilon, \tag{6.13}$$

3094   where $\mathbf{X} = (x_1, x_2, \ldots, x_m)$ are independent variables and $\Theta = (\Theta_1, \Theta_2, \ldots, \Theta_k)$

3095   are parameters and ϵ is the random error assuming the mean is equal to 0 with

3096   normal distribution, where k is the degree. A measure of the quality of non-

3097   linear fitting parameters is the chi-square value :

3098

3099
$$\chi^2 = \sum_{i=1}^{n} w_i (y_i - \hat{y}_i)^2, \tag{6.14}$$

3100   where w_i is the weighting coefficient, y_i are the experimental data points,

3101   and $\hat{y}_i$ are the theoretical points. To fit the model, the residual is defined as

3102

3103
$$r_i = y_i - \hat{y}_i. \tag{6.15}$$

3104   It conforms to a normal distribution with the mean equal to 0 and the vari-

3105   ance equal to σ_i^2. Then the maximum likelihood estimates of the parameters

3106 Θ_i can be obtained by minimizing the chi-square value , defined as

$$\chi^2 = \sum_{i=1}^{n} \frac{(y_i - \hat{y}_i)^2}{\sigma_i^2}. \tag{6.16}$$

If the error is treated as weight, $w_i = \frac{1}{\sigma_i^2}$ can be defined in the chi-square minimizing equation, where σ_i are the measurement errors. The quality of regression can be measured by the coefficient of determination, R^2, which is defined as

$$R^2 = 1 - \frac{w_i(y_i - \hat{y}_i)^2}{\sum_i^n (y_i - \bar{y})^2}. \tag{6.17}$$

In order to express the relationship between independent variables and dependent variables and a degree of confidence in regression model, the adjusted R^2 for validation of goodness of fit measurement is defined as

$$\bar{R}^2 = 1 - \frac{\frac{w_i(y_i - \hat{y}_i)^2}{n^* - k}}{\frac{\sum_i^n (y_i - \bar{y})^2}{n^*}}. \tag{6.18}$$

Note that if intercept is included in the model, the degree of freedom is $n^* = n - 1$. Otherwise, $n^* = n$. The adjusted R^2 will avoid the effect of the degrees of freedom by adding variables in the model, which results in rising of R^2. Therefore, the adjusted R^2 overcomes the rise in R^2 when fitting a small sample size by multiple predictor model.

The covariance value indicates the correlation between two variables, and the matrices of covariance in regression show the inter-correlations among all parameters. The correlation matrix rescales the covariance values. The covariance matrix of the regression and correlation between parameters are

defined as

$$Cov\ (\Theta_i, \Theta_j) = \sigma^2 (X'\ X)^{-1} \tag{6.19}$$

and

$$Cov\ (\Theta_i, \Theta_j) = \frac{Cov\ (\Theta_i, \Theta_j)}{\sqrt{Cov\ (\Theta_i, \Theta_i)}\sqrt{Cov\ (\Theta_j, \Theta_j)}}. \tag{6.20}$$

Parameter errors are equal to the square root of the covariance matrix diagonal values.

6.2.2.2 *Levenberg-Marquardt minimization*

To estimate the $\hat{\Theta}$ value with the least square method, we need to solve the normal equations which are set to be zero for the partial derivatives of χ^2 with respect to each $\hat{\Theta}_p$:

$$\frac{\partial \chi^2}{\partial \hat{\Theta}_p} = 0. \tag{6.21}$$

Employing an iterative strategy to estimate the parameter values, it starts with some initial values Θ_o. With each iteration, χ^2 value is computed and then the parameter values are adjusted to reduce the χ^2. When χ^2 values computed in two successive iterations are small enough compared with the tolerance, the fitting is converged. The Levenberg-Marquardt algorithm is employed for an iterative technique that locates a local minimum of a multivariate function that is expressed as the sum of squares of nonlinear function. Levenberg-Marquardt is considered as a combination of steepest descent and the Gauss-

189

3151 Newton method. When the solution is far from a local minimum, the algorithm

3152 behaves like a steepest descent method. When the solution is close to a local

3153 minimum, it becomes a Gauss-Newton method and exhibits fast convergence.

3154 Given the residuals r_i $(i = 1, \ldots, n)$ of parameters $\Theta = (\Theta_1, \Theta_2, \ldots, \Theta_p)$

3155 , with $n \geq k$, the Gauss-Newton algorithm finds the minimum of χ^2 given

3156 in Equation (6.16). Starting with an initial guess Θ_o for the minimum, the

3157 method proceeds by the iteration $\Theta^{s+1} = \Theta^s + \delta\Theta$ with an increment $\delta\Theta$

3158 satisfying the normal equation given as Equation (6.22) using Equation (6.21).

3159

3160
$$(\mathbf{J}_r^T \mathbf{J}_r)\delta\Theta = -\mathbf{J}_r^T \mathbf{r}, \tag{6.22}$$

3161 where $\mathbf{r}$ is the vector of r_i and $\mathbf{J}_r$ is the Jacobian of $\mathbf{r}$ with respect to Θ.

3162 The residuals r_i are defined as $r_i(\Theta) = y_i - f(x_i, \Theta)$. In order to find the

3163 parameters Θ that a given model function $y = f(x, \Theta)$ fits best data points,

3164 the increment $\delta\Theta$ can be expressed in terms of Jacobian of the function as

3165 follow:

3166

3167
$$(\mathbf{J}_f^T \mathbf{J}_f)\delta\Theta = \mathbf{J}_f^T \mathbf{r}, \tag{6.23}$$

3168 The Levenberg-Marquardt iteration is a variation on the Newton iteration.

3169 The normal equations $\mathbf{N}\delta\Theta = \mathbf{J}_f^T \mathbf{J}_f = \mathbf{J}_f^T \mathbf{r}$ are augmented to $\mathbf{N}'\delta\Theta = \mathbf{J}_f^T \mathbf{r}$

3170 where $N'_{ij} = (1 + \delta_{ij} \lambda) N_{ij}$ with δ_{ij} the Kronecker delta. The λ is initialized

3171 to a small value, e.g. 10^{-3}. If the value obtained for $\delta\Theta$ reduce the residuals,

3172 the increment is accepted and λ is divided by 10 before the next iteration. If

3173 the residuals increase then λ is multiplied by 10 and the augmented normal

equations are solved again until an increment is obtained that reduces the residuals. For large λ, the iteration approaches a steepest descent.

6.2.3 Filaments distribution and uncertainty of measurement

6.2.3.1 *onset of filamentation on jet surface*

Fig. 6.3 shows photographs of filament evolution on the Hg jet surface at 25 μs frame rate, where the beam is 10 Tp, 24 GeV and the magnetic field is 10 T. Fig. 6.4 shows the locations of filaments where the individual velocity is measured as a function of time, shown in Fig. 6.6, Fig. 6.7 (a), (b). The first collected image among 16 images is brighter than the rest of 15 images. It indicates that the radiation generated by the interaction of Hg with proton beam affects the transmittance and/or reflectance of optical components, resulting in the production of darker images as one sees at the rest of collected 15 images.

6.2.3.2 *measurement of traveled distance of filament*

To obtain the vertical filament velocity, the distance traveled by a fixed point on the jet surface is tracked over a given time period. The jet volume, where the maximal energy is deposited, results in the initial generation of the filaments. The higher jet velocity occurs when the filaments is initially protruded out of the jet surface and then the jet velocity decreases due to the magnetic damping and viscous dissipation. So, the velocity at steady state is obtained in order to evaluate the relationship with the beam intensity and

191

3196 magnetic field.

3197   The quality of optical images varies from shot to shot since the radiation or
3198 jet dispersion may make image quality varies. The most difficulty in measure-
3199 ment is to discern the edge of filaments as it moves somewhat far away from
3200 surface because the initial jet filament edge is dense(clearly black) but it looks
3201 like dissipating, dilute, disappearing (grey or similar with background) as it
3202 moves further. Because measurement is done in several points, there may be
3203 some error in measurement after some steady velocity(constant peak velocity)
3204 at weak filament velocity measurement.

3205   The image size at Viewport 2 is 240 by 240. Using graphic software, pixels
3206 on image is picked to locate the edge of filament. Therefore, the uncertainty
3207 while locate the position y_m is reported to be $\pm$ 2 pixels, which corresponds
3208 to the difference of $\sim \pm 17$ m/s filaments velocity. This uncertainty can occur
3209 randomly uniformly. The peak strong filament which gives constant velocity
3210 within $\pm$ 2 pixels until the end of 15 frames is assumed to be considered as there
3211 is constant uncertainty, $\pm$ 2 pixels. The weak filament which gives constant
3212 velocity within $\pm$ 2 pixels until the filament reaches some frames, for example, 3
3213 $\sim$ 7 frames, is also assumed to be considered as there is constant uncertainty,
3214 $\pm$ 2 pixels, where the black edge of filament is clearly observed. However,
3215 after the some frames, for example, 3 $\sim$ 7 frames, because the original edge
3216 of filament dilute or dissipates or disappear, the uncertainty in measurement
3217 may not be constant. In this case, measurement is stopped at that frames.

192

6.2.4 Linear regression with the first order polynomial

6.2.4.1 *curve fit function*

The heaviside step function is defined as the integral of the Dirac delta function as follow:

$$H(t) = \int_{-\infty}^{t} \delta(\xi)d\xi. \tag{6.24}$$

The ramp function is the antiderivative of the Heaviside step function:

$$R(t) = \int_{-\infty}^{t} H(\xi)d\xi = tH(t). \tag{6.25}$$

In discrete form, it is now defined as an alternative form for our linear regression model as follow:

$$R(t) = \begin{cases} y_m = s, & t \leq t_o \\ y_m = s + v(t - t_o), & t > t_o \end{cases}, \tag{6.26}$$

where y_m, s, v, t_o denote the measured position of the filament as projected onto the y axis in image, the position of jet surface before the filaments developed, the apparent velocity of the filament along the y axis, and onset time delay of filaments respectively.

6.2.4.2 *parameter estimation using multiple position of filaments*

Shot 11019 is chosen for illustration. Using Equation (6.26) for linear regression model with measured data points y_m and t, minimizing R^2 yields s, v, and t_o. Fig. 6.5 (a) shows the illustration of multiple data points where

193

3239 the intercept of x axis and slope approximate the onset time of filament and

3240 apparent velocity projected on y axis in image, which are $t_o = 43.6 \pm 4.5$ μs

3241 and $v = 55.5 \pm 0.8$ m/s respectively. The reduced R^2 value and adjusted $\bar{R}^2$

3242 values are 1.749 and 0.998 respectively. Based on Eqn. (6.26), the fit to data

3243 points is as follows:

3244

3245
$$y = C_1(x - B_1) + A_1, \tag{6.27}$$

3246 where x and y denote the measured position of the filaments and time

3247 respectively. Note the parameterized values of coefficients and error values to

3248 fit function are given in Table 6.1.

3249 In case of larger velocity of filaments, maximally measurable data points are

3250 limited to $\sim 2 \sim 3$ points due to the limited field of view in optical diagnostic

3251 image. Fig. 6.5 (b) shows the illustration of 3 data points. The onset time

3252 from regression model yields underestimated value such as negative time delay

3253 because the data points are equal or smaller than the number of parameters

3254 in fit function. Thus, assumption is that the real onset time for such a large

3255 velocity should be between typical onset time 50 μs and 0 μs, which yields the

3256 onset time of 25 ± 25 μs. Therefore, the slope of fit curve is determined by

3257 fixing the assumed onset time accordingly, which yields the filament velocity

3258 of 148 ± 24.5 m/s. The error is determined directly by dividing approximated

3259 filament velocity of the cases of $t_o = 0$ and $t_o = 50$ μs by 2. The shot 10008

3260 is chosen for the illustration of parameter estimation of 3 data points. The fit

3261 to data points is as follow:

$$y = C_1 x + A_1 \qquad\qquad (6.28)$$

for the case of negative onset time (black solid line) in Fig. 6.5 (b), and Eqn. (6.27) is employed for the case of having fixed $B_1 = 0$ μs and $B_1 = 50$ μs onset time (blue and red solid line) in in Fig. 6.5 (b). As one expects, this approach for a special case yields large uncertainty.

6.2.4.3 *filaments velocity distribution on jet surface*

Fig. 6.6 (a) shows the velocity distribution of filaments over the jet surface shown in Fig. 6.3. Fig. 6.6 (b) shows the approximated onset time distribution of filaments according to the approximated velocity of filaments. As the approximated apparent velocity of filaments projected on y axis in image increases, the approximated onset time of filaments decreases. This shows the evidence of the geometric effects of viewing of filaments. Assuming the filaments are generated perpendicular to the jet surface, as the filaments leaves farther from the jet surface, it takes more time to make an initial observation in images. Thus,it is possible to consider the low velocity of filaments with large onset time leaves from more close to the center of jet normal to the side view shown in images. Note that the velocity of each filament is approximated with uncertainty by doing linear regression using the fit function in order to give one representative velocity according to each filament. Low velocity of filaments close to 0 showed larger error of approximation of onset time due to the uncertainty of the very small observed traveling distance of filaments.

3284 Each filament used for measurement of velocity in Fig. 6.3 has been num-

3285 bered in Fig. 6.4 for particular indication of each filament. According to the

3286 notation in Fig. 6.4, Fig. 6.7 (a) shows the velocity of filaments on the upper

3287 free surface of jet as a function of time and Fig. 6.7 (b) shows the velocity of

3288 filaments on the lower free surface of jet as a function of time. Note that the

3289 instantaneous velocity as defined in Equation (6.30) is used for measurement

3290 in Fig. 6.7. The onset time of filament increases as the peak velocity of fila-

3291 ment decreases, which indicates the possible evidence of the geometric effect

3292 of viewing of filaments.

6.3 Velocity of Filaments on Mercury Jet Surface

6.3.1 Magnetic dissipation of energy

3296 As a conducting liquid moves through a static magnetic field, electric cur-

3297 rents are generated. This, in turn, leads to ohmic heating such as Joule dis-

3298 sipation. As the thermal energy of the fluid rises, there is a corresponding

3299 filament in its kinetic energy, and so the fluid decelerates. This results in a

3300 suppression of the motion of liquid jets. According to P. A. Davidson's ap-

3301 proximation (1999), the Eqn. (2.42) shows the energy decay with respect to

3302 time depending on the magnetic damping time constant, where $\tau = \rho/\sigma B^2$.

3303 The implication is that the filaments decelerates on a time scale of τ. Fig. 2.3

3304 (a) shows the decay of the normalized energy of flow in magnetic fields with

3305 respect to time due to the magnetic damping. Higher magnetic field dissipates

3306 energy faster. Fig. 2.3 (b) shows the integral calculation of energy with respect
3307 to time.

6.3.2 Time response of filaments in magnetic field

6.3.2.1 *averaged time response of filament in magnetic field*

3310   Since the camera is triggered before beam arrives at the Hg jet and the
3311 laser pulse width is 150 ns, the first collected image shows the status of Hg jet
3312 before beam comes. Thus, the velocity of filament can always be judged as 0
3313 m/s in the following Fig. 6.8. Fig. 6.8 represents the time response of filament
3314 average velocity as a function of magnetic field with 14 GeV, 20 TP beam
3315 and 24 GeV, 10 TP beam respectively. The expression for the calculation of
3316 average velocity is

3317

$$v_n^{avg} = \frac{1}{T_n - T_o} \int_{T_o}^{T_n} v(t)dt = \frac{y_m(T_n) - y_m(T_o)}{T_n - T_o}, \qquad (6.29)$$

3319   where T_n, T_o denotes the time taken in each framed image and the initial
3320 time of the first image respect to the proton beam arrival time respectively.
3321 Since the joule damping dissipates the energy with an exponential factor, the
3322 energy dissipation arises rapidly in the beginning depending on the magnetic
3323 field term B^2. Thus, higher magnetic field will have higher damping effect so
3324 that it takes more rising time. Therefore, the slope of rising velocity in Fig. 6.8
3325 is varying depending on the magnetic field proportional to B^2 in exponential
3326 function. The magnitude of steady peak velocity is reduced by increased ap-
3327 plied magnetic field strength, which is possible indication of the magnetic

3328 damping role induced by the joule damping dissipation. Again, in Fig. 6.8 (a),

3329 the delay of onset time of filament causes reduced steady peak velocity in same

3330 5 T, which again indicates the fluctuation of jet flow in magnetic field and the

3331 geometric effect of viewing of filaments in shadow photography as well.

3332 #### 6.3.2.2 *instantaneous time response of filament in magnetic field*

3333 Fig. 6.9 represents the time response of instantaneous filament velocity as a

3334 function of magnetic field with 14 GeV, 20 Tp beam and 24 GeV, 10 Tp beam

3335 respectively, which are reinterpretation of Fig. 6.8 in terms of instantaneous

3336 velocity analysis. The expression for the calculation of instantaneous velocity

3337 assuming ΔT_n is small enough is

3338

3339
$$v_n = \frac{y_m(T_n) - y_m(T_{n-1})}{\Delta T_n}. \tag{6.30}$$

3340 Comparing with Fig. 6.8, the velocity of filaments are fluctuating.

3341 ### 6.3.3 Beam induced filaments velocity in magnetic field

3342 #### 6.3.3.1 *filaments velocity with 14 GeV beam in magnetic field*

3343 Fig. 6.10 (a) shows the filament velocity as a function of 14 GeV beam

3344 intensity and magnetic field corresponding to the observed onset time of fil-

3345 aments shown in Fig. 6.10 (b). Note that the data points without having

3346 onset time data is measured by crude measurement of 2 positions of filament

3347 from 500 μs frame rate shot images, where the estimation of onset time by

3348 fitting is inadequate. The filament velocity increases with the beam intensity.

3349 However, the magnetic field suppresses the filament velocity. At low inten-

3350 sity of proton beam, the charged beam may be fluctuating depending on the

3351 initial conditions at experiment. Thus, the observed onset time of filaments

3352 is large at low intensity of beam and it decreases as the intensity of proton

3353 beam increases, see Fig. 6.10 (b). Therefore, there are scattering distributions

3354 of filament velocity at lower intensity of beam over the resulting data points.

3355 The slope of the data points at higher magnetic fields decreases comparing

3356 with that associated with lower magnetic field. All velocities are less than 50

3357 m/s regardless of the magnetic field. The filament velocity at 14 GeV, 30 Tp,

3358 10 T is $\sim$ 30 m/s.

3359 **6.3.3.2** *filaments velocity with 24 GeV beam in magnetic field*

3360 Fig. 6.11 (a) shows the filament velocity as a function of 24 GeV beam

3361 intensity and magnetic field corresponding to the observed onset time of fil-

3362 aments shown in Fig. 6.11 (b). Again, at low intensity of proton beam, the

3363 charged beam may be fluctuating depending on the initial conditions at exper-

3364 iment. Thus, the observed onset time of filaments is large at low intensity of

3365 beam and it decreases as the intensity of proton beam increases, see Fig. 6.11

3366 (b). The filament velocity increases with the beam intensity. The slope of

3367 the increase is $\sim 4 \times$ larger that that for the 14 GeV case, where the ratio

3368 of peak energy deposition between 14 GeV and 24 GeV beam energy is ~ 2.3

3369 based on the calculation given in Fig. 5.13 (a). It implies the relationship of

3370 peak energy deposition to maximum filament velocity. However, the magnetic

3371   field suppresses the filament velocity. At relatively low intensity of beam as in

3372   the 14 GeV case, the charged beam is unstably fluctuating depending on the

3373   event conditions at experiment. Thus, the observed onset time of filaments is

3374   large at low intensity of beam and it decreases as the intensity of proton beam

3375   increases, see Fig. 6.11 (b). All velocities are less than 180 m/s regardless of

3376   the magnetic field, and the filament velocity for the 24 GeV, 30 Tp, 15 T is $\sim$

3377   60 m/s.

6.3.3.3   *filament velocity measurement in pump probe condition as a check of experiment*

3380   Fig. 6.12 shows the measured filament velocity of multiple events with

3381   pump probe conditions as a check of experiment. The conditions of each

3382   group in pump probe events are given in Table A.3. There are 2 groups at 14

3383   GeV and each group has different number of bunches and time delay between

3384   pump and probe. Fig. 6.12 (a) shows the histogram of disruption length and

3385   Fig. 6.12 (b) shows statistics summary such as average, min/max, and median

3386   value. In group 2, qualitatively meaningful distribution of measurements are

3387   shown, which is 10.2 ± 3.6 m/s. The pump condition is meaningful due to the

3388   delay of beam delay, though there is no significant difference in sub-category

3389   of group 2. However, This check shows low velocity comparing with the results

3390   shown in Fig. 6.10 (a). One thing to evaluate is that there is another error

3391   that should be considered in filament velocity analysis, so called distribution of

3392   filament velocity under repetition with same condition of experiment. This is

3393   judged by ~ 40 % of the measured velocity, which is integrated in the following

3394   key result shown in Fig. 6.13.

6.4   Filament Velocity on Jet Surface By Peak Energy Deposition

3397   As discussed, the filament velocity ejected from jet surface is dominated by
3398   the distribution of energy deposition interacting with proton beam. The peak
3399   energy deposition plays a key role in determining the maximum filament ve-
3400   locity ejected from jet surface in viewpoint that the velocity distribution on jet
3401   surface is determined by normalization using the peak energy deposition. The
3402   peak energy deposition depending on colliding number of protons at both 14
3403   GeV and 24 GeV beam energy is calculated by Fig. 5.13 (a). Thus, Fig. 6.10
3404   and Fig. 6.11 are combined as a function of peak energy deposition, which
3405   shows the results of experiment in maximum filament velocity at a glance. As
3406   an important result for experiment, Fig. 6.13 shows the filament velocity in
3407   magnetic fields ejected from jet surface as a function of peak energy depo-
3408   sition and its extrapolation up to 25 T. Fig. 6.13 combines a key results of
3409   experiment, also provides an estimation of the filament velocity up to 25 T.
3410   The employed global fit with multi-variables for filament velocity using the
3411   measured filament velocity is

3412

$$z = A_1(x - (B_1 + B_2 y^{B_3}))^{C_1 + C_2 y + C_3 y^2}, \tag{6.31}$$

3414   where x and y are peak energy deposition and magnetic field respectively.
3415   Note that the parameterized values of coefficients and errors of the fit functions

201

3416 are provided in Table 6.1. The threshold peak energy deposition for filament

3417 velocity uses the same value with that for disruption length in order to keep

3418 consistency between the onset of disruption and filament. Note the error of

3419 each measured filament is adjusted by ~ 40 % of the measured velocity in

3420 order to expect somewhat improved fit result with reduced χ^2, as discussed

3421 previously in multiple events analysis with pump probe condition. The thresh-

3422 old of filament velocity increases in 1.4 power of magnetic field, and it is $\sim$

3423 16 J of peak energy energy deposition with no magnetic field. The filament

3424 velocity increases in linear power of peak energy deposition with no magnetic

3425 field, but it is reduced in $\sim 1.08 - 0.016B$ power of peak energy deposition

3426 with magnetic field.

3427   For muon collider in the future, higher beam intensity equivalent with

3428 80 Tp, 20 T of 24 GeV proton beam energy is required. The peak energy

3429 deposition at 80 Tp , 24 GeV is ~ 255 J. The maximum filament velocity at

3430 255 J of peak energy at 20 T is expected to be 94 m/s.

Table 6.1: Parameterized coefficients, its error, and statistics summary of fit function in figures.

Figure	1	2	3	4	5	6	7	8	9	10
6.5a	128	0.93517	43.57	4.44411	-	-	-	-	-0.26374	0.00392
6.5b(black)	112.1	-	-	-	-	-	-	-	-0.52	-
6.5b(blue)	122	0	0	0	-	-	-	-	-0.5865	0.01587
6.5b(red)	122	0	50	0	-	-	-	-	-0.81911	0.10777
6.13	1.5908	1.00492	16.2263	0	0.39275	0	1.39594	0	1.07591	0.33731

Figure	11	12	13	14	15	16	17	18	19	
6.5a	-	-	-	-	15	12	1.74908	0.99773	0.0505	
6.5b(black)	-	-	-	-	2	0	0	0	0	
6.5b(blue)	-	-	-	-	3	2	12.31396	0.99622	0	
6.5b(red)	-	-	-	-	3	2	281.74259	0.91351	0	
6.13	-0.01575	0.01702	0	0	25	22	2.15282	0.1527	0.0013	

1 : A1 value, **2** : A1 standard deviation,

3 : B1 value, **4** : B1 standard deviation, **5** : B2 value, **6** : B2 standard deviation,

7 : B3 value, **8** : B3 standard deviation , **9** : C1 value, **10** : C1 standard deviation,
11 : C2 value, **12** : C2 standard deviation, **13** : C3 value, **14** : C3 standard deviation,

15 : Number of points, **16** : Degrees of freedom, **17** : Reduced χ^2, **18** : Adjusted $\mathbf{R}^2$, **19** : χ^2 probability.
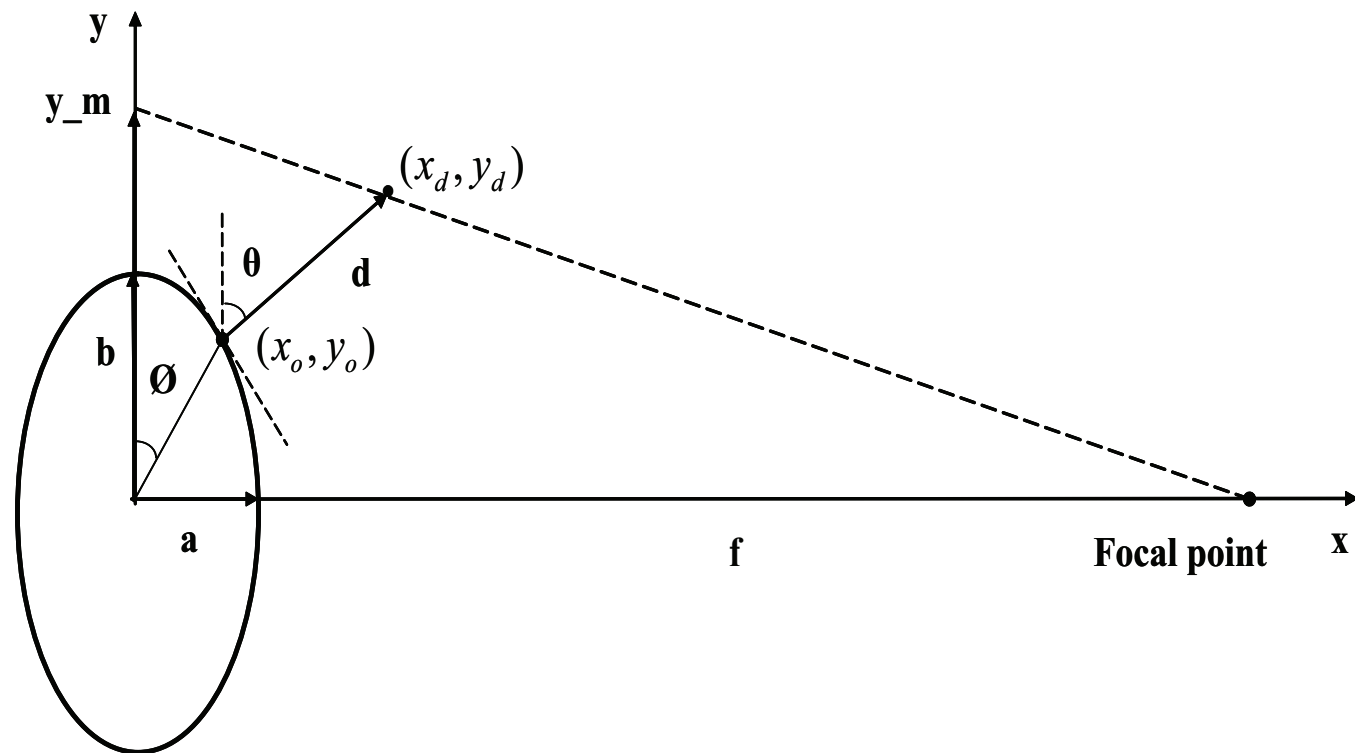
Figure 6.1: Schematic geometry of viewing mercury filaments.

Time ➤

Freeze Frame   **Beam Arrive**

T_L T_1 T_2 T_3 T_{SF}
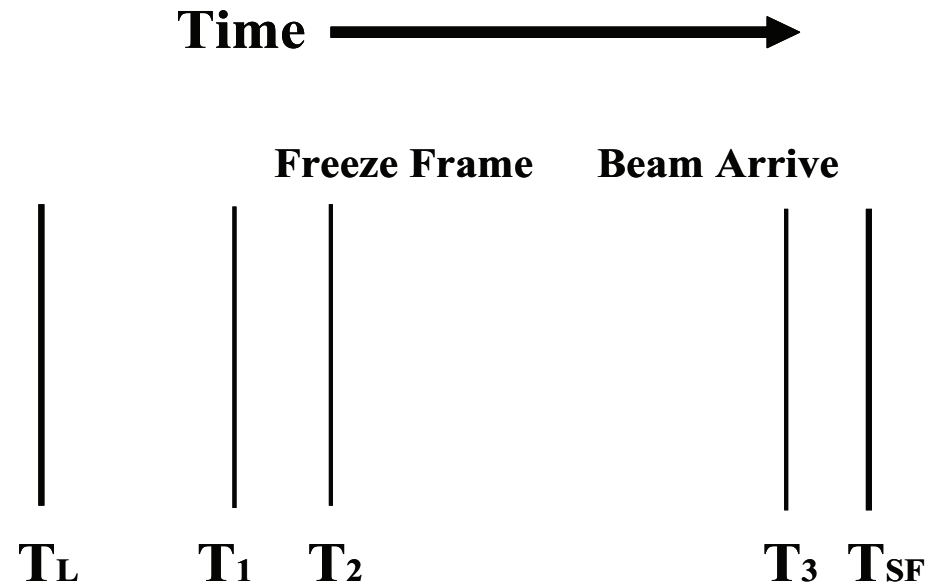
T_L : Laser Enable
T_1 : Time of Delay to Peak Laser Pulse, 250 ns
T_2 : Time of Flight to Primary Vessel, 60 ns
T_3 : Time of Flight from Primary, 60ns
T_{SF} : Scintillating Fiber Signal

Figure 6.2: Time structures between light source enabling and proton beam arrival.
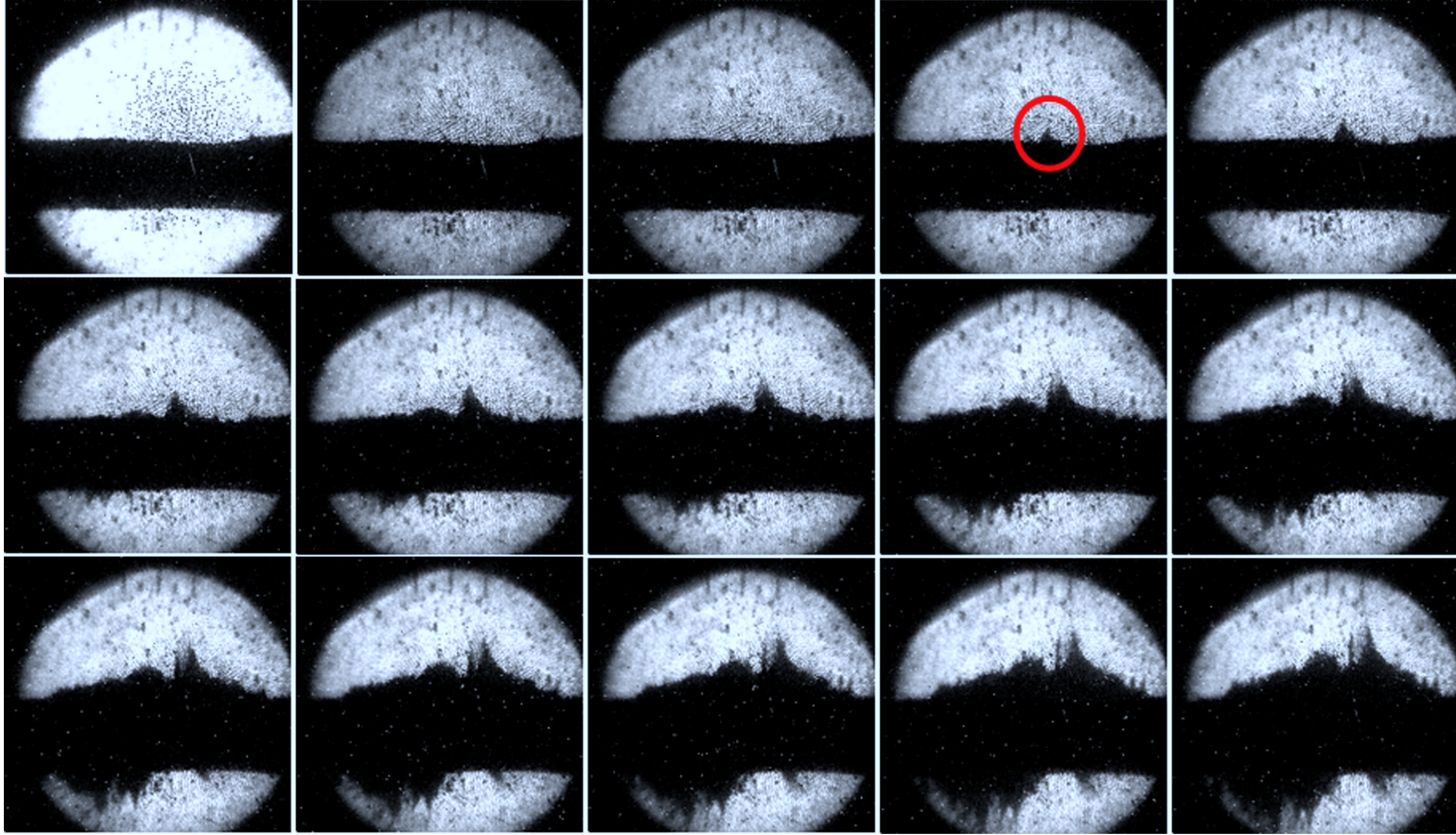
Figure 6.3: Photographs of filament evolution on the Hg jet surface as a function of time at 25 μs frame rate. The beam is 10 Tp, 24 GeV. The magnetic field is 10 T. The red circle on the 4th image of the top row points the filament that is used for velocity measurement in Fig. 6.8 (b) and Fig. 6.9 (b).
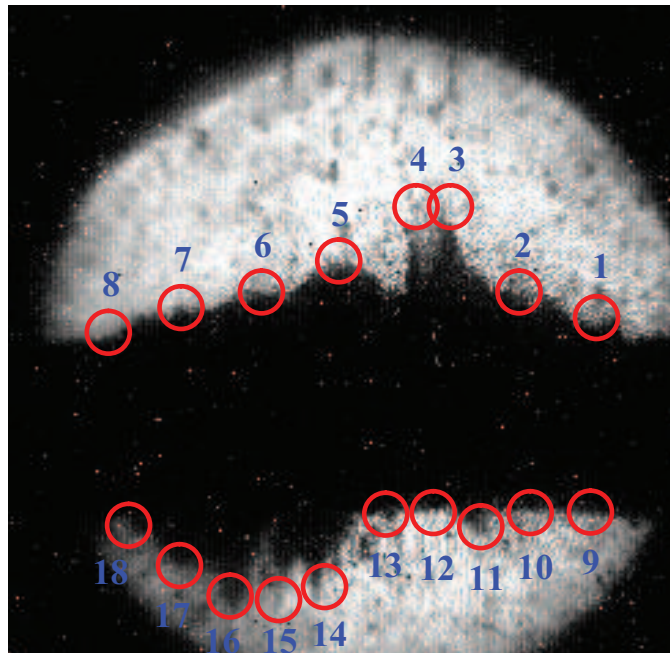
Figure 6.4: Location on the Hg jet surface for velocity measurement of 14 points of filament. The shot condition same with Fig. 6.3. The numbers above red circles points the filament that is used for velocity approximation in Fig. 6.6 and Fig. 6.7.
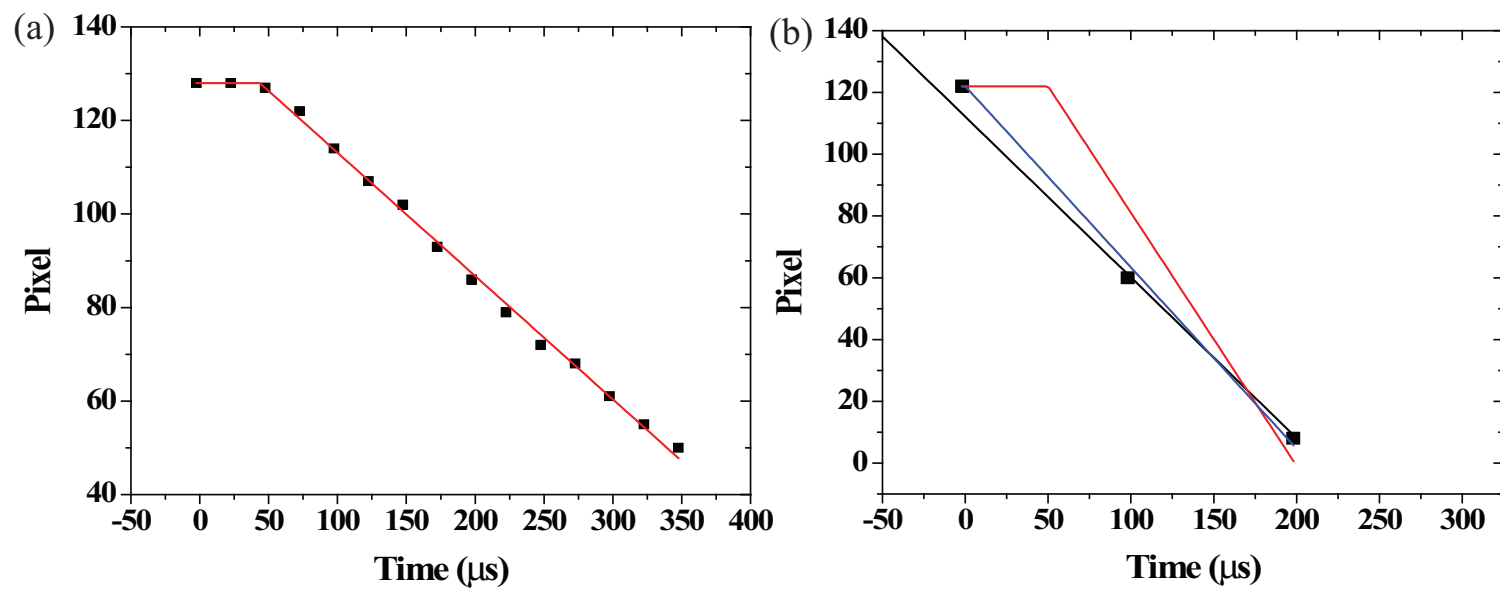
Figure 6.5: Illustration of curve fit for parameters estimation. a.) Multiple data points. b.) 3 data points.
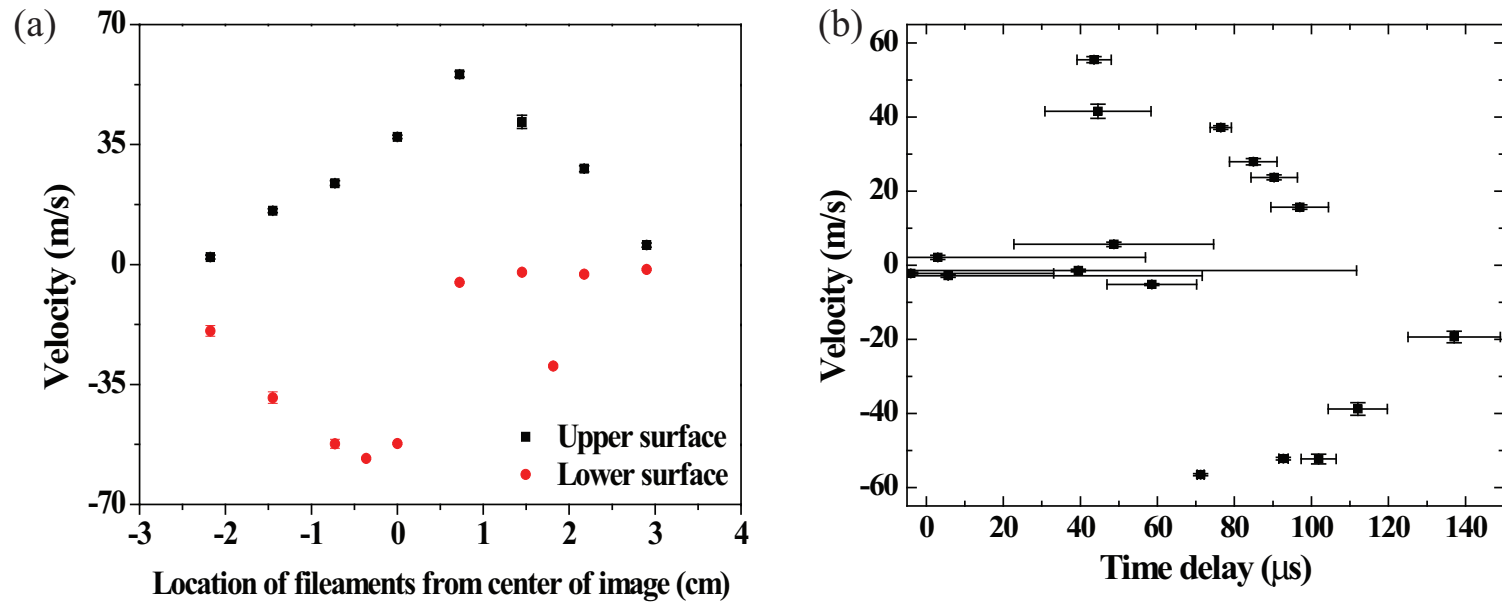
Figure 6.6: Approximation of velocity and onset time of filaments shown in Fig. 6.3. The beam is 10 Tp, 24 GeV. The magnetic field strength is 10 T. a.) Approximation of velocity of filaments. b.) Approximation of onset time of filaments.
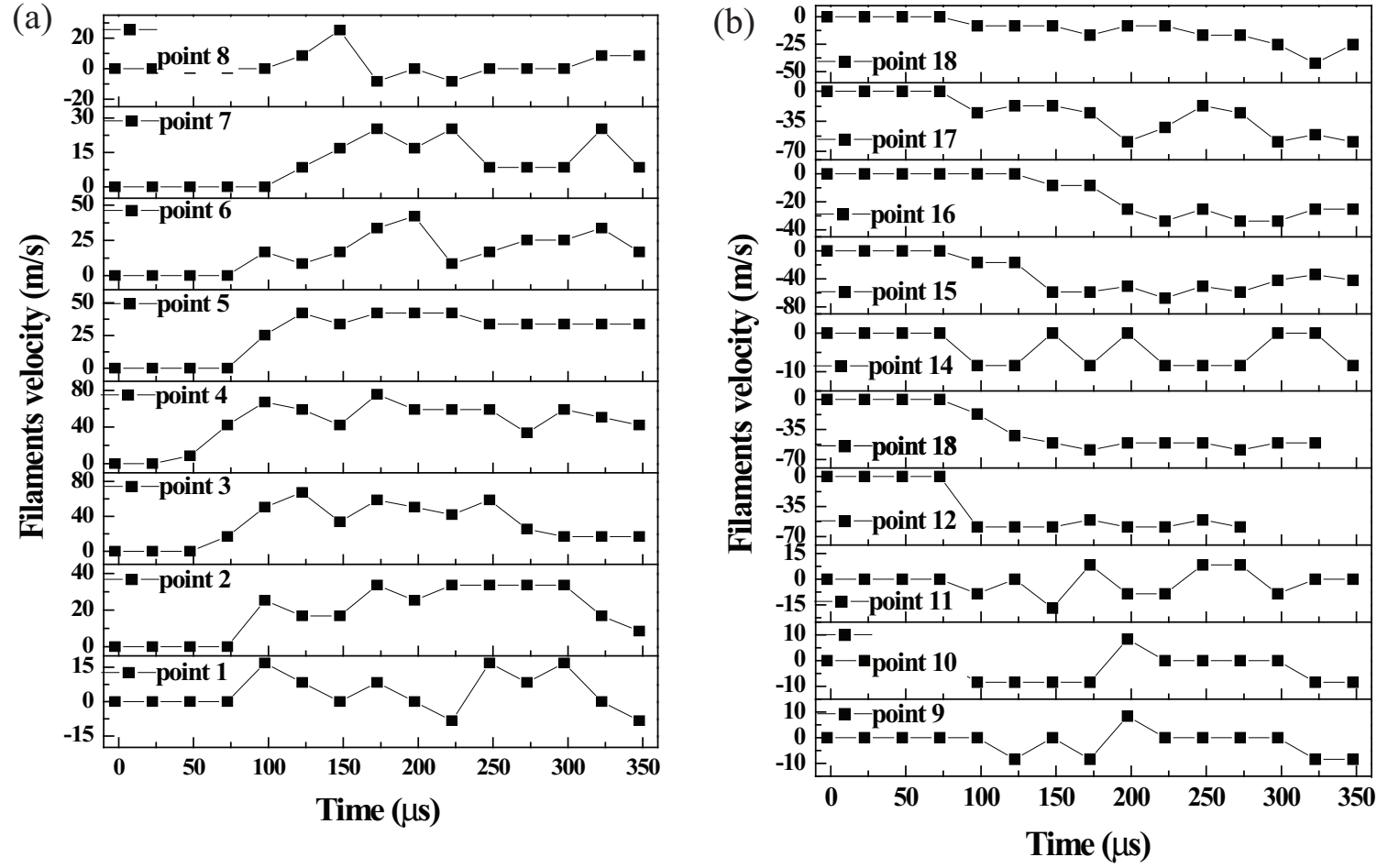
Figure 6.7: Time response of instantaneous filament velocity at jet surface in Fig. 6.3 as a function of distance from magnet center. The beam is 10 Tp, 24 GeV. The magnetic field is 10 T. a.) Upper surface. b.) Lower surface.
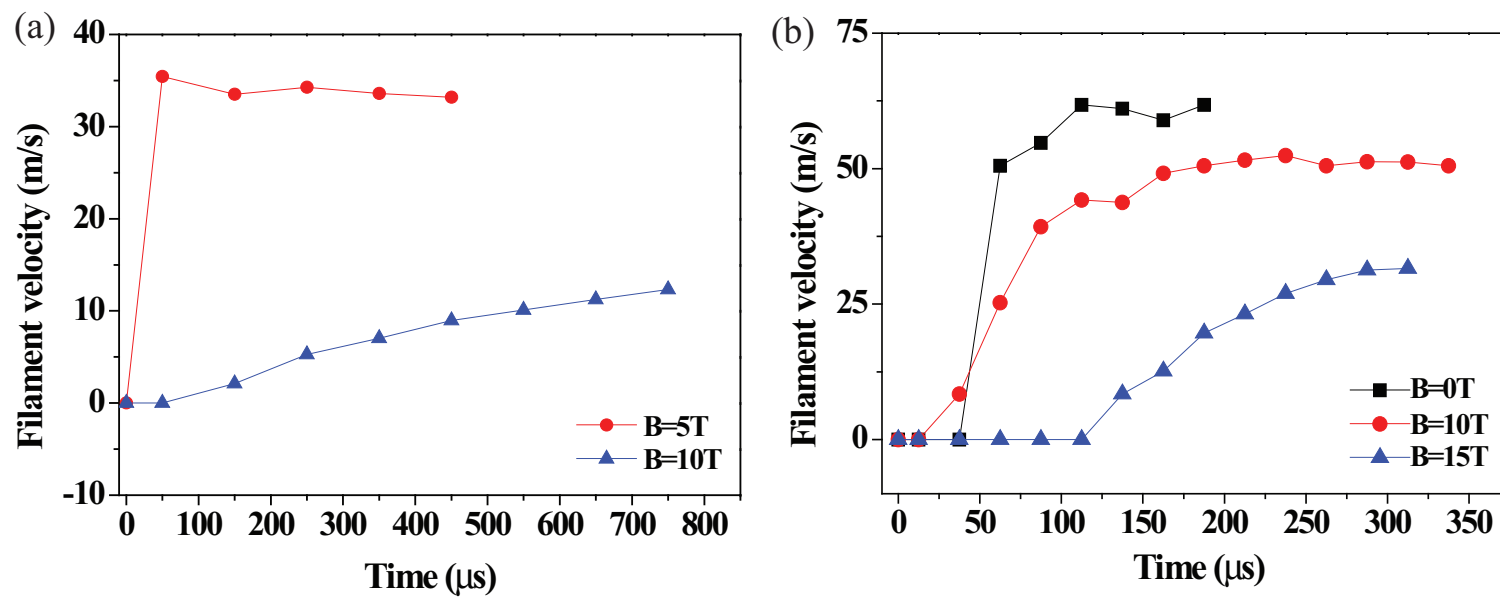
Figure 6.8: Time response of averaged filament velocity as a function of magnetic field. a.) 14 GeV, 20 Tp beam. b.) 24 GeV, 10 Tp beam.
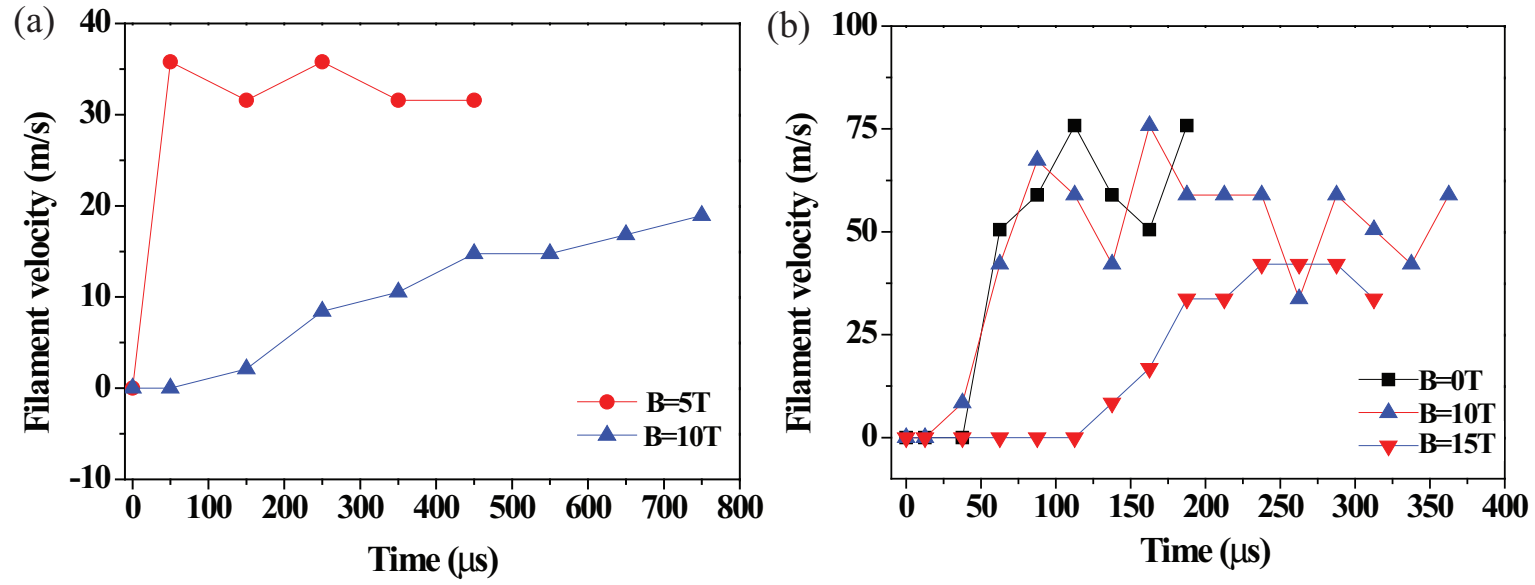
Figure 6.9: Time response of instantaneous filament velocity as a function of magnetic field. a.) 14 GeV, 20 Tp beam. b.) 24 GeV, 10 Tp beam.
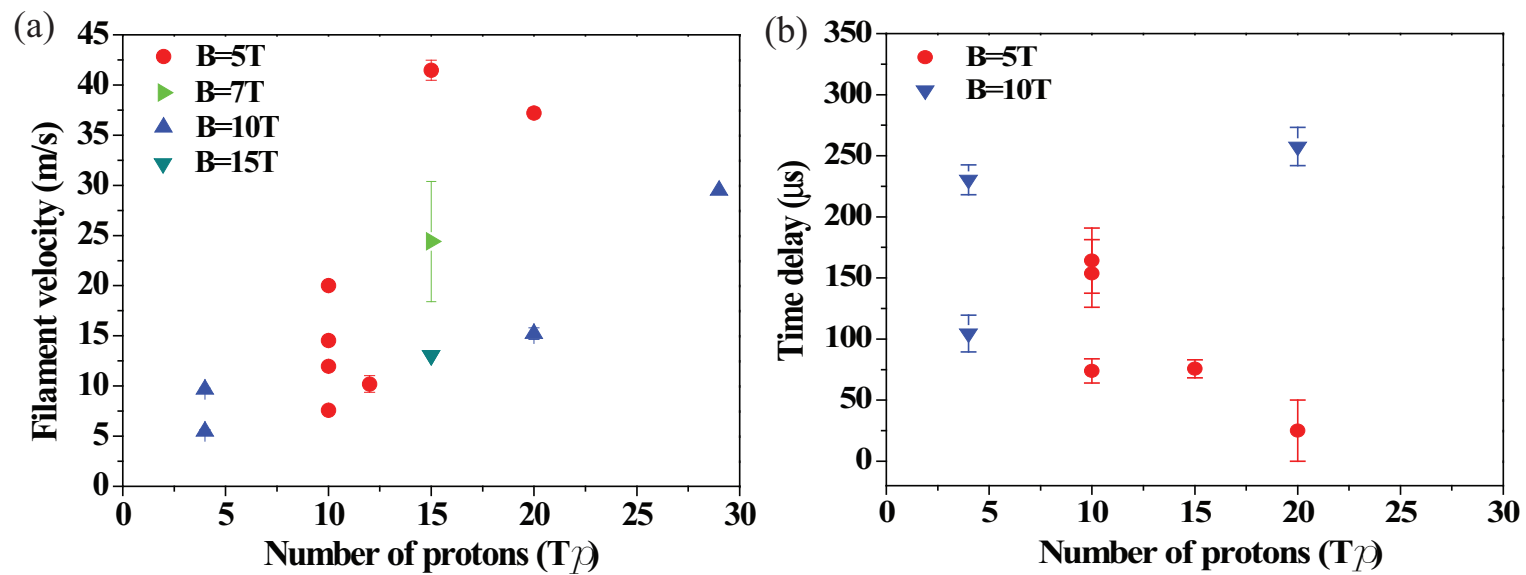
Figure 6.10: Filament velocity as a function of 14 GeV beam intensity and magnetic field. a.) Apparent filament velocity. b.) Onset time of filament.
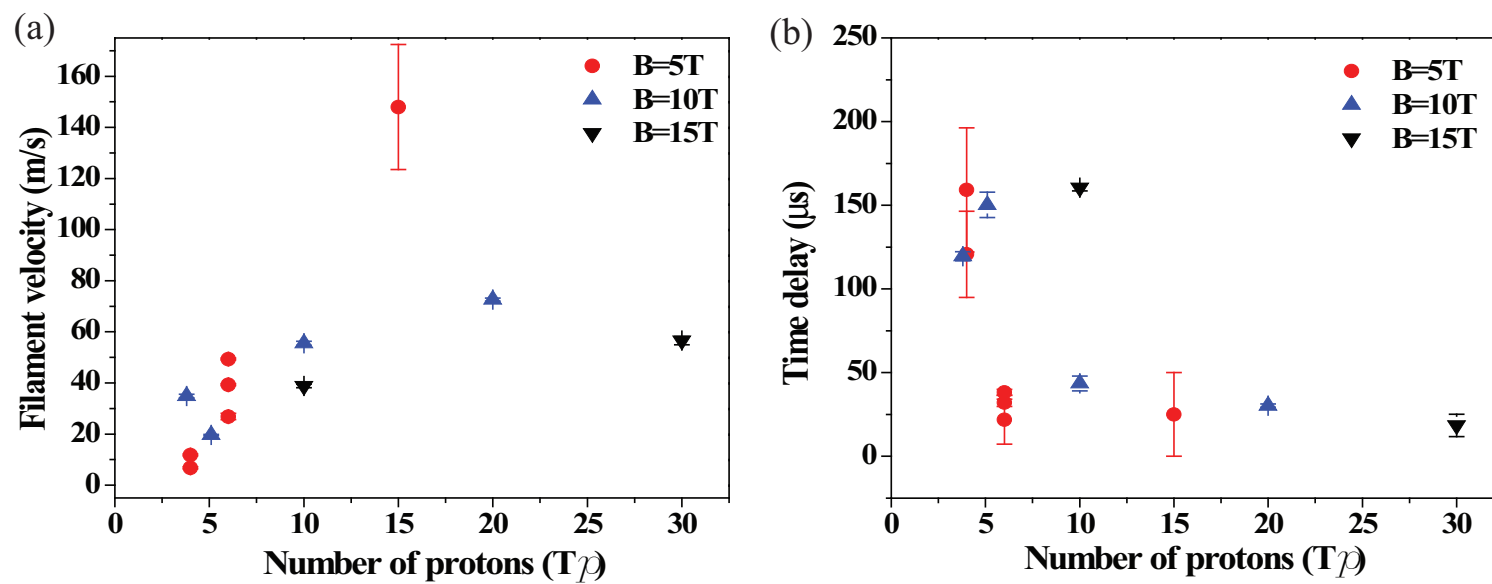
Figure 6.11: Filament velocity as a function of 24 GeV beam intensity and magnetic field. a.) Apparent filament velocity. b.) Onset time of filament.
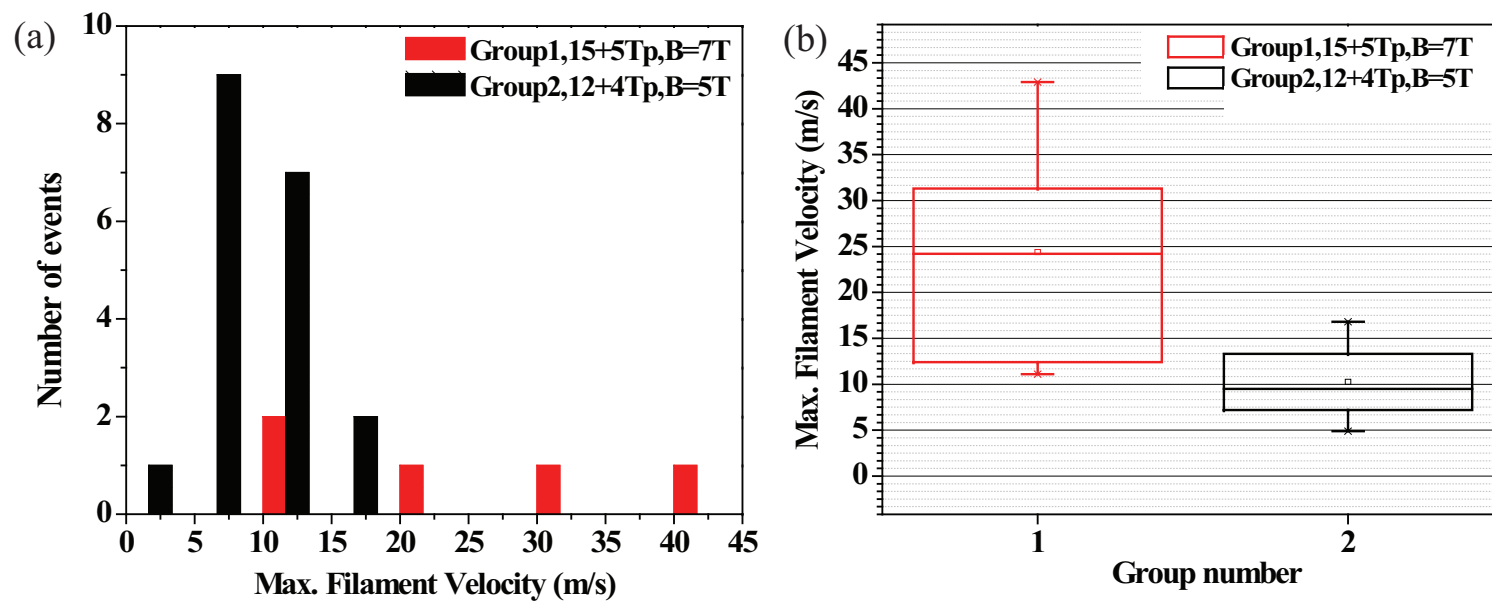
Figure 6.12: Filament velocity distribution measurement in a same condition. Pump probe conditions with harmonic 8 and 16 bunches are used.
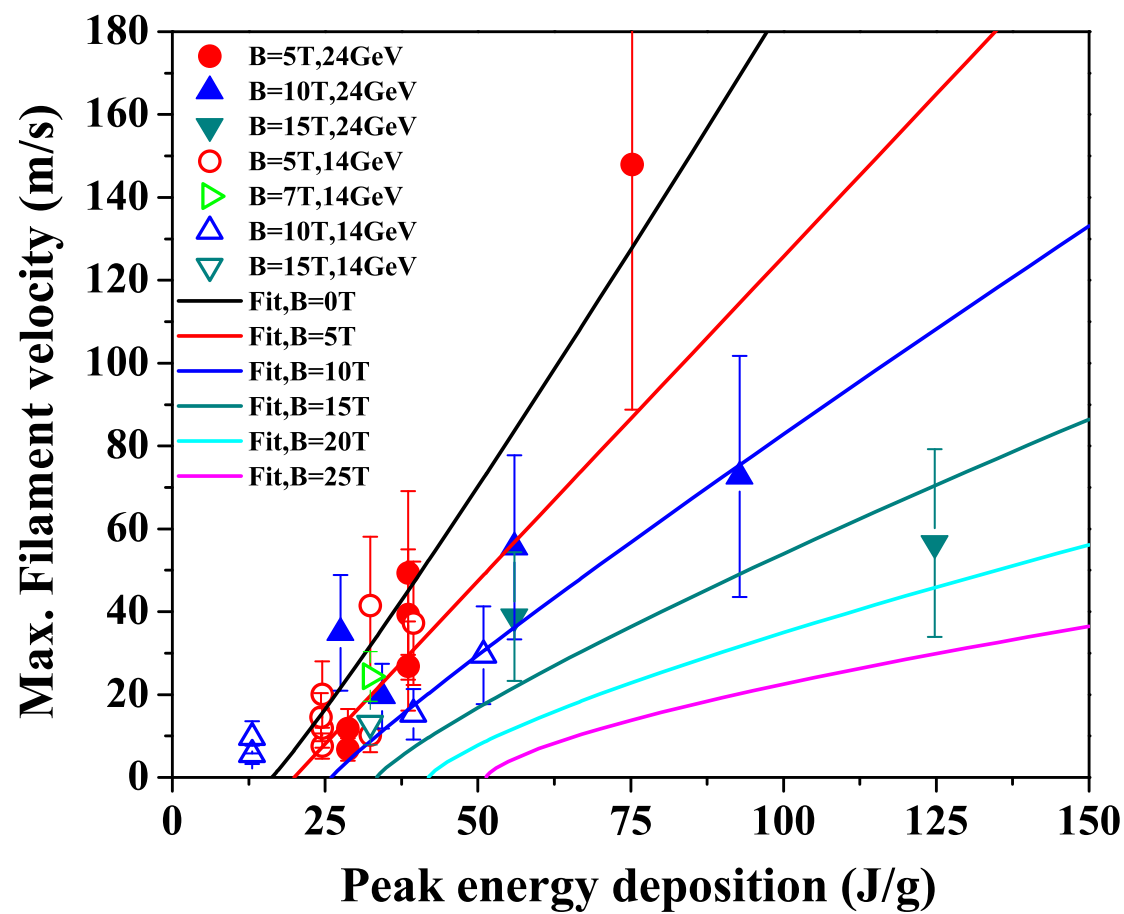
Figure 6.13: Filament velocity in magnetic fields ejected from jet surface as a function of peak energy deposition and its extrapolation.

Chapter 7

Conclusions

The experiment is a proof-of-principle test for a target system capable of accepting a high-intensity 4 MW proton beam. The system allows for the production of copious pions which subsequently decay into muons. An experiment at the CERN Proton Synchrotron that combines a free mercury jet target with a 15 T solenoid magnet and 14 GeV and 24 GeV proton beam is performed. It validates the liquid type of target concept for production of an intense secondary source of muons. When interacted with a beam pulse of 30 $\times 10^{12}$ protons on the mercury target, this generates a peak energy deposition of $\sim$ 125 J/g, which leads to the disruption of mercury target so that could result in low efficient target for particle production. For this experiment, a 15 T pulsed solenoid is designed. The Hg jet loop system generates a mercury jet from 1 cm diameter nozzle with velocity up to 15 m/s. An optical diagnostic system based on back-illuminated laser shadow photography is employed to investigate the mercury jet flow. Synchronized short laser light pulses are used to illuminate and freeze the motion of the jet. A total of four optical imaging heads for each Viewport are mounted on the exterior of the primary

containment vessel. Four high speed cameras are used to simultaneously collect images on four Viewports. Integrated all-in-one compact optical heads, consisting of ball lens, illumination fiber, objective lens, and imaging fiber bundle, are placed at the radius of curvature of a retro-reflector allowing for the illumination and imaging collection on one side of the mercury primary containment vessel. Due to the short time of frame rate, the time delay from the light source to the image arrival at the camera CCD is adjusted considering the delay from the electronics as well as the fiber-optics. The optimum timing delay is judged by the uniformity of consecutive collected image brightness as well as the triggering signal pulse on the oscilloscope for each component of device, so that timing of the motion of jet is validated. Also, note that the trigger timing is adjusted using the response of the scintillating fiber on the oscilloscope with respect to the beam triggering timing. The motions of mercury jet at Viewport 1, 2, 3 and 4, which enables to understand mercury jet condition at upstream, midstream, and downstream. Image processing provides the mercury jet thickness at various magnetic field strengths. The optical diagnostic observation shows the effects of the magnetic field on the distortion of mercury jet. In addition, it reveals the jet instability which might be caused by the strong induced axial magnetic field, which is possibly the onset of a quadrupole effect. Nevertheless, the experimental results clearly show that the magnetic field stabilizes the mercury jet by smoothing out the edges of the otherwise turbulent mercury flow, as previously reported in the literatures (Shercliff 1956, Gold 1962, Kozyrev 1981, Bernshtam 1982). The comprehen-

3473   sive optical diagnostic method allows us to have a better understanding of the

3474   behavior of a conducting jet moving in a high magnetic field environment.

3475   In order to achieve an understanding of conducting flow in a magnetic field,

3476   magnetohydrodynamic equations considering Lorentz force effect based on the

3477   Navier-Stokes equations as well as Maxwell equations are studied. Also, the

3478   suppression of vorticity by the perpendicular magnetic field is studied based

3479   on the role of Stuart number. As a result, the rotational motion of jet on the

3480   surface becomes more two dimensional motion of flow and thus the jet surface

3481   is more stabilized, which is observed qualitatively.

3482   For investigation of flow in magnetic field, the mercury jet behavior is

3483   observed for various magnetic field strengths and then the jet height for de-

3484   formation is measured. The fluctuation on the jet surface decreases as the

3485   magnetic field increases and the jet height increases slightly with magnetic

3486   field assuming the major and minor axis of Hg jet is reversed at 10 T. Gravity

3487   affects the jet trajectory, so that the jet bends down as it goes downstream.

3488   But this deflection of the jet by gravity is reduced at higher magnetic field.

3489   The jet axis becomes more straight toward the direction of magnetic field line.

3490   The stabilizing effect of the magnetic field on a turbulent jet is observed.

3491   It is well known that the turbulent fluctuation is suppressed by magnetic field

3492   and it is observed that the wave length on the jet surface increases. Thus, the

3493   jet surface is getting flattened as the magnetic field increases. Therefore, the

3494   jet is getting more stabilized. However, the jet has a different type of instability

3495   at magnetic fields larger than 10 T. The jet height becomes larger at larger

219

3496   magnetic field than 10 T. This seems to be induced by the longitudinal current

3497   due to the tilted jet axis with respect to the magnet axis. Thus, the induced

3498   current generates a Lorentz force. As a result, additional anisotropic magnetic

3499   force is changing the jet height. As the magnetic field increase up to 5 T, the

3500   jet fluctuation decreases and the jet is more elongating to the flow direction.

3501   Thus, the jet height decreases from 0 T to 5 T. However, the magnetic pressure

3502   is influencing at larger than 5 T. Since the optical diagnostics depends on the

3503   side view of jet flow, it is hard to tell in which direction the jet deflects since

3504   the jet and the magnetic field line is axially symmetric. However, the jet

3505   height clearly increases at 15 T, which indicates that the magnetic pressure

3506   apparently affects the jet height at 15 T.

3507   The longitudinal jet velocity is not varied. Again, the jet elongation to the

3508   field direction by the magnetic field is indicated from this result. The longi-

3509   tudinal magnetic field does not influence the jet flow velocity. The transverse

3510   magnetic field will change the jet velocity. This is known as the Hartmann

3511   flow. The longitudinal magnetic field does not influence the longitudinal jet

3512   flow as indicated in governing MHD equation.

3513   The pipe pressure driven by the syringe piston is measured. It shows that

3514   the Hg driving pressure is same regardless of the magnetic field. The driving

3515   pressure at Hg pipe inlet is independent of the magnetic field strength. There-

3516   fore, the mercury delivery is not influenced by the longitudinal magnetic field.

3517   However, there may be some pressure loss or jet velocity profile change due to

3518   pipe bend. According to the velocity measurement at upstream, mid-stream,

3519 and downstream, it is not significantly different and it is same comparing with

3520 the flow velocity at 0 T. Therefore, the field effect at the pipe bend is expected

3521 to be somewhat negligible. To support this result, the pipe loss due to the

3522 geometry and friction is given.

3523 Numerical Monte Carlo simulation is performed for calculation of energy

3524 deposition into mercury jet, where jet size, trajectory, and beam spot size

3525 from experimental result are used. The peak energy deposition as well as

3526 total energy deposition into mercury jet are calculated. Multi-variable fit

3527 provides the relation of peak energy deposition and total energy deposition

3528 with number of protons, beam energy, and magnetic field. Also, the averaged

3529 energy deposition shows the distribution of energy along jet axis as well the

3530 relation with number of protons and magnetic field.

3531 The observation of interaction of proton beam up to 30 Tp at both 14

3532 GeV and 24 GeV with jet is performed, which provides clue to validate the

3533 performance of high power target for future accelerator. The disruption as

3534 manifested by the jet break up is caused by energy deposition of proton beam.

3535 The disruption begins on the bottom surface of Hg jet where the proton beam

3536 enters. The disruption ends on the top surface of Hg jet where the proton

3537 beam leaves. The jet breakup is occurring at midstream of jet flow where the

3538 maximum energy is deposited. This phenomenon is consistent with the beam

3539 trajectory across the jet as well as the result of distribution of energy depo-

3540 sition calculation by MARS code. However, Hg jet breakup is influenced by

3541 the magnetic field. In order to validate the measured disruption length, ellip-

221

3542   tic jet shape are modeled in MARS code for calculation of energy deposition.

3543   Deposition of peak energy to Hg jet according to the beam intensities and

3544   magnetic field strengths are analyzed. Based on the hypothesis of threshold

3545   of beam intensity causing the disruption of Hg jet at various magnetic field

3546   strength, the disruption length is estimated, which gives good agreement with

3547   experimentally measured disruption length. The beam pulse structure is com-

3548   posed of 8 and 16 bunches with a doubled time difference. The effect of pulse

3549   structure to disruption length is negligible qualitatively, which means that the

3550   instantaneous time of pulse incident to mercury jet does not affect to differ-

3551   ence of energy deposition into mercury jet. Using the values from fit to total

3552   energy deposition, the total energy deposition into mercury jet according to

3553   number of protons, beam energy, and magnetic field is estimated, so that it is

3554   possible to show the disruption length as a function of total energy deposition

3555   and magnetic field, which also provides an estimation up to 25 T for future

3556   possible feasibility. The threshold of disruption increases in ~ 0.8 power of

3557   magnetic field, and it is ~ 338 J of energy energy deposition with no magnetic

3558   field. The disruption length increases in square root power of total energy

3559   deposition with no magnetic field, but it is suppressed in $\sim 1/(2 + 0.04B)$

3560   power of total energy deposition with magnetic field.

3561   The time scale of magnetic damping indicates the rate of decay of global

3562   kinetic energy due to the magnetic field strength. Thus, the energy decreases

3563   faster as the magnetic field increases. Therefore, the rising time to the max-

3564   imum velocity increases as the magnetic field increases. It indicates that the

222

3565 magnetic damping is getting larger by magnetic field in terms of the transient

3566 response time. At low intensity of proton beam, the charged beam may be

3567 fluctuating depending on the initial conditions at experiment. Thus, the ob-

3568 served onset time of filaments is large at low intensity of beam and it decreases

3569 as the intensity of proton beam increases. Therefore, the distribution of fila-

3570 ment velocity at lower intensity of beam is more scattered. Also, the geometric

3571 effect of viewing the filament is observed. The onset time of filament decreases

3572 as filament velocity on uniformly distributed jet surface increases. The maxi-

3573 mum filament velocity increases as beam intensity increases due to increased

3574 peak energy deposition but the magnetic field slows the filament velocity. The

3575 peak energy deposition plays a key role in determining the maximum filament

3576 velocity ejected from jet surface in viewpoint that the velocity distribution on

3577 jet surface is determined by normalization using the peak energy deposition.

3578 Using the values from fit to peak energy deposition, the peak energy de-

3579 position into mercury jet according to number of protons, beam energy, and

3580 magnetic field is estimated, so that it is possible to show the filament veloc-

3581 ity as a function of peak energy deposition and magnetic field, which also

3582 provides an estimation up to 25 T for future possible feasibility. Note that

3583 multiple events with repetition under same condition using pump probe shot

3584 shows well agreement with disruption length results and provides possible er-

3585 ror value occurred by repeating experiment. To be consistent with the onset

3586 of disruption, the threshold of filament velocity is forced to be ~ 16 J of peak

3587 energy deposition with no magnetic field and it increases in 1.4 power of mag-

223

3588 netic field. The filament velocity increases in linear power of peak energy

3589 deposition with no magnetic field, but it is slowed in $\sim 1.08 - 0.016B$ power

3590 of peak energy deposition with magnetic field.

3591   Finally, to conclude, the performance and feasibility of utilizing liquid

3592 metal jet as a high power target is investigated. The liquid jet target con-

3593 cept is based on the target being recycled after each pulse. Therefore, the

3594 power of the target is evaluated in terms of the replacing capability. The op-

3595 timal interaction length for the 24 GeV beam energy is in the region of 30

3596 cm which corresponds to approximately 2 interaction length for mercury. For

3597 a 20 m/s jet velocity, replacing two interaction lengths will be taken in 14

3598 ms thus allowing for operations with a repetition rate of up to 70 Hz. The

3599 disruption length at 15 T is less than 20 cm and the total energy deposition is

3600 ~ 8000 J. Therefore, $100 \sim 133$ kJ of beam energy can be recycled with a 70

3601 Hz repetition rate for 20 m/s jet. This result validates that a target system

3602 capable of supporting proton beams with powers of up to 8 MW, which con-

3603 cludes the experiment for investigation of feasibility of mercury jet as a high

3604 power target.

Bibliography

[1] J. Alessi *et al*, 1998, "A proposal for an *R&D* program for targetry and capture at a muon collider source," *Approved as BNL E951*

[2] M. M. Alsharoa *et al*, 2003, "Recent progress in neutrino factory and muon collider research within the muon collaboration," *submitted to Phys. Rev. ST Accel. Beams., http : //www.cap.bnl.gov/mumu/pubs/prstab − 030422/prstab.pdf*

[3] C. M. Ankenbrandt *et al*, 1999, "Status of muon collider research and development and future plans" *Phys. Rev. ST Accel. Beams 2*, **081001**

[4] Robert P. Benedict, 1980, *Fundamentals of pipe flow*, John Wiley & Sons, Inc.

[5] V. A. Bernshtam, S. V. Kozyrev, A. I. Él'kin, 1982, "Stability of flow of films of a conducting viscous liquid in longitudunal magnetic field," *Magnetohydrodynamics*, **18**, pp.132

[6] Herman Branover, 1978, *Magnetohydrodynamic flow in ducts*, John Wiley & Sons, Inc.

[7] Michael P. Brenner, 2002, "Single bubble sonoluminescence," *Reviews of Modern Physics*, **74**, pp.425-440

[8] G. A. Carlson, 1975, "Dynamic tensile strength of mercury," *J. Appl. Phys.*, v.46, pp.4069-4070

[9] Donald Chang, Thomas Lundgren, 1961, "Duct flow in magnetohydrody-namics," *Z. angrew. Math. Phys.*, **12**, pp.100-114

225

3627   [10] I. G. Currie, 1993, *Fundamental Mechanics of Fluids*, Marcel Dekker, Inc.

3628   [11] P. A. Davidson, 1999, "Magnetohydrodynamics in materials processing,"
3629   *Annu. Rev. Fluid Mech.*, **31**, pp.273-300

3630   [12] G. F. D. Duff, D. Naylor, 1966, *Differential equations of applied mathe-*
3631   *matics*, John Wiley & Sons, Inc.

3632   [13] I. Efthymiopoulos, A. Fabich, J. Lettry, 2005, "CERN installation,"
3633   *http://cern.ch/proj-hiptarget*

3634   [14] I. Efthymiopoulos, 2008, "The MERIT ex-
3635   periment (nToF11)," *MUTAC review*, *http* :
3636   *//www.hep.princeton.edu/ mcdonald/mumu/target/Ilias/$ie_0$80408.pdf*

3637   [15] A. Fabich, 2005, "nToF11: Multi-MW target experiment in TT2A,"
3638   *http://cern.ch/proj-hiptarget*

3639   [16] A. G. Fedin, 1973, "Use of optical methods in investigating MHD pro-
3640   cesses" *Magnetohydrodynamics (English translation of Magnitaya Gidro-*
3641   *dinamika)*, **9**, pp.301-308

3642   [17] T. A. Gabriel *et al*, 2001, "Targets for high-intensity particle production,"
3643   *Part. Accel. Conf.*, Chicago, pp.737

3644   [18] T.A. Gabriel, J.R. Haines, T. J. McManamy, P. Spampinato, B. W.
3645   Riemer, 2001, "Targets for high intensity particle production," *Part. Ac-*
3646   *cel. Conf.*, Chicago, pp737-741

3647   [19] J. Gallardo *et al*, 2001, "Calculation for a mercury jet target in a solenoid
3648   magnet capture system," *Part. Accel. Conf.*, Chicago, pp627-629

3649   [20] J. Gallardo *et al*, 2002, "First order perturbative calculations for a con-
3650   ducting liquid jet in a solenoid," *MUC-NOTE-TARGET-242, MU-047*

3651   [21] D. Gao, N. B. Morley, 2002, "Equilibrium and initial linear stability anal-
3652   ysis of liquid metal falling film flows in a varying spanwise magnetic field,"
3653   *Magnetohydrodynamics*, **38**, No.4, pp. 359-375

3654 [22] A. K. Geim, M. D. Simon, M. I. Boamfa, M. J. Lighthill, 1999, "Magnetic
3655   levitation at your finger tips," *Nature*, **400**, pp. 323

3656 [23] M. B. Glanert, M. J. Lighthill, 1955, "The axissymmetric boundary layer
3657   on a long thin cylinder," *Proc. Roy. Soc. Ser.*, **A 230**, pp. 188

3658 [24] Richard R. Gold., 1962, "Magnetohydrodynamic pipe flow: Part 1.," *J.*
3659   *Fluid Mech.*, **13**, pp.505-512

3660 [25] R. J. Goldstein, 1991, *Optical systems for flow measurement*, McGraw-
3661   Hill, Inc.

3662 [26] Andrew Gray and G. B. Mathews, 1966, *A treatise on Bessel functions*
3663   *and their applications to physics*, Dover, Inc.

3664 [27] V. Graves, 2007, "MIT testing results" *MUTAC review, http :*
3665   *//www.hep.princeton.edu/ mcdonald/mumu/target/graves/VGraves−*
3666   *070418.pdf*

3667 [28] J. Hartmann, 1937, "Hg dynamics I," *Kgl. Danske Videnskab Selskabs*
3668   *Math. Fys.*, Medd. 15, No.6

3669 [29] A. Hassanein, I. Konkashbaev, 2001, "Dynamics of liquid metal jets pene-
3670   trating a strong magnetic field in high power colliders," *Part. Accel. Conf.*,
3671   Chicago, pp624-626

3672 [30] H. Ito, 1960, "Pressure losses in smooth pipe bends," *Trans. ASME., J.*
3673   *Basic Eng.*, **82**, pp.131

3674 [31] Uhlenbusch J., Fishcer E., 1961, "Hydromagnetische strömung im
3675   kreiszylindrischen rohr," *Z. Phys.*, **165**, pp.190-198

3676 [32] Colin Johnson, 2002, "A self focusing mercury jet target," *CERN-*
3677   *NUFACT-113*

3678 [33] T. Kakuta, T. Shikama, M. Marui, 1999, "Optical fibers and their appli-
3679   cations for radiation measurement," *Seventh Int. Conf. on Nuclear Engi-*
3680   *neering*, Tokyo, Japan, pp.19

3681 [34] H. G. Kirk *et al*, 2001, "Target studies with BNL E951 at the AGS,"
3682   *Part. Accel. Conf.*, Chicago, pp.1531-1537

[35] H. G. Kirk *et al*, 2008, "The MERIT high power target experiments at the CERN PS," *European Part. Accel. Conf.*, Genoa, Italy, *WEPP169*

[36] B. A. Kolovandin, 1965, "Stability of flow of conducting liquid with free surface in the presence of magnetic and electric fields," *Prikl. Mekh.*, **1**, No. 11, pp.95

[37] S. V. Kozyrev, A. I. Él'kin, 1981, "Stability of flow of thin films of electrically conducting liquid in crossed magnetic and electric fields," *Magnetohydrodynamics*, **17**, No. 4, pp.353

[38] H. C. Lee, 1977, "Boundary layer around a liquid jet," *IBM J. Res. Develop.*, pp.48

[39] J. Lettry *et al*, 2003, "Thermal shocks and magnetohydrodynamics in high power mercury targets," *J. Phys. G: Nucl. and Part. Phys.*, **29**, pp.1621

[40] Junwoo Lim *et al*, 1998, "Control of streamwise vortices with uniform magnetic fluxes," *Physics of Fluids*, **10**, 8, pp.1997

[41] S. P. Lin, D. J. Kang, 1987, "Atomization of a liquid jet," *Physics of Fluids*, **30**, pp.2000-2006

[42] K. T. McDonald *et al.*, 2001, "The primary target facility for a neutrino factory based on muon beams," *Proc. Part. Accel. Conf.*, Chicago, IL, pp.1583

[43] K. T. McDonald, 2000, "Cooling of a target by helium gas," *Princeton /μ/μ/00-25*

[44] K. T. McDonald, 2000, "Damping of radial pinch effects," *Princeton /μ/μ/00-26*

[45] K. T. McDonald, 2000, "Magnetohydrodynamics of a continuous mercury jet coaxially entering a solenoid," *Princeton /μ/μ/00-29*

[46] K. T. McDonald, 2000, "Magnetohydrodynamics of a pulsed mercury jet entering a solenoid at an angle," *Princeton /μ/μ/00-30*

[47] K. T. McDonald, 2000, "Optics for E951 target tests in the A3 beamline," *Princeton /μ/μ/00-28*

[48] K. T. McDonald, 2009, *Private communication*

[49] N. V. Mokhov, 2001, "Paricle production for a muon storage ring: I. Targetry and π/μ yield" *Nucl. Inst. Methods in Phy. Res.*, **A 472**, pp.546-551

[50] N. V. Mokhov, O. E. Krivosheev, 2000, "MARS code status," *FERMILAB-Conf-00/181*

[51] Neil B. Morley *et al*, 2000, "Liquid megnetohydrodynamics - recent progress and future directions for fusion," *Fusion Engineering and Design*, **51**, pp.701-713

[52] Neil B. Morley, Sergey Smolentsev, Donghong Gao, 2002, "Modeling infinite/axisymmetric liquid metal magnetohydrodynamic free surface flows," *Fusion Engineering and Design*, **63**, pp. 343-351

[53] S. Ozaki, R. Palmer, M. Zisman, J. Gallardo, 2001, "Neutrino factory feasibility study 2," *BNL-52623*, Ch.3, *http : //www.cap.bnl.gov/mumu/studii/FS2 − report.html*

[54] N. Otsu, 1979, "A threshold selection method from gray-level histograms," *IEEE Trans. Sys., Man., Cyber.*, **9**, pp. 62-66

[55] Shuzo Oshima, Ryuichiro Yamane, Yoshihiro Mochimaru, Toshihiro Matsuoka, 1987, "The shape of a liquid metal jet under a non-uniform magnetic field," *JSME International Journal*, **30**, No.261, pp.437-448

[56] R. B. Palmer, 1998, "Muon collider design," *Report BNL-65242, CAP-200-MUON-982C*

[57] Mark A. Pinsky, 1991, *Partial differential equations and boundary value problems with applications*, McGraw-Hill, Inc.

[58] R. D. Reitz, F. V. Bracco, 1982, "Mechanism of atomization of a liquid jet," *Physics of Fluids*, **25**, pp.1730-1742

3739   [59] Uflyand Y. S., 1960, "Hartmann problem for a circular tube," *Soviet*
3740   *Phys.*, **5**, pp.1194-1196

3741   [60] Roman Samulyak, 2006, "Target simulations," *MUTAC Review, http :*
3742   *//www.hep.princeton.edu/ mcdonald/mumu/target/samulyak/*
3743   *mutac06_samulyak_targetsimulations.pdf*

3744   [61] SAE, 1960, "Aero-space thermodynamics manual," pp. A18-A20

3745   [62] R. Samulyak, 2006, "Target simulations" *MUTAC review, http :*
3746   *//www.hep.princeton.edu/ mcdonald/mumu/target/samulyak/*
3747   *mutac06_samulyak_targetsimulations.pdf*

3748   [63] R. Samulyak, J. Du, J. Glimm, Z. Xu, 2007, "A numerical algorithm for
3749   MHD of free surface flows at low magnetic Reynolds numbers," *Jorunal*
3750   *of Computational Physics*, **226**, pp.1532-1549

3751   [64] J. A. Shercliff, 1953, "Steady motion of conducting fluids in pipes under
3752   transverse magnetic fileds," *Proc. Camb. Phil. Soc.*, **49**, pp.136-144

3753   [65] J. A. Shercliff, 1956, "The flow of conducting flows in circular pipes under
3754   transverse magnetic fields," *J. Fluid Mech.*, **13**, pp.644-666

3755   [66] J. A. Shercliff, 1962, "Magnetohydrodynamic pipe flow: Part 2 High Hart-
3756   mann number," *J. Fluid Mech.*, **13**, pp.513-518

3757   [67] J. A. Shercliff, 1965, *A textbook of magnetohydrodynamics*, Pergamon
3758   Press

3759   [68] N. Simos, 2005, "MERIT experiment window study," *BNL Review, http :*
3760   *//www.hep.princeton.edu/ mcdonald/mumu/target/simos/*
3761   *Simos_121205.pdf*

3762   [69] P. Sievers, P. Pugnat, 2000, "Response of solid and liquid targets to high
3763   power proton beams for neutrino factories," *Report CERN LHC/2000-4,*
3764   *CERN-NuFACT Note 035*

3765   [70] G. Skoro, 2008, "MERIT beam spot size : satura-
3766   tions and projections," *MERIT collaboration review, http :*
3767   *//www.hep.princeton.edu/ mcdonald/mumu/target/Skoro/Saturation_profiles.pdf*

3768 [71] K. Stewartson, 1955, "The asymtotic boundary layer on a circular cylinder
3769 in axial incompressible flow," *Q. Appl. Math.*, **13**, pp. 113

3770 [72] P. T. Spampinato *et al*, 2005, "A free jet mercury system for use in a high
3771 power target experiment," *Part. Accel. Conf.*, Knoxville, TN, pp.1637

3772 [73] S. Striganov, 2009, Private communication

3773 [74] P. Thieberger, H. G. Kirk, R. J. Weggel, K. T. MacDonald, 2003, "Moving
3774 solid metallic targets for pion production in the muon collider/neutrino
3775 factory project," *Proc. Part. Accel. Conf.*, Portland, OR, pp.1634

3776 [75] N. Tsoupas *et al*, 2003, "Injection acceleration and extraction of high
3777 intensity proton beam for the neutrino facility project at BNL," *Part.*
3778 *Accel. Conf.*, Portland, OR, pp.1637

3779 [76] C. D. West, 2000, "Cavitation in a mercury target," *ORNL/TM-2000-*
3780 */263*

3781 [77] H. Q. Yang, 1992, "Asymmetric instability of a liquid jet," *Physics of*
3782 *Fluids*, **30**, pp.681-689

3783 [78] K. T. Yen, 1967, "Role of intermittency in free turbulent flows," *American*
3784 *Institute of Aeronautics and Astronautics*, **5**, No. 12 pp.2187-2192

3785 [79] W. M. Yao *et al*, 2006, "Accelerator physics of colliders" *Journal of*
3786 *Physics*, **33**, No.1, pp.35-62

³⁷⁸⁷ Appendix A

³⁷⁸⁸ Tabular Data for Chapter 3,
³⁷⁸⁹ Chapter 5, and Chapter 6

³⁷⁹⁰
³⁷⁹¹

³⁷⁹² A.1 Specifications of Optics

Table A.1: Specifications of optical components in optical diagnostics.

Item	Value
Right angle prism mirror	Gold coated, $25 \times 25 \times 35.4$, Surface flatness $\lambda/10$
Gradient index lens	
Size	d=1.0 mm, L=2.48 mm
Numerical aperture	0.5
Working distance	Infinity
Coating	AR coated at $800 \sim 960$ nm
Sapphire ball lens	D=0.5 mm, Al_2O_3, Index of refraction=1.77
Retro-reflecting Parabolic mirror	
Diameter	76.2 mm
Thickness	12.7 mm
Focal length	444 mm
Coating	Gold
Microscope objective	
Magnification	$40 \times$

³⁷⁹³

Table A.1: *Continued from previous page*

Item	Value
Numerical aperture	0.65
Working distance	0.6 mm
Clear aperture	5.0 mm
Power	160 mm (tube length) / f
Optical fiber	
Number of picture elements	30000
Jacketing diameter	800 μm
Picture elements area diameter	720 μm
Coating diameter	960 μm
Core material	GeO_2 containing Silica
Coating material	Silicone
Numerical aperture	0.35
Allowable bending radius	40 mm
Core diameter	200 μm

3794

A.2 Characteristic Response of 25 W Laser
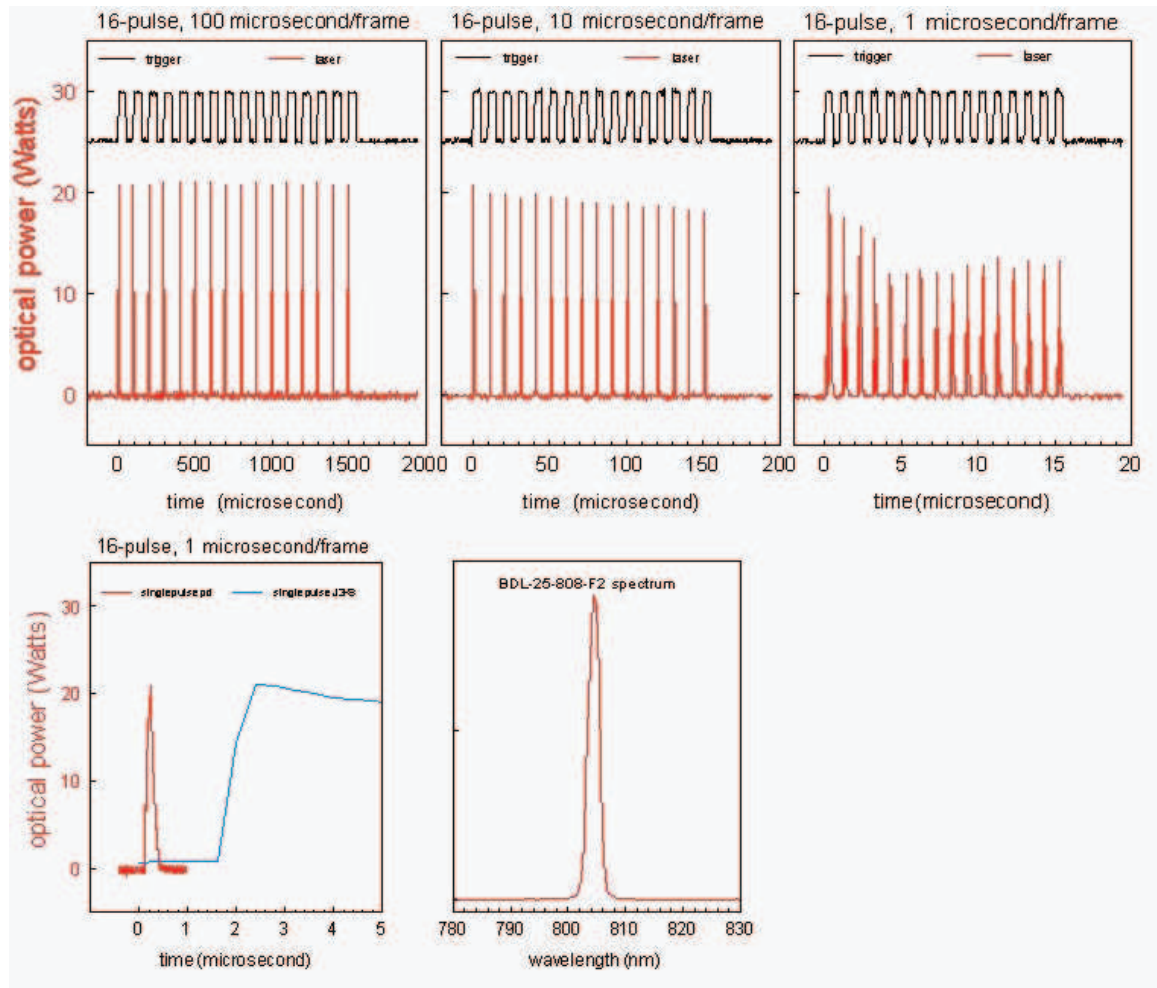
Figure A.1: Measurement of characteristic response of 25 laser used for high speed camera at Viewport 2 (Tsang, 2006).

A.3 Mercury Properties

Table A.2: Properties of mercury.

Property	Value	Unit
Atomic number	80	-
Atomic mass	200.59	-
Number of protons/electrons	80	-
Number of neutrons	121	-
Classification	Transition metal	-
Melting point	-38.87	°C
Boiling point	356.58	°C
Density	13.456 at 25 °C	g/cm^3
Naturally occurring isotopes	Hg-194 Hg-206	-
Group in periodic table	12	-
Period in periodic table	6	-
Electrical conductivity	1.06×10^6 at 25 °C	$\Omega^{-1}m^{-1}$
Thermal conductivity	8.34	$W\ m^{-1}\ K^{-1}$ at 27 °C
Specific heat	0.139	$J\ g^{-1}\ K^{-1}$
Heat of vaporization	59.229	kJ/mol
Heat of fusion	2.295	kJ/mol
Electrical resistivity	961 at 25 °C	$n\Omega \cdot m$
Speed of sound	1451.4 at 20 °C	m/s
Coefficient of thermal expansion	60×10^{-6} at 20 °C	K^{-1}
Bulk modulus	25	GPa
Dynamic viscosity	1.552×10^{-3}	$kg\ m^{-1}\ s^{-1}$
Kinematic viscosity	1.145×10^{-7}	$m^2\ s^{-1}$
Dielectric constant	1.00074	-
Surface tension	485.5 (Hg-Air) at 25 °C	mN/m °C
Magnetic permeability	$4\pi \times 10^{-7}$	H/m

235

A.4 Measurement of Events with Pump Probe Condition

Table A.3: Measurement of disruption and filament velocity in pump probe condition with 8 and 16 harmonic bunches.

Condition		N[1], DL[2]	A[3], DL	S[4], DL	N, V[5]	A, V	S, V
Group 1	12+4 bunches 15+5 Tp 7 T	5	19.5	4.1	5	24.4	13.4
Group 2	6+2 bunches 12+4 Tp 5 T	30	19.8	6.1	19	10.2	3.6
Group 2, Spec. 1	700 μs delay	12	19	5	6	12.4	3.7
Group 2, Spec. 2	350 μs delay	11	22.2	7.2	7	8.4	1.9
Group 2, Spec. 3	40 μs delay	7	17.3	5	6	10.2	4.1
Group 3	8 bunches 16 Tp 5 T	6	24.8	7.1	-	-	-
Group 4	8 bunches 6 Tp 5 T	6	5.9	3.8	-	-	-

[1] N represents number of events for measurement.

[2] DL (cm) represents disruption length of jet.

[3] A represents average of measurement.

[4] S represents standard deviation of measurement.

[5] V (m/s) represents filament velocity on jet surface.

A.5 Beam Program List and Disruption Length Measurements

1. Shot number
2. Number of bunches
3. Number of protons (Tp)
4. Magnetic field (T)
5. Jet velocity (m/s)
6. Disruption length (m)
7. Error ($\pm$ cm)

Table A.4: Measured disruption length and beam shot program.

1	2	3	4	5	6	7
2002	1	0.25	0	0	-	-
2003	1	0.25	0	0	-	-
2004	1	0.25	0	0	-	-
2005	1	0.25	0	0	-	-
2006	1	0.25	0	0	-	-
2007	1	0.25	0	0	-	-
2008	1	0.25	0	0	-	-
2009	1	0.25	0	0	-	-
2011	1	0.25	0	0	-	-
2012	1	0.25	0	0	-	-
2013	1	0.25	0	0	-	-
2014	1	0.25	0	0	-	-
2015	1	0.25	0	0	-	-
2016	1	0.25	0	0	-	-
2017	1	0.25	0	0	-	-
2018	1	0.25	0	0	-	-
2019	1	0.25	0	0	-	-
2020	1	0.25	0	0	-	-
2021	1	0.25	0	0	-	-
2022	1	0.25	0	0	-	-

Continued on Next Page...

1	2	3	4	5	6	7
2023	1	0.25	0	0	-	-
2026	1+1	0.50	0	15	0.085	4.0
3003	1+1	0.50	0	0	-	-
3005	1+1	0.50	0	0	-	-
3006	12+4	4.00	0	0	-	-
3007	12+4	4.00	0	0	-	-
3008	12+4	4.00	0	0	-	-
3011	12+4	4.00	0	0	-	-
3012	12+4	4.00	0	0	-	-
3014	1	0.25	0	0	-	-
3015	1	0.25	0	0	-	-
3016	1	0.25	0	15	No image	-
3017	1	0.25	0	15	0	0.0
3018	1	0.25	0	15	0	0.0
3019	1	0.25	0	15	0.013	0.7
3020	1	0.25	0	15	0	0.0
3021	1	0.25	0	15	0.005	0.5
3022	1	0.25	0	15	0.029	2.4
3023	1	0.25	0	15	0	0
3024	1	0.25	0	15	No image	-
3025	1	0.25	5	15	0	0
4001	1	0.25	0	15	0.018	1.5
4002	1	0.25	5	15	0	0
4003	1	0.25	5	15	0	0
4004	1	0.25	5	15	0	0
4005	1	0.25	5	15	0.054	3.4
4006	1	0.25	5	15	0.019	1.6
4007	1	0.25	5	15	0	0
4008	1	0.25	5	15	0	0
4009	1	0.25	5	15	No image	-
4010	1	0.00	5	0	-	-
4011	1	0.30	0	0	-	-
4012	1	0.30	5	0	-	-
4013	1	0.30	0	0	-	-
4014	1	0.30	5	15	0.007	0.7
4015	16	10.00	5	15	0.031	2.5

1	2	3	4	5	6	7
4016	16	10.00	5	0	-	-
4017	16	10.00	0	15	0.038	2.9
4019	16	10.00	0	15	0.062	3.6
4020	2	0.50	0	0	-	-
4021	2	0.50	0	0	-	-
4023	2	0.50	0	0	-	-
4024	2	0.50	0	0	-	-
4025	2	0.50	0	0	-	-
4026	2	0.50	0	0	-	-
4028	16	10.00	0	0	-	-
4030	16	10.00	0	15	0.143	4.5
4031	16	10.00	5	15	0.080	3.9
5003	4	1.00	5	15	0	0
5004	16	10.00	5	15	0.111	4.3
5005	16	10.00	5	15	No image	-
5006	16	10.00	5	15	No image	-
5007	16	10.00	5	15	0.024	2.1
5008	16	10.00	5	15	0.031	2.5
5009	8	5.00	5	15	0.033	2.6
5010	8	5.00	5	15	0.022	1.9
5011	8	5.00	0	15	0.084	4.0
5012	16	10.00	5	15	No image	-
5014	16	15.00	0	15	No image	-
5015	16	15.00	5	15	0.189	4.8
5016	16	15.00	5	15	0.180	4.7
5017	16	20.00	5	15	0.303	5.1
5018	16	20.00	5	15	0.283	5.1
5019	16	20.00	5	15	0.204	4.8
5020	16	20.00	10	15	0.184	4.7
6001	16	4.00	0	15	0	0
6002	16	4.00	0	15	0.027	2.3
6003	16	10.00	5	15	0.105	4.2
6004	16	10.00	5	15	0.105	4.2
6005	16	10.00	5	15	0.035	2.7
6006	16	10.00	5	15	0.173	4.7
6007	16	10.00	5	15	0.028	2.3

1	2	3	4	5	6	7
6008	16	10.00	5	15	0.052	3.3
6009	16	10.00	5	15	0.079	3.9
6010	16	10.00	5	15	0.074	3.8
6011	16	10.00	5	0	-	-
6012	1	0.25	0	0	-	-
6013	1	0.25	0	0	-	-
6014	1	0.25	0	0	-	-
6015	1	0.25	0	0	-	-
6016	1	0.30	0	0	-	-
6017	1	0.30	0	0	-	-
6018	1	0.30	0	0	-	-
6019	1	0.30	0	0	-	-
6020	1	0.30	0	0	-	-
6021	1	0.30	0	0	-	-
6022	1	0.30	0	0	-	-
6023	1	0.30	0	0	-	-
6024	16	4.00	0	0	-	-
6025	16	4.00	0	0	0.092	4.1
6026	16	4.00	0	15	0.101	4.2
6027	16	4.00	0	15	0.095	4.1
6028	16	4.00	5	15	0.005	0.5
6029	16	4.00	5	15	0.038	2.9
6030	16	4.00	10	15	0.044	3.1
6031	16	4.00	10	15	0.058	3.5
7001	16	4.00	0	0	-	-
7002	16	4.00	5	0	-	-
7003	16	4.00	10	0	-	-
7004	16	4.00	0	15	0.019	1.5
7005	16	4.00	0	15	0.036	2.8
7006	16	4.00	10	15	0.014	0.8
7008	16	4.00	0	0	-	-
7009	16	4.00	0	0	-	-
7010	16	4.00	0	0	-	-
7011	16	4.00	0	0	-	-
7012	16	4.00	0	0	-	-
7013	16	4.00	0	0	-	-

Continued on Next Page. . .

1	2	3	4	5	6	7
7014	16	4.00	0	0	-	-
7015	16	4.00	0	0	-	-
7016	16	4.00	10	15	0	0
7017	16	4.00	10	0	-	-
7021	16	4.00	0	0	-	-
7022	16	4.00	0	0	-	-
7023	16	4.00	10	15	0.082	3.9
7024	16	4.00	10	0	-	-
7025	16	4.00	10	0	-	-
8001	16	4.00	0	0	-	-
8002	16	4.00	0	15	0.016	1.1
8003	16	4.00	0	15	0.024	2.1
8004	16	4.00	0	0	-	-
8005	16	4.00	0	15	0.051	3.3
8006	16	4.00	0	0	-	-
8007	16	4.00	0	15	0.147	4.6
8008	16	4.00	0	0	-	-
8009	16	4.00	0	15	0.132	4.5
8010	16	4.00	0	15	0.419	5.3
8011	16	4.00	0	0	-	-
8012	16	4.00	0	15	0.041	3.0
8013	16	4.00	0	0	-	-
8014	16	4.00	0	15	0.107	4.2
8015	16	4.00	0	0	-	-
8016	16	4.00	5	15	0	0.0
8017	16	4.00	5	0	-	-
8018	16	4.00	5	15	0.027	2.2
8019	16	4.00	5	0	-	-
8020		0.00	5	15	0	0
8021	16	4.00	5	15	0	0
8022	16	4.00	5	0	-	-
8029	16	4.00	7	15	No image	-
8030	16	4.00	7	15	0	0
8031	16	4.00	7	0	-	-
8032	16	4.00	7	15	0	0
8033	16	4.00	7	0	-	-

Continued on Next Page. . .

1	2	3	4	5	6	7
8034	12+4	15+5	7	15	0.208	4.8
8035	12+4	15+5	7	15	0.152	4.6
8036	12+4	15+5	0	0	-	-
8037	12+4	15+5	7	15	0.160	4.6
8038	0	0.00	7	0	-	-
8039	-	-	0	0	-	-
8040	-	-	0	0	-	-
8041	12+4	15+5	7	15	0.203	4.8
8042	12+4	15+5	7	0	-	-
8043	12+4	15+5	7	0	-	-
8044	12+4	15+5	7	15	0.253	5.0
8045	12+4	15+5	7	15	0.165	4.7
8046	12+4	15+5	0	0	-	-
8047	12+4	15+5	7	0	-	-
9003	1	0.25	5	15	0	0
9004	16	4.00	5	15	0.064	3.6
9005	16	4.00	5	15	0.082	3.9
9006	16	4.00	5	15	0.215	4.9
9008	16	4.00	5	15	0.080	3.9
9009	12	3.00	5	15	0.108	4.2
9010	8	2.00	5	15	0	0
9011	-	-	-	-	0.068	3.7
9012	10	2.50	5	15	0.040	2.9
9013	-	-	-	-	0.040	3.0
9014	12	3.00	5	15	0.078	3.9
9015	16	6.00	7	15	0.162	4.6
9016	16	4.00	7	15	0.109	4.3
9017	12	3.32	7	15	0.005	0.5
9018	12	3.64	7	15	0	0
9019	12	3.78	7	15	0.040	3.0
9020	12	5.10	10	15	0.079	3.9
10001	16	4.00	0	0	No image	-
10002	16	4.00	0	0	No image	-
10003	16	4.00	0	15	0.188	4.8
10004	16	4.00	5	15	0.202	4.8
10005	16	4.00	5	15	0.128	4.4

Continued on Next Page. . .

242

1	2	3	4	5	6	7
10006	18	4.00	10	15	0.038	2.9
10007	16	10.00	5	15	0.258	5.0
10008	16	15.00	5	15	0.291	5.1
10009	4	6.00	5	15	0.154	4.6
10010	2+2	6.00	5	15	0.184	4.7
10011	2+2	6.00	5	15	0.294	5.1
10012	4	6.00	5	15	0.228	4.9
10013	4	6.00	5	15	0.182	4.7
10014	4	6.00	5	0	-	-
10015	2+2	6.00	5	15	No image	-
10016	8	6.00	5	15	0.155	4.6
10017	8	6.00	5	0	-	-
10018	4+4	6.00	5	15	0.250	5.0
10019	4+4	6.00	5	0	-	-
11001	4	1.0	0	15	0.029	2.4
11002	16	6.0	5	15	0.202	4.8
11004	4	6.0	5	15	0.260	5.0
11005	4	6.0	5	15	0.246	5.0
11006	4	6.0	5	15	0.239	5.0
11007	4	6.0	5	15	0.174	4.7
11008	4	6.0	5	15	0.122	4.4
11010	4	6.0	5	15	0.194	4.8
11019	16	10.0	10	15	0.167	4.7
11020	16	3.5	10	15	0	0
11021	16	3.8	10	15	0.062	3.6
11022	16	15.0	10	15	0.158	4.6
11032	16	20.0	10	15	0.218	4.9
11033	16	30.0	10	15	0.214	4.9
11034	16	30.0	15	15	0.164	4.7
12001	4	5.0	0	15	0.201	4.8
12003	4	5.0	0	15	0.238	5.0
12004	4	5.0	0	15	0.273	5.1
12005	4	5.0	0	15	0.245	5.0
12007	-	-	0	15	0.039	2.9
12006	4	4.0	0	15	0.149	4.6
12008	4	4.0	0	15	0.252	5.0

Continued on Next Page. . .

1	2	3	4	5	6	7
12009	4	4.0	5	0	-	-
12010	4	4.0	5	15	0.103	4.2
12011	4	4.0	5	15	0.079	3.9
12012	4	4.0	5	15	0	0
12013	4	4.0	5	0	-	-
12014	4	4.0	0	0	-	-
12015	4	4.0	5	15	0.105	4.2
12016	4	4.0	5	0	-	-
12029	8	15.0	15	15	0.046	3.2
12031	8	10.0	0	15	0.368	5.3
12032	8	10.0	15	15	0.149	4.6
12033	16	30.0	15	20	0.170	4.7
13001	2	2.5	0	15	0.042	3.0
13002	4	5.0	0	15	0.129	4.4
13003	4	5.0	0	15	0.138	4.5
13004	4	8.0	0	15	0.156	4.6
13007	6+2	16.0	5	15	0.157	4.6
13008	6+2	16.0	5	15	0.202	4.8
13009	6+2	16.0	5	15	0.196	4.8
13010	6+2	16.0	5	15	0.157	4.6
13011	6+2	16.0	5	15	0.170	4.7
13012	6+2	16.0	5	0	-	-
13013	6+2	16.0	5	15	0.221	4.9
13014	6+2	16.0	5	0	-	-
13015	6+2	16.0	5	15	0.167	4.7
13016	6+2	16.0	5	0	-	-
14008	6	6.0	5	15	0.061	3.6
14009	6	6.0	5	15	0.103	4.2
14010	6	6.0	5	15	0	0
14011	6	10.0	5	15	0.174	4.7
14012	6	10.0	5	0	-	-
14013	6	10.0	5	0	-	-
14014	6	10.0	5	15	0.151	4.6
14015	6	10.0	5	15	0.261	5.0
14017	6+2	16.0	5	15	0.290	5.1
14018	6+2	16.0	5	15	0.239	5.0

Continued on Next Page. . .

1	2	3	4	5	6	7
14019	6+2	0.0	5	15	0.127	4.4
14020	6+2	16.0	5	0	-	-
14021	6+2	16.0	5	0	-	-
14022	6+2	16.0	5	15	0.233	4.9
14023	6+2	16.0	5	0	-	-
14024	6+2	16.0	5	15	0.119	4.3
14025	6+2	16.0	5	0	-	-
14026	6+2	16.0	5	15	0.215	4.9
14027	6+2	16.0	0	0	-	-
14028	6+2	16.0	5	15	0.186	4.8
14029	6+2	16.0	5	15	0.283	5.1
14030	6+2	16.0	5	0	-	-
14031	6+2	16.0	5	15	0.138	4.5
14032	6+2	16.0	5	0	-	-
14033	6+2	16.0	5	15	0.189	4.8
14034	6+2	16.0	5	15	0.383	5.3
14035	6+2	16.0	5	0	-	-
14036	6+2	4.0	5	15	0.032	2.6
14037	8	4.0	5	15	0	0
15001	8	4.0	5	15	0.014	0.8
15002	6+2	16.0	5	15	0.228	4.9
15003	6+2	16.0	5	15	0.117	4.3
15004	6+2	16.0	5	15	0.259	5.0
15005	6+2	16.0	5	0	-	-
15006	6+2	16.0	5	15	0.245	5.0
15007	6+2	16.0	5	0	-	-
15008	6+2	16.0	5	15	0.200	4.8
15009	6+2	16.0	5	0	-	-
15010	6+2	16.0	5	15	0.103	4.2
15011	6+2	16.0	5	15	0.188	4.8
15012	6+2	16.0	5	15	0.260	5.0
15013	6+2	16.0	5	0	-	-
15014	6+2	16.0	5	15	0.195	4.8
15015	6+2	16.0	5	0	-	-
15016	6+2	16.0	5	15	0.173	4.7
15017	6+2	16.0	5	0	-	-

Continued on Next Page. . .

1	2	3	4	5	6	7
15018	6+2	16.0	5	15	0.157	4.6
15019	6+2	16.0	5	15	0.132	4.4
15020	8	16.0	5	15	0.341	5.2
15021	8	16.0	5	15	0.165	4.7
15022	8	16.0	5	15	0.236	4.9
15023	8	16.0	5	15	0.260	5.0
15024	8	16.0	5	0	-	-
15025	8	16.0	5	15	0.175	4.7
15026	8	16.0	5	0	-	-
15027	8	16.0	5	15	0.313	5.2
15028	8	16.0	5	15	-	-
15029	8	6.0	5	15	0.066	3.7
15030	8	6.0	5	0	-	-
15031	8	6.0	5	15	0.068	3.7
15032	8	6.0	5	0	-	-
15033	8	6.0	5	15	0.026	2.2
15034	8	6.0	5	0	-	-
15035	8	6.0	5	15	0.021	1.8
15036	8	6.0	5	0	-	-
15037	8	6.0	5	15	0.115	4.3
15038	8	10.0	5	15	0.080	3.9
15039	8	8.0	5	15	0.053	3.4
15040	8	8.0	5	15	0.054	3.4
15041	8	6.0	5	15	0.008	0.8
15042	8	6.0	5	15	0.007	0.7
15043	16	6.0	5	15	0.027	2.3
15044	4	12.0	5	15	0.043	3.1
15045	4	12.0	5	15	0.027	2.3
16001	4	2.0	0	15	0.082	3.9
16002	4	10.0	4.1	15	0.068	3.7
16003	4	12.0	4.1	15	0.205	4.8
16004	4	14.0	6	15	0.222	4.9
16005	8	12.0	5	15	0.136	4.5
16006	8	12.0	5	15	0.208	4.9
16007	8	12.0	5	15	0.189	4.8
16008	4+4	6+6	5	15	0.212	4.9

Continued on Next Page. . .

1	2	3	4	5	6	7
16009	4+4	6+6	5	15	0.071	3.8
16010	4+4	6+6	5	15	0.164	4.7
16011	4+4	6+6	5	15	0.215	4.9
16012	4	14.0	5	15	0.229	4.9
16013	4	14.0	10	15	0.188	4.8
16014	4	12.0	10	15	0.172	4.7
16015	4	12.0	15	15	0.144	4.5
16016	4	10.0	5	15	0.131	4.4
17001	16	6.0	5	15	0.015	1.0
17002	16	8.0	5	15	0.125	4.4
17003	16	6.0	5	15	0.037	2.8
17004	16	6.3	5	15	0.048	3.2
17005	16	6.0	5	15	0.013	0.7
17006	16	6.0	7	15	0.093	4.1
17007	16	4.2	7	15	0	0
17008	16	8.0	7	15	0.101	4.2
17009	8+8	8.0	7	15	0.074	3.8
17010	8+8	8.0	7	15	0.062	3.6
17011	8+8	8.0	7	15	0.155	4.6
17012	8+8	8.0	7	15	-	-
17013	8+8	8.0	7	15	0.047	3.2
17014	8+8	8.0	7	15	0	0
17015	8+8	7.5	7	15	0.016	1.2
17016	8+8	7.4	7	15	0.086	4.0
17017	8+8	8.4	7	15	0.111	4.3
17018	8+8	6.0	7	15	0.057	3.5
17019	8+0	4.0	7	15	0.007	0.7
17020	8+0	6.0	7	15	0.059	3.5
17021	16	15.0	10	15	0.174	4.7
17022	16	15.0	15	15	0.148	4.6
17023	16	29.0	15	15	0.180	4.7
17024	16	29.0	10	20	0.230	4.9

3811

Appendix B

Image Data for Chapter 6

B.1   Images for filament velocity measurement at Viewport 2

1. Shot number
2. Camera frame rate (μ s)
3. Beam energy (GeV)
4. Number of bunches
5. Number of protons (Tp)
6. Magnetic field (T)
7. Jet velocity (m/s)
8. Lag time between peak laser emittance and proton beam arrival (μ s)

Table B.1: Properties of shots used for filaments velocity analysis.

1	2	3	4	5	6	7	8
11004	25	24	4	6	5	15	-4.03
11007	25	24	4	6	5	15	-3.97
11010	25	24	4	6	5	15	-3.99
11019	25	24	16	10	10	15	-2.43
11021	25	24	16	3.8	10	15	-2.43
11032	25	24	16	20	10	15	-2.03
12031	25	24	8	10	0	15	-1.93
12032	25	24	8	10	15	15	-1.83
12033	25	24	16	30	15	20	-1.85

248
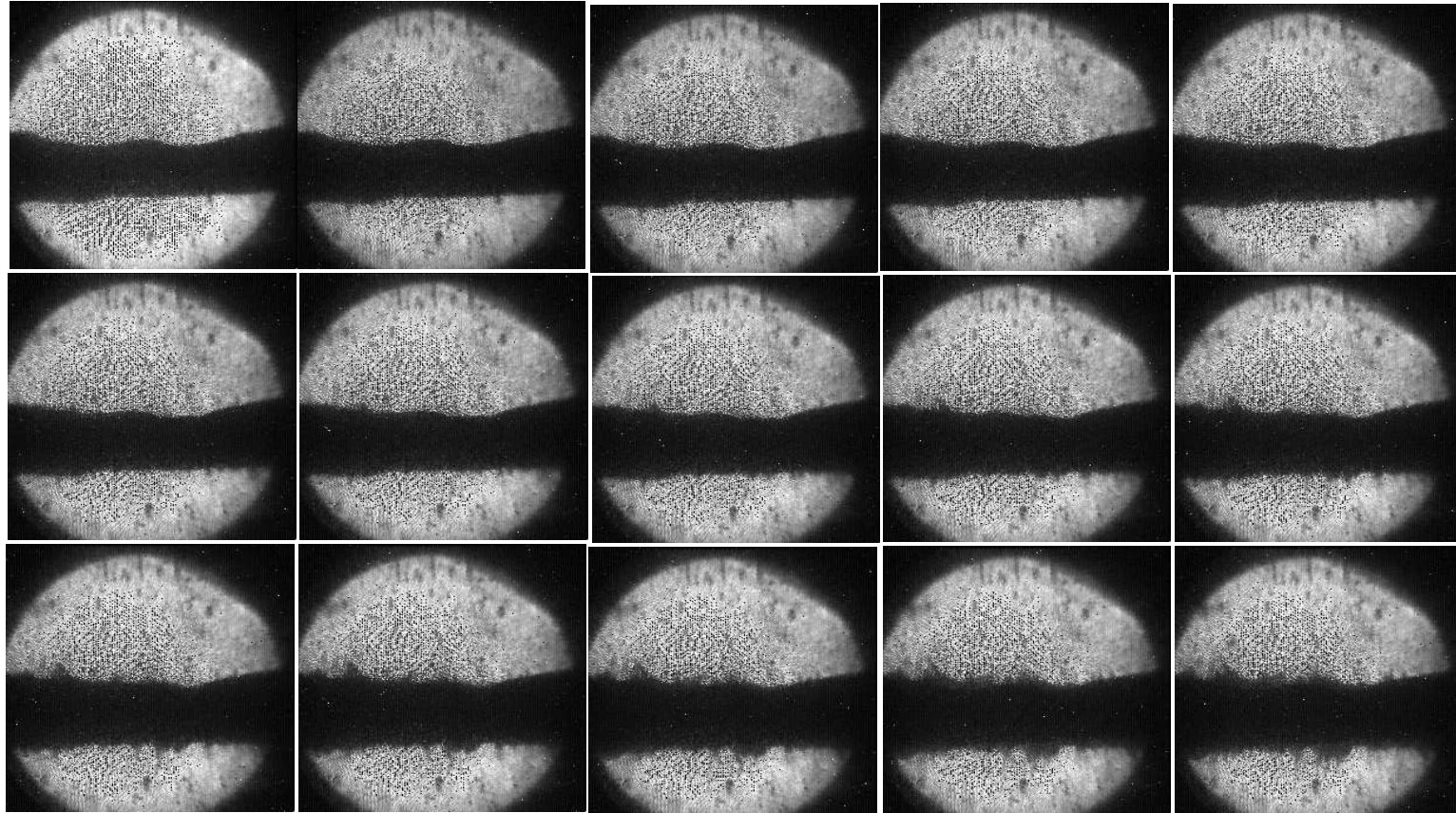
Figure B.1: Photo of continuous 15 frames of captured image. The timing for the 1st image is given in Table B.1. Shot number is 11004.
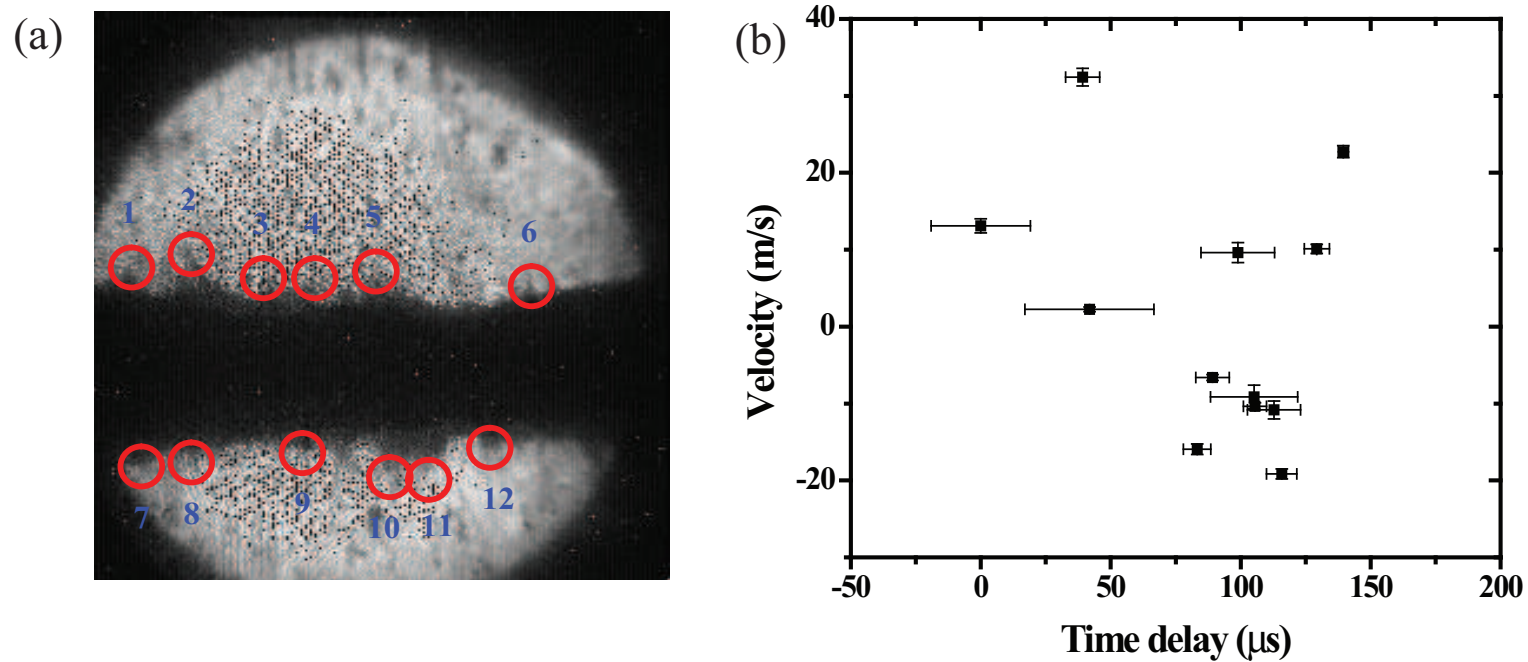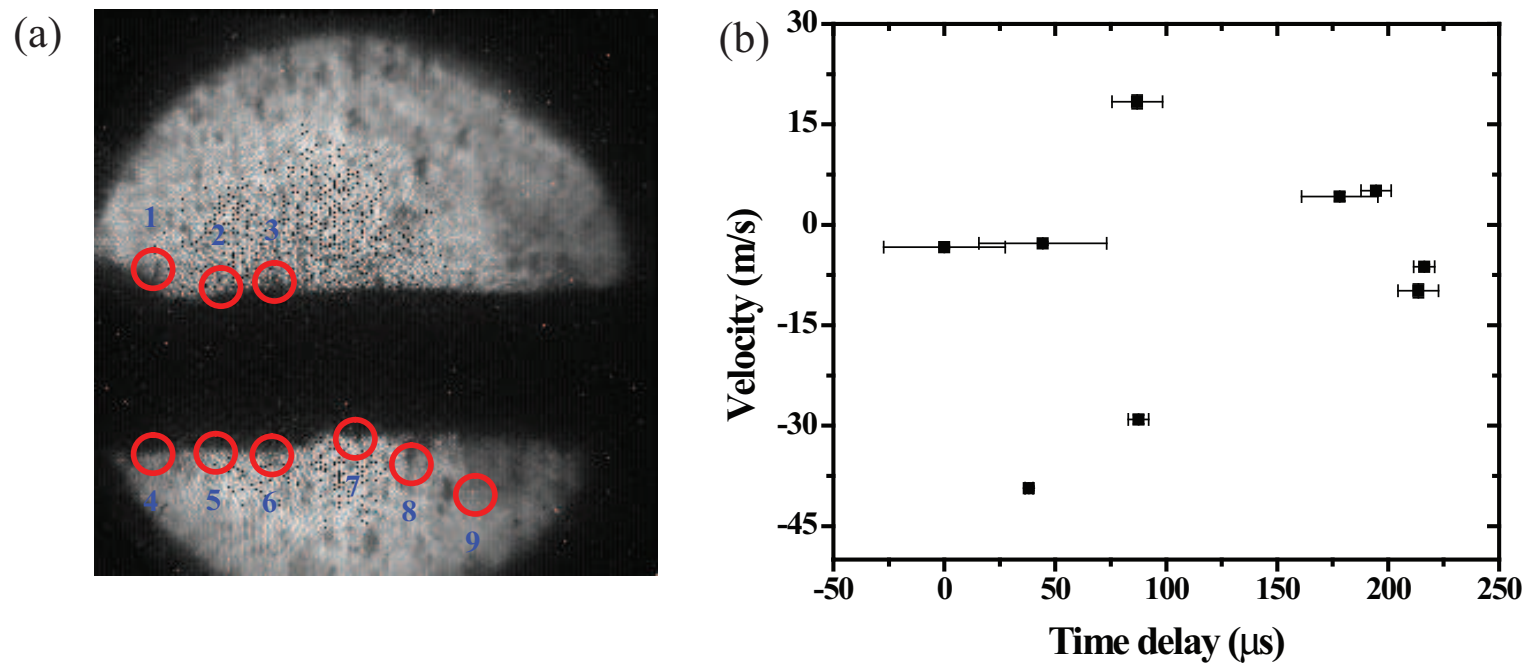
Figure B.2: Location on the Hg jet surface for velocity measurement of filaments. The numbers above red circles points the number of filaments that is used for velocity approximation. Shot number is 11004. a.) Illustration of measured filaments. b.) Velocity of filaments with it's onset time.
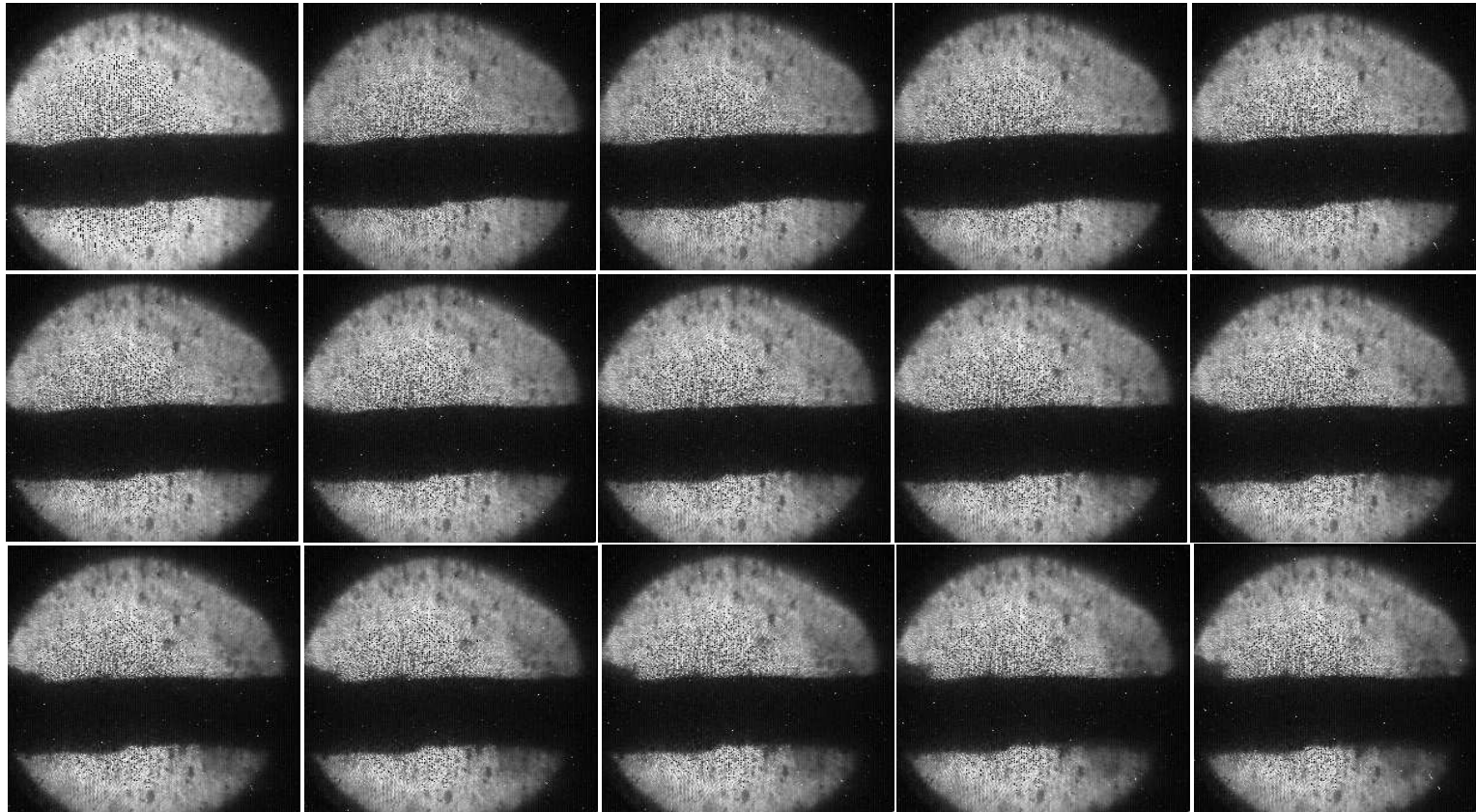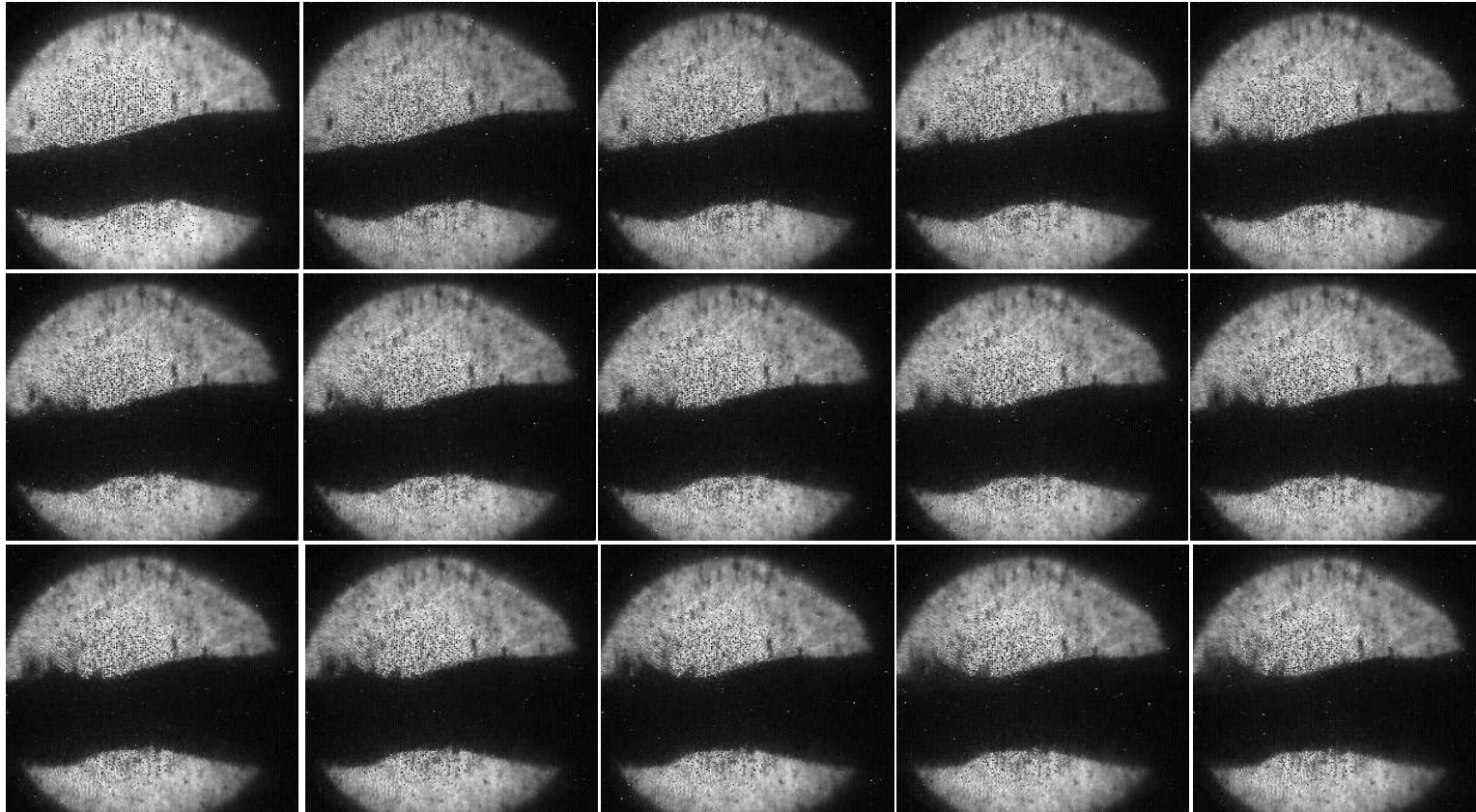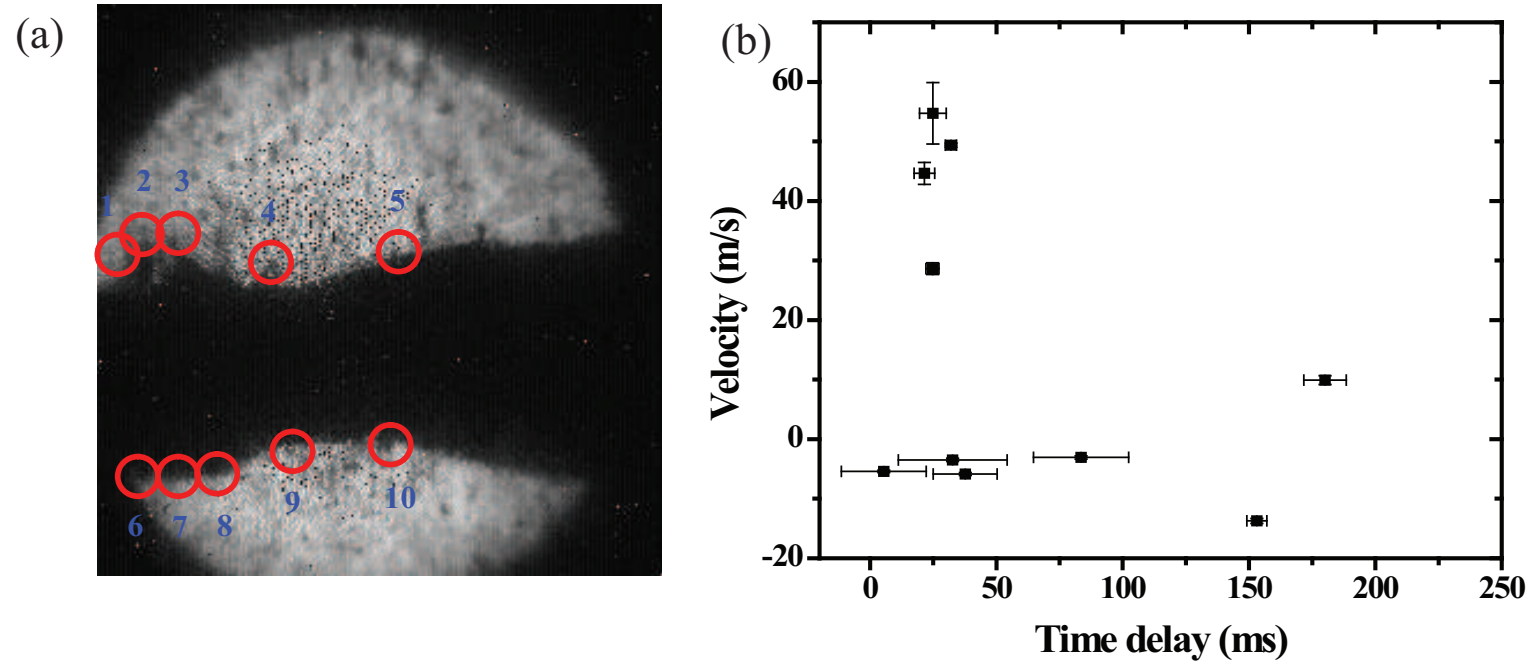
Figure B.3: Photo of continuous 15 frames of captured image. The timing for the 1st image is given in Table B.1. Shot number is 11007.

Figure B.4: Location on the Hg jet surface for velocity measurement of filaments. The numbers above red circles points the number of filaments that is used for velocity approximation. Shot number is 11007. a.) Illustration of measured filaments. b.) Velocity of filaments with it's onset time.
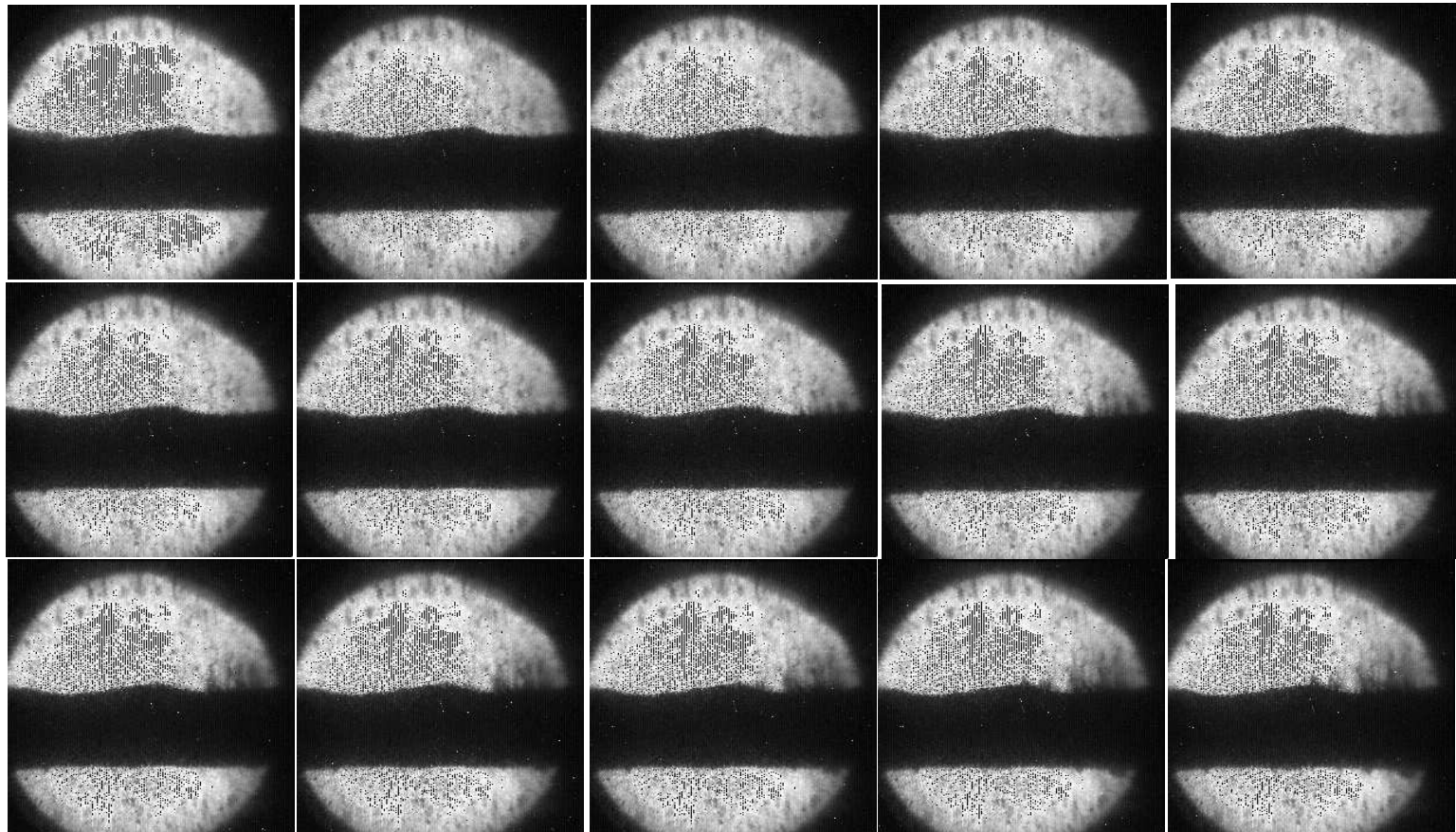
Figure B.5: Photo of continuous 15 frames of captured image. The timing for the 1st image is given in Table B.1. Shot number is 11010.
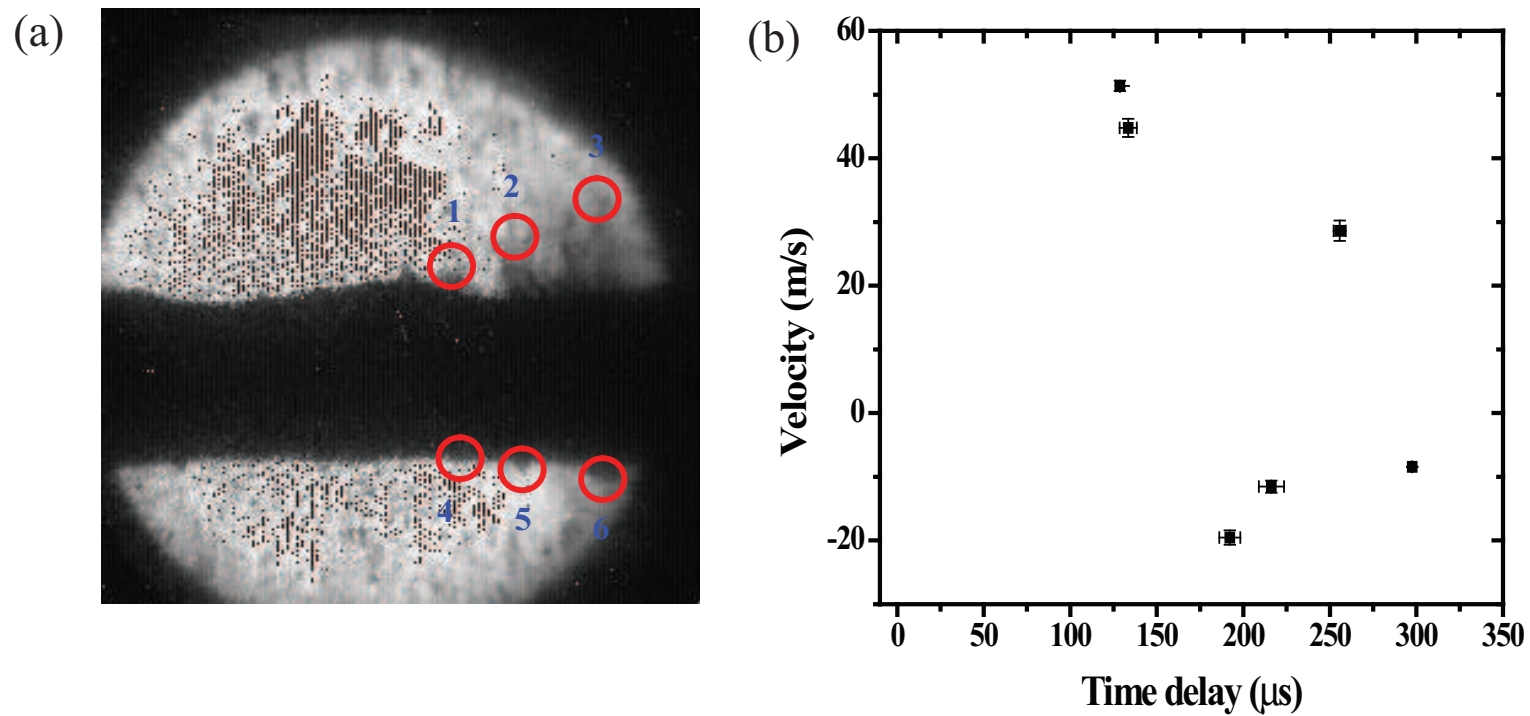
Figure B.6: Location on the Hg jet surface for velocity measurement of filaments. The numbers above red circles points the number of filaments that is used for velocity approximation. Shot number is 11010. a.) Illustration of measured filaments. b.) Velocity of filaments with it's onset time.
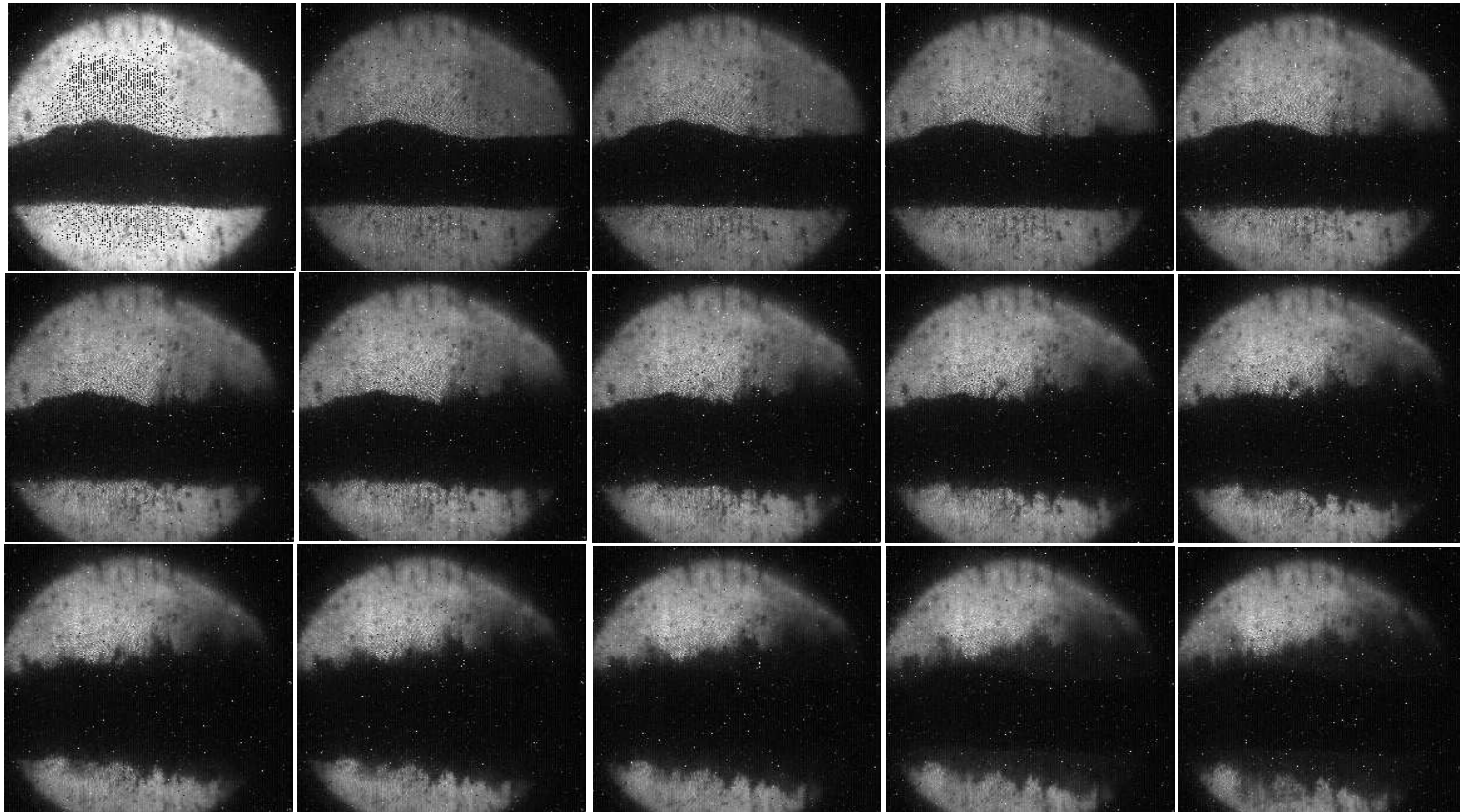
Figure B.7: Photo of continuous 15 frames of captured image. The timing for the 1st image is given in Table B.1. Shot number is 11021.
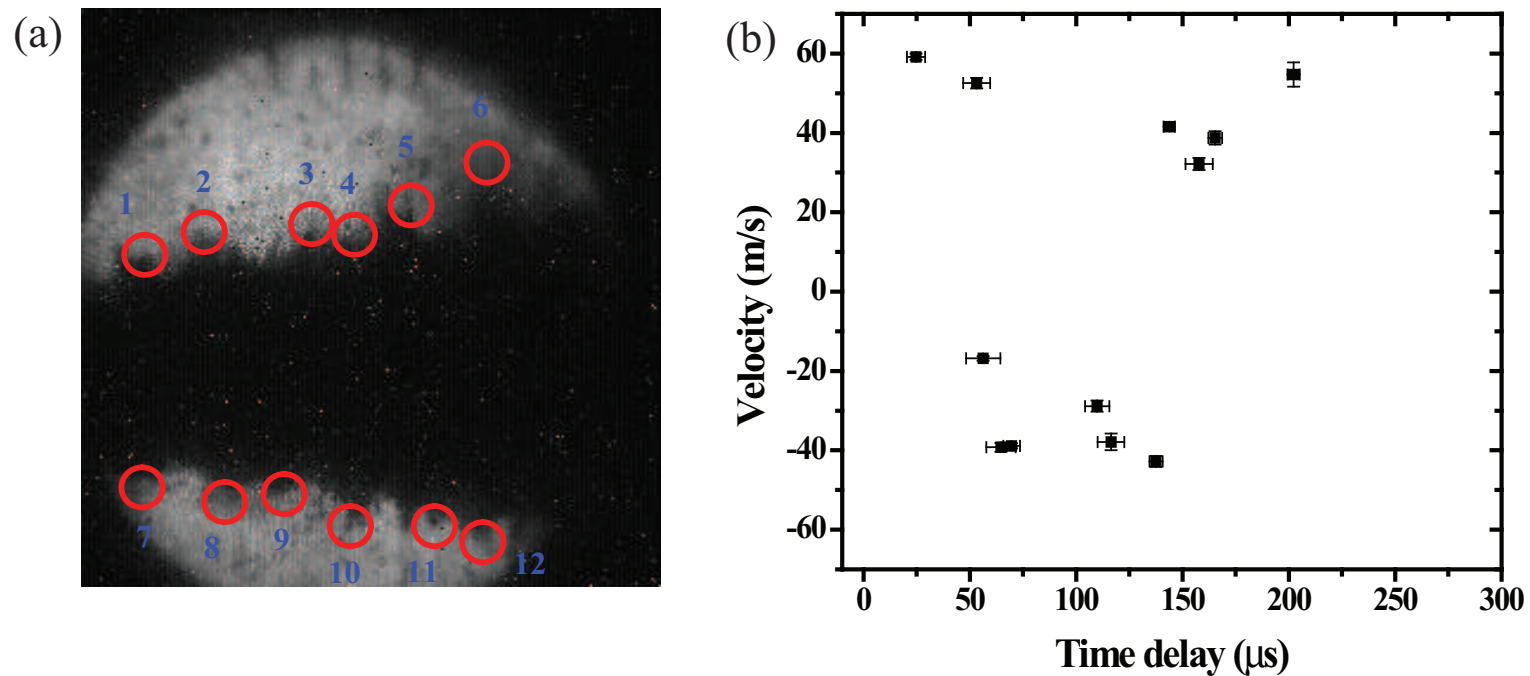
(a)

(b)

Figure B.8: Location on the Hg jet surface for velocity measurement of filaments. The numbers above red circles points the number of filaments that is used for velocity approximation. Shot number is 11021. a.) Illustration of measured filaments. b.) Velocity of filaments with it's onset time.

Figure B.9: Photo of continuous 15 frames of captured image. The timing for the 1st image is given in Table B.1. Shot number is 11032.

Figure B.10: Location on the Hg jet surface for velocity measurement of filaments. The numbers above red circles points the number of filaments that is used for velocity approximation. Shot number is 11032. a.) Illustration of measured filaments. b.) Velocity of filaments with it's onset time.
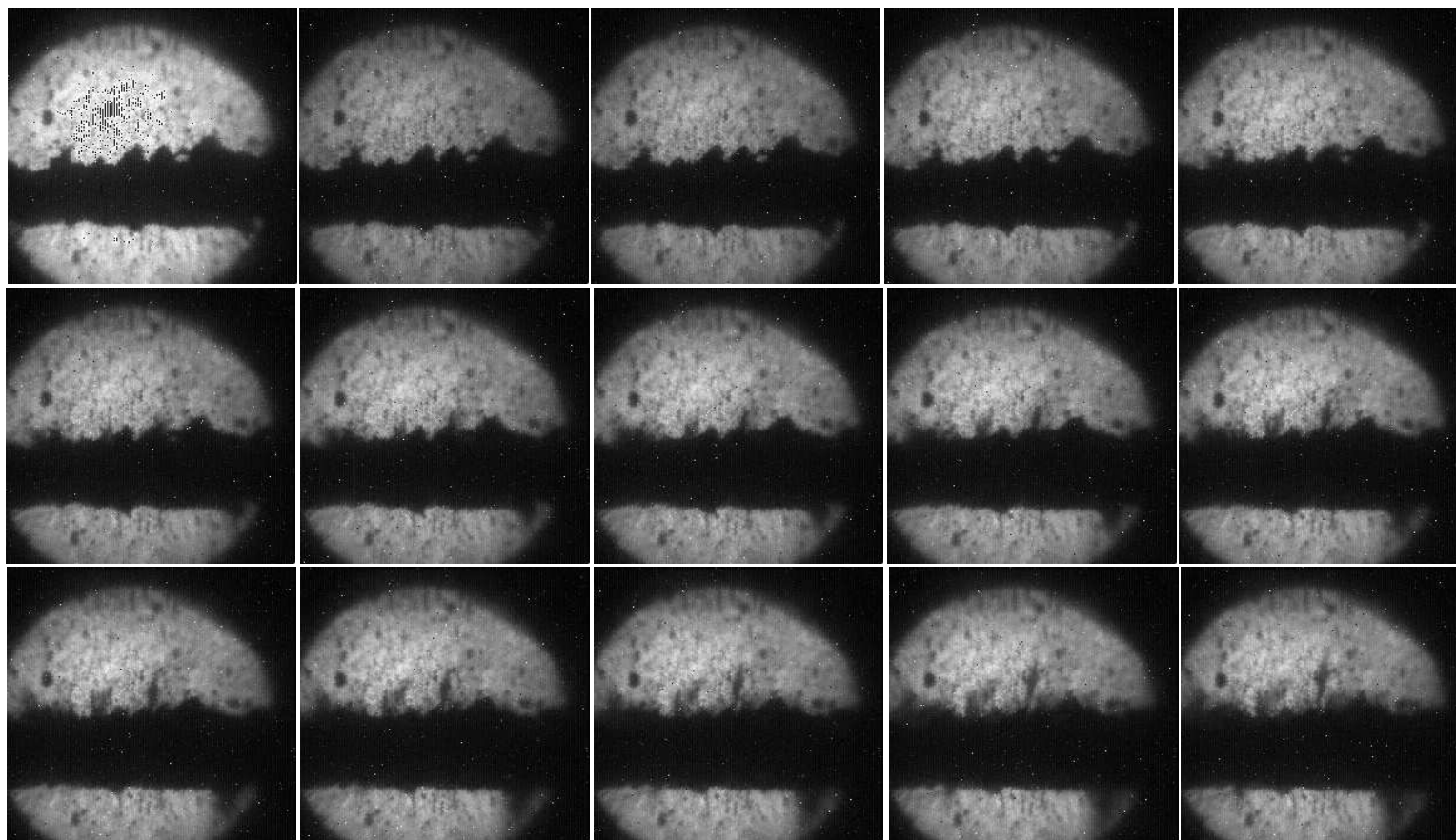
Figure B.11: Photo of continuous 15 frames of captured image. The timing for the 1st image is given in Table B.1. Shot number is 12031.
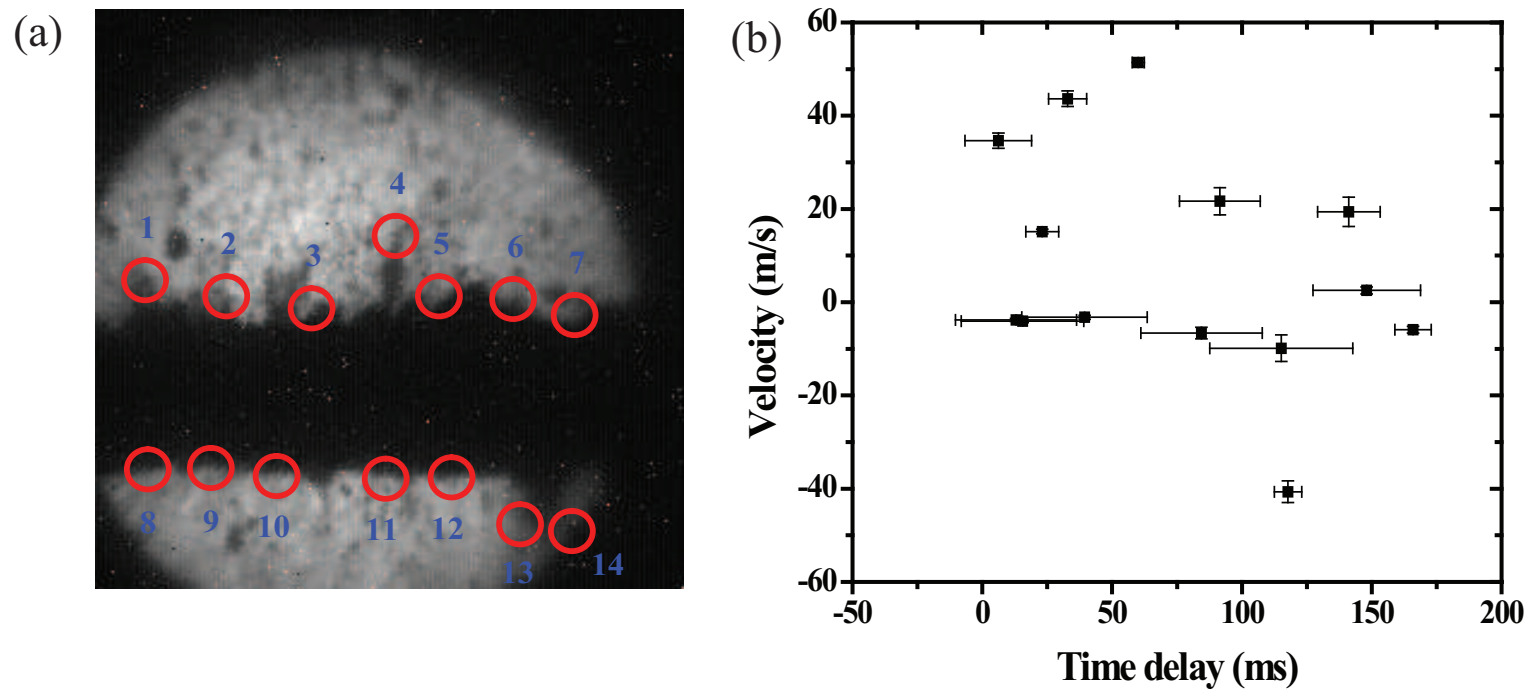
Figure B.12: Location on the Hg jet surface for velocity measurement of filaments. The numbers above red circles points the number of filaments that is used for velocity approximation. Shot number is 12031. a.) Illustration of measured filaments. b.) Velocity of filaments with it's onset time.
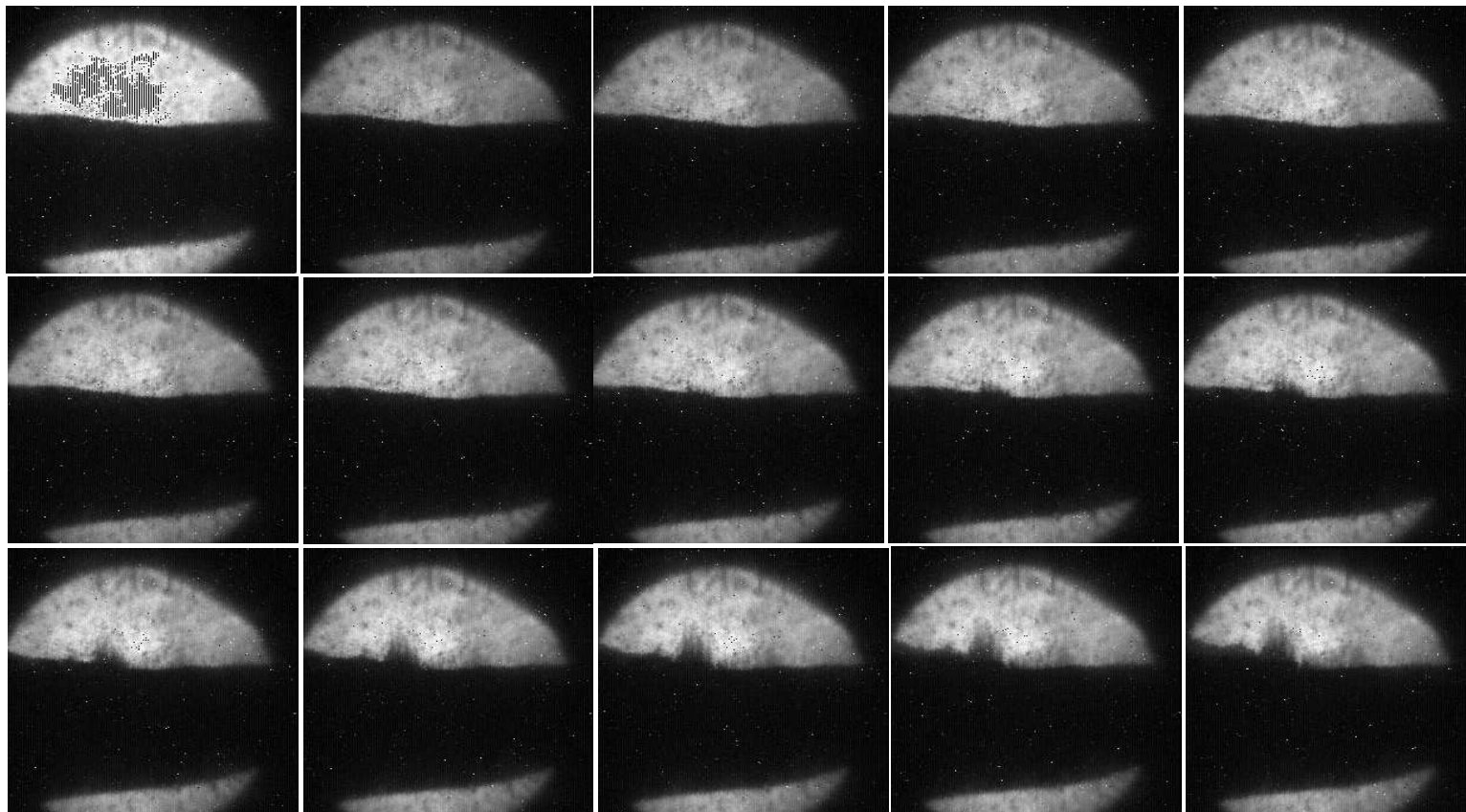
Figure B.13: Photo of continuous 15 frames of captured image. The timing for the 1st image is given in Table B.1. Shot number is 12032.
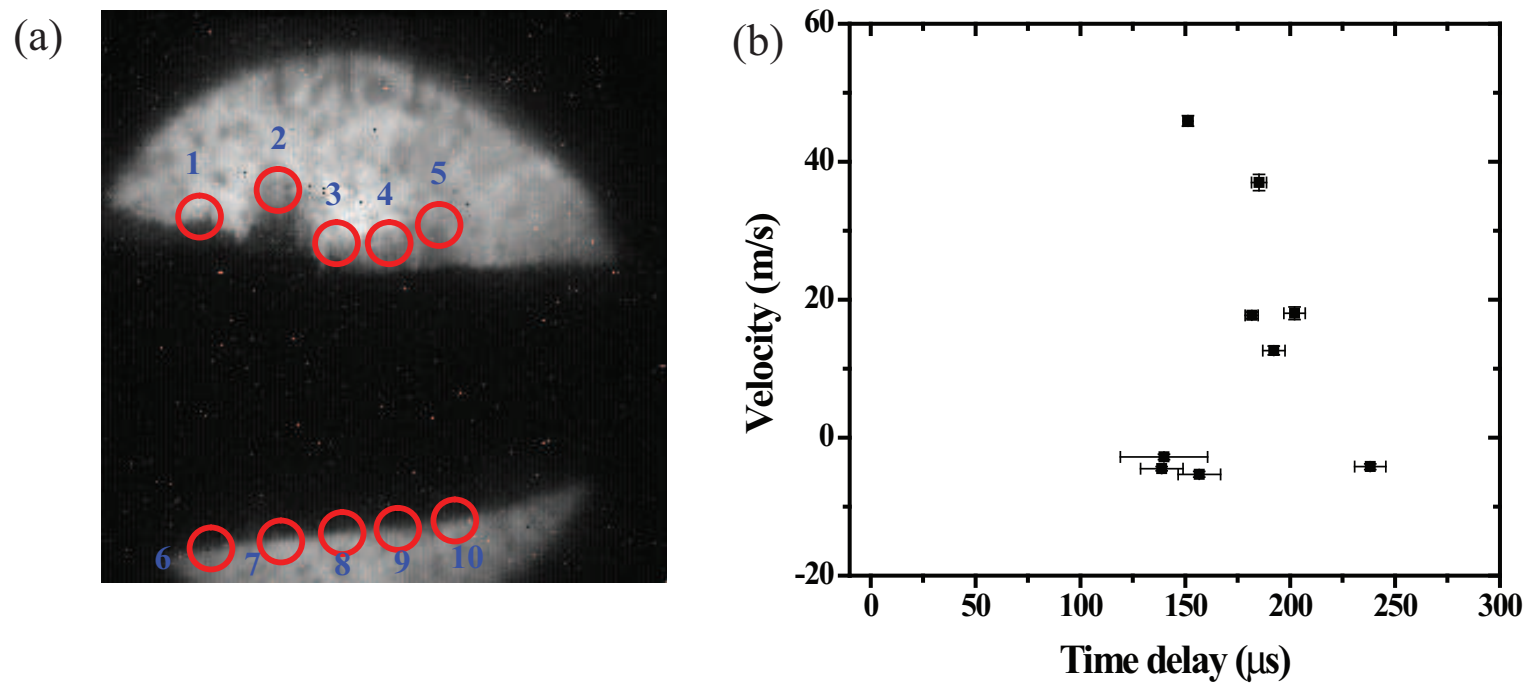
Figure B.14: Location on the Hg jet surface for velocity measurement of filaments. The numbers above red circles points the number of filaments that is used for velocity approximation. Shot number is 12032. a.) Illustration of measured filaments. b.) Velocity of filaments with it's onset time.

Figure B.15: Photo of continuous 15 frames of captured image. The timing for the 1st image is given in Table B.1. Shot number is 12033.

Figure B.16: Location on the Hg jet surface for velocity measurement of filaments. The numbers above red circles points the number of filaments that is used for velocity approximation. Shot number is 12033. a.) Illustration of measured filaments. b.) Velocity of filaments with it's onset time.
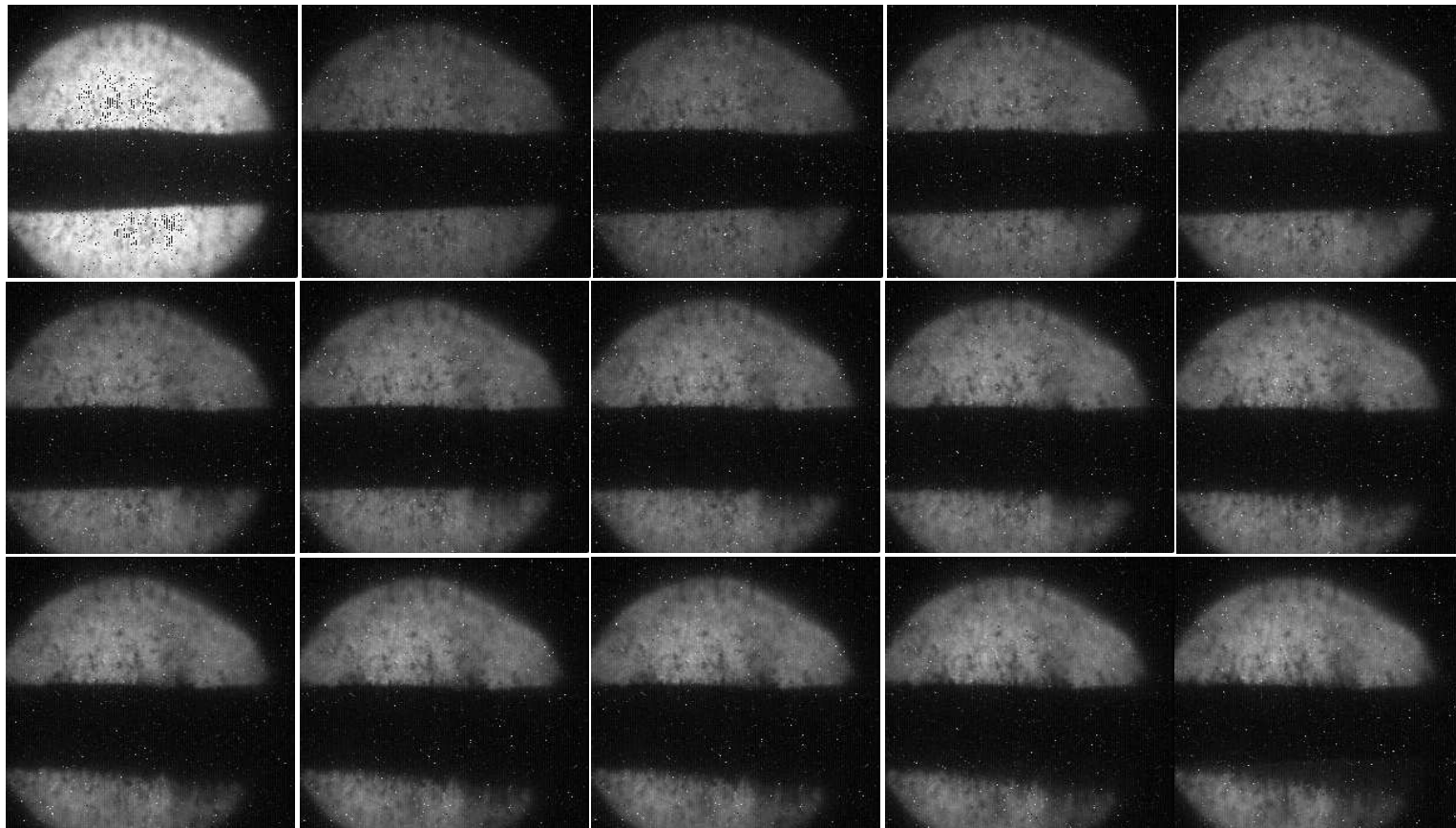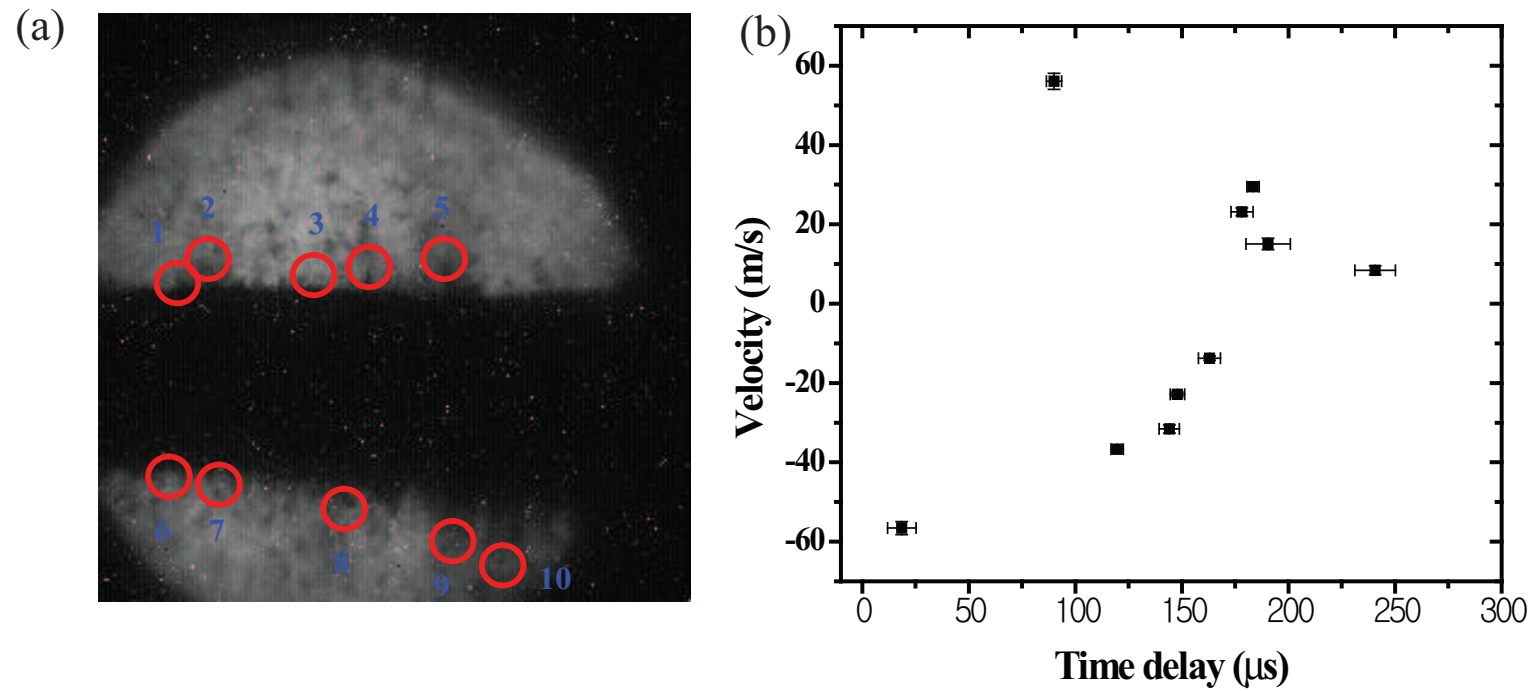
Appendix C

Mathematical Derivation for Chapter 2

C.1 The governing equations for MHD in cylindrical coordinates

The momentum equations in the (r, θ, z) coordinates in Fig. 2.2 can be written as follows:

$$
-\rho\left(v_r \frac{\partial v_r}{\partial r} + \frac{v_\theta}{r}\frac{\partial v_r}{\partial \theta} + v_z \frac{\partial v_r}{\partial z}\right) - \frac{\partial p_t}{\partial r} - \rho g \cos\theta + \eta\left(\frac{\partial^2 v_r}{\partial r^2} + \frac{1}{r}\frac{\partial v_r}{\partial r} + \frac{1}{r^2}\frac{\partial^2 v_r}{\partial \theta^2} + \frac{\partial^2 v_r}{\partial z^2}\right)
$$
$$
+ \frac{1}{\mu}\left(B_r \frac{\partial B_r}{\partial r} + \frac{B_\theta}{r}\frac{\partial B_r}{\partial \theta} + B_z \frac{\partial B_r}{\partial z}\right) = \rho \frac{\partial v_r}{\partial t}\ ,
$$

$$(C.1)$$

$$
-\rho\left(v_r \frac{\partial v_\theta}{\partial r} + \frac{v_\theta}{r}\frac{\partial v_\theta}{\partial \theta} + v_z \frac{\partial v_\theta}{\partial z}\right) - \frac{1}{r}\frac{\partial p_t}{\partial \theta} + \rho g \sin\theta + \eta\left(\frac{\partial^2 v_\theta}{\partial r^2} + \frac{1}{r}\frac{\partial v_\theta}{\partial r} + \frac{1}{r^2}\frac{\partial^2 v_\theta}{\partial \theta^2} + \frac{\partial^2 v_\theta}{\partial z^2}\right)
$$
$$
+ \frac{1}{\mu}\left(B_r \frac{\partial B_\theta}{\partial r} + \frac{B_\theta}{r}\frac{\partial B_\theta}{\partial \theta} + B_z \frac{\partial B_\theta}{\partial z}\right) = \rho \frac{\partial v_\theta}{\partial t}\ ,
$$

$$(C.2)$$

265

$$- \rho(v_r \frac{\partial v_z}{\partial r} + \frac{v_\theta}{r} \frac{\partial v_z}{\partial \theta} + v_z \frac{\partial v_z}{\partial z}) - \frac{\partial p_t}{\partial z} + \eta(\frac{\partial^2 v_z}{\partial r^2} + \frac{1}{r} \frac{\partial v_z}{\partial r} + \frac{1}{r^2} \frac{\partial^2 v_z}{\partial \theta^2} + \frac{\partial^2 v_z}{\partial z^2})$$

$$+ \frac{1}{\mu}(B_r \frac{\partial B_z}{\partial r} + \frac{B_\theta}{r} \frac{\partial B_z}{\partial \theta} + B_z \frac{\partial B_z}{\partial z}) = \rho \frac{\partial v_z}{\partial t} \ ,$$

(C.3)

where $p_t = p + \frac{\mathbf{B}^2}{2\mu}$. The magnetic induction equation in the (r, θ, z) coor-
dinate directions can be written as follows:

$$\frac{1}{\mu\sigma}[\frac{\partial^2 B_r}{\partial r^2} + \frac{1}{r} \frac{\partial B_r}{\partial r} + \frac{1}{r^2} \frac{\partial^2 B_r}{\partial \theta^2} + \frac{\partial^2 B_r}{\partial z^2}] + \frac{1}{r} B_r(r \frac{\partial v_r}{\partial r}) + \frac{1}{r} B_\theta \frac{\partial v_r}{\partial \theta} + B_z \frac{\partial v_r}{\partial z}$$

$$- \frac{1}{r} v_r(r \frac{\partial B_r}{\partial r}) - \frac{1}{r} v_\theta \frac{\partial B_r}{\partial \theta} - v_z \frac{\partial B_r}{\partial z} = \frac{\partial B_r}{\partial t} \ ,$$

(C.4)

$$\frac{1}{\mu\sigma}[\frac{\partial^2 B_\theta}{\partial r^2} + \frac{1}{r} \frac{\partial B_\theta}{\partial r} + \frac{1}{r^2} \frac{\partial^2 B_\theta}{\partial \theta^2} + \frac{\partial^2 B_\theta}{\partial z^2}] + \frac{1}{r} B_r(r \frac{\partial v_\theta}{\partial r}) + \frac{1}{r} B_\theta \frac{\partial v_\theta}{\partial \theta} + B_z \frac{\partial v_\theta}{\partial z}$$

$$- \frac{1}{r} v_r(r \frac{\partial B_\theta}{\partial r}) - \frac{1}{r} v_\theta \frac{\partial B_\theta}{\partial \theta} - v_z \frac{\partial B_\theta}{\partial z} = \frac{\partial B_\theta}{\partial t} \ ,$$

(C.5)

$$\frac{1}{\mu\sigma}[\frac{\partial^2 B_z}{\partial r^2} + \frac{1}{r} \frac{\partial B_z}{\partial r} + \frac{1}{r^2} \frac{\partial^2 B_z}{\partial \theta^2} + \frac{\partial^2 B_z}{\partial z^2}] + \frac{1}{r} B_r(r \frac{\partial v_z}{\partial r}) + \frac{1}{r} B_\theta \frac{\partial v_z}{\partial \theta} + B_z \frac{\partial v_z}{\partial z}$$

$$- \frac{1}{r} v_r(r \frac{\partial B_z}{\partial r}) - \frac{1}{r} v_\theta \frac{\partial B_z}{\partial \theta} - v_z \frac{\partial B_z}{\partial z} = \frac{\partial B_z}{\partial t} \ .$$

(C.6)

The Ampère's law can be written as

$$j_r = \frac{1}{\mu}(\frac{1}{r} \frac{\partial B_z}{\partial \theta} - \frac{\partial B_\theta}{\partial z}) \ ,$$

$$j_\theta = \frac{1}{\mu}(-\frac{\partial B_z}{\partial r} + \frac{\partial B_r}{\partial z}) \ ,$$

$$j_z = \frac{1}{\mu}(\frac{\partial B_\theta}{\partial r} - \frac{1}{r} \frac{\partial B_r}{\partial \theta}) \ ,$$

(C.7)

and the equation of continuity and the solenoidal condition for the magnetic field are

$$\frac{1}{r}\frac{\partial}{\partial r}(rv_r) + \frac{1}{r}\frac{\partial v_\theta}{\partial \theta} + \frac{\partial v_z}{\partial z} = 0 \ , \tag{C.8}$$

$$\frac{1}{r}\frac{\partial}{\partial r}(rB_r) + \frac{1}{r}\frac{\partial B_\theta}{\partial \theta} + \frac{\partial B_z}{\partial z} = 0 \ . \tag{C.9}$$

C.2 Derivation of Rayleigh's instability at an interface separating two flows in magnetic field

C.2.1 *kinematic boundary condition at interface*

We consider the (x, y, z) coordinate system in Fig. 2.1. A particle of fluid that is at some time on the free surface will always remain on the free surface. Then, since the equation of the free surface is $y - (\xi + a) = 0$, it follows that

$$\frac{D}{Dt}(y - (\xi + a)) = 0 \ . \tag{C.10}$$

Neglecting quadratically small terms, Eqn. (C.10) yields at the interface($y = \pm a$),

$$\frac{\partial \xi}{\partial t} + U_i \frac{\partial \xi}{\partial x} = \frac{\partial \phi_i}{\partial y} \tag{C.11}$$

In the region $(-a < y < a)$, the velocity potential ϕ_i must satisfy $\frac{\partial^2 \phi_1}{\partial x^2} + \frac{\partial^2 \phi_1}{\partial y^2} = 0$, $|\nabla \phi_1|$=finite. In the region $y > a$, $y < -a$, the velocity potential must satisfy $\frac{\partial^2 \phi_2}{\partial x^2} + \frac{\partial^2 \phi_2}{\partial y^2} = 0$, $|\nabla \phi_2|$=finite. In view of the shape of the interface, the solutions should be trigonometric in x, then the y dependence will be exponential. In view of the finite conditions of velocity potentials, the negative exponential should be rejected for ϕ_1 and the positive exponential should be rejected for ϕ_2. Therefore, the general solutions are

267

3878

$$\phi_1(x,y,t) = A_1 e^{(2\pi/\lambda)y} e^{i(2\pi/\lambda)(x-ct)} \ ,$$

3879
$$\phi_2(x,y,t) = A_2 e^{-(2\pi/\lambda)y} e^{i(2\pi/\lambda)(x-ct)} \tag{C.12}$$

3880   Imposing the kinematic conditions on these solutions, the coefficients are
3881 determined at $y = a$ and $y = -a$ respectively.
3882

$$\phi_1(x,y,t) = -i\epsilon(c - U_1)e^{i(2\pi/\lambda)(x-ct)} \ ,$$

3883
$$\phi_2(x,y,t) = i\epsilon(c - U_2)e^{i(2\pi/\lambda)(x-ct)} \tag{C.13}$$

3884   ,where $U_1 = U_1(a), \ U_2 = U_2(a)$.
3885

$$\phi_1(x,y,t) = i\epsilon(c - U_1)e^{i(2\pi/\lambda)(x-ct)}$$

3886
$$\phi_2(x,y,t) = -i\epsilon(c - U_2)e^{i(2\pi/\lambda)(x-ct)} \tag{C.14}$$

3887   ,where $U_1 = U_1(-a), \ U_2 = U_2(-a)$.
3888   Since the perturbed surface at $y = a$ and $y = -a$ are supposed to be
3889 symmetric, half of the jet section for the surface stability is considered in the
3890 following work.

3891 ## C.2.2 *hydrodynamic stability in magnetic field*

3892   Substituting the perturbed expressions into the equations of motion, ne-
3893 glecting second order terms in the perturbed quantities, and making use of the
3894 fact that U, P satisfy the flow equations and the current density in Lorentz
3895 force term can be represented using Ohm's law, we have the linearized equa-
3896 tions governing the motion of disturbance.
3897

$$\frac{\partial v'_{xi}}{\partial t} + U_i \frac{\partial v'_{xi}}{\partial x} + v'_{xi}\frac{dU_i}{dy}$$

3898
$$= -\frac{1}{\rho_i}\frac{\partial p'_i}{\partial x} - \frac{\sigma_i}{\rho_i}\mathrm{B}_y^2 v'_{xi} + \frac{\sigma_i}{\rho_i}\mathrm{B}_x\mathrm{B}_y v'_{yi} \tag{C.15}$$

3899

$$\frac{\partial v'_{yi}}{\partial t} + U_i \frac{\partial v'_{yi}}{\partial x}$$

$$= -\frac{1}{\rho_i}\frac{\partial p'_i}{\partial y} - \frac{\sigma_i}{\rho_i}\mathrm{B}_x^2 v'_{yi} + \frac{\sigma_i}{\rho_i}\mathrm{B}_x\mathrm{B}_y v'_{xi} \tag{C.16}$$

3900

3901 ,where $p'_i = f_i(c, \lambda, y)e^{i(2\pi/\lambda)(x-ct)}$.

3902 The perturbed velocity v'_x, v'_y are given

3903

$$v'_x = \frac{\partial \phi_1}{\partial x} = i(\frac{2\pi}{\lambda})A_1 e^{(2\pi/\lambda)y}e^{i(2\pi/\lambda)(x-ct)}$$

$$v'_y = \frac{\partial \phi_1}{\partial y} = (\frac{2\pi}{\lambda})A_1 e^{(2\pi/\lambda)y}e^{i(2\pi/\lambda)(x-ct)} \tag{C.17}$$

3904

3905 Putting Eqn. (C.17) into Eqn. (C.15)and Eqn. (C.16), equate the hydrody-

3906 namic pressures since it is isotropic, which leads to Rayleigh's stability equa-

3907 tion for the flow in magnetic field.

3908

$$\sigma_1 B_x B_y + i\sigma_1 B_x^2 = \sigma_1 B_y^2 i - \sigma_1 B_x B_y + \rho_1(\frac{\lambda}{2\pi})\frac{d^2 U_1}{dy^2} \tag{C.18}$$

3909

3910 ,where $U_1 = U_1(y)$.

3911 In the same manner, the Rayleigh's stability equation for the upper flow

3912 in magnetic field is be derived.

3913

$$\sigma_2 B_x^2 + \sigma_2 B_x B_y i = \sigma_2 B_y^2 - i\sigma_2 B_x B_y - \rho_2 i(\frac{\lambda}{2\pi})\frac{d^2 U_2}{dy^2} \tag{C.19}$$

3914

3915 ,where $U_2 = U_2(y)$.

C.2.3 *dynamic boundary condition at interface*

3916

3917 The difference of the normal stresses must be balanced by the normal stress

3918 induced by surface tension at the interface.

3919

$$(P_1 + \frac{\partial P_1}{\partial y}\xi + \frac{\partial^2 P_1}{\partial y^2}\xi + \ldots + p'_1) - (P_2 + \frac{\partial P_2}{\partial y}\xi + \frac{\partial^2 P_2}{\partial y^2}\xi + \ldots + p'_2) + \Gamma\frac{\partial^2 \xi}{\partial x^2} = 0 \tag{C.20}$$

3920

3921   , where Γ is surface tension.

3922   Considering the gravity force in the free surface waves, Eqn. (C.20) can be
3923   rewritten as follows.

3924

$$(\rho_2 - \rho_1)g\cos\theta + \rho_1(c - U_1)^2(\frac{2\pi}{\lambda}) + \rho_2(c - U_2)^2(\frac{2\pi}{\lambda})$$

$$+ \rho_1(c - U_1)\frac{dU_1}{dy} - \rho_2(c - U_2)\frac{dU_2}{dy} + iB_y^2(\sigma_1(c - U_1) + \sigma_2(c - U_2))$$

3925 $$+ B_x B_y(\sigma_2(c - U_2) - \sigma_1(c - U_1)) - \Gamma(\frac{2\pi}{\lambda})^2 = 0 \qquad \text{(C.21)}$$

3926   ,where $U_1 = U_1(a)$, $U_2 = U_2(a)$.

3927   Consider the case that $U_2 = 0, \frac{dU_2}{dy} = 0, \rho_2 = 0, \sigma_2 = 0$. This would corre-
3928   spond to the stationary fluid on the upper and the density and conductivity
3929   of the upper fluid are very small compared with these of the lower fluid. The
3930   wave velocity is represented as follow.

3931

$$c = [\quad -\rho_1\frac{dU_1}{dy} + B_x B_y \sigma_1 - iB_y^2\sigma_1 + 2(\frac{2\pi}{\lambda})\rho_1 U_1$$

$$\pm \sqrt{\rho_1^2(\frac{dU_1^2}{dy}) + 4(\frac{2\pi}{\lambda})\cos\theta g\rho_1^2 - 2B_x B_y \rho_1\sigma_1\frac{dU_1}{dy} + 2iB_y^2\rho_1\sigma_1\frac{dU_1}{dy}}$$

3932 $$\overline{+ B_x^2 B_y^2\sigma_1^2 - 2iB_x B_y^3\sigma_1^2 - B_y^4\sigma_1^2 + 4(\frac{2\pi}{\lambda})^3\rho_1\Gamma} \quad] \times \frac{1}{2(\frac{2\pi}{\lambda})\rho_1} \qquad \text{(C.22)}$$